

Automated Computational Techniques for High-throughput Image Analysis of Skin Structure

By

Osman Sharif Osman

A Thesis

Submitted for the Degree of Doctor of Philosophy

School of Science and Medicine

University of Buckingham

2015

Buckingham, United Kingdom

DECLARATION

I declare that this written submission represents my ideas in my own words and where others' ideas, work or words have been included, I have adequately cited and referenced the original sources.

Osman Sharif Osman

ACKNOWLEDGEMENTS

This thesis would not have been successful without help and support from God, my family, friends, my thesis supervisors and work colleagues which contribute in the preparation and completion of this research.

First, my gratitude to supervisors Professor Sabah A. Jassim, Dr. Joanne Selway and Dr. Kenneth Langlands for their support, invaluable guidance and encouragement that I will never forget. Special thanks to Professor Jassim for his guidance and invaluable suggestions in computational and mathematical works, and his support from the beginning to the end of my work. My deepest gratitude is also due to Dr. Langlands for his unfailing support, guidance and useful research ideas. I am appreciative of his academic and moral support during my thesis research and writing. I also gratefully thank Dr. Selway for her endless support, encouragement and hard work. Without her help, this work would not have been successful, and I would not have established the collaborations described herein.

I want to thank all my colleagues and friends in the lab for their help and support. Many thanks to Research Associate Parvathy Harikumar who helped prepare the histological specimens. Many thanks also to Research Fellow Dr Malgosia Kepczynska, who prepared the tissue and performed the manual analysis in the adipocyte measurement part of my work, and to Dr Mohamed Zaibi and Mr Ed Wargent who contributed in data acquisition.

I sincerely appreciate the support of my Head of Department, Professor Michael Cawthorne, and Research Officer Dr Claire Stocker for their encouragement and suggestions (and financial support in the case of Professor Cawthorne). I also would like to thank Professor Jonathan Arch, Professor Paul Trayhurn, and Professor John Clapham for their advice and encouragement.

Many thanks also to all the collaborators involved in this work. I would like to thank Mr David Melvin and Dr. Chris Lelliott of the Wellcome Trust Sanger Institute who provided the high-throughput micrographs, and also Dr. Veronique Bataille of Kings College London for help in the non-invasive skin analysis project and providing the silicone moulds.

My gratitude to Dr. Hisham Al-Assam (Lecturer in the Department of Applied Computing), for his support, encouragement and his meaningful ideas and suggestions in my computational work.

Special and deepest thanks go to Mrs. Julie Cakebread, Clore lab Department Administrator and Mr David Hislop, Laboratory Manager for providing managerial assistance and support in all respects and encouragement.

Most importantly, I would like to express my gratitude to my mother, my family and family-in-law for all their love, support and encouragement. I also would like dedicate this achievement to my father's soul.

Finally, my special thanks and love to my wife Shan who made my life vital and full of happiness for her support, encouragement and love. Without her I could never have completed my studies. Thanks to my daughter Lena and my son Land who ensured that I was never tired after a hard day's study. They will make me happy forever.

This thesis is dedicated to Shan, Lena and Land, and to all my family.

ABSTRACT

Biological image processing and analysis are concerned with enhancing and quantifying features that reflect different pathological states, based on the use of combinations of image processing algorithms. The integration of image processing and analysis techniques to evaluate and assess skin integrity in both human and mouse models is a major theme in this thesis. More specifically, this thesis describes computational systems for high-throughput analysis of skin tissue section images and non-invasive imaging techniques. As the skin is a largest organ in the mammalian body, and is complex in structure, manual quantification and analysis a hard task for the observer to determine an objective result, and furthermore, the analysis is complex in terms of accuracy and time taken.

To look at the gross morphology of the skin, I developed high throughput analysis based on an adaptive active contour model to isolate the skin layers and provide quantification methods. This was utilised in a study to evaluate cutaneous morphology in 475 knockout mouse lines provided by the Mouse Genetics Project (MGP) pipeline, that was generated by the Wellcome Trust Sanger Institute (WTSI). This is a major international initiative to provide both functional annotation of the mammalian genome and insight into the genetic basis of disease. I found 53 interesting adipocyte phenotypes, 18 interesting dermal phenotypes and 3 interesting epidermal phenotypes.

I also focussed on the analysis of collagen in the dermis of skin images in several ways. For collagen structure analysis, I developed a combined system of Gabor filtering and Fast Fourier Transform FFT. This analysis allowed the detection of subtle changes in collagen organisation. Using similar images, I also measured collagen bundle thickness by computing the maximum frequency of the FFT power spectrum. To assess collagen dynamics, I developed *k*-means clustering for segmentation based on colour distribution. The use of this approach allowed the measurement of dermal degradation with age and disease, which was not possible by existing means.

Obtaining human skin material to facilitate the drug discovery and development process is not an easy task. The manipulation, monitoring and cost of human subjects makes the use of mouse models more suitable for high-throughput screening. Therefore, I have

evaluated skin integrity from mouse tissue rather than human skin, however, mouse skin is thinner than human skin and many morphological features are easier to visualise in human skin, which has implications for analysis.

Skin moulds can be used to create an impression of the skin surface. Changes in texture of skin can reflect skin conditions. I developed a skin surface structure analysis system to measure the degree of change in texture of the human skin surface. The alterations detected in texture parameters in skin mould impressions reflected changes caused by sun exposure, ageing and many other clinical parameters. I compared my analysis with the existing Beagley-Gibson scoring system to find correlations between automated and manual analysis to inform a decision on the use of optimal methods. By removing subjectivity of manual methods, I was able to develop a robust system to evaluate, for example, damage resulting from UV exposure.

My experimental analysis indicated that techniques developed in this thesis were able to analyse both histological samples and skin surface images in high-throughput experiments. They could, therefore, make a contribution to biological image analysis by providing accurate results to help clinical decision making, and facilitate biological laboratory experiments to improve the quality of research in this field, and save time.

Overall, my thesis demonstrated that accurate analysis of the skin to gain meaningful biological information requires an automated system that can achieve feature extraction, quantification, analysis and decision making to find interesting phenotypes and abnormalities. This will help the evaluation of the effects of a specific treatment, and answer many biological questions in fields of cosmetic dermatology and drug discovery, and improve our understanding of the genetic basis of disease.

ABBREVIATIONS

ANOVA	Analysis of variance
BG	Beagley-Gibson scoring system
CH	Chow diet
CI	Confidence interval
CIELAB, L*a*b*	L* luminosity, a*&b* chromaticity colour space
<i>db/db</i>	Diabetic mouse
DFT	Discrete Fourier Transform
ECM	Extracellular matrix
FFT	Fast Fourier Transform
GLCM	Grey level co-occurrence matrix
H&E	Haematoxylin & eosin
HFD	High fat diet
HSV	Hue, saturation, value colour space
kNN	k-nearest neighbour classifier
KO	Knockout animals
LBP	Local binary pattern
MGP	Mouse Genome Project
MPM	Multiphoton microscopy
MRI	Magnetic resonance imaging
NIH	National Institutes of Health
O&G	Orcein and giemsa
OI	Orientation index
PAS	Periodic acid Schiff
RGB	Red, green, blue colour space
ROI	Region of interest
STD	Standard deviation
SVM	Support vector machine classifier
VIS	Visiopharm Integrator System
<i>wt</i>	Wild-type
WTSI	Wellcome Trust Sanger Institute

TABLE OF CONTENTS

ABSTRACT	IV
ABBREVIATIONS.....	VI
CHAPTER 1	1
1.1 INTRODUCTION AND MOTIVATION	1
1.2 SKIN STRUCTURE AND SKIN HISTOPATHOLOGY	3
1.2.1 <i>Layers of the Skin</i>	4
1.2.2 <i>Function of the Skin</i>	6
1.2.3 <i>Histology Staining Methods in Skin Analysis</i>	6
1.2.4 <i>Skin Ageing</i>	9
1.2.5 <i>Diabetes and Obesity</i>	12
1.3 BIOLOGICAL IMAGE PROCESSING AND ANALYSIS BACKGROUND.....	13
1.3.1 <i>Image Acquisition (Image Sources)</i>	13
1.3.2 <i>Image Processing</i>	16
1.3.3 <i>Image Analysis</i>	26
1.3.4 <i>Existing Biological Image Analysis Tools</i>	30
1.3.5 <i>Automated or Computational Biological Image Analysis</i>	33
1.4 RESEARCH AIM AND OBJECTIVES.....	37
CHAPTER 2	39
COLLAGEN ASSESSMENT IN HISTOLOGICAL SKIN SECTIONS.....	39
2.1 BACKGROUND	39
2.1.1 <i>Collagen in the Skin</i>	39
2.1.2 <i>Visualisation of Collagen in Skin</i>	39
2.2 AIMS AND OBJECTIVES.....	47
2.3 AUTOMATED COLLAGEN ASSESSMENT	47
2.3.1 <i>Collagen Orientation Assessment</i>	47
2.3.2 <i>Collagen Thickness Quantification</i>	63
2.3.3 <i>Collagen Dynamics</i>	74
2.4 DISCUSSION.....	88
CHAPTER 3	91
HIGH THROUGHPUT CUTANEOUS PHENOTYPE DETECTION AND QUANTIFICATION.....	91
3.1 BACKGROUND	91
3.1.1 <i>H&E Staining of Skin</i>	91
3.1.2 <i>Wellcome Trust Mouse Genome Project</i>	91
3.1.3 <i>Secondary Phenotyping from WTSI Resources</i>	93
3.1.4 <i>Skin Histopathological Image Analysis</i>	93
3.1.5 <i>Existing Skin Feature Quantification Techniques</i>	94
3.2 AUTOMATED CUTANEOUS PHENOTYPING BASED ON MORPHOLOGICAL FEATURES	96
3.2.1 <i>Skin Layer Segmentation using Active Contour Models</i>	96
3.2.2 <i>A Method for Automatic Skin Layer Segmentation</i>	100
3.2.3 <i>Quantification of Cutaneous Features</i>	112
3.2.4 <i>Automated Adipocyte Size and Number Quantification</i>	116
3.3 RESULTS AND DISCUSSION	125

3.3.1	<i>Data Sets and Experimental Protocol</i>	125
3.3.2	<i>Measurement of Skin Phenotypes in a High-throughput Screen</i>	125
3.3.3	<i>Quantification of Wild-type Data</i>	126
3.3.4	<i>Analysis of the Development Set</i>	130
3.3.5	<i>Analysis of the Full Dataset</i>	137
3.3.6	<i>Comparison with Other WTSI Phenotyping Data</i>	139
3.4	CONCLUSION AND FUTURE WORK.....	145
CHAPTER 4		149
NON-INVASIVE ASSESSMENT OF SKIN SURFACE STRUCTURE		149
4.1	INTRODUCTION.....	149
4.1.1	<i>Skin Surface Topography</i>	150
4.1.2	<i>Skin Surface Structure Analysis</i>	150
4.2	AIMS AND OBJECTIVES	155
4.3	TOWARDS AUTOMATIC SKIN TEXTURE ANALYSIS	156
4.3.1	<i>Clinical Parameters and Skin Impression Moulds (TwinsUK Database)</i>	156
4.3.2	<i>Manual Analysis Using Beagley-Gibson Scoring</i>	157
4.3.3	<i>Methods</i>	161
4.4	LOCAL BINARY PATTERN OF IMAGE-BASED TEXTURE ANALYSIS	164
4.4.1	<i>Evaluation and Results of LBP 3rd Neighbour Pixel Calculation</i>	166
4.4.2	<i>Evaluation and Results of LBP 6th Neighbour Pixel Calculation</i>	166
4.4.3	<i>A Block-based LBP Approach</i>	169
4.4.4	<i>The Uniform LBP Approach</i>	170
4.5	GREY LEVEL CO-OCCURRENCE MATRIX (GLCM) FEATURE-BASED ANALYSIS	172
4.5.1	<i>Calculating the GLCM of the Original Training Skin Mould Images</i>	173
4.5.2	<i>Evaluation of GLCM of Whole Images</i>	176
4.5.3	<i>Evaluation of GLCM of LBP Images</i>	177
4.6	DEVELOPMENT OF STRUCTURE-BASED ANALYSIS.....	178
4.6.1	<i>Feature Extraction from Skeletonized LBP Images</i>	178
4.6.2	<i>Structure-based Analysis using LBP (3rd Neighbour Pixel)</i>	183
4.6.3	<i>Structure-based Analysis of LBP (6th Neighbour Pixel)</i>	184
4.7	NOVEL METHODS PERFORMANCE COMPARED TO BG SCORING.....	185
4.8	COMPARISON WITH CLINICAL PARAMETERS	186
4.8.1.	<i>Correlation between BG Scores and Clinical Data</i>	186
4.8.2.	<i>Comparison of Structure-based Method with Clinical Parameters</i>	188
4.8.3.	<i>Correlating Structural Features with BG Scores</i>	191
4.9	DISCUSSION.....	193
CHAPTER 5		197
5.1	OVERALL CONCLUSION AND GENERAL DISCUSSION	197
5.1.1	<i>Application of Techniques to Different Image Datasets</i>	198
5.1.2	<i>Application of Computational Techniques in Industry</i>	199
5.2	FUTURE WORK.....	204
REFERENCES		207

TABLE OF FIGURES

Figure 1. 1: Overview of the organisation of the skin of mammalian.	3
Figure 1. 2: Upper layers of the skin.	4
Figure 1. 3: Examples of histological staining of <i>C57B16</i> mouse skin.	8
Figure 1. 4: Collagen (col) structure in the dermis.	11
Figure 1. 5: Dermal elastic fibres (EF).	12
Figure 1. 6: Limitations of the human eye and microscopy for visualizing small objects.	15
Figure 1. 7: Aperio ScanScope Scanner.	16
Figure 1. 8: Contrast stretching.	17
Figure 1. 9: Input and output produced using a linear filter (convolution filtering).	19
Figure 1. 10: Example of median filtering.	20
Figure 1. 11: Intensity thresholding.	22
Figure 1. 12: Principles of binary morphological erosion, dilation, closing and opening operators.	24
Figure 1. 13: Skeleton of a rectangle defined in terms of bi-tangent circles.	25
Figure 1. 14: Examples of skeletons and binary images.	26
Figure 1. 15: Image processing and analysis.	28
Figure 1. 16: Noise reduction using ImageJ.	32
Figure 2. 1: Picrosirius stained skin.	41
Figure 2. 2: Herovici stained mouse skin.	41
Figure 2. 3: Analysis of picrosirius stained skin.	50
Figure 2. 4: Analysis of picrosirius images and edge detection in 8 directions.	52
Figure 2. 5: The effect of hair follicles and sebaceous glands on the FFT power spectrum.	52
Figure 2. 6: Picrosirius stained reticular dermis from 3 months old <i>wt</i> mouse.	53
Figure 2. 7: FFT power spectra of Gabor filtered images.	54
Figure 2. 8: Ellipses generation from FFT power spectrum of Gabor filtered image.	55
Figure 2. 9: Overview of edge detection using a Gabor filter and collagen quantification in picrosirius images.	56
Figure 2. 10: Use of a multi-directional Gabor filter.	58
Figure 2. 11: Alterations in dermal integrity with age in <i>wt</i> animals.	59
Figure 2. 12: Increasing age demonstrates differential patterns of decline in collagen organisation in the different layers of the dermis in <i>wt</i> mice.	60
Figure 2. 13: Dermal collagen organisation in lean and diabetic mice.	62
Figure 2. 14: Maximum frequencies FFT power spectra from ageing mice.	64
Figure 2. 15: Power spectrum of two the image and measurement of collagen bundle thickness.	64
Figure 2. 16: Analysis of binary of maximum power spectrum.	66
Figure 2. 17: Representation of collagen bundles, and the two parameters of the bundle thickness T, and the bundle spacing BS.	67
Figure 2. 18: Collagen bundle thickness and spacing plots.	68
Figure 2. 19: Flow diagram for collagen bundle thickness quantification.	70
Figure 2. 20: Generation and measurement of ellipses.	71
Figure 2. 21: The result of collagen bundle thickness in cross-polar images of picrosirius stained mouse skin from different animals at age 3, 12, and 20 months.	72
Figure 2. 22: Collagen bundle thickness in diabetic and misty models.	72
Figure 2. 23: Collagen auto-fluorescent confocal imaging in mouse skin.	73
Figure 2. 24: Colour filtering and segmentation.	76
Figure 2. 25: Colour filtering and segmentation in cropped ROI images.	77
Figure 2. 26: Segmentation of images using <i>k</i> -means clustering from the entire snapshot of <i>wt</i> mouse.	80
Figure 2. 27: <i>k</i> -means clustering method to assess collagen dynamics and age in <i>wt</i> mice.	81

Figure 2. 28: ROI selection in a typical Herovici stained image of <i>wt</i> mouse.	83
Figure 2. 29: Segmentation using <i>k</i> -means clustering without thresholding.	84
Figure 2. 30: Quantification of the ratio of blue pixels to red pixels in different age groups without post-process thresholding in <i>wt</i> animals.	84
Figure 2. 31: Automated ROI cropping and removing image background.	86
Figure 2. 32: <i>k</i> -means clustering method with thresholding.	87
Figure 2. 33: Collagen dynamics in an ageing series in <i>wt</i> mice.	87
Figure 2. 34: Collagen dynamics in an ageing diabetic series.	88
Figure 3. 1: Overview of the functional annotation process by the Mouse Genome Project (MGP) at the start of this project.	92
Figure 3. 2: Image segmentation with existing methods.	97
Figure 3. 3: Result of active contour- based segmentation in grayscale image.	101
Figure 3. 4: Result of active contour-based segmentation using absolute difference of greyscale.	101
Figure 3. 5: Use of RGB colour space.	104
Figure 3. 6: HSV colour space.	105
Figure 3. 7: Segmentation process using the active contour model applied to H&E stained image and segmented image after 1000 iterations.	106
Figure 3. 8: Generating an initialization curve.	106
Figure 3. 9: Active contour iterations and segmented epidermis and dermis region.	107
Figure 3. 10 Image pre-processing for epidermal segmentation.	108
Figure 3. 11: Epidermis and dermis segmentation.	109
Figure 3. 12: Adipocyte segmentation and quantification.	110
Figure 3. 13: Result of active contour-based segmentation.	111
Figure 3. 14: The development of thickness measurements.	113
Figure 3. 15: Skeletonization process and flowchart of skin layer depth quantification.	114
Figure 3. 16: An explanation of manual method for calculating size on an individual adipocyte (actual cell represented in red).	115
Figure 3. 17: Transformation to HSV colour space.	118
Figure 3. 18: Use of background subtraction to improve adipocyte segmentation.	118
Figure 3. 19: Use of morphological operators to improve fat segmentation.	119
Figure 3. 20: Three typical examples of comparison between manual and automated methods. Segmented adipocytes using automated method include cells overall the image including small cells. Note that all cells in the image were counted with the automated method.	122
Figure 3. 21: Comparison of automated and manual methods to determine adipocyte size in a model of obesity.	122
Figure 3. 22 Comparing the automated technique with the imageJ macro tool in terms of segmentation and quantification.	123
Figure 3. 23: Adipocytes size distribution in chow and high fat diet of gonadal adipose sections using manual and automatic quantification method.	124
Figure 3. 24: Adipocyte quantification of gonadal adipose tissue using different methods.	124
Figure 3. 25: Effect of diet on epidermal depth in <i>wild-type</i> animals.	127
Figure 3. 26: Effect of diet on dermal measurement in <i>wild-type</i> animals.	128
Figure 3. 27: Effect of diet on adipocyte size in <i>wild-type</i> animals.	129
Figure 3. 28: Comparison of adipocyte size distributions between specific knockouts and <i>wt</i> animals. .	131
Figure 3. 29: Images of genotypes with that influence adiposity compared to <i>wt</i> from development data set (202 images at 20X magnification).	132
Figure 3. 30: Adipocytes distribution in <i>wild-type</i> animals in development data set.	133
Figure 3. 31: Dermis measurements in development data.	134
Figure 3. 32: Epidermis depth measurements in development data.	135
Figure 3. 33: Adipocyte quantification result of development data.	136
Figure 3. 34: Number of hits in each skin layer and overlap.	137

Figure 3. 35: Venn diagram of the cutaneous and metabolic phenotypes.	139
Figure 3. 36: Epidermal depth in four genotypes in relation to <i>wt</i>	142
Figure 3. 37: The dermal depth in 24 different gnotypes in relation to <i>wt</i>	142
Figure 3. 38: Adipocyte size and numbers in eight different genotypes in comparison to <i>wt</i> skin.	144
Figure 3. 39: Segmentation of immature keratinocytes and hair follicles.	148
Figure 3. 40: Colour normalization.	148
Figure 4. 1: Example images representing BG categories.	154
Figure 4. 2: Correlation of observer scoring for all images using BG score.	158
Figure 4. 3: Correlation of observer scoring in images of silicone moulds from sun exposed skin.	159
Figure 4. 4: Correlation of observer scoring in images of silicon moulds from sun protected skin.	160
Figure 4. 5: Example of an SVM classifier with an optimal hyper-plane between the two classes of support vectors.	163
Figure 4. 6: Calculation of the LBP value for each pixel.	164
Figure 4. 7: LBP transformation outputs.	165
Figure 4. 8: Texture based analysis using 3rd LBP neighbourhood.	167
Figure 4. 9: Texture based analysis using 6th LBP neighbourhood.	168
Figure 4. 10: Block-based LBP feature extraction.	169
Figure 4. 11: Comparison of LBP using 4 blocks with radius=6 with BG Scores.	170
Figure 4. 12: Comparison of uniform LBP with radius = 6 performance with BG scores.	171
Figure 4. 13: GLCM analysis.	172
Figure 4. 14: Four directions for finding the relationship between pixels to calculate texture features. ...	172
Figure 4. 15: Illustration of the methodology of GLCM texture based analysis.	174
Figure 4. 16: Fourteen feature measurements from twins from the training data set for arm and face skin images.	175
Figure 4. 17: Comparison of GLCM grading scores with BG scores.	176
Figure 4. 18: Comparison of GLCM of LBP image grading scores with BG scores.	177
Figure 4. 19: Difference between the binary of the original image without LBP transformation.	180
Figure 4. 20: Overview of the structure- based analysis process.	181
Figure 4. 21: Inverse skeletonised images of arm and face.	182
Figure 4. 22: Comparison of structure-based LBP (r=3) performance with BG Scores.	183
Figure 4. 23: Comparison of structure-based LBP (r=6) performance with BG Scores.	184
Figure 4. 24: Comparison of BG scores with BMI.	187
Figure 4. 25: Comparison of BG scores and age.	187
Figure 4. 26: Comparison of LBP structure-based scores and BMIs.	189
Figure 4. 27: Comparison of LBP structure-based scores and age.	190
Figure 4. 28: Correlation between features from structure-based analysis with BMI.	191
Figure 4. 29: Correlation between various structural features and BG scores in sun protected skin.	192
Figure 4. 30: Correlation between structural features in sun exposed skin and BG scores.	193

TABLE OF TABLES

Table 2. 1: Correlation of ageing with collagen structure in papillary and reticular dermis using FFT with and without edge detection.	57
Table 2. 2: Statistical analysis of diabetic skin data.	62
Table 2. 3: Average measurements of bundle thickness and spacing of replicated animal in one age group (3 months).	67
Table 2. 4: Average bundle thickness and bundle spacing at different ages.	67
Table 3. 1: Comparison of typical measurements from a subset of adipocytes obtained by manual and automated methods.	121
Table 3. 2: Knockout mice whose phenotype impacted on the dermis, epidermis and adipose.	138
Table 3. 3: A typical hit map of phenotyping information curated by the MGP for four genotypes with epidermal impact.	140
Table 3. 4: A typical hit map of phenotyping information curated by the MGP for 21 genotypes with dermal impact.	141
Table 3. 5: A typical hit map of phenotyping information curated by the MGP for seven genotypes with adipocyte impact.	143
Table 4. 1: Clinical information from the TwinsUK phenotyping clinic.	157
Table 4. 2: Matrix of scores and calculation of Cohen’s kappa for all images.	158
Table 4. 3: Matrix of scores and calculation of Cohen’s kappa for sun exposed silicone mould images.	159
Table 4. 4: Matrix of scores and calculation of Cohen’s kappa for sun protected silicone mould images.	160
Table 4. 5: Typical structural information from 8 measurements extracted from images of the arm and face.	183
Table 4. 6: Summary of automated measurements and BG scoring.	185

CHAPTER 1

1.1 Introduction and Motivation

In this thesis, I discuss measuring progressive changes in skin structure caused by aging and pathological mechanisms, and also changes that are caused by environmental factors such as sun exposure. The techniques of image processing and analysis have a critical role in histopathology by providing accurate diagnosis, and reducing time and laboratory costs. Automated image analysis enables investigation of therapies that reverse damage and abnormalities, and could theoretically replicate the expertise of a specialist in clinical and cosmetic dermatology. The skin is a fascinating tissue to study as it can reveal evidence of inflammation, hyperplasia, connective tissue disorders and underlying metabolic changes (in changes to the underlying fat layer) resulting from local and systemic influences.

The skin is the largest mammalian organ, and although apparently simple, it is a highly-organised tissue comprised of the epidermis, underlying dermis containing connective tissue and a deeper subcutaneous adipose layer. The overall structure of the skin is consistent throughout the body, but thickness and other skin features are different depending on function and location (Zaidi and Lanigan, 2010). Cutaneous integrity is known to degrade with chronological age, a process exacerbated by environmental stress with cosmetic and pathological implications (Sauermann et al., 2002). Strategies to mitigate or restore damaged matrix are highly desirable, thus objective morphological criteria and histological analysis are required to assess skin integrity.

Many aspects of dermatology and associated treatments are widely researched. This research requires detailed understanding of the skin structure and organisation, and can require quantitative measurements. Many research studies utilize manual methods for the quantification of skin features, which is a challenging task. Recently, however, there has been a move towards the automation of these techniques to improve accuracy and efficiency. This thesis is aimed at contributing to automation efforts in this area.

Chapter 1

The skin contains many features that change quantitatively and qualitatively due to both innate mechanisms such as chronological ageing and environmental factors such as UV exposure. Among the features existing in digital images of skin sections, texture is probably the most important feature to be studied in terms of orientation, size, length and variety of shapes. In any image, the texture can be recognized, but it is difficult to define it, thus efficient image analysis techniques are required to analyze the skin texture in a histological skin section. In some images there are many textures that have different physical properties, whilst some textures have similar properties such as colour and intensity. In the analysis of skin histology, texture of collagen is an important factor. For example, collagen orientation and organisation in the dermis can qualitatively discriminate different ages, and measuring skin integrity to discriminate disease and healthy states is an important tool for investigators.

Morphological changes in the skin layers indicate different clinical factors such as age, gender, body mass index (BMI) and disease. Classical manual analysis of skin morphology is a challenging task, and time consuming. This was the motivation behind developing automated morphological analysis, to measure alteration in all of three main skin layers by quantifying changes in the thickness of each of these layers, and (more specifically) the number and size of adipocytes in the subcutaneous layer, and collagen organisation.

Overall in this study, I aimed to identify features that characterized age- and disease-related changes in the skin, using novel automated methods to enhance, segment and analyze images acquired from different types of microscope platforms in both mouse and human samples, either from biopsies or non-invasive techniques.

For such research, a number of metrics are desired, including collagen organisation (particularly changes in texture), compartment size (to assess tissue loss), cell counting (for example, in assessing immune infiltration), levels of new collagen synthesis, measuring the thickness of each skin tissue layer and quantifying the subcutaneous fat (both area and number of cells). Ultimately, these analysis methods will facilitate accurate measurement of novel skin-restorative modalities.

1.2 Skin Structure and Skin Histopathology

The skin consists of three main layers. Firstly, the outer layer is the highly-organised epidermis, secondly the underlying connective tissue layer (dermis), and finally a deeper adipose layer (the subcutis) as illustrated in Figure 1.1.

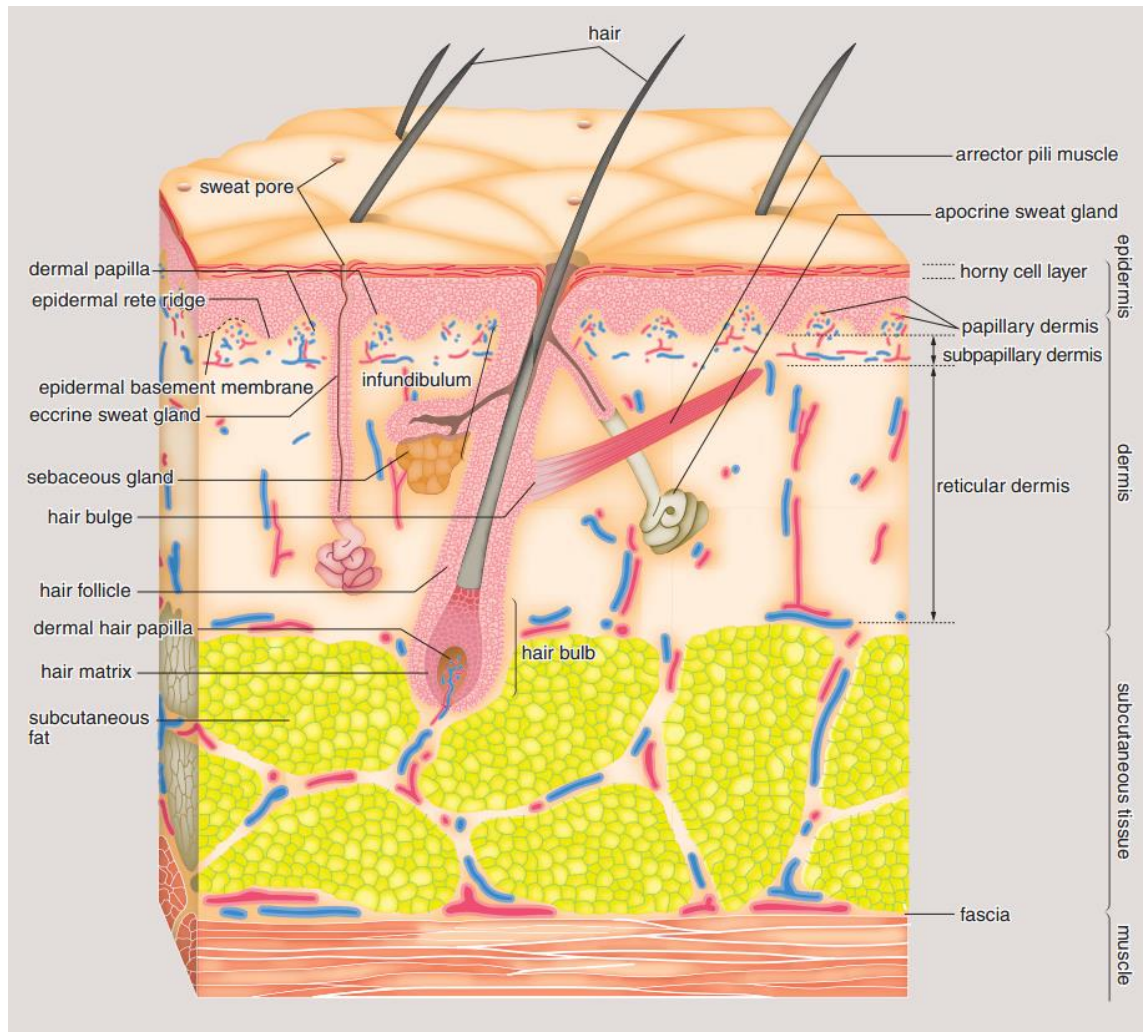


Figure 1. 1: Overview of the organisation of the skin of mammalian. Adopted from (Shimizu 2007).

1.2.1 Layers of the Skin

1.2.1.1 *The Epidermis*

The epidermis is the outer layer that serves as the physical and chemical barrier between the interior of the body and the exterior environment, and is composed of layers of keratinocytes but also contains melanocytes, Langerhans cells and Merkel cells. The epidermis is composed of four layers: the stratum basal (basal or germinativum cell layer), the stratum spinosum (spinous or prickle cell layer), stratum granulosum (granular cell layer) and the stratum corneum (horny layer) as shown in Figure 1.2.

Epidermal thickness depends on body site, e.g. on the eyelids it is about 0.05 mm, but on the soles of the feet and the palms of the hand (plantar skin), it is 0.8 ± 1.5 mm (Gawkrodger, 1997). In thick epidermis, an additional layer called stratum lucidum can be seen, which represents a transition between the stratum granulosum and the stratum corneum (Montagna et al., 1992).

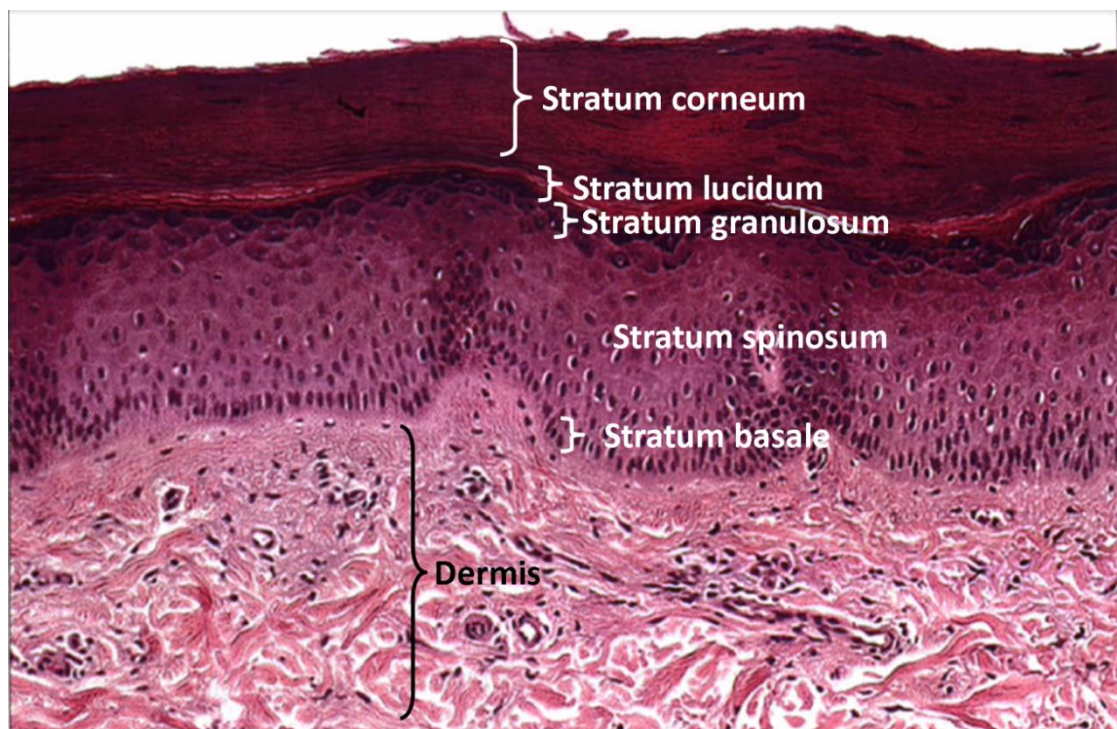


Figure 1. 2: Upper layers of the skin. The four epidermal layers are shown, as well as the underlying dermis (Bolognia, Jorizzo et al. 2008).

1.2.1.2 Dermis

The dermis is a deeper layer, providing structural support to the skin. The dermis is the area of supportive connective tissue between the epidermis and the underlying subcutis, and contains sweat glands, hair follicles, nerve cells and fibres, and blood and lymph vessels. The dermis is a relatively thick layer, varying in thickness from about 0.6 mm on the eyelids to 3 mm in plantar skin (Gherardi, 2008). The dermis is composed of two main layers: the papillary layer and the reticular layer. The papillary dermis is thin and lies below and connects with the epidermis. It contains thin and loosely arranged collagen fibres. The reticular layer contains thicker bundles of collagen that run parallel to the skin surface. The reticular dermis extends from the base of the papillary layer to the subcutis. The dermis is made up of fibroblasts, which produce collagen, elastin and proteoglycans, together with immuno-competent mast cells and macrophages (Shimizu, 2007). More than 70% of the dermis consists of collagen fibres that give this layer strength and resilience. Elastin in the dermis maintains normal elasticity, while proteoglycans provide viscosity and hydration. The dermal vasculature, lymphatic system, nervous cells and fibres are embedded within the fibrous tissue of the dermis, and there are also sweat glands, hair follicles and small amounts of striated muscle (depending on site).

1.2.1.3 The Subcutis (or Hypodermis)

The innermost layer of the skin is the subcutis. It lies below the dermis and it contains loose connective tissue and fat cells, and it is also known as the adipose tissue layer. The human body contains many fat depots, including fat surrounding different organs (visceral fat), but the subcutis contains the largest depot of fat in the human body (Burns et al., 2010). The thickness of the subcutis varies in different parts of the body: this layer can be up to 3 cm thick on the human abdomen. Subcutaneous fat is separated from the rest of the body by a vestigial layer of striated muscle (Burns et al., 2010). There are two type of adipocyte in the human body, white and brown adipocyte, which have different properties, for example white adipocytes have less cytoplasm due to the large fat store within the cell. Brown adipocytes have a large amount of cytoplasm with a centrally located nucleus and smaller pockets of fat stores within each cell. The location and function of white and brown fat in the human body is different. White adipocytes function as energy stores and brown adipocytes function as energy

consumers. Normal skin contains only white adipocytes, however, the size and number of adipocytes can change in different pathological states, so a decrease or increase in fat can indicate an abnormality e.g. obesity or diabetes (Britannica, 2014, Jo et al., 2009).

1.2.1.4 Dermal-epidermal Interface (Dermoepidermal Junction)

The boundary between the epidermis and dermis consists of a specialized aggregation of attachment molecules and connective tissue, collectively known as the basement membrane (Gawkrodger, 1997). This structure is complex and is of considerable interest as genetic defects in its composition leads to a variety of diseases, and it also serves as a target of autoimmune attack (Bolognia et al., 2008). The dermoepidermal junction flattens during ageing (Farage et al., 2010), which accounts in part for some of the visual signs of ageing.

1.2.2 Function of the Skin

The most obvious function of skin is to maintain a barrier that prevents the loss of fluids and protects against penetration by micro-organisms and UV radiation (Bolognia et al., 2008). However the skin provides several other functions: it regulates body temperature by blood flow and limits the inward and outward passage of water. The secretion of sweat and lipids causes the elimination of a number of harmful substances resulting from metabolic activity. The skin also provides flexibility and strength to protect the body from friction and impact wounds. Also, the skin can act as a sensory organ as it has a large number of nerve fibres and nerve endings. The skin also produces vitamin D when it is exposed to the sun, which is an important substance in bone health (Gawkrodger, 1997, Gherardi, 2008).

1.2.3 Histology Staining Methods in Skin Analysis

The use of special stains highlights features and different structures within a specimen. In terms of analysis, staining can also facilitate image segmentation. Several staining methods are used in histopathology for highlighting different features in skin tissue sections (Key, 2006), and the main ones used in this study are explained below:

Haematoxylin & eosin (H&E) is a general stain. It can allow assessment of overall structure. Acidic substances (i.e. nuclei) are stained blue and alkaline substances (the majority of other tissues) stain shades of pink. Figure 1.3a illustrates a skin tissue

Chapter 1

section stained with H&E (provided by The Wellcome Trust Sanger Institute [WTSI] Mouse Genome Project [MGP]; unless otherwise stated all other tissues were generated in the Buckingham Institute for Translational Medicine). This staining is widely used in morphological analysis, where each skin layer can be discriminated, which helps to measure the depth of layers.

Orcein and giemsa (O&G) staining is used to identify multiple features in the skin including collagen (staining pink), immune cells (red or purple), elastic fibres (black) and nuclei (blue) (Bancroft and Gamble, 2008, S.p.A., 2013). Figure 1.3b illustrates a skin section stained with O&G.

Picrosirius staining can illustrate various features (Figure 1.3c-e). Collagen organisation can be identified under cross polar microscopy (Figure 1.3e), so that the basket-weave arrangement, and size and type of the collagen can be identified. Bright-field picrosirius imaging illustrates the loops and whirls of collagen (red) and the epidermis (yellow) as illustrated in Figure 1.3c. Under fluorescent imaging, collagen can be visualized, while epidermis does not autofluoresce to the same extent, and 3D imaging is possible with confocal microscopy (Figure 1.3d).

Herovici's polychrome staining allows collagen dynamics and organisation to be assessed. Newly formed collagen appears in blue and mature collagens appear in purple or red. Figure 1.3f shows a skin tissue section stained with Herovici (Watt and Fujiwara, 2011, Turner et al., 2013).

Periodic acid Schiff staining (PAS) highlights glycated proteins in the basement membranes and blood vessel walls, where they appear in dark pink. This makes collagen more distinguishable from the basement membranes due to the appearance of collagen in very light pink (Bancroft and Gamble 2008). Figure 1.3g is a skin section that has been stained with PAS, and the basement membrane of the epithelium in dark pink is highlighted.

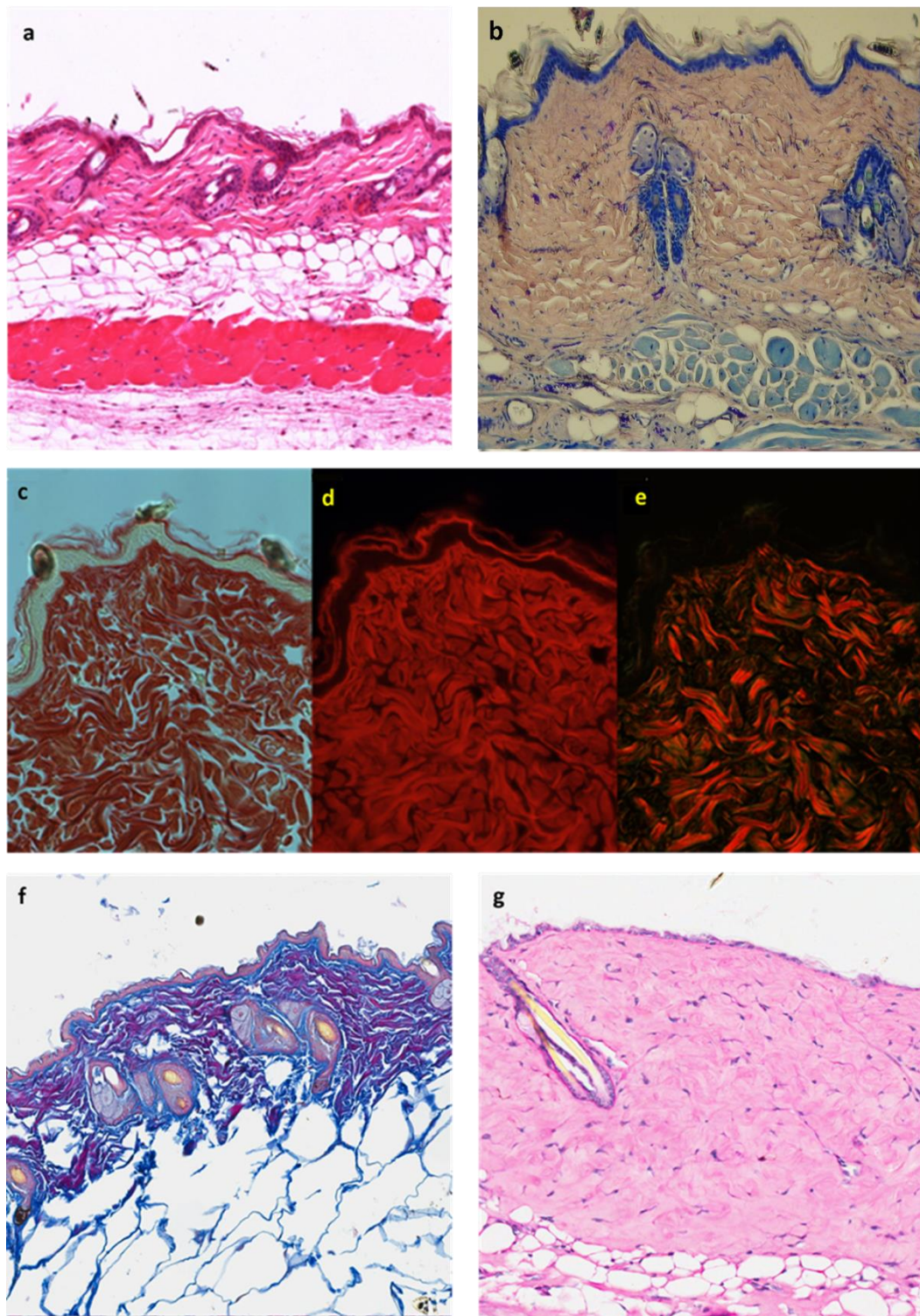


Figure 1. 3: Examples of histological staining of C57B16 mouse skin. a) typical H&E stained skin section (20X original magnification); b) an example of an O&G stained skin section at 20X optical magnification. c) picosirius stained skin section under bright-field, d) fluorescence (absorbance/emission ~581/644 nm), e) dark-field cross-polar optics (original magnification 90X). f) an example of a Herovici stained skin section (20X). g) An example of a PAS stained skin section (20X).

1.2.4 Skin Ageing

All organs lose functionality with age, and changes in the skin are the most visible signs of ageing (Sauermann et al., 2002). Skin ageing is induced by two main processes; intrinsic ageing, which is determined by genetics and time, and extrinsic ageing caused by environmental factors such as UV radiation. With ageing, greater variation in epidermal thickness is seen, and keratinocyte size is also increased (Farage et al., 2010). In addition, the number of pigment-containing cells (melanocytes) decreases, but the size of the remaining melanocytes increases (Farage et al., 2010). Aging skin appears paler and large pigmented spots (called age spots or liver spots) may appear in sun-exposed areas. The skin loses its strength and elasticity because of changes in connective tissue, either changes in elastic fibres (elastosis) or in loss or fibrosis (thickening) of collagen, leading to the appearance of wrinkles and ridges in elderly skin. The blood vessels of the dermis become more fragile, this leads to bruising and bleeding under the skin. In elderly skin, the sebaceous glands produce less oil, which can make it harder to keep the skin moist, resulting in dryness and itchiness. With increasing age, the subcutaneous fat layer may get thinner (Burns et al., 2010, Farage et al., 2010), which reduces its normal insulation and mechanical protection function. This increases the risk of skin injury and reduces the ability to maintain body temperature.

1.2.4.1 Epidermal Changes in Ageing

The most obvious change in the epidermis is that the dermal-epidermal junction is flattened in elderly skin and the surface contact between the epidermis and dermis is reduced, which causes a reduction in transfer of nutrients between these two layers. Cell turnover is decreased, so that the transit time goes from about 20 to about 30 days. The epidermis may grow thinner, and the number of melanocytes and Langerhans cells decrease (Sauermann et al., 2002, Puizina-Ivi, 2008, Farage et al., 2010). Keratohyalin granules decrease in the stratum granulosum. With age the skin becomes dehydrated, especially in stratum corneum, which exacerbates the appearance of wrinkles, where they often appear on the forehead, mouth and eyes. There are major clinical considerations in that wound healing is delayed (Minimas, 2007), and age-related malignancies are increasingly manifested, particularly basal and squamous cell carcinomas, which are among the most common human tumours.

1.2.4.2 Dermal Changes in Ageing

With increasing age, the dermal layer can lose up to 20% of its thickness. With ageing the collagen fibrils in the dermal layer become disorganised and deteriorate, and the accumulation of abnormal elastin (elastosis) is increased. In elderly skin, collagen is characterized by thickened fibrils that organise in bundles, with loss of “basket-weave” structure (Bailey et al., 1998). The ratio of collagen types also changes with the ageing, seen in the loss of type I collagen in aged skin, accompanied by the loss of type IV and VII collagens, which contribute to wrinkle formation. In aged skin, the collagen bundles appear thicker, with increased spaces between bundles compared to young skin (Gogly et al., 1997), as illustrated in Figure 1.4. Collagens decrease if the skin is exposed to UV due to the action matrix metalloproteinases (MMPs) that degrade collagen fibres, and UV radiation also induces a thickening and coiling of elastic fibres.

In the dermis, the elastic fibre network in younger people is composed of well distinguished oxytalan fibres oriented perpendicularly to the epidermis (Figure 1.5a). The oxytalan fibres that connect with elaunin fibres in the deep dermis run parallel to the epidermis (Figure 1.5b). Elastic fibres appear long and regularly positioned in the deep and middle of the dermis. In aged skin, oxytalan fibres fragment and thicken (Gogly et al., 1997). The amount of sugar and lipids decreases in elastin with age, and skin elasticity is gradually lost.

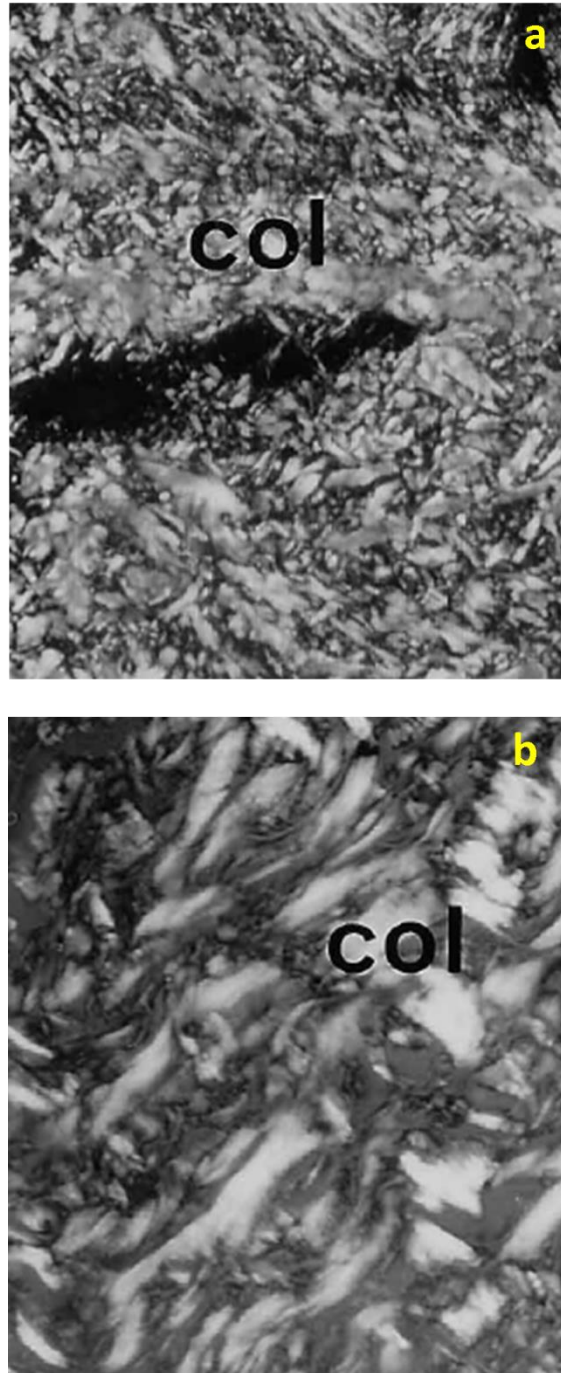


Figure 1. 4: Collagen (col) structure in the dermis. a) collagen in young skin, b) collagen in aged skin. Images at 150X original magnification, taken from (Gogly, Godeau et al. 1997).

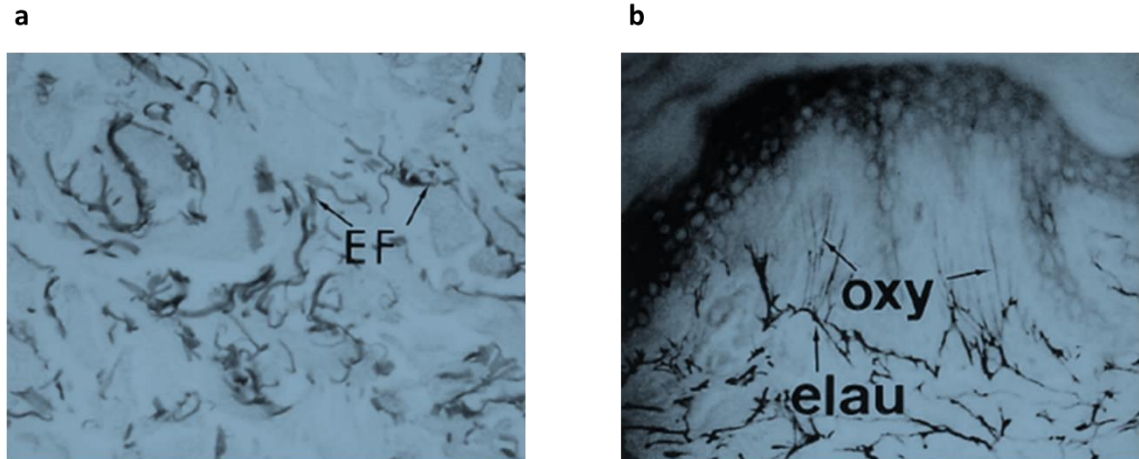


Figure 1. 5: Dermal elastic fibres (EF). a) elauin in young skin, b) oxytalan (oxy) and elauin (elau) in young skin. Original images at 200X magnification, adapted from (Gogly, Godeau et al. 1997).

1.2.5 Diabetes and Obesity

Diabetes and obesity are known to cause alterations in skin structure and function (Petrofsky et al., 2008, Sabol et al., 2014). Almost all individuals with diabetes and obesity will suffer skin complaints at some point, for example the attachment of glucose to proteins (glycation) affects the structure and function of many organs, including connective tissue. Diabetes is associated with skin complaints resulting from reduced blood flow and nerve damage, and people with diabetes are reported to have thinner skin. Diabetic skin is more sensitive to burns and injuries, wound healing is slower and nerve damage leads to loss of sensation, increasing the risk of physical injury (Petrofsky et al., 2008).

Obesity also affects skin health. Obesity results from the enlargement in adipose tissue required to store excess energy intake. Wound healing is impaired in obese individuals, as is barrier function. Obesity also effects sebaceous glands, sweat glands, collagen structure and function, and most obviously the amount and composition of subcutaneous fat (Medical, 2013). Therefore, the development of automated methods for the determination of adipocyte size, both in the skin and at other sites, is important to studies of energy balance and glucose metabolism (Chen and Farese, 2002).

1.3 Biological Image Processing and Analysis Background

Digital images contain a huge amount of information, and the interpretation of the information in these images needs effective image analysis solutions.

Image processing techniques are the image operators that transform the original image (input image) to produce an output image (as described in equation (eq1.1)) that is more suitable for analysis. Image operators either manipulate spatial information (transformation in the spatial domain) or manipulate frequency information (frequency domain) (Gonzalez et al., 2004).

$$g(x, y) = T(f(x, y)) \quad (\text{eq1.1})$$

$g(x, y)$ is the output image, $f(x, y)$ is the input and T is the image operator.

Computer science plays an important role in the quantification of information within images by using automatic and semi-automatic algorithms to perform image analysis with high levels of accuracy, speed and throughput.

Biological images come in many different forms, and even within the field of microscopy images can be acquired from many different types of microscopes and other devices such as whole-slide scanners. Extracting the complex information contained in these images is a demanding task, and manual methods tend to be inaccurate and not necessarily reproducible. Therefore, the biologist or physician increasingly needs automated image processing and analysis techniques to get an accurate result to reach an informed decision to help with diagnosis and appropriate management (Meijering and van Cappellen, 2006, Toennies, 2012).

MATLABTM is a powerful scripting environment that readily allows the deployment of a broad range of image analysis operators, and is very powerful in prototyping novel analysis pipelines. Image analysis methods devised for extracting cutaneous features and analysis, are written in MATLAB 2011b. Packages can be made available to users without a MATLAB compiler as standalone .exe files.

1.3.1 Image Acquisition (Image Sources)

Biological images can be acquired from different sources, and most are now digital, which may require enhancement prior to analysis. Before capturing biological images

there are many processes to prepare the tissue or cells for photomicrography. These included fixation, sectioning and staining to preserve and highlight specific features of the section.

1.3.1.1 Microscopy

The human eye has a detection limit of wave lengths in the visible range of 400 to 750 nm. In addition, perceiving the contrast in an image or object depends on the difference in intensity for two different regions (I_1 , I_2) in an image, given by:

$$\text{Contrast} = \log_{10}(I_1/I_2) \quad (\text{eq1.2})$$

The human eye is limited to resolution of ~ 0.1 mm. The limitations in wavelength, contrast and resolution leaves the human eye insensitive to detect small objects, and unable to detect some polarization states (Rittscher et al., 2008).

The microscope has been used to overcome limitations of the human eye. There are many different microscopic techniques that one can use to visualize small objects in any tissue and study cells or other structures. Figure 1.6 illustrates techniques for visualizing small objects with the human eye, and some types of microscopy.

Microscopic techniques are based on specimen types that fall into three categories: single molecules, cells, and tissues. There are different imaging techniques that are used to study different biological specimens; in this thesis the following techniques are described:

- Brightfield illumination: used to study stained tissue, naturally coloured specimens, hair and fibres.
- Fluorescence illumination: suitable for fluorescent specimen such as cells in tissue culture or fluorochrome-stained sections. This is used in fluorescence and confocal microscopy.
- Polarized illumination: commonly used to study birefringent specimens with a regular structure such as thin mineral sections, hairs and fibres, bones and feathers. Herein, I used this technique to identify collagen.

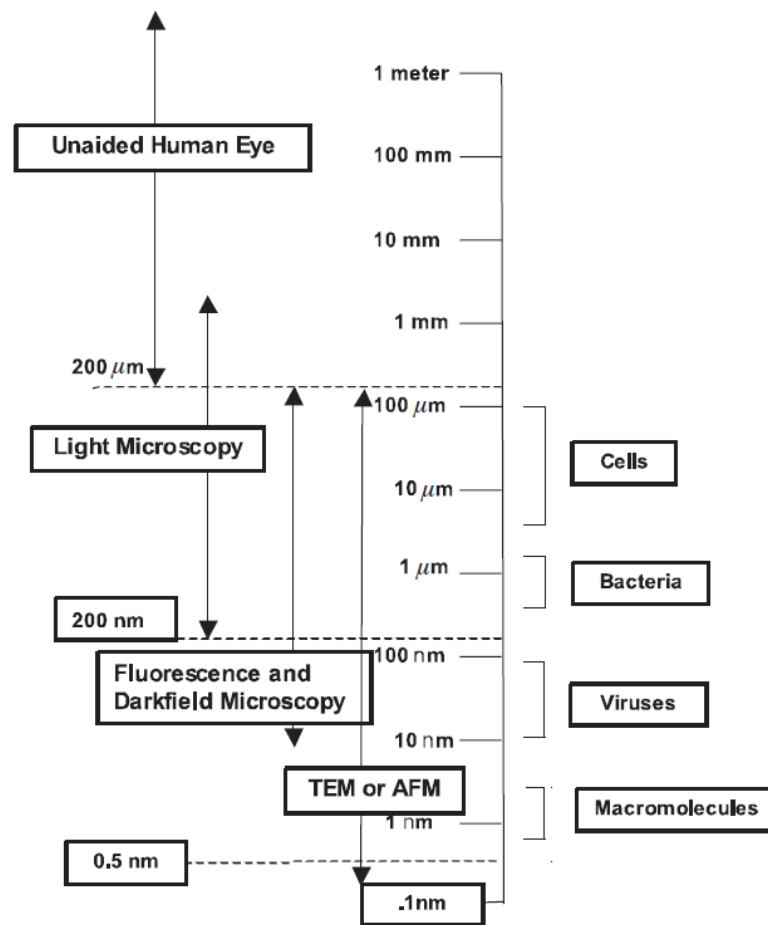


Figure 1. 6: Limitations of the human eye and microscopy for visualizing small objects. TEM: transmission electron microscopy. AFM: atomic force microscopy (Rittscher, Machiraju et al. 2008).

1.3.1.2 Whole-slide Scanners (Digital Pathology Platforms)

Whole-slide scanners produce huge image with a very high-resolutions, often by performing line-scanning followed by image stitching. Scanners such as the Aperio ScanScope provide images of up to 40x optical magnification and allow “virtual microscopy”. This technique has advantages in that it incorporates a huge amount of information in one file, and can show the entire tissue in one image that can be analyzed in one pass. However, the size of these images might slow down batch processing, and they cannot be easily analyzed by traditional image analysis techniques and require expensive commercial software, which requires expert optimisation and is generally not fast enough to give timely results. Figure 1.7 illustrates the Aperio whole-slide scanner and a typical display of the software.

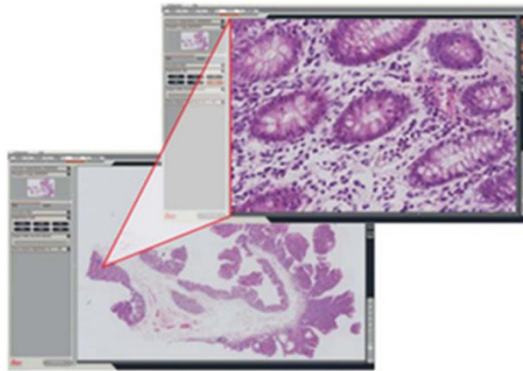


Figure 1. 7: Aperio ScanScope Scanner. Taken from www.Aperio.com.

1.3.2 Image Processing

Object detection is a common biological image processing task that forms the first stage of automated bio-image analysis. There are many artefacts (including noise) in an image that need to be removed, and many other properties that need to be enhanced in a given image before the process of detection and quantification. The next stage is the partitioning of the image into meaningful regions and extracting the features that could be interesting for quantification and analysis. Image pre-processing comprises a range of image processing techniques as described in the following sub-sections.

1.3.2.1 Image Enhancement

Image enhancement is used to increase the visualization of specific objects and makes the object more easily detectable in the image by a human observer. Another use of enhancement is in pre-processing before further image processing and analysis. The general purpose of image enhancement is to map the image into another image, so that

the objects in the processed image become easily detected and recognized. There are different enhancement techniques, which I will discuss below.

1.3.2.1.1 Contrast Enhancement

Contrast enhancement is the manipulation of the dynamic range in a given image, and is needed when the objects and the background are difficult to separate. There are different measurements to calculate contrast in an image, including global contrast, global variance, entropy, and contrast from the co-occurrence matrix. If the image has a high dynamic range, they tend to have a high contrast. The contrast of an image can be improved considerably by mapping its input range to the full output range. Contrast stretching is a good example of this operation (Gonzalez, Woods et al. 2004). Figure 1.8 illustrates contrast stretching and the output image, taken from (Meijering and van Cappellen 2006).

Global contrast enhancement is one of the methods for contrast enhancement; the method transform each pixel value f as follows:

$$g(f) = (f - f_{min}) \frac{I_{max} - I_{min}}{f_{max} - f_{min}} + I_{min} \quad (eq1.3)$$

Where f_{min} and f_{max} are the minimum and the maximum of colour intensities of the input image, and I_{min} and I_{max} are given parameters that represent the minimum and the maximum of colour intensities of the output image after contrast enhancement. The function to map f on g is called the transfer function (Toennies 2012).

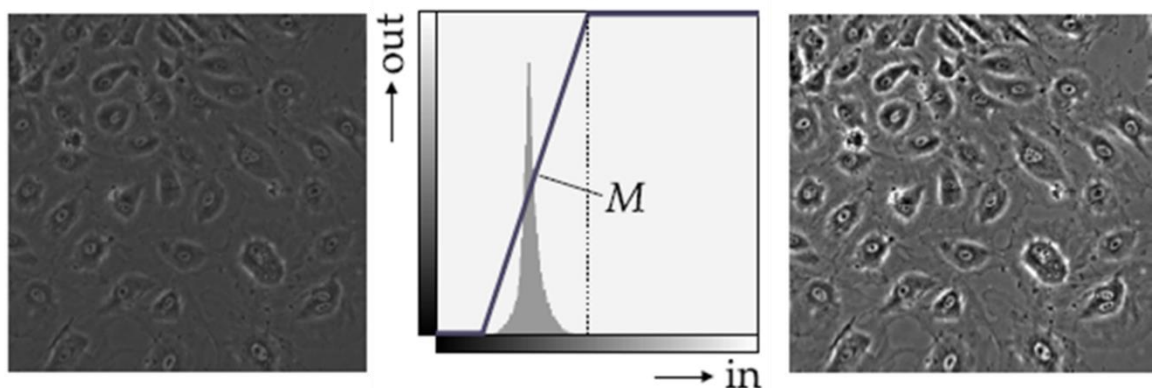


Figure 1. 8: Contrast stretching. Input cell image (left); centre panel, the mapping function M ; and right panel the output image with increased contrast (Meijering and van Cappellen 2006).

1.3.2.1.2 Edge Enhancement

Edge enhancement and detection is a common task in bio-image analysis, which starts with enhancing and detecting the object boundary. This process helps object detection and structure recognition. Edges in an image are local changes in the intensity in that image, this means that edges have a high frequency. However, image noise is a problem at high frequencies. Enhancing edges in a given image is associated with increasing the noise in that image, which is why edge enhancement should be combined with smoothing, and this is computed by convolving the image with different smoothing kernels. The Sobel operator, Gaussian kernel and Laplace operator are good examples of the different kernels used to enhance edges in images (Toennies, 2012). There many other examples of convolution filters to enhance edges, such as averaging and sharpening.

In some directional structure studies, edge enhancement is associated with the direction of edges, and this needs to combine different operators with a directional smoothing operator. The Gabor filter is an example of an enhancement model of directionally sensitive structure to provide edge detection by direction (Scherzer, 2011 , Toennies, 2012).

1.3.2.1.3 Noise Reduction

Noise is additional random information in an image that is produced by the sensor or camera that captures the image. In biological image analysis, it is very important to remove the noise in a given image, because it will affect the quantification process and results will not be accurate. Noise reduction can be classified into three schemes: linear filtering, non-linear filtering and diffusion filtering. Linear filtering and non-linear filtering are the most used noise reduction filters in biological image analysis (Meijering and van Cappellen, 2006, Kueh, Marco et al., 2013).

Linear filtering

By using linear filtering, the output pixel value is computed as a linear combination of the values of the corresponding input pixel and its neighbours. These filters are called kernels. There are some examples of linear filters that work to remove the noise in an image (Figure 1.9). The averaging, sharpening, smoothing, and derivative filters of varying sizes are examples of this kind of filter (Meijering and van Cappellen 2006).

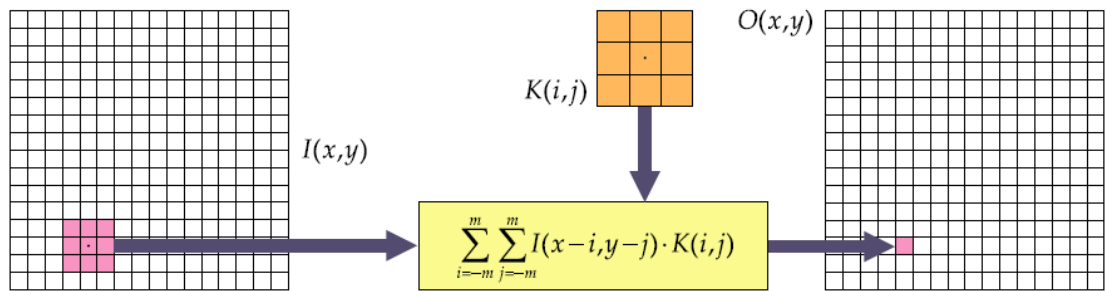


Figure 1. 9: Input and output produced using a linear filter (convolution filtering).

Non-linear filtering

The image output pixel value comes from a nonlinear combination of neighbouring input pixel values. The median filter is a non-linear filter, where each output pixel value is computed as the median of the corresponding input values in a neighbourhood of given size (Meijering and van Cappellen, 2006). This filter is widely used to remove noise in the image while preserving the edges in the image (Chan et al., 2005).

The median filter neighbourhood is usually a square, covering an odd number of pixels of size 3×3 , 5×5 , or 7×7 neighbourhoods. The median filter is used for preserving sharp edges if the neighbourhood region of a median filter contains an edge. Figure 1.10 shows an example of a nonlinear median filter with mask size 3×3 . In Figure 1.10a, the intensity value 20 replaces the centre pixel, and the resulting image without noise is shown in Figure 1.10b.

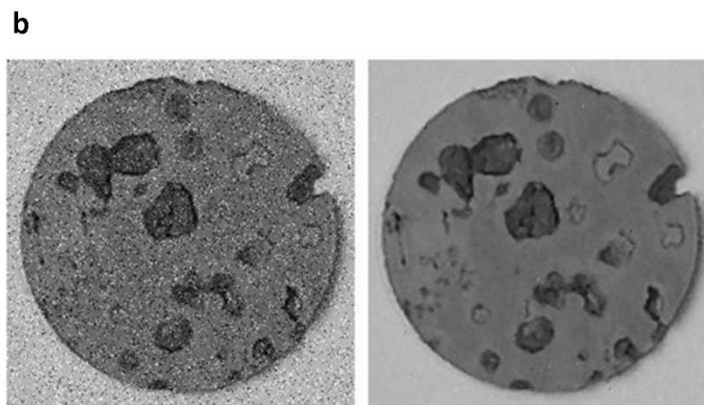
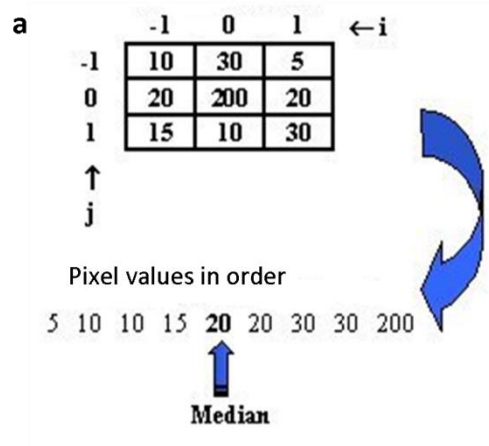


Figure 1. 10: Example of median filtering. a) filter of size 3×3 , b) example of replacing the centre pixel with the median value of window pixels. A typical noisy image is shown in the left panel, and the median filtered image is shown in the right panel.

1.3.2.2 Segmentation and Feature Extraction

Segmentation is a process that is used to subdivide an image into different regions or objects. Segmentation depends on properties and structure in the image, and the pixels related to the object region (Gonzalez et al., 2004).

Biological image analysis and quantification needs objects to be detected and the features of objects identified. After segmentation, the segmented region can be analysed, then a meaning assigned to this region (Cisneros et al., 2011). The inputs in the segmentation method are images and the outputs are attributes extracted from those images.

Segmentation approaches are divided into two categories. The first category applies to monochrome images and the second category applies to colour images (Hosea et al., 2011). Segmentation of monochromatic images is based on properties of image intensity values such as discontinuity and similarity. There are many segmentation methods to detect points, lines and edges in images that depend on intensity discontinuity by running different masks through the image. Segmentation in colour images depends on the colour and texture of that image.

1.3.2.2.1 Thresholding

The technique of thresholding is widely used in biological image segmentation because of the simplicity of implementation. This process results in a fast image analysis if the threshold value can be chosen automatically and adaptively to be applied to all images. The idea of a threshold is that the object and background in a given image $f(x, y)$ have intensity levels grouped into two modes. These modes are separated by the threshold T , in the intensity histogram of that image (Figure 1.11), such that any point at which $f(x, y)$ is greater than the threshold T is an object, otherwise it is background.

1.3.2.2.2 Piecewise Linear Transformation

This intensity transformation works as an approach to brighten or darken a desired range of grey levels that makes the target object more suitable to be identified whilst preserving the grey level tonalities in the image (Gonzales and Woods, 2002).

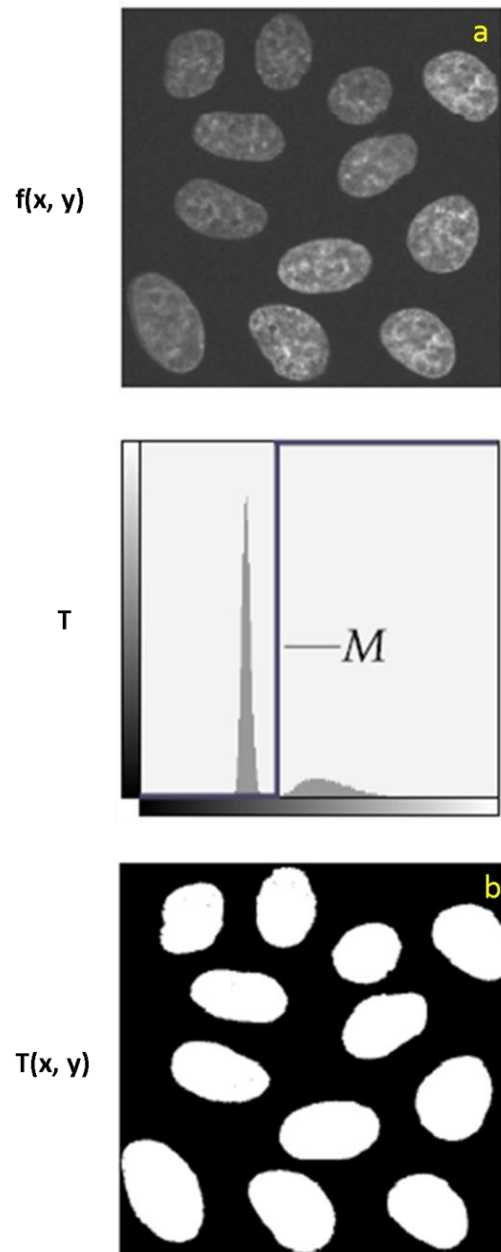


Figure 1. 11: Intensity thresholding. Thresholding achieved by applying the threshold or mapping function M to the input image $f(x,y)$ and producing the thresholded output $T(x,y)$ so that $T(x,y)= M(f(x,y))$. a) grayscale image with the corresponding histogram underneath, b) segmented objects in binary form. Adapted from (Meijering and van Cappellen 2006).

1.3.2.2.3 Colour Segmentation

Colour-based segmentation is the process that segments or subdivides an image into regions depending on the colour-texture pattern distribution in that image (Deng et al., 1999). This process is about finding homogenous colour regions, and those not similar to the segmented region. Biological image segmentation should be accurate and robust, and subdivide an image to target objects and non-objects for further quantification.

Colour segmentation is different from one colour space to another as there are many colour spaces representing colour in image. Example of colour spaces are: RGB that includes three channels red, green and blue; HSV that includes hue (colour information, H) and saturation (S) used to isolate regions in the hue image, and the intensity or value image (V), which carries no colour information (Gonzalez et al., 2004); and CIELAB represents lightness, where A and B are two colour dimensions in this colour space. There are many other colour spaces, however the above are widely used in image analysis (Ford and Roberts, 1998).

Biological image segmentation is a difficult task because images are rich in colour and texture. Colour quantization facilitates the segmentation process, using a criterion for extraction of a few representative colours, where neighbouring regions can be differentiated in the image (Deng et al., 1999).

1.3.2.3 *Mathematical Morphology*

Morphological techniques can be used in the pre-processing and post-processing of geometrical structure in an image. Techniques can be applied to binary images and greyscale images. Mathematical morphology transforms the image according to the size, shape and connectivity. Binary morphology techniques control how the shape fits or misses the exact shape of the object in the image by using different morphological operations that help image analysis before and after segmentation (Gonzalez et al., 2004, Fisher et al., 2005, Meijering and van Cappellen, 2006).

1.3.2.3.1 Erosion and Dilation

Erosion and dilation are two basic mathematical morphology operators that are typically applied to a binary image. The erosion operator erodes away the boundaries of

foreground regions, and the dilation operator will enlarge the boundaries of foreground regions (i.e. white pixels).

1.3.2.3.2 Closing and Opening

Closing is similar to the dilation operator in that it enlarges the boundaries of a foreground image and shrinks the background in such regions. The closing operator can be derived from both erosion and dilation operations. This operator does not affect the background regions that have similar shape to the structuring element, while it changes all other background regions. The closing operator is defined simply as dilation followed by erosion using the same structuring element for both operations.

Opening is another important mathematical morphology operator, derived from dilation and erosion and its effect on the image is similar to the erosion operator, in that it removes some pixels from the boundaries of the foreground region. This operator does not affect foreground regions that have a similar shape to the structuring element. An opening operation is defined as erosion followed by dilation using the same structuring element for both operations.

Figure 1.12 illustrates the mathematical morphology operators using dilation, erosion, closing and opening, which are widely used in this thesis.

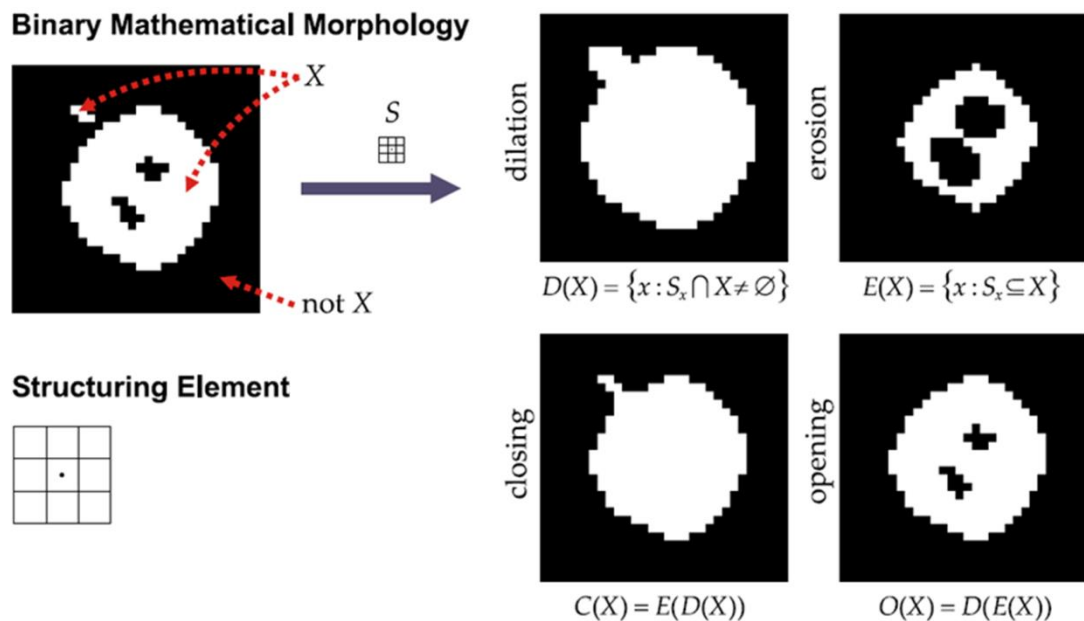


Figure 1. 12: Principles of binary morphological erosion, dilation, closing and opening operators.

1.3.2.3.3 Skeletons

Any shape can be represented as a graph in any planar region, in other words one can reduce the shape to a graph by obtaining the skeleton of the region using a thinning algorithm (Gonzalez et al., 2004). Skeletonization is the morphological process that reduces the foreground region of the binary image to a skeleton without losing the extent and connectivity of the original region of the image. The resulting skeleton can be described as the loci of centres of bi-tangent circles that fit entirely within the foreground region being considered. Figure 1.13 illustrates this in a rectangular shape.

The skeleton of any region is defined by *medial axis transformation* (MAT). R is a region and b is the border for that region, the MAT for each point p in the R is created by finding the closest neighbour in b , if p has more than one neighbour it means that it belongs to the skeleton (Gonzalez, Woods et al. 2004). Figure 1.14 shows examples of skeletonisation.

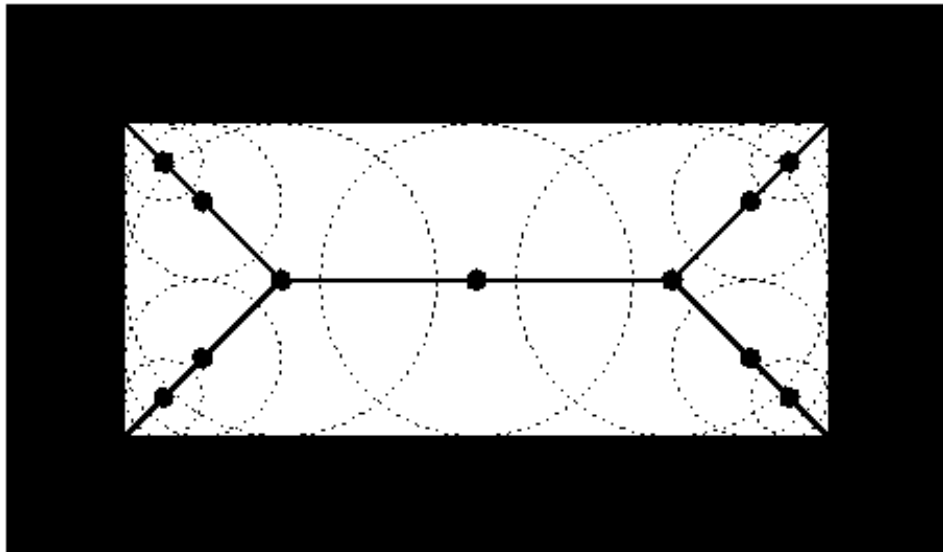


Figure 1. 13: Skeleton of a rectangle defined in terms of bi-tangent circles.

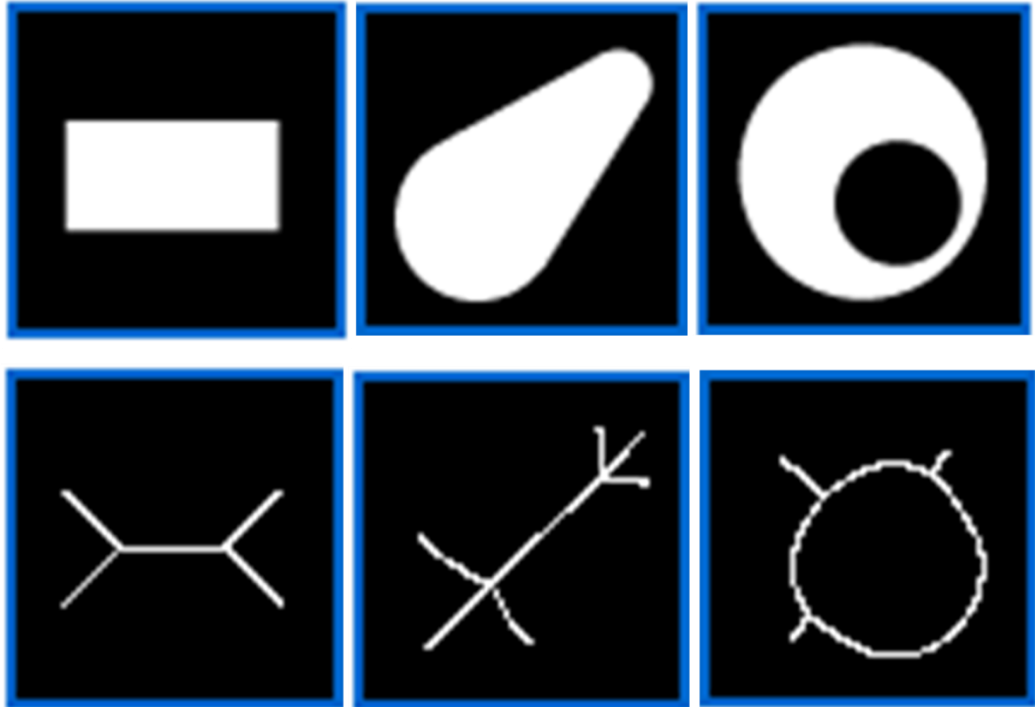


Figure 1.14: Examples of skeletons and binary images. The first row shows binary images; the second row shows skeletons. Adapted from (Fisher, Perkins et al. 2005).

1.3.3 Image Analysis

In general, analysis methods are divided into two categories: image processing and analysis in either spatial or frequency domains.

1.3.3.1 Image Analysis in the Spatial Domain

The spatial domain is the standard image space, and all techniques that work in this domain are based on grey level mapping, and work on the intensity values on the image plane. Processing in the spatial domain is described by equation (eq1.1), and Figure 1.15 shows an example of image analysis and quantification in the spatial domain.

There are two main categories of processing in the spatial domain:

1. Intensity transformation: works on a single pixel
2. Spatial filtering: works on a neighbourhood of every pixel.

Chapter 1

Intensity transformations are used as enhancement techniques in the spatial domain, and most of these processes have been used in this project including:

- Threshold transformation
- Log Transformation
- Contrast stretching transform
- Image negative
- Gamma transformation
- Histogram equalization
- Piecewise linear transform (Gonzalez, Woods et al. 2004).

Spatial filtering techniques are very important in image processing, in particular when the image contains noise and other artefacts.

$$\boxed{f(x, y)} \longrightarrow \boxed{\text{Filter}} \longrightarrow \boxed{g(x, y)}$$

Application of analysis in the spatial domain:

There are many techniques that have been used in the study and analysis of images of skin tissue sections in the spatial domain. Such analysis techniques work with properties of the image pixels as intensity, colour and texture (Rich and Whittaker, 2005, Cisneros et al., 2011, Aymeric Histace, 2014), and these will be described in the appropriate context in each Chapter.

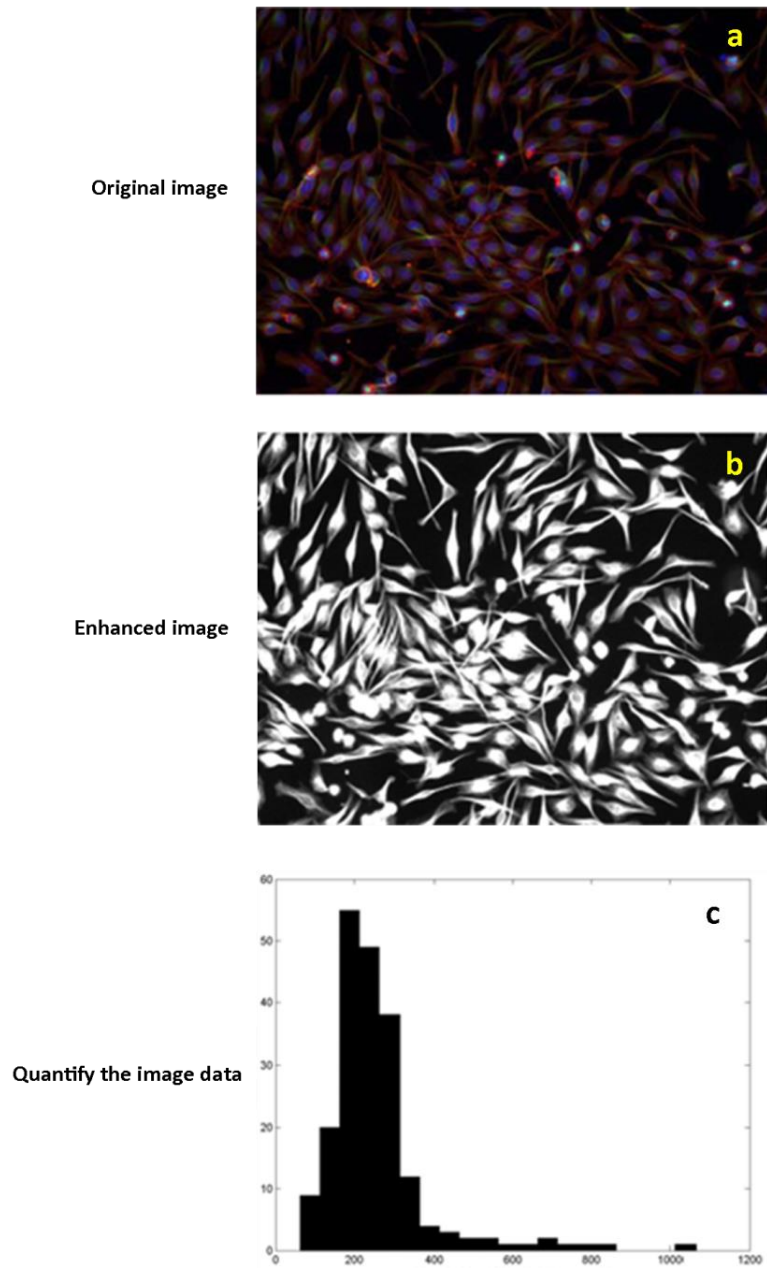


Figure 1. 15: Image processing and analysis. a) original microscopic cell image, b) enhanced image using contrast adjustment, c) example of quantification stage (Kueh, Marco et al.).

1.3.3.2 Image Analysis in Frequency Domain

The analysis in the frequency domain can find a signal in a given frequency band over a range of frequencies. The operator that transforms the image from the spatial domain (time domain) to the frequency domain is called a Fourier transform, which separates a signal (image) into its spectral components depending on its frequency content.

The change in grey level in an image and the pixel intensity values affects the frequency content of that image. High frequencies come from rapid changes in the intensity values, while the low frequencies come from slower changes in intensity values, which can be analysed using a Fourier transform (Gonzalez, Woods et al. 2004).

Fast Fourier Transform FFT:

The Fast Fourier transform FFT is one of the algorithms used to compute the discrete Fourier transform to find the strength of the different frequencies in the image. The FFT is an efficient algorithm that returns the strength of the different frequency waveforms contributing to the pixel values of the entire image. The Discrete Fourier transform (DFT) of a signal and its inverse can be computed using FFT. The DFT of an image extracts the strength of the different frequency waveforms contributing to the pixel values of the entire image (Gonzalez, Woods et al. 2004).

The DFT of an image f for any frequency pair (u, v) is a complex number that depends on all the spatial pixel values $f(x, y)$ computed by the formula:

$$f(u, v) = \frac{1}{MN} \sum_{X=0}^{M-1} \sum_{Y=0}^{N-1} f(x, y) e^{-j2\pi(\frac{ux}{M} + \frac{vy}{N})} \quad (eq1.4)$$

This technique has been used to measure the structure of collagen in images previously (Wu, 2011).

Application of analysis in frequency domain

There are many biological analysis applications in the frequency domain, and there are various studies of the influence of different factors on collagen architecture, such as age (Wu et al., 2011, Zhuo et al., 2009, Noorlander et al., 2002), and these will be described in the appropriate context in each Chapter.

1.3.4 Existing Biological Image Analysis Tools

There are many existing tools for digital image processing and analysis, including both commercial and open-access software. The following applications were previously used in the Buckingham Institute for Translational Medicine.

1.3.4.1 *Commercial Software*

Visiopharm Integrator System (VIS) is commercial software package designed to perform complete analysis in digital pathology. The user can extract a great deal of information, such as numbers, length, area, volume, intensity, shape, and texture information in a short time. The software guides the user in a step-by-step fashion to find significant information in fields such as diabetes, dermatology and neuroscience research. Visiopharm^{DP} enables the user to work with whole slide images, and can analyse the image in different magnifications, which help the user to save time if the analysis can be performed at lower magnification, i.e. analysis at 10X is faster than at 20X magnification (Grunkin, 2008). However this software is very expensive and needs the user to be highly trained to create an optimal protocol for any particular analysis. Moreover, analysis of digital slides is very time consuming.

1.3.4.2 *Free Open-source Software*

ImageJ is a freely available tool used widely in biomedical image analysis. ImageJ is java- based open-source platform that has a list of plug-ins that make it helpful in a range of fields in science and engineering, including medical imaging and microscopy. Figure 1.16a illustrates the user interface of this program. One important feature in ImageJ is that it supports a variety of standard image formats, including 48-bit colour composite images. LOCI is a bundle of plug-ins that was developed to open over 65 different image formats from bioscience, (www.loci.wisc.edu). ImageJ has a number of useful tools for intensity processing such as image filtering (as illustrated in Figure 1.16 b and c), background subtraction and histogram manipulation, as well as a number of automated segmentation techniques such as Otsu thresholding, mixture modelling, maximum entropy, colour-based thresholding and k -means clustering (Collins, 2007, Baecker, 2010). There is also a growing range of user-written plug-in filters.

Chapter 1

There are many image enhancement techniques that can be easily performed by the user including:

- Brightness and contrast adjustment
- Enhance Contrast
 - Normalization or contrast stretching
 - Histogram equalization
- Noise suppression
 - Mean filter
 - Gaussian blur filter
 - Edge enhancing filter
- Filtering in frequency domain
- Background subtraction.

Tasks can be automated using the ImageJ scripting environment. However, implementing these tasks needs an experienced user, and it is not particularly suitable for high-throughput analysis which requires an unsupervised, adaptive and automated system.

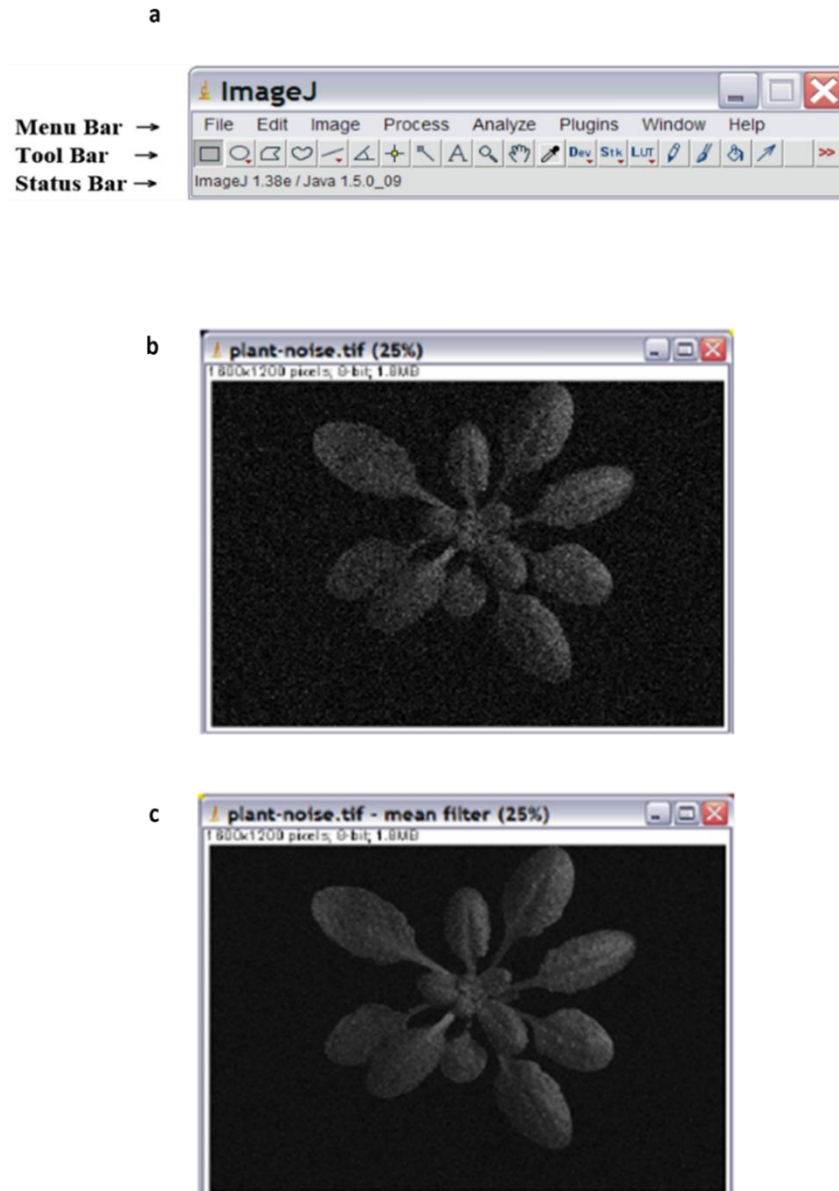


Figure 1. 16: Noise reduction using ImageJ. a) The ImageJ window. b) An example of an image containing noise before using mean filters, c) the image filtered with a mean filter. Taken from (Baecker 2010).

1.3.5 Automated or Computational Biological Image Analysis

Biological images contain a variety of objects, which may need to be extracted and quantified. Many of the existing tools do not cater for the array of objects found in the research or pathology context and there are difficulties in doing this in a time-efficient manner. For example there are few whole-slide application tools, and few resources for cutaneous research.

Automated image analysis exists within the computational field, but is limited in biological applications. Automation has two major advantages: firstly it prevents bias and secondly the process can be applied to a large number of images (Kueh, Marco et al., 2013). Biological images are often complex and contain noise that necessitate image processing to enhance the image and allow extraction of meaningful quantitative information. Attempts have been made to automate biological image analysis; some of these studies are described in this section.

Mathematical morphology and other segmentation methods using image processing techniques such as edge detection and region growing are used in biological applications (Sadeghian et al., 2009). Two segmentation processes were described in this work, nucleus segmentation and cytoplasm segmentation. The nucleus was segmented using edge detection and gradient vector flow (GVF) followed by an active contour snake model to segment and detect the boundary of the nucleus. The cytoplasm was segmented using intensity thresholding. However, nucleus segmentation in blood samples required an adaptive technique as the boundary of the nucleus was not very clear when using a region based technique for segmentation. In the process of cytoplasm segmentation, the threshold had to be adaptive to all images because of variation in cytoplasm intensity in order to achieve more accurate segmentation results.

A method of characterizing different tissues by extracting morphological and topological features using segmentation and classification of different types of cells in epithelial and adipose tissue was reported by de Assis Zampiroli et al. (de Assis Zampiroli et al., 2010). Mathematical morphology was used for automated epithelial cell segmentation, beginning with converting the H&E stained colour image to greyscale, then thresholding before opening operators were used to segment cells and create a marker. Adipocytes were segmented by transforming the original image into an

inverse image, followed by a dilation operator to create a marker for each cell, followed by creating the outlines of cells using a watershed calculation. After the cells were outlined, a neighbourhood graph was constructed that extracted 16 features from each cell of the epithelial and adipose tissue. The extracted features described in this method are: perimeter, area, mean distance to the neighbours, major axis length, minor axis length, orientation, convex area, eccentricity, diameter, extent, solidity, form factor, roundness, aspect ratio and convexity. These features were fed into a Support Vector Machine Classifier (SVM) to evaluate how these features were able to describe the two types of tissues, as well as the ability to describe abnormalities such as cancer. The result of classification showed 100% of the epithelial cells were correctly predicted, and 99.76% of the adipocytes were correctly classified, these results show that this feature was a good predictor using histological images. However, this technique cannot be utilized for clinical use for two reasons: firstly, the method to segment cells must be able to segment all cells accurately, which is not necessarily achieved using the watershed method. Secondly, only five images of epithelial tissue and five images of mammary gland adipose tissue were studied, which not enough to assess classification performance.

In the diagnosis of neuromuscular diseases, the evaluation of the size and shape of muscle fibres revealed important information. The automated muscle fibre analysis of histology images was described by Brox et al. (Brox et al., 2006) by segmenting myofibres using an active contour model followed by post-process refinement with morphological filters. To determine the outline of myofibres in RGB H&E images, an active contour model was applied to separate the fibres from other parts of the image. The proposed active contour model was based on two parts; firstly, region-based separation of fibres of similar colour and texture from the intermyofibrillar connective tissue. Secondly, the edge based part of the active contour model separated these regions according to the properties of the edges of muscle fibres. Thirty images of five human muscle specimens were segmented, and the automated segmentation result was compared to the manual method, and this showed only a 2% misclassification rate. The accuracy of automated morphometric analysis was compared to human measurements performed by three observers in ten images containing 191 muscles. Area, perimeter, circularity, and diameter were calculated with both automated and manual methods, and the results didn't show any significant difference between the manual and automated

analysis. This indicates that the system was valuable in muscle research, but further work was required if it was to be used for clinical diagnosis. In particular, it must work adaptively if there were variations in the properties of larger, or distinct, image sets.

An automated evaluation of the quality of segmentation in cytological and histological images of stained samples in different colour spaces was proposed by Meas-Yedid et al. (Meas-Yedid et al., 2004). Two criteria were proposed to evaluate automatic segmentation, and this was compared to Liu's and Borossoti criteria (Philips et al., 2005), to test and evaluate the quality of segmentation without human interaction. Two segmentation methods were used, thresholding a 1D-histogram, which split the histogram into two classes, and segmentation based on colour quantization that reduced the number of colours in the image without colour distortion. Segmentation was tested in different colour spaces such as RGB, normalized RGB (NRGB), opponent colours (H1H2H3), I1I2I3, XY Z, Y IQ, Lab and Luv. Segmenting cytology images showed very good results in normalized RGB (NRGB) colour space. When applied to histology, the H1H2H3 and Luv colour spaces showed the best segmentation using the Meas-Yedid criteria, whereas using Liu's and Borsotti's, the two colour spaces I1I2I3 and Y IQ showed best performance.

An automated system of nuclear segmentation in bladder and skin images was proposed by Korde et al. (Korde et al., 2009), in which karyometric analysis was used to evaluate variation in the nucleus. Cell nucleus segmentation was performed by both manual and fully automated methods, and the results were compared in terms of the proportional difference in the nuclear area and the total optical density, and median proportional difference in the karyometric features. Manual segmentation was performed with a user selected greyscale level threshold, and then nuclear boundaries were adjusted by the user until adequate segmentation was achieved. Automated segmentation used a 5×5 median filter to remove noise, and this was followed by segmentation, categorization and cusp correction. The properties of the image histogram were used to select an optimal threshold at the segmentation stage. Finally, erosion and dilation operators were used to improve nuclear segmentation. In ten bladder and ten skin histology images, segmentation resulted in a sensitivity of 76.4% in bladder and 83% in skin. By comparison, manual and automatic segmentation for bladder cell nuclei showed a proportional difference in nuclear area of 4.1%, the proportional difference in total

Chapter 1

optical density was 2.2% and the median proportional difference over all non-zero karyometric features was 3.1%. In skin images the proportional difference in nuclear area was 1.3%, the proportional difference in the total optical density was 1.1% and the median proportional difference over all non-zero karyometric features was 2.9%. The result of automatic segmentation showed agreement with karyometric analysis, however, the histogram-based threshold method for some images did not give clear peaks for nuclear and non-nuclear objects, and some of the images contained more than two peaks, making the segmentation process more complicated.

Segmentation of any object in a digital image requires a robust algorithm for enhancing colour information and image intensity to account for variations in contrast and staining of input images. Feature extraction from H&E stained human skin using morphological processing and object classification rules to detect the class of tissue damage in epidermis was described by Haggerty et al (Haggerty et al., 2014). H&E stained images in this study were generated in skin explant assays that were developed to investigate the immunobiology of graft versus host disease occurring post hematopoietic stem cell transplantation in HLA-matched siblings. Skin biopsies were fixed, sectioned and stained with H&E. Forty skin samples were investigated in this study, and for each skin sample a digital 10X magnification image was created.

Segmentation differed from other traditional methods in pre-processing, thresholding, segmentation and post-processing. Haggerty et al's approach started with cropping the tissue area, followed by colour normalization to improve algorithm efficiency. The images were enhanced using colour conversion and contrast enhancement. Otsu thresholding was used to minimize the intra-class variance in images and segment the region of interest followed by the use of closing and opening morphological operations to create a binary mask of the epidermis. The objects that were not a part of the epidermis were excluded by classifying each object pixel. It is important to note that user interaction was necessary to improve object classification. Performance of the algorithm was evaluated, and the results showed that the mean specificity was 98.0%, the mean sensitivity was 91.0% and the mean accuracy was 96.8%. Without user interaction, the mean specificity was 97.7%, the mean sensitivity was 89.4% and the mean accuracy was 96.5%. This algorithm showed a high performance, however, there were some techniques used in this study that might adversely affect the accuracy of

segmentation for independent datasets, e.g. the colour normalization in some images might make objects of interest disappear, or other non-objects may appear as an object. Also, the use of threshold and morphological operators must work adaptively to handle variation in colour and intensity to reduce errors.

1.4 Research Aim and Objectives

Mouse models are invaluable in understanding human disease. Histological analysis provides a “gold standard” method to investigate tissue disruption in disease states. However, this has proved largely intractable to high-throughput image analysis that would allow quantification of diverse pathology, and so inform our understanding of disease aetiology and improve diagnosis and treatment.

The overall aim of this research was to develop novel automated and computerized methods that can analyse histological images of skin in high-throughput analysis to help the biomedical scientist in identifying interesting features in images of tissues prepared with different histological stains, acquired from various invasive and non-invasive imaging platforms. Therefore, biological image analysis methods need to be able to deal with all intensity, colour, shape, and texture information in images, and work adaptively with different image datasets to evaluate skin integrity by assessing the morphology of skin layers, and to detect and quantify changes.

In this research, the images were acquired from different microscope sources, a whole slide scanner, and from skin mould impressions. For quantification, the features of interest had to be highlighted and distinguished from other objects, as well as the image background, using intensity, colour, shape and texture. The analysis methods started with improving image processing techniques to work unsupervised and adaptively to enhance images in order to improve the reliability and accuracy of the experimental results, i.e. by enhancing contrast and reducing noise to make objects more identifiable, and prepare the region of interest (ROI) for segmentation. This thesis also aims to perform quantification and data analysis following feature extraction using computational techniques to detect interesting textural and morphological changes in the skin that describe discrete biological states. Once a technique was developed using representative sample images, it could then be applied to a broader image dataset to investigate a specific biological question.

Chapter 1

Many aspects of skin integrity change in ageing, and in disease states, including loss of skin strength, reduction in collagen synthesis and change in subcuticular fat. I set out to create a set of tools to evaluate diverse aspects of skin pathology in human subjects, and mouse models of human disease. These included:

- Measuring skin integrity in skin stained with picosirius red and imaged with cross-polar microscopy to evaluate loss of collagen integrity. This involved quantifying the directions of collagen bundles and measuring degradation in collagen organisation and changes in bundle thickness in an ageing series, as well as in a model of diabetic skin.
- Development of a technique to quantify collagen dynamics by assessing Herovici stained skin from ageing and diabetic subjects.
- Development of quantification techniques to assess skin layer morphology (size, number of adipocytes and depth of each skin layer) in high-throughput analysis and application of these techniques to a large bank of highly-indexed images from the WTSI MGP in order to identify novel genes involved in the pathogenesis of skin disease.
- Development of a technique to measure the surface texture of the skin through the automated analysis of skin moulds from sun exposed and non-exposed human subjects.

CHAPTER 2

Collagen Assessment in Histological Skin Sections

2.1 Background

Automatic extraction of texture information and quantifying collagen orientation in skin tissue is very important to assess skin structure. Cross-polar picosirius images can visualize the organisation of collagen in the dermis. In this Chapter, I describe the quantification of changes in the basket-weave structure in different ageing states, and detect more subtle pathological changes in the dermis. Measuring collagen bundle thickness and investigating the decrease in thickness with aging was done by quantifying the foci distance from the vertex of the ellipse that was generated from the FFT scatter of the cross-polar images. Another analysis of collagen dynamics by evaluating new collagen synthesis in Herovici polychrome stained images was made using my novel scheme, which works adaptively with images with variations in hue and intensity.

2.1.1 Collagen in the Skin

Collagen is a structural extracellular matrix (ECM) protein that provides a supportive framework for cells in the dermis (Mays, McAnulty et al. 1995). The dermis contains the basket-weave conformation of healthy collagen, which changes with aging and other disorders. Alteration and damage to collagen structure can reflect the level of sun exposure or cutaneous pathology (Fligiel, Varani et al. 2003).

2.1.2 Visualisation of Collagen in Skin

There are different staining techniques that are used for visualising different components of skin tissue as described in Chapter 1, section 1.2.3. I describe two of these techniques that have been used in the collagen assessment in the skin.

Picosirius staining:

The picosirius staining and polarization procedure has been used in various studies to evaluate collagen structure and assess the basket-weave structure of the dermis (Junqueira, Bignolas et al. 1979; Rich and Whittaker 2005). Images of picosirius

stained skin can reveal the exquisite structure of collagen and can be used for different purposes, such as the study of collagen orientation, collagen thickness and study of different types of collagen. Bright-field microscopy of picrosirius staining demonstrates the loops and whirls of collagen (red; Figure 2.1a) and the epidermis (yellow). Fluorescent microscopy of picrosirius stained skin identifies collagen but not the epidermis (Varani, Warner et al. 2000; Wu, Li et al. 2011), and 3D imaging is possible with confocal microscopy (Figure 2.1b). With cross-polar microscopy, the collagen basket-weave can be observed (Figure 2.1c) (Montes and Junqueira 1991).

Herovici staining:

Herovici staining colours larger mature collagen fibres red and the thinner young collagen blue. I used this discrimination to assess collagen dynamics, or how new and mature collagen appears, in the dermis (Turner, Pezzone et al. 2013) (Figure 2.2). Figure 2.2 illustrates the ability of this histochemical staining to visualize the different type of collagen in ECM in the dermis, so that the collagen in the reticular dermis is stained in blue or purple, and the collagen in the papillary layer is stained blue (Watt and Fujiwara 2011).

There are other staining methods used in the study of collagen architecture. H&E staining is another method that can be used in the assessment of collagen content in the dermal layer, which colours the collagen pink. Many other staining methods are used also in collagen detection and analysis. Periodic acid Schiff (PAS) stains collagen pink, and is also used in the study of basement membranes, which stain dark pink. Verhoeff's van Gieson stains collagen pink and elastic fibres brown/ black. Masson's trichrome stains collagen blue and muscle red. Orcien-giemsma (O&G) stain stains collagen pink and elastic fibres black, and also gives information about inflammatory cells.

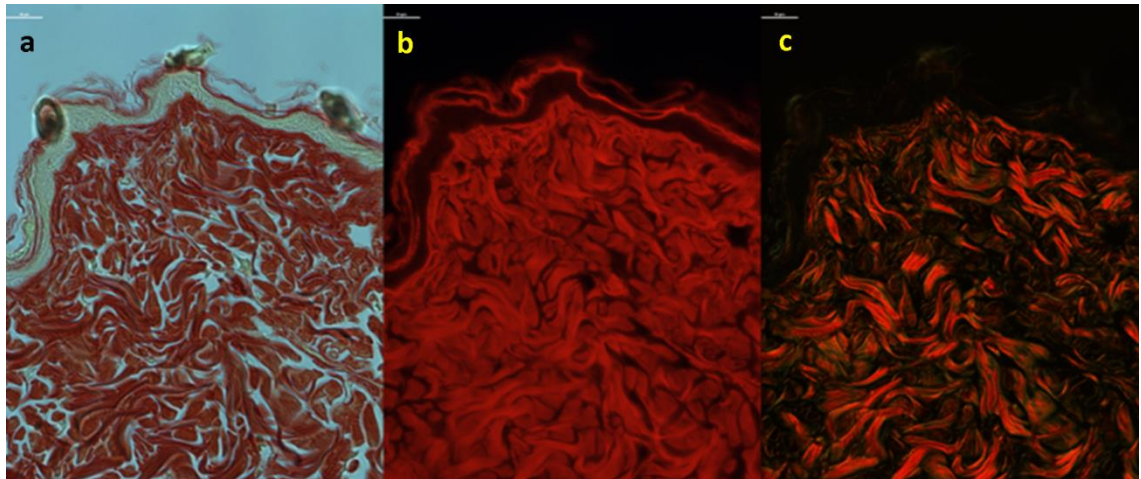


Figure 2. 1: Picrosirius stained skin. C57Bl6 mouse skin was stained with picrosirius and viewed under bright-field (left panel), fluorescence (absorbance/emission $\sim 581/644$ nm, centre panel) or dark-field cross-polar optics (right panel). Original magnification 90X, scale bar = $10\mu\text{m}$ in each case.

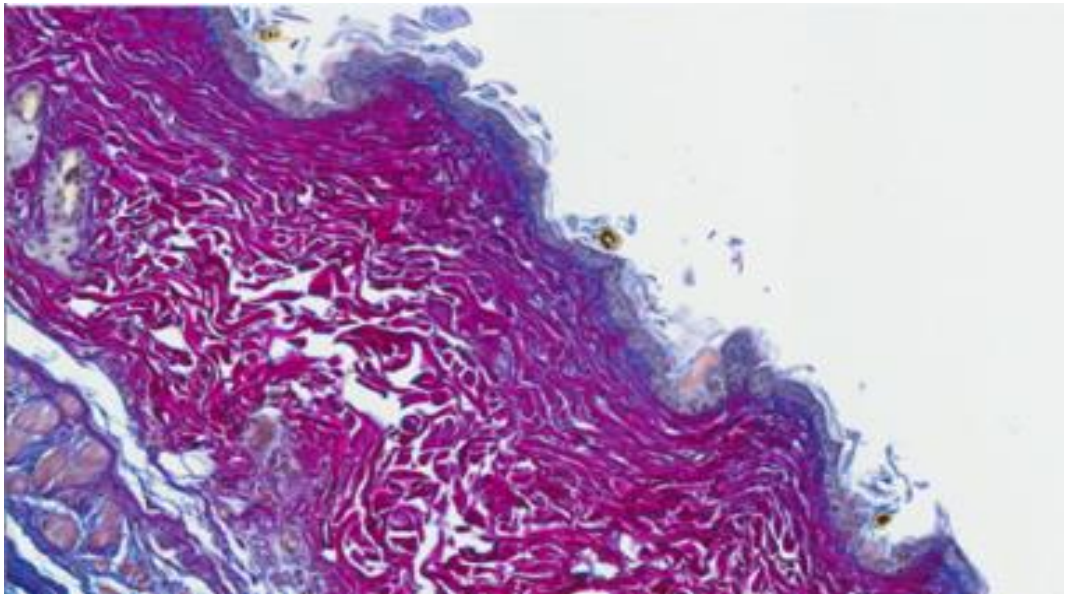


Figure 2. 2: Herovici stained mouse skin. Mature collagen appears red and new collagen appears blue. Pixel dimensions = 1712×1074 pixels, $552.12 \times 346.36 \mu\text{m}$.

Measurement of Collagen in the Skin

Existing techniques measure gross pathological changes, such as fibrosis, but are not sufficiently sensitive to detect more subtle and progressive pathological changes in the dermis, such as those seen in aging. Although most collagen staining is simply a tool to

allow the visualization of the dermis, some attempts were made to manually quantify collagen and its structure, which are time consuming and observer biased, and automated methods would solve problems of observer bias and provide more precise results. Existing automated analysis and measurement of collagen structure are based on the frequency spectrum obtained by transforming the image to its frequency domain using FFT (Gogly, Godeau et al. 1997; van Zuijlen, de Vries et al. 2002).

In this section, I discuss existing methods to assess collagen thickness, content and orientation, including the pathological or diagnostic utility of these techniques.

a. Fast Fourier Transform FFT

The main image processing technique used to assess collagen architecture is the Fast Fourier Transform FFT, (as described in Chapter 1, section 1.3.3.2). Although there are other orientation estimation methods such as radon transformation (Jafari-Khouzani and Soltanian-Zadeh 2005) and the dual-tree complex wavelet transform CWT (Selesnick, Baraniuk et al. 2005), these are more suitable for ordinary texture analysis that captures variation in specific directions. Consequently, these transforms are not suitable for the analysis of collagen in the dermis due to the fact that in skin collagen fibres are oriented in different directions and organised (seemingly) randomly. I required a technique that could detect random variation in collagen organisation and direction throughout an image. There are other image processing techniques that could be used for texture information extraction in the spatial domain, such as Local Binary Pattern (LBP) described in detail in Chapter 4, section 4.4. However, this technique is only suitable for analysing the local texture inside a predefined LBP window. On the other hand, the FFT spectrum gives information about texture direction and organisation in the whole image, because each pixel in the FFT spectrum provides information about the variation in the values of all the pixels in the spatial domain of the image.

b. Collagen Orientation

Once the DFT has been computed, the resulting power spectrum from the FFT is used to determine the relative organisation or directionality of the original image texture (de Vries, Enomoto et al. 2000).

A binarised image of the shifted FFT power spectrum can be generated using a suitable threshold. The significant pixel values cluster in the centre of the binarised spectrum

Chapter 2

image in an approximately elliptical shape. The orientation index can be calculated from the major and minor axes of the fitted ellipse of significant values using the following equation:

$$\text{Orientation Index} = 1 - \frac{\text{minor axis}}{\text{major axis}} \quad (\text{eq2.1})$$

These resulting index measurements can then be used to quantify structural changes in dermal collagen because the change of the index value represents the change of the object orientation, so that the zero and close to zero corresponds to randomly orientated collagen bundles, and one and close to one corresponds to parallel orientation of collagen bundles (de Vries, Enomoto et al. 2000; Wu, Li et al. 2011; Verhaegen, Marle et al. 2012).

The FFT power spectrum and the corresponding orientation index method has been used to measure collagen bundle orientation and spacing, as well as collagen orientation in lesional scleroderma skin (de Vries, Enomoto et al. 2000). Scleroderma is a skin disorder that exhibits fibrosis in the dermis, which is characterised by the parallel alignment of collagen fibres. Lesional skin showed parallel alignment of fibres, in contrast to collagen in normal skin, which was in a basket-weave orientation. Briefly, H&E stained skin from non-lesional and lesional scleroderma tissue were subjected to laser scatter (passing light through the sample and then assessing the diffraction pattern) and the difference in the light diffraction patterns was assessed using a computer image analyser to assess collagen organisation, and the FFT and the orientation index method was also utilised to estimate collagen orientation in the image. The FFT was found to be more accurate than the laser scatter method, and as the laser scatter method uses expensive software, the FFT method was preferred. However, this study used a small number of samples, thus a more thorough investigation of the use of FFT in this way is required.

Multiphoton microscopy (MPM) and second-harmonic generation (SHG) were also used in the study of collagen related changes in aging skin texture, and the changes associated with cancer progression (Zhuo, Chen et al. 2009; Wu, Li et al. 2011). Collagen morphology in aging skin has been quantified in images acquired using MPM and analysed using FFT (Wu, Li et al., 2011). Changes in collagen structure were monitored in mouse dermis in chronologically aged and photo-aged *in vivo*. This

analysis identified significant differences in collagen structure in different ages. The power spectra of the FFTs that were generated from the MPM images were assessed by calculating the Orientation Index as described previously (eq2.1). The result showed collagen changes in aged skin. The SHG also allowed the visualization of collagen structure status at different depths, where the SHG signal was strong in young skin at a depth of 56 μm and in elderly skin at a depth of 48 μm , and in photoaging was at a depth of <40 μm . This indicated that depth decreased with age and with a high level of UV sun exposure. The results in this work could allow one to monitor collagen changes in aged skin and photoageing, however, the use of MPM is expensive, and the SHG signal didn't show any change between 50- 60 weeks or between 8-16 weeks, indicating that a more sensitive technique was required to detect the variation in collagen structure within these narrower age ranges.

A microscopic method for determining collagen orientation changes in dermis resulting from mechanical stress was reported (Noorlander, Melis et al. 2002). Picrosirius stained piglet skin sections were used in this method to demonstrate changes in collagen orientation in skin stretched for 30 minutes. ImageJ image analysis software was used to determine the length of collagen fibres as a parameter of fibre orientation. In brief, the binary image was produced from the greyscale image and the best fitting oval was calculated for each numbered white object in the binary image. The minor and major axes of the oval were determined for all white objects and the mean length of the ten longest major axes was calculated and used as the parameter for the orientation of collagen fibres. From this value across three serial sections of a specimen, the collagen alignment index was calculated. The results showed significant differences with the p-value <0.005 between control skin and stretched skin, however, the software used in this study is very limited, and for more precise measurement of collagen changes, a more sensitive image processing and analysis was again required.

c. Collagen Thickness and Spacing

Fourier first-order maximum analysis and distance mapping using Qwin Pro image analysis software (version 2.8, Leica Imaging Systems, Cambridge, U.K.) was used to assess collagen orientation, thickness and bundle spacing in H&E stained skin (Verhaegen, Marle et al. 2012). These parameters were calculated using distance mapping. The first step was to create a binary image from the bright-field H&E grey

image in order to segment the collagen bundles. A distance map and skeleton were then created, and the thickness measured by doubling the distance from the skeleton, which represented the centre of the object and the edge of the resulting grey image of the object from the distance map. The technique of FFT first-order maximum analysis was used by calculating the DFT to quantify bundle centre distance by measuring the distance from the centre of the gravity of the FFT power spectrum to the centre of the first order power spectrum. This study demonstrated that there were significantly thicker collagen bundles and significantly more spacing between the collagen bundles in healthy skin compared to scar tissue. Furthermore, this analysis introduced a technique to measure degradation in the collagen structure, and identified a need to assess collagen structure variation more precisely.

Another technique was developed from FFT analysis to measure collagen bundle packing. 3D reconstructions of FFT plots acquired using MPM was followed by a quantification technique using FFT (Wu, Li et al. 2011). This quantitative analysis of collagen orientation index and collagen bundle packing was used to discriminate chronological and photo-ageing in the skin.

d. Collagen Type/ Colour Separation

Segmentation of the components of histological images of neuroma, and analysis of specific component in biological tissue sections was proposed by Cisneros et al (Cisneros, Cordero et al. 2011). This method examined the properties of each pixel in order to evaluate colour, then measured the distance between the colour of the pixel using Mahalanobis distance, and the average colour of each one of the components to be segmented. This was used in neuroma images from amputees to evaluate the effects of stimulation on the peripheral neuroprosthetic nerves. This method began with segmentation using pixel-based techniques, and classified pixels into component 1 and component 2 using colour features of individual pixels. Pixel determination (component 1 compared to component 2) was based on the Mahalanobis distance that measured the distance between the colour of the pixel and the average colour of each one of the components to segment the target object. This method was compared to other segmentation methods used to count cancer cells in histological sections from different squamous cell carcinomas (Loukas et. al, 2003), using Laplacian of Gaussian (LoG) edge detection (Marr and Hildreth 1980). In this work, the components (brown cells)

were segmented and the results compared with segmentation using a *k*-means clustering algorithm (He, Long et al. 2010). The proposed technique could be adapted to any histological image. The limitation was that the speed of analysis, and implementation was not easy to improve because of the small number operations used.

Differences in collagen content, fibre colour, and fibre distribution were assessed in rat skin tissue and myocardium, and rabbit iliac arteries using picosirius red stained sections in order to detect thin fibres (Rich and Whittaker 2005). An image subtraction technique and colour threshold filters were used to quantify collagen content and assess the spatial distribution of fibres. In skin samples, there was a good correlation between the collagen content in skin obtained by two investigators. In the analysis of myocardium, there was an increase in scar collagen content one, three and five weeks after injury. There was a decrease in green (thin) fibres and increase in orange (thick) fibres. The analysis of arterial tissue showed that the *tunica adventitia* contained mainly yellow fibres, while the *tunica media* contained the least collagen (mainly green and orange) within the lesion. Subtraction and colour separation methods were used to analyse specific tissue sections, and so may not be applicable to another type of tissue.

Colour segmentation was used in biomedical applications for detecting tumours in brain mass resonance imaging (MRI) scans images using *k*-means clustering for colour segmentation (Wu, Lin et al. 2007). The proposed method of clustering MRI images into three clusters showed good segmentation by combining histogram statistics and *k*-means clustering to segment and track the tumour in the image by distinguishing the lesion size and region. The method started with generating an RGB colour image from the grey MRI image, followed by conversion into CIE Lab colour space and then clustering the colour image into three clusters. The result of *k*-means clustering and histogram-based clustering showed a segmented tumour in the image, however, some other white regions were segmented with the lesion region, indicating an error in the segmentation process. Therefore, more work was required to optimise this technique. The use of *k*-means clustering has important roles in other applications, as well as in biomedical images, and has been applied to satellite images. In satellite image analysis *k*-means clustering was used to segment images into five groups, and de-correlation stretching was used to enhance the colour separation in images to make geographical feature discrimination easier (Chitade and Katiyar 2010). These examples indicate that

k-means clustering has wide utility across image analysis problems, and can be used effectively as a segmentation tool.

2.2 Aims and Objectives

The research reported in the rest of the Chapter aims to develop an automated system to measure dermal integrity using texture orientation analysis. In general, I used picosirius stained mouse skin of varying ages, in healthy and diabetic states, and assessed collagen dynamics in Herovici polychrome stained images. Specifically, my aims were to:

- Develop image-based techniques to assess collagen orientation and the changes in collagen structure in picosirius stained skin. This involves quantification of collagen bundle directions, and measurement of degradation in collagen organisation, as well as changes in bundle thickness in a calibrated series of ageing and diabetic skin.
- Develop a technique to assess collagen dynamics in Herovici's polychrome stained images by quantifying the ratio of newly formed (blue) to mature (red) collagen.
- Test the performance of these techniques in a chronically aged databank of images of both healthy skin and skin from a model of type 2 diabetes.

2.3 Automated Collagen Assessment

2.3.1 Collagen Orientation Assessment

Collagen orientation and organisation in the dermis can qualitatively discriminate different ages. The dermal layer of the skin contains the basket-weave conformation of healthy collagen, which changes with aging and other disorders. Cross-polar images of picosirius stained skin reveal this exquisite structure. Herein, I shall utilize these images to create an automated measurement of collagen basket-weave and fibre orientation.

2.3.1.1 Sources of Skin, and the Image Databank

Reagents were supplied by Sigma-Aldrich (Poole, Dorset). Animal procedures were performed by Mr Ed Wargent and Dr Mohamed Zaibi, and histological preparations were provided by Mrs Parvathy Harikumar and Dr Joanne Selway. All animal procedures were conducted in accordance with the UK Government Animals (Scientific

Chapter 2

Procedures) Act 1986 and approved by the University of Buckingham Ethical Review Board. For the calibrated series of ageing, wild-type C57Bl6 mice were killed at 7 weeks, and 3, 8, 12 and 20 months of age. These provide a meaningful model of human ageing, ranging from young adult to extreme old age. Males were used for all studies, and tissues from at least 3 animals per group were studied (90 images from papillary and 90 images from reticular dermal layer).

For the series of diabetic skin, both misty (normal control for *db/db*) and *db/db* mice were sacrificed at 6 weeks, 3, 5 and 6 months of age. *db/db* mice do not express a functional receptor for leptin, a hormone that regulates energy balance. These animals are hyperphagic and show rapid post-natal weight gain. By 12 weeks *db/db* animals are hyperglycaemic, providing a meaningful model of human type 2 diabetes. The animals in the ageing studies were in a C57Bl6 background. Males were used for all studies, and tissues from at least 3 animals per group were studied (78 images *db/db* and 90 images from misty mice).

For picrosirius staining, skin sections were stained for one hour at room temperature in 0.1% Direct Red 80 in saturated picric acid prior to differentiation in 0.5% acetic acid, dehydration, clearing and mounting as standard. Slides were imaged in bright-field, with cross-polars and under fluorescence with a Nikon TEi inverted microscope equipped with cross-polar optics (Nikon, Kingston, UK) and a QImaging CCD camera coupled to Nikon NIS imaging software. Images for each slide were captured using a 90X objective in at least 3 different locations. For Herovici staining, nuclear staining with an acid-resistant nuclear stain (Weigert's Iron Haematoxylin) for one minute was followed by 2 minute incubation in Herovici staining solution following by a tap water rinse. Slides were then immersed in 1% acetic acid before dehydration, clearing and mounting. Slides were visualised under bright-field using a whole-slide scanner (ScanScope CS2, Aperio, San Diego, CA, USA).

Statistical analysis was performed in GraphPad Prism™ 5.0. Two-group tests between *db/db* and misty animals or between papillary and reticular compartments, were carried out using either Students' t-test. One-way ANOVAs followed by Dunnett's post-hoc analysis (where the ANOVA demonstrated significance) were performed when analysing more than two groups. Where appropriate, Pearson's correlation analysis was performed ($p < 0.05$).

FFT and Gabor filter techniques were implemented using the MATLABTM 2011b image processing toolbox.

2.3.1.2 Implementation of an Existing FFT Technique

In order to assess the effectiveness of existing methodologies in measuring collagen orientation, I used the methodology described by Wu et al (Wu, Li et al. 2011) (section 2.1.3.a). I investigated the qualitative decline in dermal integrity in young (3 months) and old (20 months) dermis of mouse skin. This was done by computing the FFT power spectrum for each image in the dataset of picosirius stained papillary dermis for different age groups at 3, 8, 12, and 20 months (Figure 2.3a). Collagen orientation indexes were generated from the elliptic shape of the FFT power spectrum of each image, and then the orientation index calculated by equation *eq2.1*. I was able to measure the structural changes discriminating the extreme age groups (3 and 20 months, Figure 2.3b). However, I was not able to detect age-related changes between 3 and 12 months (an approximation of middle-age), thus a more sensitive approach was required. This suggested that existing techniques were designed to measure gross pathological changes, such as fibrosis, but were not sufficiently sensitive to detect more subtle and progressive pathological changes in the dermis, such as those seen in aging.

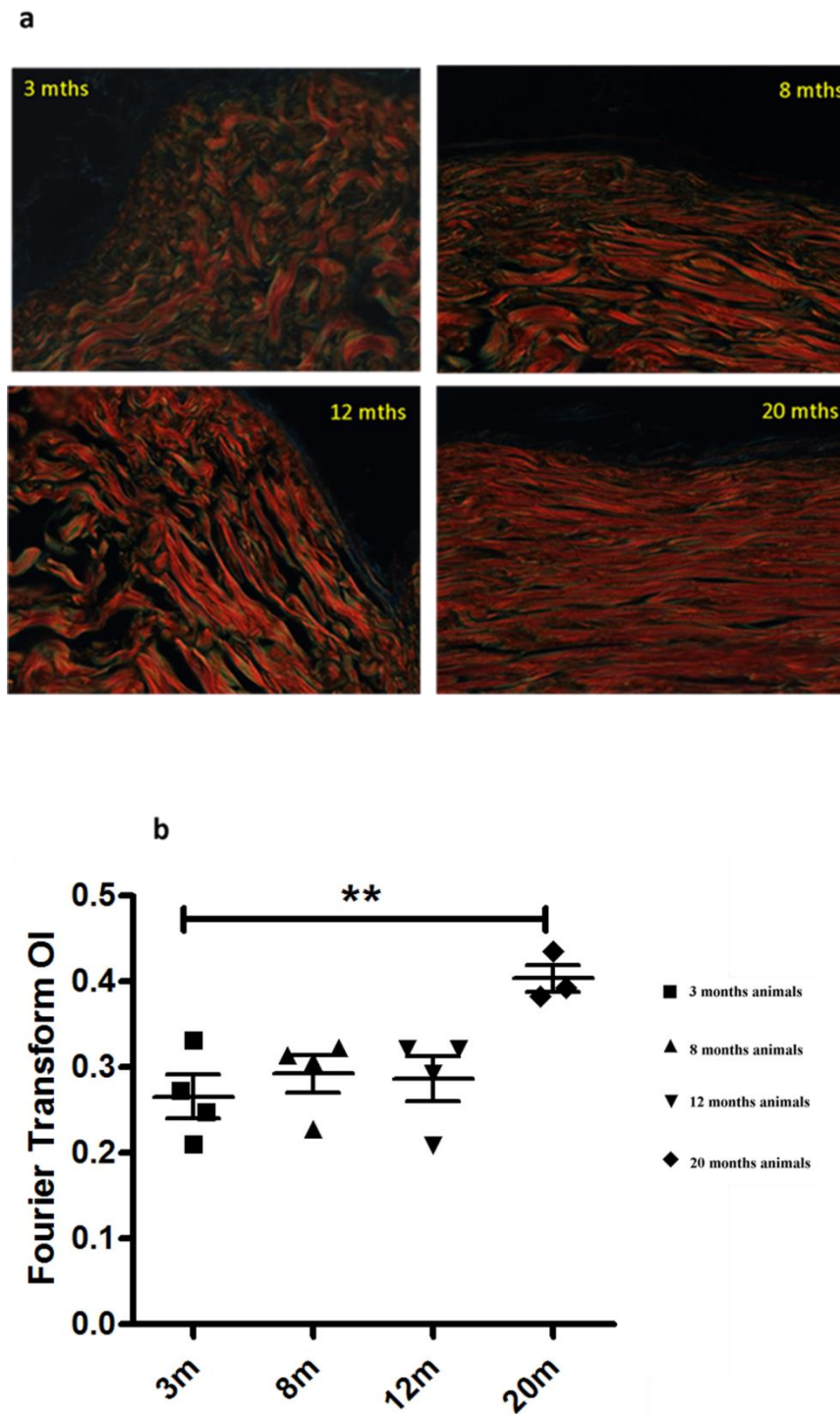


Figure 2. 3: Analysis of picosirius stained skin. |a) picosirius stained papillary dermis in 3, 8, 12 and 20 month old *wt* mouse skin, magnification= 90X, pixel dimensions = 1600×1200 pixels, 114.72×86.04 μm , b) scatter plot (vertical) of the result of the FFT analysis of chronological skin ageing, at least 3 animals per age group, 2 sections per animal (a total of 90 images). The mean and standard deviation is shown for each group.

2.3.1.3 Development of a Gabor Filter with Fourier Transform method

Collagen in the dermis is organised with fibres in different directions. To assess changes in collagen orientation, the amount of collagen in each direction has to be quantified, and one way of doing this was to use a directional or ‘wavelet’ filter such as a Gabor filter before texture analysis. In this thesis, I opted to exploit the directional characteristics of the Gabor filter (see section 2.3.1.3c). However, there were several pre-processing and other technical considerations to be evaluated first.

a. Image Capture Parameters

Initially 20X magnification (pixel dimensions = 2560×1920 pixels, 825.6×619.2 µm) picrosirius images were prepared (Figure 2.4). Figure 2.4b shows the 20X magnification picrosirius stained image and the objects detected in 8 directions using a Gabor filter. It was expected that the presence of hair follicles and sebaceous glands would affect collagen directional quantification because they are oriented in different directions, and to solve this problem I captured images in areas without hair follicles and glands. Another issue that affected the analysis process is that the FFT power spectrum in young skin and elderly skin at 20X magnification didn’t show a difference in collagen structure, as shown in Figure 2.5. Thus, to reduce the effect of hair follicles and other non-collagen fibres in images, 90X images (pixel dimensions= 1600×1200 pixels, 114.72×86.04 µm) were used for analysis. Using a 90X image magnification, I could analyse the collagen in papillary and reticular dermis separately.

b. Pre-processing Steps

To detect the directional structure of collagen in each image, many pre-processing techniques were used before the final technique to enhance edges in images. For example, using the minimum and maximum filters separately in the colour space channels to emphasize the dark and bright area respectively in images provided the desired edge enhancement. Afterwards, an unsharp mask filter was used as a final filter to enhance the edges of collagen fibres in the dermal skin layer in images. Figure 2.6 shows the result of a filtered image using the above techniques, and shows some of the non-fibre objects as a directional structure. Also, it is of note that in collagen orientation analysis, the unsharp filter caused excessive collagen fibre detection. Therefore, I opted to limit pre-processing to the use of a 3×3 median filter in order to reduce noise and other artifacts that are generated by capturing picrosirius cross-polar micrographs.

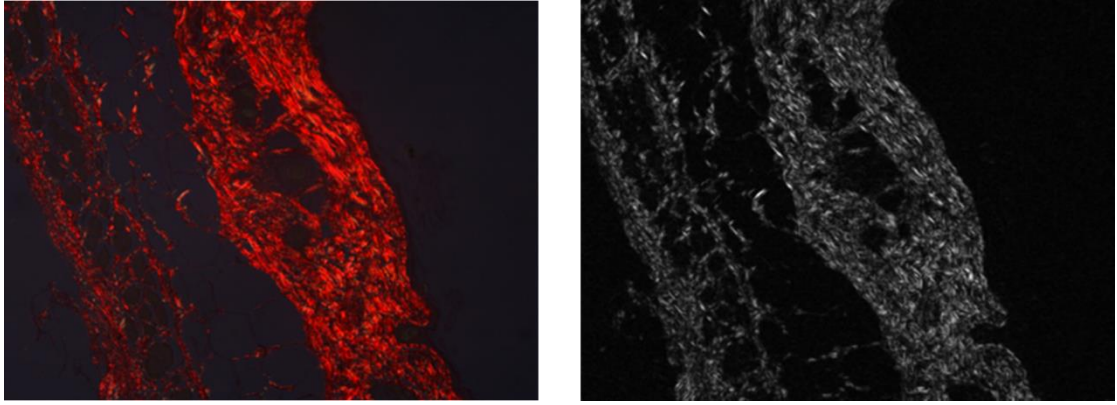


Figure 2. 4: Analysis of picosirius images and edge detection in 8 directions. Left panel is the original 20X picosirius stained image, right panel is the Gabor filtered image.

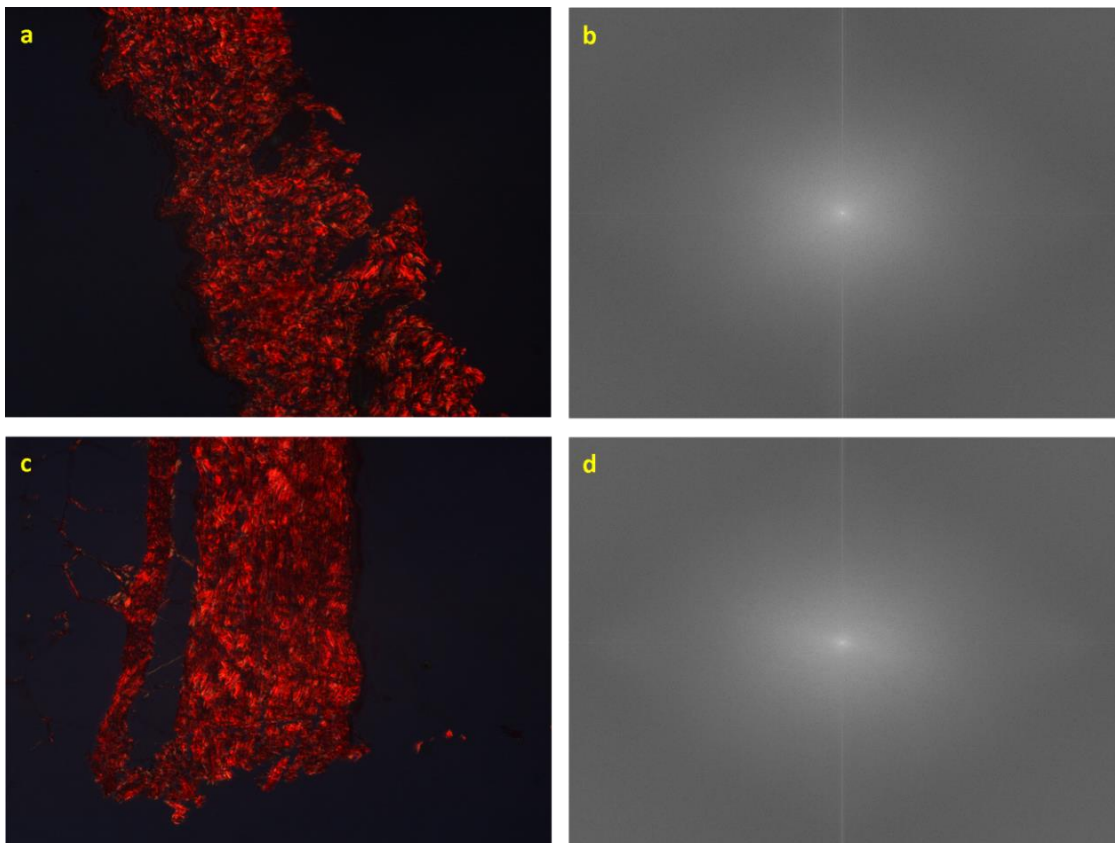


Figure 2. 5: The effect of hair follicles and sebaceous glands on the FFT power spectrum. a) picosirius stained 3 month mouse skin and b) its FFT power spectrum. c) 20 month *wt* mouse skin and d) the FFT power spectrum. Images captured at 20X original magnification.



Figure 2. 6: Picrosirius stained reticular dermis from 3 months old *wt* mouse. Original image (a), the unsharp mask filtered image (b), image filtered with maximum filter (c) and (d) image filtered with minimum filter. Image captured at 90x original magnification.

c. Gabor Filter Parameters

A Gabor function in the spatial domain is a sinusoidal modulated Gaussian. For a 2D Gaussian with a spread of σ_x and σ_y in the x and y directions, respectively, and a modulating frequency ω , the real impulse response of the filter is given by:

$$g(x, y; \lambda, \theta, \psi, \sigma, \gamma) = \frac{1}{2\pi\sigma_x\sigma_y} e^{-\frac{1}{2}(\frac{x^2}{\sigma_x^2} + \frac{y^2}{\sigma_y^2})} \cos(2\pi\omega x) \quad (\text{eq2.2})$$

Where λ = wavelength of the sinusoidal factor, θ is the orientation of Gabor function, ψ is the phase offset, σ is the sigma/standard deviation of the Gaussian factor and γ is the spatial aspect ratio of x and y axis of Gaussian.

A Gabor filter calculates all the orientations of the input image with the Gaussian filter for all combinations of orientations and all phase offsets using the parameter values below:

Chapter 2

Wavelength (λ) = 8; Orientation degree (θ) = 0; Phase offset(s) (deg.) = $[0, \pi/2]$; Aspect Ratio = 0.5; Bandwidth = 1; Number of orientations = 8. The result is a 4 dimensional matrix consisting of image coordinates, phase offset and the orientation:

$$\text{Result} = (x, y, \text{phase offset}(i), \text{orientation}(j))$$

A Gabor filter was applied on an input image using θ values of 0° (and its equivalent 180°), 45° (and its equivalent 225°), 90° (and its equivalent 270°), and 135° (and its equivalent 315°) for all of 8-Directions, to detect and highlight collagen fibre edges. The use of 16-directions didn't produce interesting information for analysis because of the ambiguity in the close directions resulting from the output Gabor filter when followed by a FFT transform. However, the shape of the generated binary images from differed ages could be discriminated by applying a Gabor filter in 8-directions (Figure 2.7, 3 and 20 months *wt* mouse).

Each two opposite directions of collagen, e.g. $(0^\circ, 180^\circ)$, $(45^\circ, 225^\circ)$, $(90^\circ, 270^\circ)$ and $(135^\circ, 315^\circ)$, generated an ellipse perpendicular to the collagen structure in these two directions, achieved by transforming the Gabor filtered image by FFT to create the power spectrum of each direction, and then converting the spectrum to its binary form. For all 8 directions, there were four ellipses generated, and an orientation index was calculated for each ellipse by use of the equation *eq2.1*.

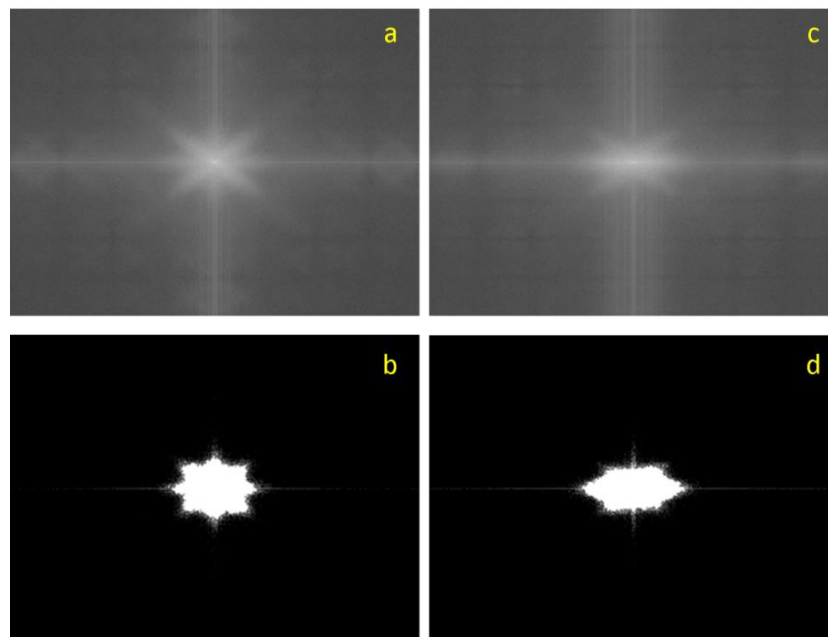


Figure 2. 7: FFT power spectra of Gabor filtered images. a) 3 month *wt* reticular dermis and its binary image (b), 20 month *wt* reticular dermis (c) and its binary image (d).

d. FFT and Quantification

The Fourier spectrum of Gabor-filtered images in each direction pair was represented as an ellipse, i.e. $(0^\circ, 180^\circ)$, $(45^\circ, 225^\circ)$, $(90^\circ, 270^\circ)$ and $(135^\circ, 315^\circ)$ are in opposite directions. Figure 2.8 shows the direction of ellipses. For quantification, the power spectrum was transformed to a binary representation, and each ellipse was quantified as a function ($N_{\omega n}$) of the length of its minor and major axes.

$$N_{\omega n} = 1 - \frac{\text{minor axis}}{\text{major axis}} \quad (\text{eq2.3})$$

Figure 2.9 illustrates the whole process with a flow chart and the result of each step before the elliptical quantification process.

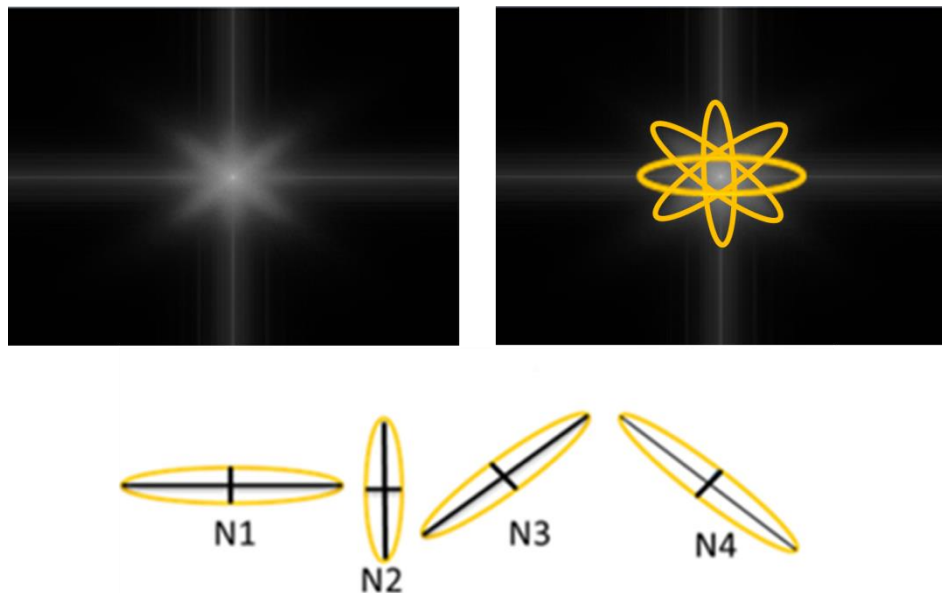


Figure 2. 8: Ellipses generation from FFT power spectrum of Gabor filtered image. A typical FFT spectrum is shown in the upper left panel. In the upper right panel is an illustration of the elliptical measurements taken from the FFT for each ellipse. Below is the illustration of the ellipse measurements generated to produce the collagen orientation index (N) from the elliptical axes generated from ω values N1-N4.

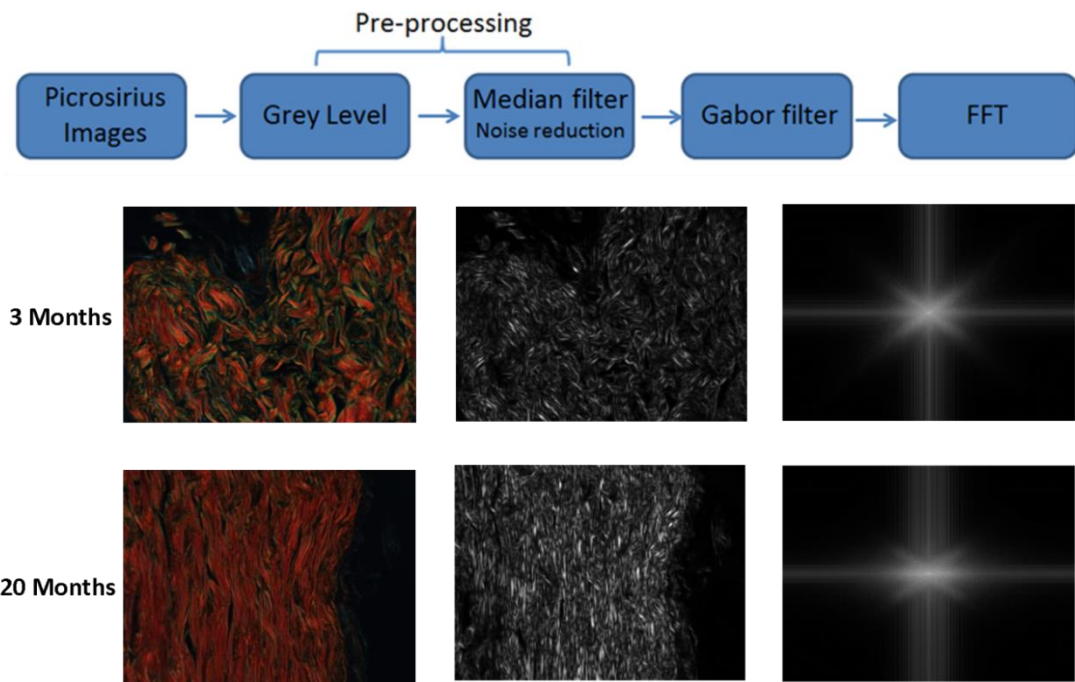


Figure 2. 9: Overview of edge detection using a Gabor filter and collagen quantification in picrosirius images. Top panel, is flow diagram of FFT power spectrum generation. Lower figure: the left columns shows the original images; the middle columns shows Gabor filtered images, and in right columns shows the Fourier spectra of Gabor filtered images.

2.3.1.4 Final Gabor Filter with Fourier Method and Validation

In summary, the combination of Gabor filtering and FFT was used to produce a frequency spectrum from each direction of collagen bundles in the dermis (Figure 2.10). This spectrum was quantified using ellipse parameters that generated by converting the FFT spectrum to its binary form using Otsu threshold as explained in MATLAB script below, to measure subtle changes in collagen fibre orientation and progressive pathological changes in the dermis.

```
Level = graythresh(image); // Compute global threshold.
```

```
bwI = im2bw(image,level); // Convert image to binary image by thresholding.
```

2.3.1.4.1 Collagen structure in Ageing Skin

By quantifying the spectra resulting from FFT images, either with or without an eight direction Gabor filter, I sought to evaluate the ability of my methodology to provide an index of collagen organisation. I assessed collagen integrity by determining collagen organisation in skin samples prepared from mice of increasing age. Superficially, a loss

Chapter 2

of basket-weave structure was apparent in elderly skin by 20 months of age, and this difference could be determined in FFT images with or without Gabor filtering. However, FFT alone did not identify a progressive decline in skin integrity from 8 months as I would have anticipated from qualitative observations and published observations of ageing skin structure (Varani, Warner et al. 2000; Wu, Li et al. 2011). Rather, a trend was only detectable with the introduction of the Gabor filtering process (Figure 2.11).

I was able to demonstrate a significant inverse correlation between time and collagen organisation (Table 2.1). When compared to the use of FFT alone, the correlation between age and collagen organisation increased with Gabor filtering, with R^2 values of 0.842 and 0.95 respectively.

	Overall Dermis	Papillary	Reticular	Overall Dermis	Papillary	Reticular
	Gabor+FFT (max.OI/min.OI)	Gabor+FFT (max.OI/min.OI)	Gabor+FFT (max.OI/min.OI)	FFT (OI)	FFT (OI)	FFT (OI)
95% <i>CI</i>	-0.999 to 0.209	-0.999 to 0.284	-0.999 to 0.276	-0.370 to 0.999	-0.574 to 0.997	-0.171 to 0.999
<i>P</i> <i>value</i>	0.0128	0.0206	0.0111	0.0413	0.0683	0.0272
R^2	0.950	0.920	0.956	0.842	0.7454	0.8941

Table 2. 1: Correlation of ageing with collagen structure in papillary and reticular dermis using FFT with and without edge detection.

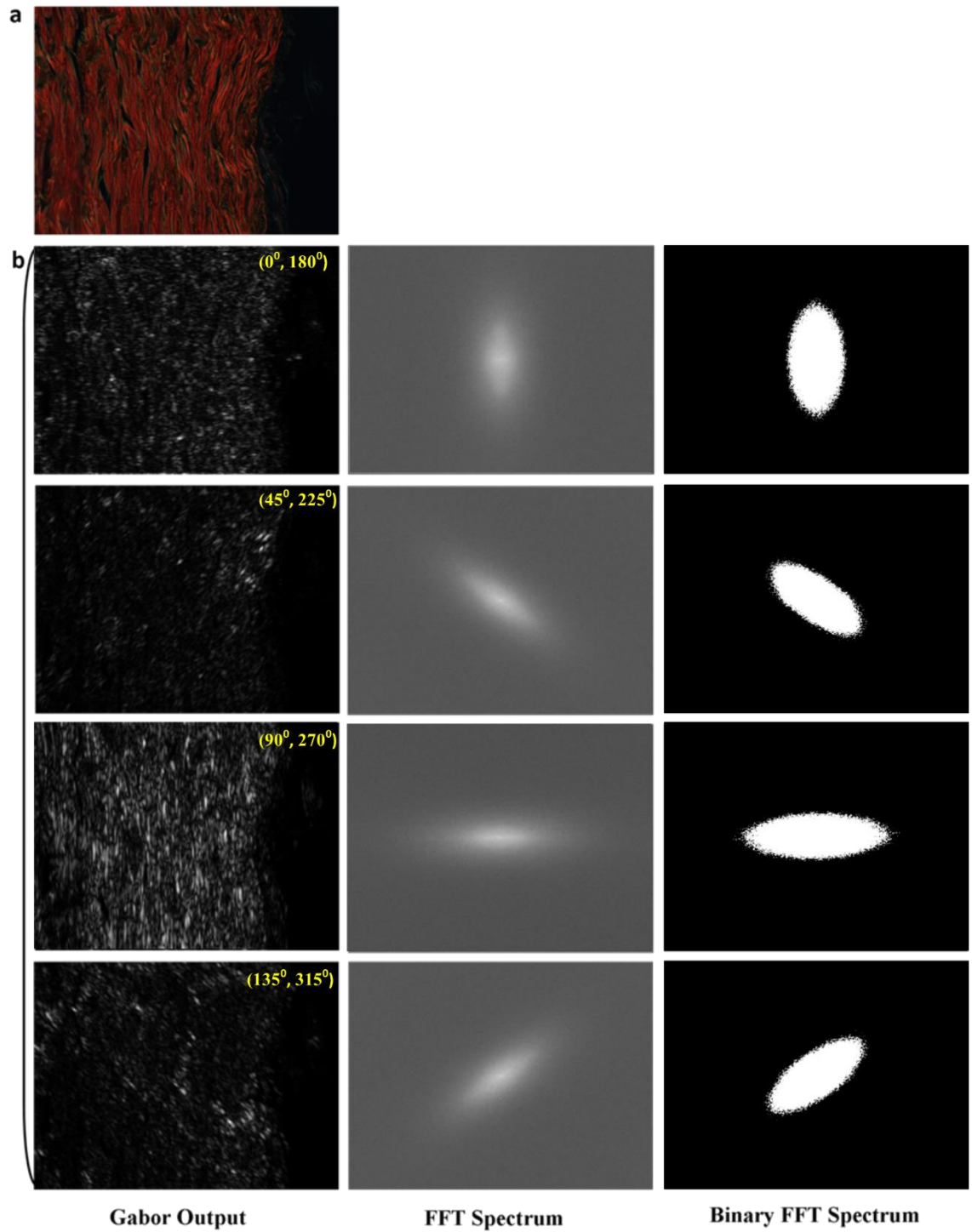


Figure 2. 10: Use of a multi-directional Gabor filter. a) original cross polar image, b) the Gabor filter result image for each opposite direction pair (left panels), FFT spectrum (middle panels) and binary image of each ellipse (right panels).

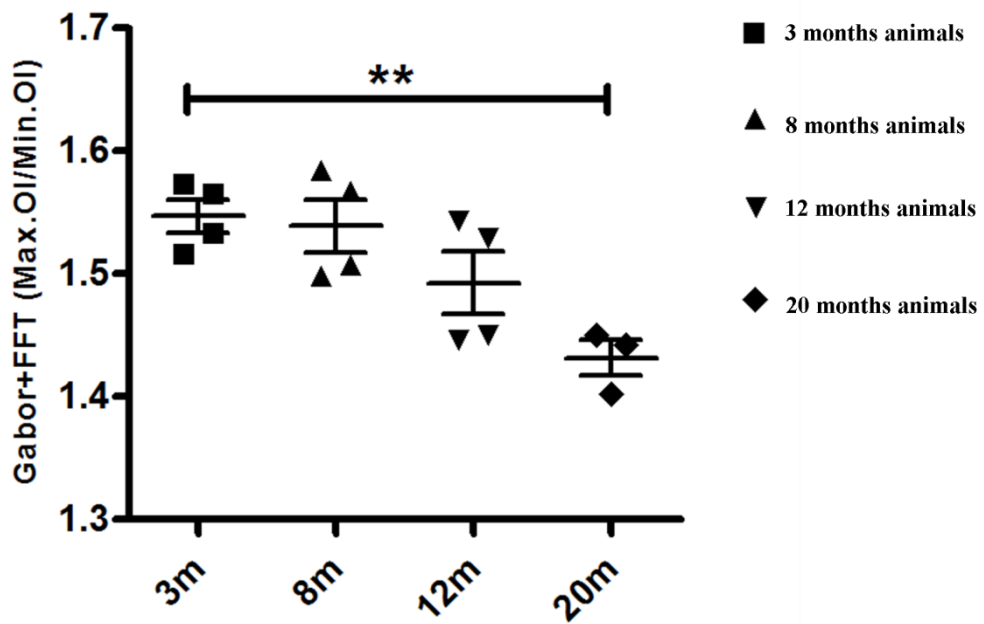


Figure 2. 11: Alterations in dermal integrity with age in *wt* animals. Scatter plot, vertical, of the result of analysis showing p value = 0.005 represented by **, 3m, 8m and 12m 4 animals per group and 20m 3 animals, 3 images from each animal (90 images).

The dermis is divided into superficial papillary and deeper reticular layers, distinguishable by collagen organisation. I went on to evaluate differences in age-related changes in these two compartments. The reticular dermis consistently exhibited a lower orientation index in the presence or absence of the Gabor filter (Figure 2.12), and while this difference did not achieve significance, it is suggestive of a higher level of organisation in the papillary dermis. More importantly, the use of a Gabor filter revealed differential rates of collagen degradation in the two layers. The papillary dermis maintained consistent collagen organisation until 8 months, with a reduction in mean integrity by 12 months that was exacerbated by 20 months using a combination of a Gabor filter and FFT.

A more progressive loss of structure was seen in the reticular compartment, with the changes between 8 and 20 months being less marked. A significant change in reticular collagen structure between 3 months and 20 months *wt* was observed with the FFT alone ($p < 0.038$) and with the inclusion of the Gabor filter ($p < 0.039$) according to Students' t-test. Both quantification methods demonstrated an inverse correlation between age and collagen orientation, but only with the addition of the Gabor filter was

Chapter 2

the correlation significant in both the papillary and reticular dermis. Overall, with the Gabor filter, the reticular dermis has a higher correlation co-efficient ($R^2=0.956$) compared to the papillary dermis ($R^2= 0.920$) suggesting that the latter compartment is slightly more resilient to age-related damage.

A progressive decline in integrity was seen in both papillary and reticular compartments by my method. While FFT alone was able to detect changes by 20 months, this method could not detect progressive decline in either compartment. Significance was established using an ANOVA with post-hoc Dunnett's test relative to the 3 month group ($n>3$ animals per group).

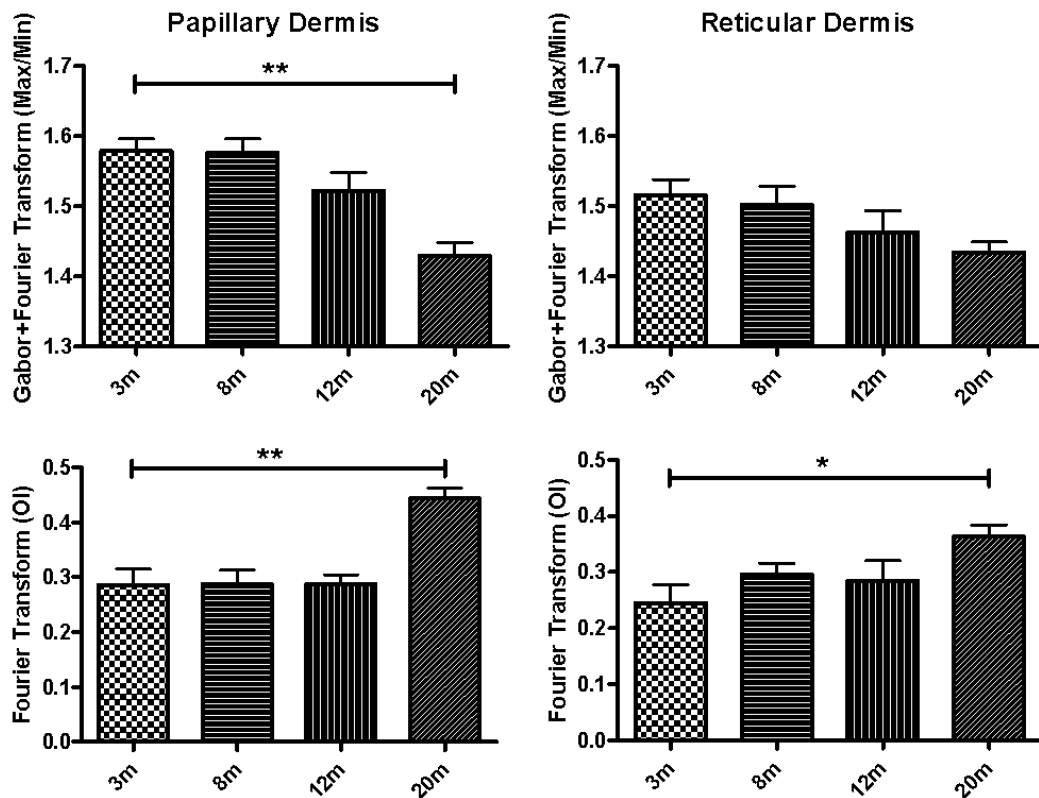


Figure 2. 12: Increasing age demonstrates differential patterns of decline in collagen organisation in the different layers of the dermis in *wt* mice. Using FFT with Gabor filter showed a decrease of Max.OI/Min.OI with age, which is significant in papillary dermis (3-4 animals per age group, 3 images per animal, 90 images) p value=0.0023, **. Whereas using FFT without Gabor filter showed increase of orientation index OI with age, in reticular dermis (same number of samples of papillary dermis) p value= 0.02, represented by 1 asterisk*).

2.3.1.4.2 Diabetic Skin Evaluation

By using my new techniques, collagen organisation in an *in vivo model* of type 2 diabetes mellitus (the *db/db* mouse) was evaluated.

Analysis of picosirius stained skin by FFT alone showed a change in structure between 6 weeks and 3 months, (by which time mice were hyperglycaemic), although after this time integrity appeared to stabilize (Figure 2.13). However, no statistically-significant differences in dermal integrity discriminated diabetic and lean mice. Application of the Gabor filter revealed a progressive loss in structure, and the variation seen at 6 months was consistent with the variation one would anticipate from an *in vivo* model. Misty skin, however, did appear to have a more ordered basket-weave structure compared to the C57Bl6 mouse, and this strain variation is a current avenue of biological investigation. Critically, inclusion of the Gabor filter allowed clear discrimination between lean and diabetic skin at each time point.

Although there were qualitative differences between control misty and matched *db/db* picosirius stained skin, more subtle changes between *db/db* time points were difficult to assess. When comparing the original Fourier transform alone with my refined method incorporating the Gabor filter, only my method differentiated between control and *db/db* skin. Furthermore, I demonstrate that the orientation indices calculated from my Gabor plus Fourier method exhibited a significant inverse correlation with increasing age of diabetic skin ($R^2= 0.9936$) but not within the control skin ($R^2= 0.3737$), whilst no correlation was observed with the Fourier alone method (Table 2.2).

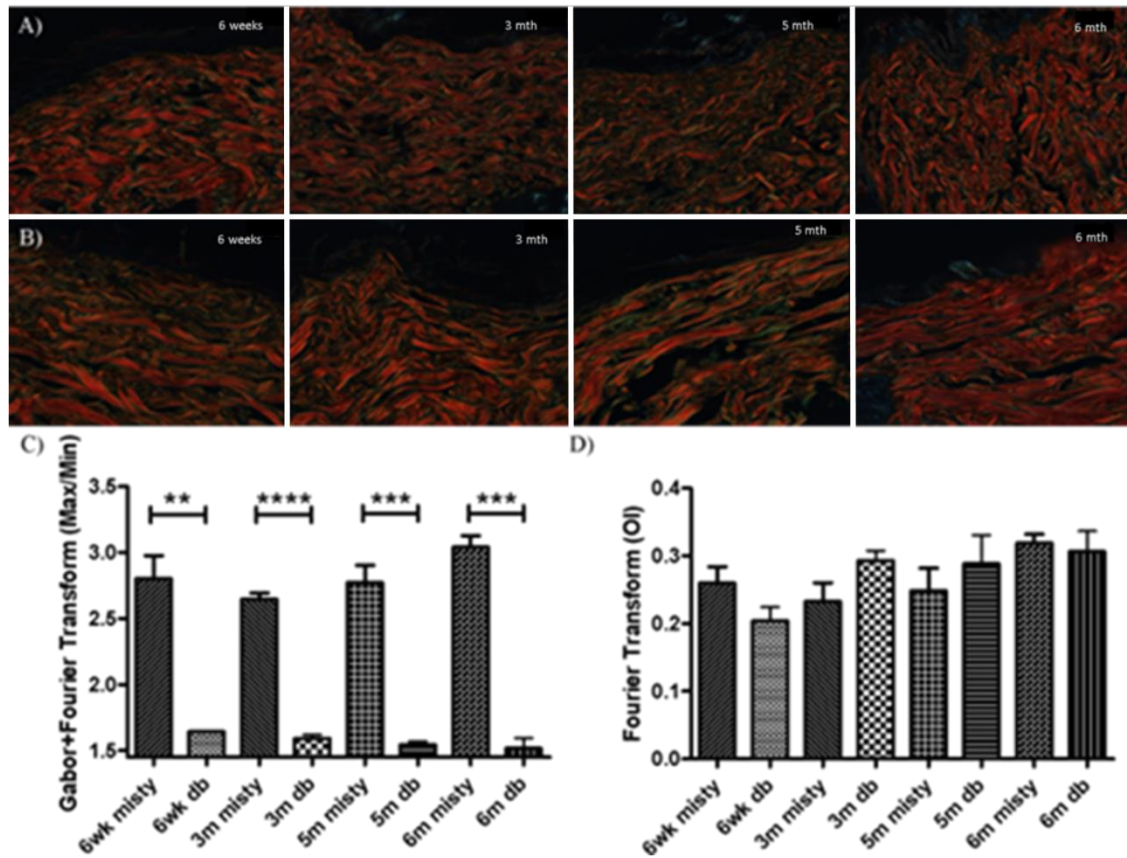


Figure 2. 13: Dermal collagen organisation in lean and diabetic mice. A) *db/db* and B) misty skin quantification using the Gabor/ FFT methodology (C), ** is significance with p value= 0.002, *** p value= 0.0005, **** p value<0.0001 , or by FFT alone (D).

	<i>db/db</i> using Gabor (max.OI/min.OI)	Misty using Gabor (max.OI/min.OI)	<i>db/db</i> FFT (OI)	Misty FFT (OI)
95% CI	-0.9999 to 0.8511	-0.8481 to 0.9905	-0.6437 to 0.9964	-0.8531 to 0.9901
P value	0.0032	0.3887	0.1676	0.4002
R ²	0.9936	0.3737	0.6929	0.3598

Table 2. 2: Statistical analysis of diabetic skin data. Statistical comparison between each of *db/db* and misty collagen structure using Gabor filter with FFT and FFT along.

2.3.2 Collagen Thickness Quantification

Collagen bundle thickness is strongly related to change in collagen dynamics caused by ageing or environmental factors and skin disease (Verhaegen, Marle et al. 2012). The aim of this experiment was to quantify changes in collagen structure through assessing changes in FFT spectra associated with collagen bundle thickness.

As illustrated in the earlier sections of this thesis, the FFT spectrum of a picosirius image provides information about collagen structure in different ages. This section describes a method for quantifying collagen bundle thickness in skin tissue sections stained with picosirius from chronologically-aged mouse skin as described above based on the maximum amplitude of the FFT spectrum. This was achieved by transforming the original picosirius stained image from the spatial domain to its frequency domain using FFT as shown in Figure 2.14.

2.3.2.1 Existing Methods for Bundle Thickness

It is difficult to measure collagen bundle thickness because each section of the skin might not go through the thickest part of the fibre, and there are no many existing methods to measure the thickness of collagen. Therefore, this was my motivation in seeking an automated method to quantify collagen bundle thickness.

The only method described in the literature to measure collagen bundle thickness used the FFT first order maximum spectrum followed by calculating the distance between the centre of gravity and the centre of the FFT power spectrum (Figure 2.15) (Verhaegen, Marle et al. 2012). One problem with this method is that well-ordered skin, i.e. young skin, doesn't present these two gravities in the power spectrum, therefore, an alternative is required. I developed quantification exploiting the ellipse parameter as described in the final methods section (2.3.2.2). The difference between old and young skin power spectra is illustrated in Figure 2.14.

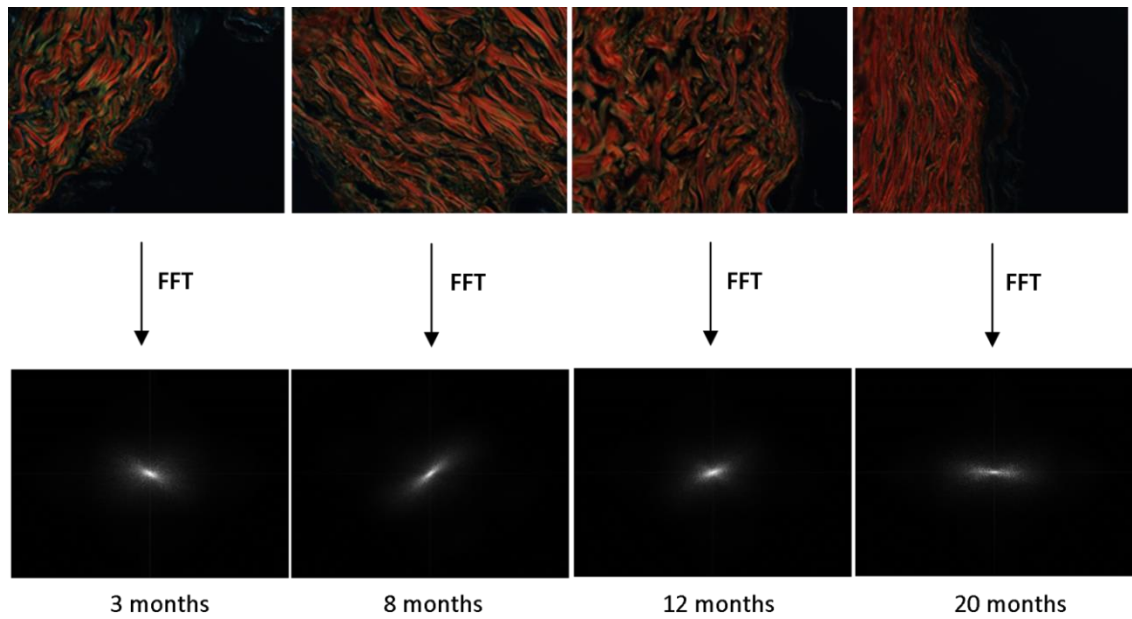


Figure 2. 14: Maximum frequencies FFT power spectra from ageing mice. Top row: picrosirius stained collagen images from skin at 3, 8, 12 and 20 months. Lower panels, maximum amplitude of corresponding FFT spectra.

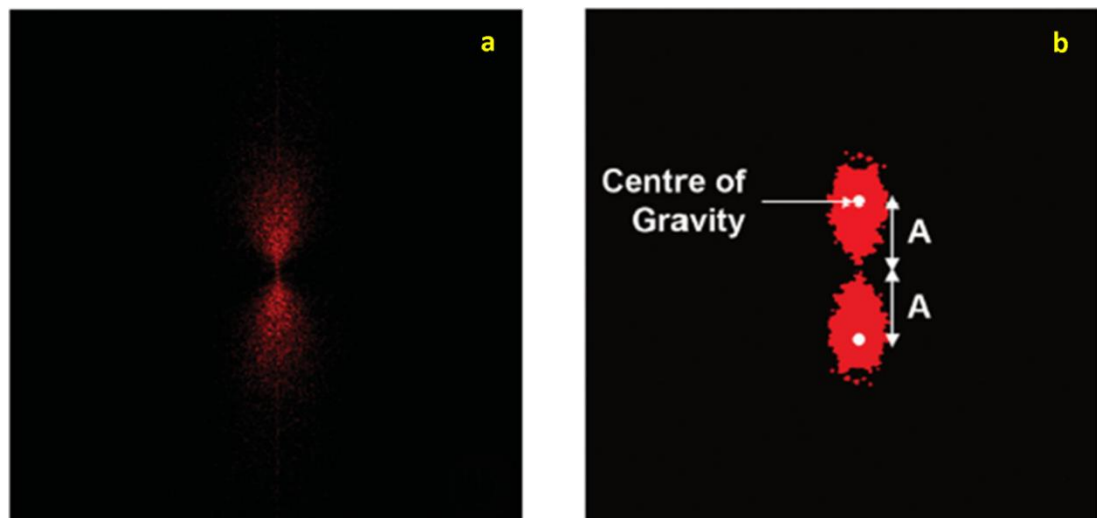


Figure 2. 15: Power spectrum of two the image and measurement of collagen bundle thickness. a) FFT first order maximum spectrum, b) binary of the power spectrum that shows two gravity centres and the distance A (Verhaegen, Marle et al. 2012).

2.3.2.2 Determination of Collagen Thickness

The collagen thickness method started by converting RGB images of picrosirius stained skin into greyscale images, and then measuring the maximum frequencies of the FFT that represent sudden changes of intensity in edges of collagen bundles using MATLAB according to this function:

$$FFTmax = \max(\max(\log(\text{abs}(FFT2(image))))))$$

Calculation of the maximum FFT frequencies was followed by generating a power plot of the FFT spectrum. The resulting spectrum was transformed into a binary image, which was used in collagen thickness quantification.

Elliptical Measurements:

Two parameters were measured during the initial stage: the thickness of the collagen bundle and the bundle spacing (BS). These two parameters were based on quantifying the maximum amplitude in the FFT spectrum. Quantification was done by measuring the distance between the foci and vertex of the ellipse that fit to the binary image of the FFT power spectrum of the high frequencies in the picrosirius images as illustrated in Figure 2.16. The corresponding ellipse was found by finding the ellipse that has the same second central moments as the binary form of FFT spectrum, and major and minor axis were found using the MATLAB command below:

```
I = regionprops (BW, 'MajorAxisLength', 'MinorAxisLength');
```

Bundle thickness was calculated by the formula:

$$T = A - F \quad (eq2.4)$$

Where T is the bundle thickness, A is the major radius of the ellipse, and F is the distance from each focus to the centre of the ellipse (foci distance). The bundle spacing calculated in development stage, by subtracting T from foci distance.

The foci distance was calculated as:

$$F = \sqrt{A^2 + B^2} \quad (eq2.5)$$

Where A and B are the major and the minor radii of the ellipse respectively.

Chapter 2

Figure 2.17 illustrates the origin of these two parameters. The results for each of the measurements were averaged for each animal, and then for each age in the ageing series, as shown in the Table 2.3.

The results of quantifying collagen bundle thickness and bundle spacing demonstrated that there was a change in collagen architecture as a result of aging. Table 2.4 shows the degradation in the bundle thickness with increased age, and the bundle spacing increase in aging is shown in Figure 2.18.

In the quantification stage, determining the distance between the gravity centre and the centre of the power spectrum was not an easy task. Some of the images, especially the image of young mice, showed one circle instead of the two gravities (Figure 2.16a). The final decision step for quantifying collagen thickness was by measuring the distance between the ellipse foci and the ellipse vertex. Figure 2.20e illustrates the thickness measurements from ellipse parameters.

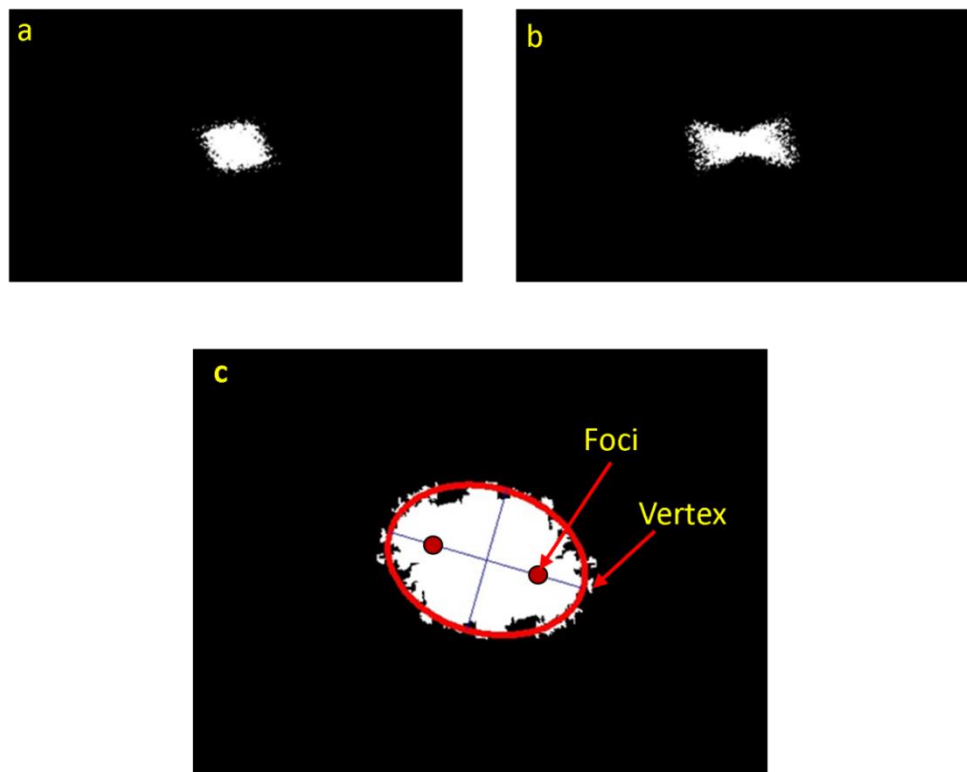


Figure 2. 16: Analysis of binary of maximum power spectrum. The binary of the maximum of the FFT power spectrum of a) 3 months *wt* picosirius stained skin, b) 20 months *wt* skin, c) the fitted ellipse to the binary power spectrum with the foci and vertex of the ellipse and the distance between foci and vertex.

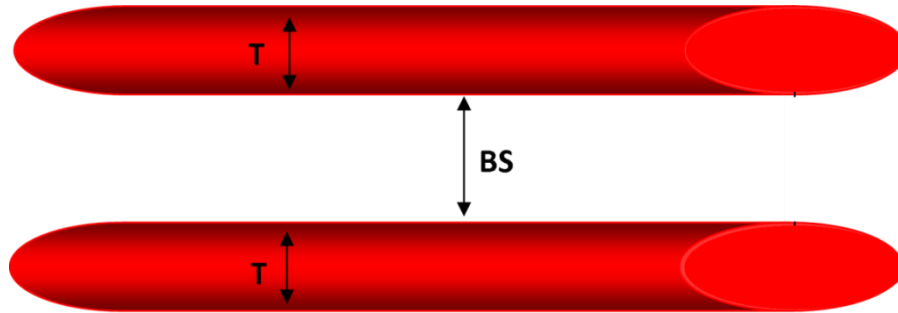


Figure 2. 17: Representation of collagen bundles, and the two parameters of the bundle thickness T, and the bundle spacing BS.

	Foci Distance	Bundle Thickness	Bundle Spacing
Animal 1	90.7	22.6	68.1
Animal 2	114.7	17.4	97.2
Animal 3	72.9	39.7	33.1
Animal 4	136.4	27.4	109
Mean	103.7	26.8	76.9

Table 2. 3: Average measurements of bundle thickness and spacing of replicated animal in one age group (3 months).

Age	Bundle Thickness (mean)	Bundle Spacing (mean)
3 months	26.8	76.9
12 months	17.9	74.6
20 months	9.4	186.5

Table 2. 4: Average bundle thickness and bundle spacing at different ages. A significant decrease of bundle thickness ($p=0.029$), and increased bundle spacing with age ($p=0.003$) was seen.

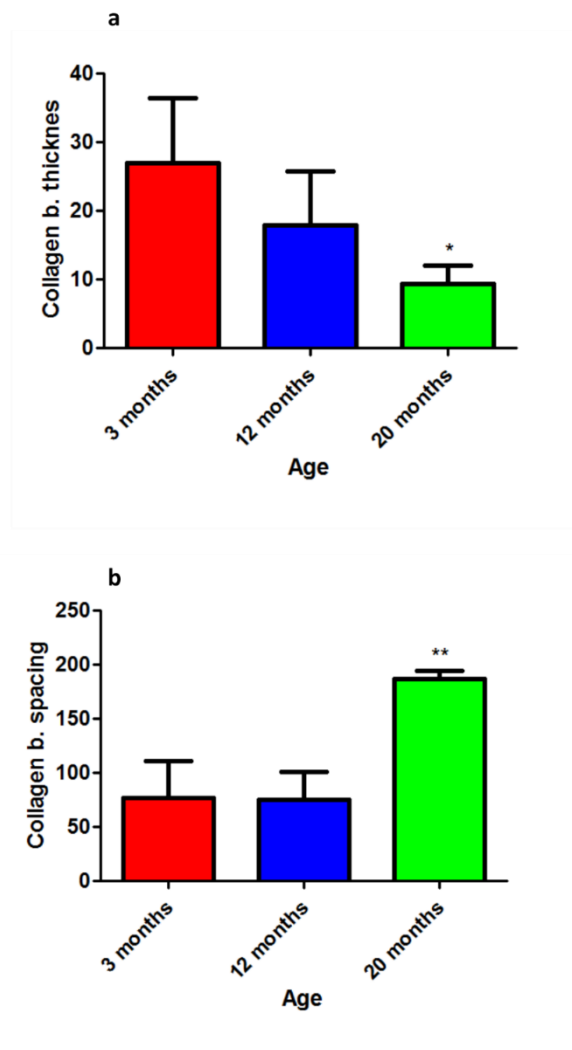


Figure 2. 18: Collagen bundle thickness and spacing plots. a) bundle thickness with age, *p = 0.029, b) bundle spacing in ageing wild-type animals without pre-processing, **p = 0.003.

2.3.2.3 A Refined Method for Collagen Bundle Quantification

Having developed a method to quantify collagen bundles, I was satisfied that this provided optimal analysis, so I investigated the value of additional pre-processing filters. The final technique described herein for quantifying collagen thickness starts by converting cross-polar RGB images of picrosirius staining at 90X magnification into a greyscale image. This was followed by image pre-processing using an unsharp mask filter to enhance edges in images in various orientations to highlight high-frequency components (Polesel, Ramponi et al. 2000; Mahmood, Razif et al. 2011), followed by generating the FFT power spectrum from the enhanced image to improve sensitivity. The sharpening process was implemented by:

$$G(x, y) = f(x, y) - f_{smooth}(x, y) \quad (eq2.6)$$

Where $f_{smooth}(x, y)$ is the smooth version of original image $f(x, y)$.

The resulting sharpened image is produced by:

$$F_{sharp}(x, y) = f(x, y) + k * G(x, y) \quad (eq2.7)$$

Where k is a scaling constant between 0.2 (the default value in MATLAB) and 0.7

The sharpening process was implemented using the following MATLAB functions:

```
h = fspecial('unsharp');  
sharp_image = imfilter (image, h);
```

The negative Laplacian operator and mean smoothing filter were also used to implement an unsharp mask. The collagen thickness quantification method measured the maximum frequencies of the FFT as described in section 2.3.2.2. Binary image of resulting FFT spectra were then used in collagen architecture quantification. The flow chart in Figure 2.19 illustrates the final process, including image enhancement using an unsharp mask filter. In the quantification stage, each spectrum was transformed to binary (Figure 2.20), and quantification was based on the location of the foci and the length of major and minor axis of the corresponding ellipse to the maximum FFT power spectrum. The foci locations F were calculated by eq2.5 and bundle thickness T calculated by eq2.4. Elliptical measurements are illustrated in Figure 2.20e.

2.3.2.4 Collagen Bundle Thickness in Ageing

Aging can cause skin dermal structural change, including effects on collagen bundle architecture (Varani, Dame et al. 2006). I applied my new method to an image bank of picrosirius stained dermis from the series of ageing animals described in section 2.3.1.1 to measure collagen bundle thickness (Figure 2.21). This analysis showed a significant decrease in collagen bundle thickness with age, in particular, a significant change at 12 months was detected.

2.3.2.5 Collagen Organisation in a Diabetic Series

A change in dermal structure in diabetes was previously reported (Romano 1998, Al-Habian, 2011). Figure 2.22a shows the result of collagen bundle thickness analysis of in a series of diabetic mice. The analysis methods were applied the 4 age groups (6 weeks,

and 3, 5 and 6 months). There was not a significant decrease in collagen bundle thickness in this age range, although there was a trend for a decrease overall.

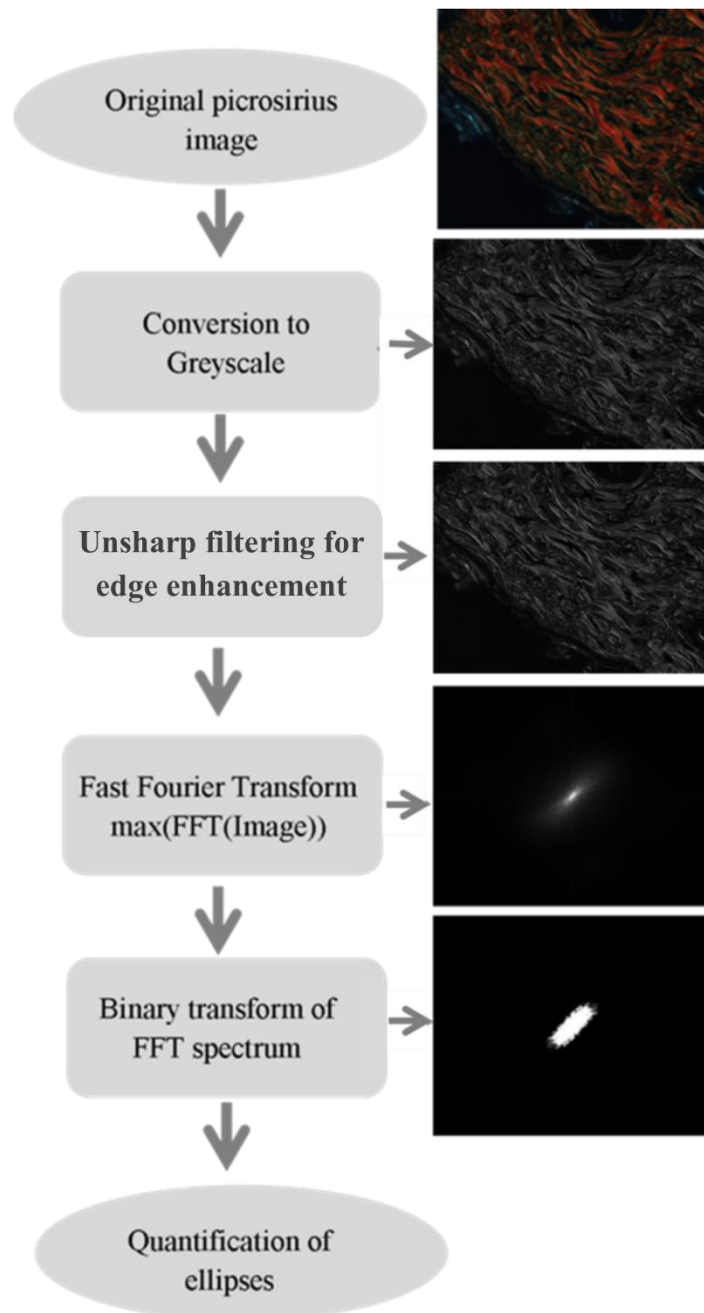


Figure 2. 19: Flow diagram for collagen bundle thickness quantification.

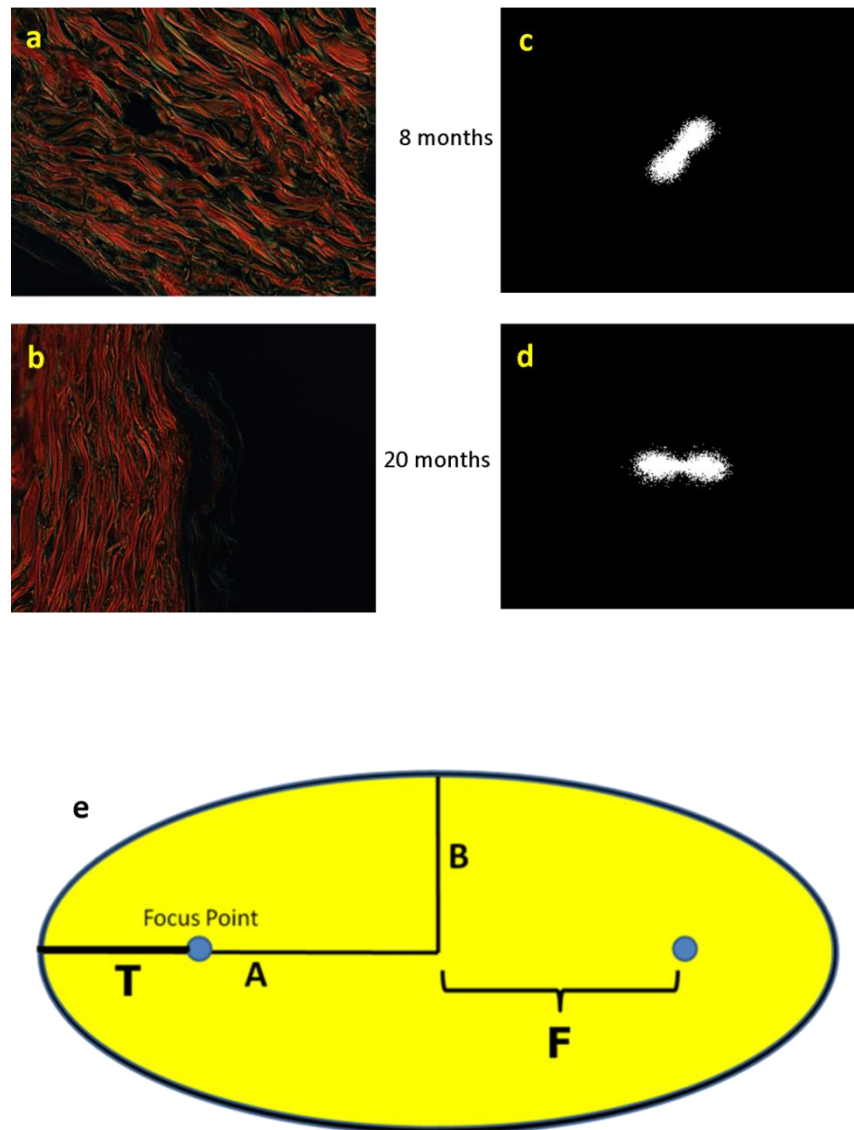


Figure 2. 20: Generation and measurement of ellipses. a,b) original picosirius cross-polar image of 8 and 20 months mice skin respectively, c,d) the corresponding binary power spectra, e) ellipse parameters and thickness measurement.

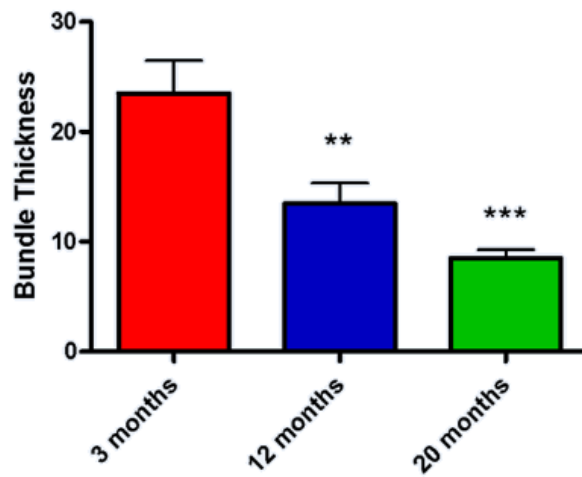


Figure 2. 21: The result of collagen bundle thickness in cross-polar images of picosirius stained mouse skin from different animals at age 3, 12, and 20 months. This shows the decrease in collagen bundle thickness in an ageing skin series, p value< 0.001 represent with ** between 3mth and 8mth, and p value<0.0005, *** between 3mth and 20mth.

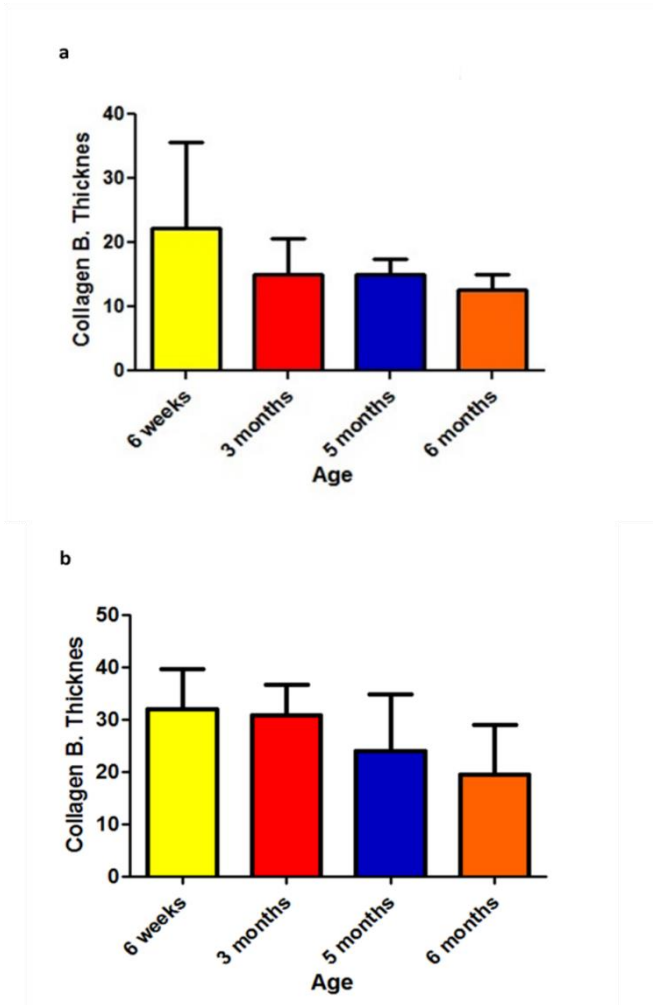


Figure 2. 22: Collagen bundle thickness in diabetic and misty models. a) bundle thickness diabetic animals with age, b) bundle thickness in lean (misty) animals with age.

2.3.2.6 Use of Optical Sections to Improve Collagen Quantification

Confocal microscope images of eosin or picrosirius autofluorescence allows the use of optical sections, meaning that images can be sampled in multiple planes. For most effective analysis, this requires the use of thick sections, but I investigated the information available in existing 5 μm sections. Figure 2.23 shows “side-on” views created from optical sections, and these do indeed contain information about collagen structure. This is an area for future study, which may yield useful information on collagen bundle organisation.

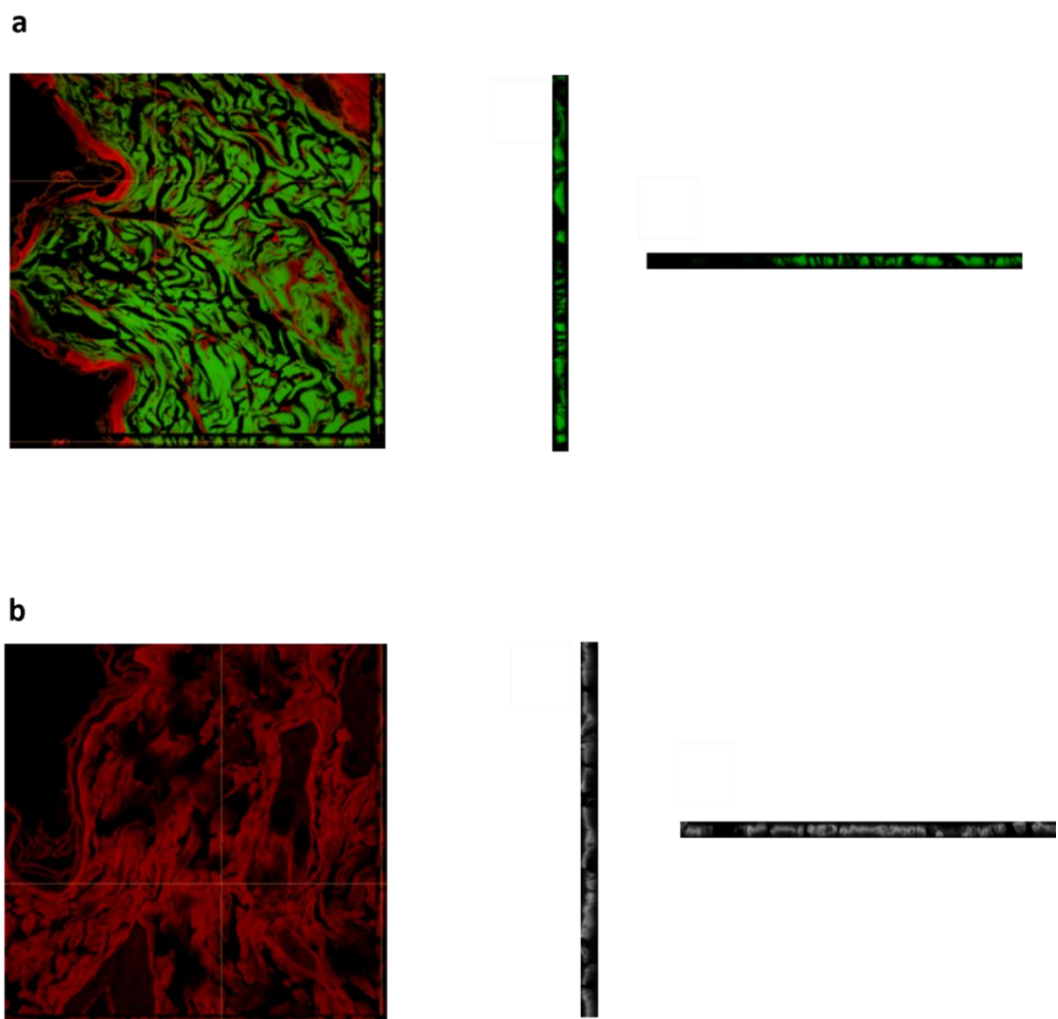


Figure 2. 23: Collagen auto-fluorescent confocal imaging in mouse skin. Collagen bundle thickness visualisation in multiple planes in a) 3 month H&E stained image with a normal field of view (left panel), and “side-on” views compiled from optical sections of a 5 μm slide in perpendicular planes (centre and right panel)., and b) as above using picrosirius rather than eosin auto-fluorescence.

2.3.3 Collagen Dynamics

As described above, the dermis is primarily composed of ECM proteins assembled into a mesh-work of primarily collagen fibres. The reticular dermis consists of large mature, well-organised collagen fibres in the lower layer of the dermis, interfacing with the subcutaneous fat. The papillary dermis is adjacent to the basement membrane, with thinner collagen fibres and distinct collagen organisation, also with a basket-weave structure.

Histological stains can effectively identify collagen in tissue specimens, and one may make qualitative assessments of ECM integrity from photomicrographs. However, unbiased image analysis methods are preferable. The Herovici staining method is an informative connective tissue stain used to identify different objects in distinct colours. Therefore, colour segmentation of images of Herovici stained sections is of great benefit in distinguishing different types of collagen fibres as red pixels represent old fibres, while blue pixels indicate new fibres. This allows the determination of the ratio of young to mature collagen in the dermis, revealing any age-related change in collagen synthesis.

2.3.3.1 Existing Methods for Colour Segmentation in Histology

Different objects can be separated depending on the pixel colour value of that object, i.e. red, green and blue values in the RGB colour space (Hosea, Ranichandra et al. 2011; Menesatti, Angelini et al. 2012).

2.3.3.1.1 Simple Thresholding Experiments

Colour segmentation is widely used in different applications. The simplest way is to separate the hue value of the image (Rich and Whittaker 2005). This method starts with converting 8-bit RGB images to HSV colour space, and then separating 256 hue values as a proxy for colours. Thresholding red, green and blue pixel values is another method that has been used to segment different regions in RGB images (Dadwal and Banga 2012), and I implemented colour filter-based collagen segmentation in Herovici stained images to quantify newly synthesized and mature collagen within the dermis. This technique involved implementing pixel intensity values for each red, green and blue channel in the Herovici RGB image. This then allowed segmentation of red and blue pixels by reducing multiple colours in the image and selecting all red and reddish pixels, as well as the blue and bluish pixels using these two steps:

- Segment red range values using the follow criteria:

$$\text{Red} = \begin{cases} \text{Red} & \text{if Value of } R > (G+B)*C1 \\ 255 & \text{otherwise} \end{cases}$$

- Segment blue range values using the follow criteria:

$$\text{Blue} = \begin{cases} \text{Blue} & \text{if Value of } B > (G+R)*C2 \\ 255 & \text{otherwise} \end{cases}$$

The constants $C1$ and $C2$ are different for differently stained images, due to variations in image colour as a result of differences in the process of tissue fixation and staining.

I optimised the constants to the values of $C1=0.75$ and $C2=0.93$ for the wild-type mice dataset that I described in section 2.3.1.1, according to the principles shown in the flow chart in Figure 2.24a, and the resulting segmented blue and red collagen images are shown in Figure 2.24b-d.

The result of colour filtering in the cropped region of an image without any skin appendages (e.g. hair follicles) is shown in Figures 2.25a and 2.25b, and the number of red and blue pixels and their ratio was quantified.

A qualitative (but not significant) increase in mature (red) collagen relative to newly synthesized (blue) fibres was demonstrated by calculating the ratio of blue to red pixels ($n=3$ animals per age group). The result of segmentation, pixel values and the ratio of red to blue collagen using colour filtering is illustrated in Figure 2.25c-f. I found no correlation between collagen synthesis and age (3 to 20 months inclusive; $R^2=0.8723$, $p>0.05$) due to the influence of inter-image variation (Figures 2.25g and 2.25h).

2.3.3.1.2 Shortcomings of the Simple Colour Thresholding

The calculation of constant values will need some modification for different data sets, even if images were stained with the same staining methods, as in a different laboratory (or at different time) there will be some variation in intensity and colour. Moreover, variation could also result in images within the same data set due to the fact that humans cannot exactly replicate the same procedure consistently. These variations meant that

Chapter 2

the use of the above colour thresholding alone is not sufficient for accurate colour segmentation. For these reasons, I have developed a new segmentation methodology for these images using *k*-means clustering for segmenting red and blue fibres in Herovici polychrome stained skin images. This technique was used previously in different applications e.g. nuclear segmentation in H&E stained histological sections (Sertel, Kong et al. 2009).

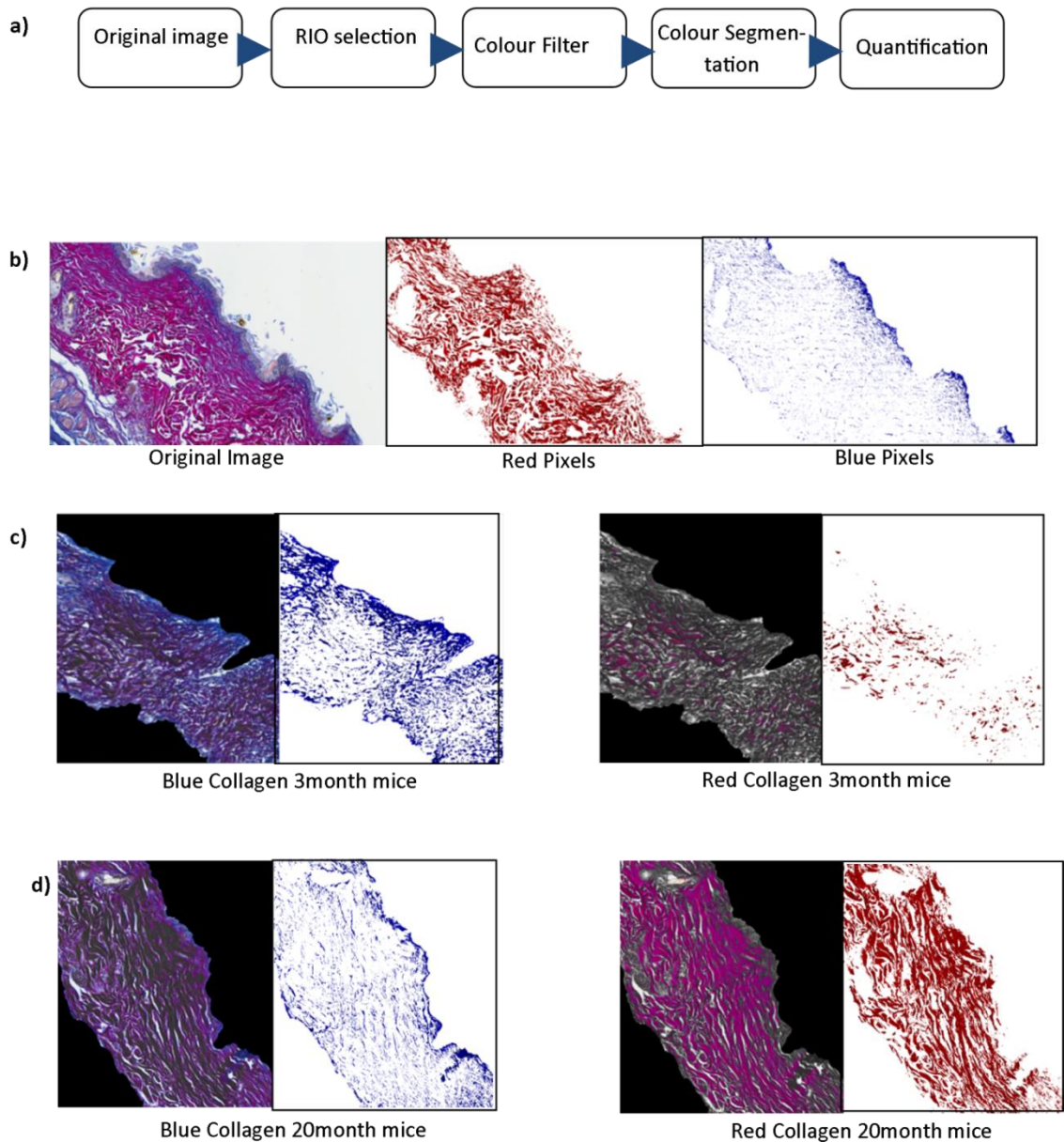


Figure 2. 24: Colour filtering and segmentation. a) segmentation process flow chart, b) the original Herovici stained *wt* mouse skin section, $n=5$ groups of ages, 4 animals in each group, 4-6 images per each section. (left) and the red (mature) and blue (young) collagen pixels, c) cropped 3 month *wt* mouse skin and the segmented red and blue collagen, d) cropped 20 *wt* month mouse skin and the red and blue collagen images.

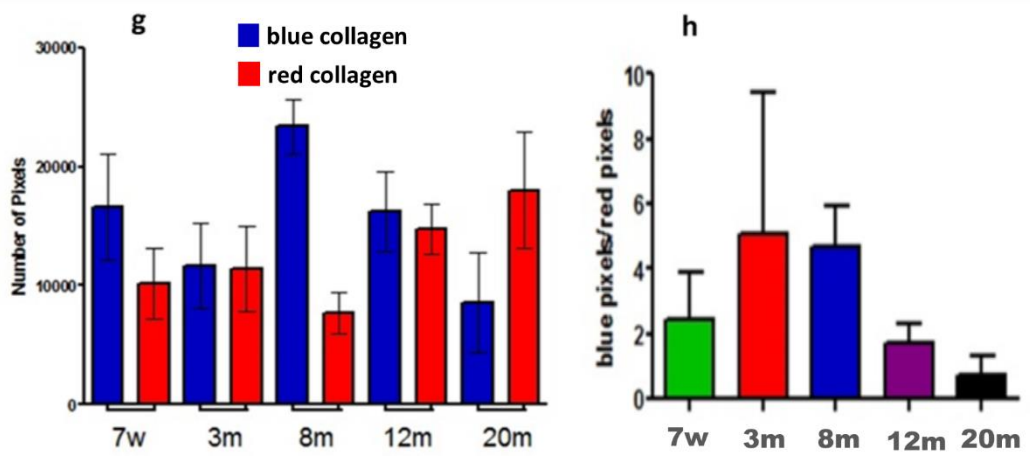
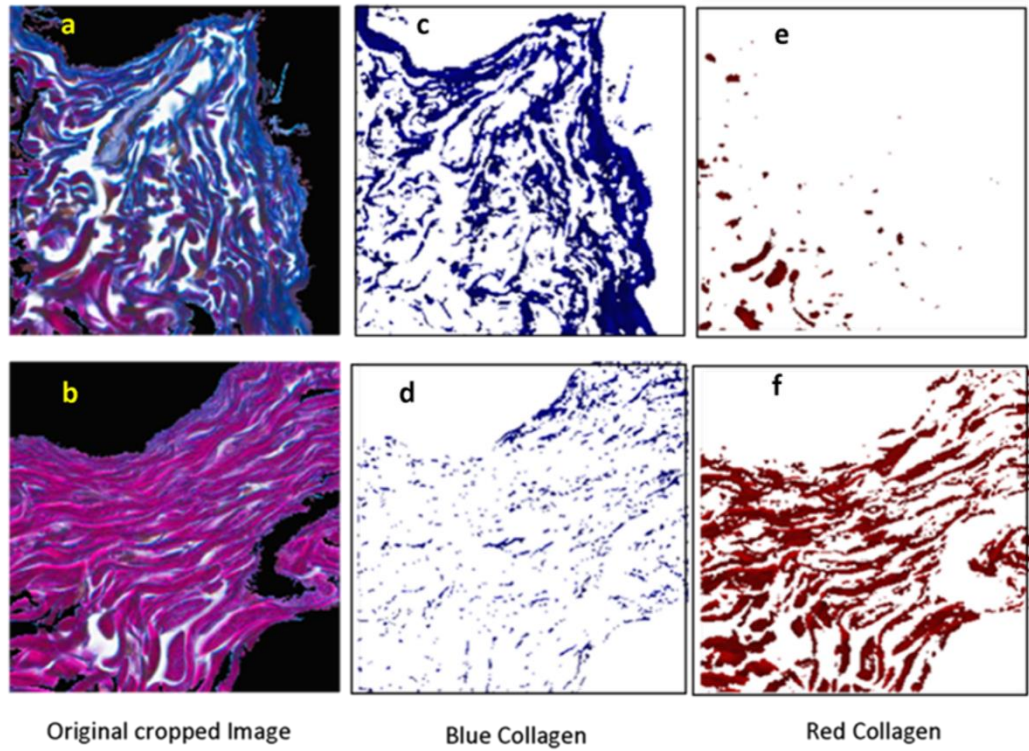


Figure 2. 25: Colour filtering and segmentation in cropped ROI images. a,b) automatically cropped dermis for 3 month and 20 month mouse skin respectively, c,d) blue (young collagen) e,f) red (mature collagen). g,h) quantification of red and blue pixels, and the ratio of blue to red using the colour filtering method. At least 3 animals per each age group, 3-4 images per each animal.

2.3.3.2 Development of an Improved Herovici Segmentation Method

a. k -means clustering

To improve upon inconsistency between different images and datasets, I sought to use k -means clustering to separate the pixels within each image to identify the core colours.

k -mean clustering classifies the data points (pixels) into a certain number of clusters that are sensitive to the location of the cluster centroids, in other words, different locations of the centroids lead to different results, and that causes batch analysis problems. k -means clustering assigns the objects in the image to a group that has a closest initial centroid and then recalculates the position of the centroid by calculating the new means for the centroids of the new cluster until the all data points are grouped in that cluster. The clustering steps are as follows:

- Choose the number of the clusters k .
- k initial means are randomly generated within the data set e.g. $k=3$.
- k clusters are created by associating every data point with the nearest mean.
- The centroid of each cluster becomes the new mean.
- Steps 3, 4 are repeated until the clustering has been reached.

The cluster centroids are calculated by calculating the means of the data points in that cluster (c_j). The Euclidian distance calculates the distance between the data points ($xi(j)$) and the cluster centroid.

$$d = \| xi(j) - c_j \| \quad (eq2.8)$$

The aim of k -means clustering is to partition the n data points xi into a centroidal Voronoi diagram $S = (Si)$ of minimal squared error by:

$$\sigma(S) = \sum_{j=1}^k \sum_{i=1}^n \| xi(j) - c_j \|^2 \quad (eq2.9)$$

a. *k*-means Clustering-based Segmentation

The RGB colour space was then converted to $L^*a^*b^*$ (luminosity or brightness layer, chromaticity layer 'a*' red-green, and chromaticity layer 'b*' blue-yellow) to reduce the multi-colour dimensionality of the RGB image.

k-means clustering was then used to cluster the pixels in the image into a certain number of non-overlapping clusters using the Euclidian distance metric. I chose three clusters, the objects in the image having either a^* or b^* pixel value or neither a^* nor b^* . The last step in this process was segmenting each of the groups (clusters) of pixels in the original image. The two described steps of segmentation implemented using following MATLAB scripts:

```
cform = makecform ('srgb2lab');  
transformed_image=applycform (he,cform); // To convert RGB to  $L^*a^*b^*$ 
```

k-means clustering:

```
[cluster_idx cluster_center] =kmeans(ab,nColours,'distance','sqEuclidean','Replicates',3)
```

Where ab represents the chromaticity colours a^* and b^* in $L^*a^*b^*$ colour space and $nColours$ is the number of clusters (k). This repeats the clustering 3 times to avoid local minima.

Figures 2.26 and 2.27 show the result of segmenting the training images without cropping the ROI. However, this shows that the presence of hair follicles and sebaceous glands in a region of the tissue section is an issue in the analysis process, and the ratio of the blue to red between the different ages did not show significant changes. This issue was solved by cropping a region from the image without hair follicles or glands.

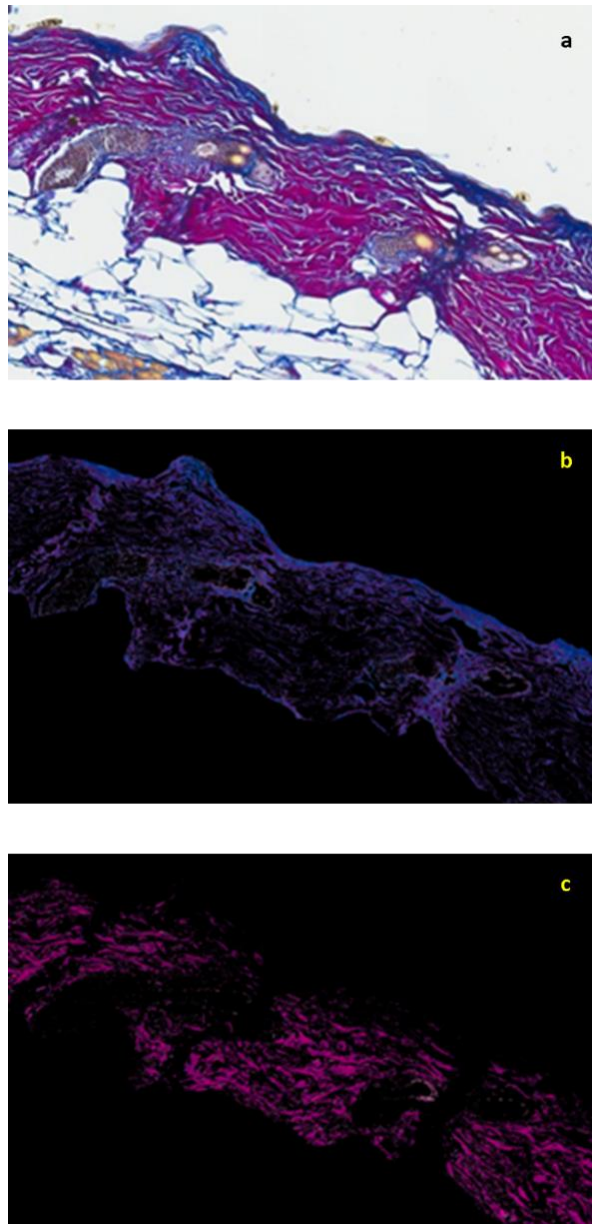


Figure 2. 26: Segmentation of images using k -means clustering from the entire snapshot of *wt* mouse. a) original Herovici stained skin image, b) blue pixels (young collagen, c) red pixels (mature collagen).

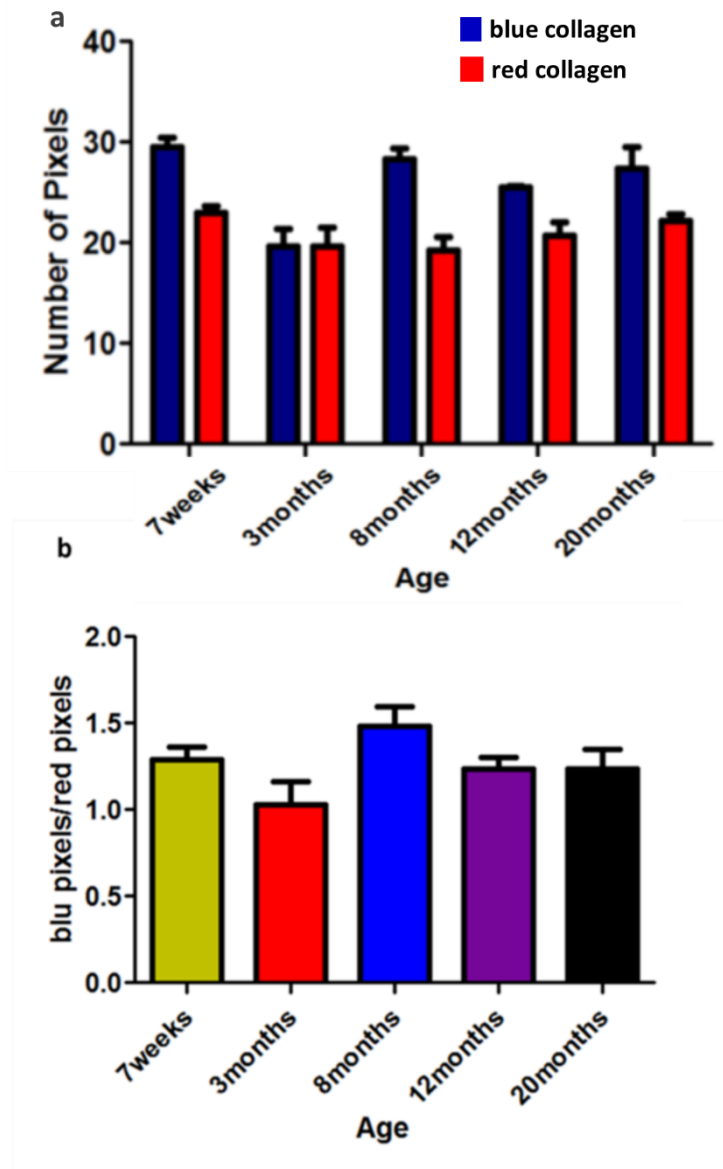


Figure 2. 27: *k*-means clustering method to assess collagen dynamics and age in *wt* mice. a) blue and red pixels in each age group, b) ratio of the blue to red pixels. At least 3 animals per each age group, 3-4 images per each animal.

b. Snapshot Magnification or Automated Region of Interest (ROI) Cropping

A 20X magnification snapshot (pixel dimensions=1712×1074 pixels, 552.12×346.36 μm) contains hair follicles and glands and many pixels around and inside these structures incorrectly segment as collagen. Therefore, the presence of skin appendages might affect the result of young and mature collagen area quantification, which may cause the overestimation of the collagen area. To solve this problem, a cropped region was used in the final method to measure just the collagen dynamics in Herovici stained skin images (Figure 2.28, pixel dimensions=257×257 pixels, 82.88×82.88 μm). The cropping process was done by converting the RGB image to HSV colour space, and then transforming the saturation channel to binary. The binary image area was then used as a mask to superimpose the original image to represent the ROI.

c. Thresholding

The *k*-means clustering method was applied to images in two different strategies, one with the post-process of histogram-based threshold by finding the optimum threshold that divides the histogram into two classes using Otsu threshold method. This removes all the bright pixels (non-object) in the segmented red or blue collagens. The second method omitted the last step of thresholding after the *k*-means clustering-based segmentation. The resulting images and quantification results were compared. Segmented images without thresholding are shown in Figure 2.29 and the quantitative results are shown in Figure 2.30. This method didn't show discrimination of young and mature collagen in different age groups. The thresholding method (described in the following sections) showed a more promising result that can detect subtle changes in the ratio of young and mature collagen between different age groups of *wt* animals, as shown in Figure 2.33.

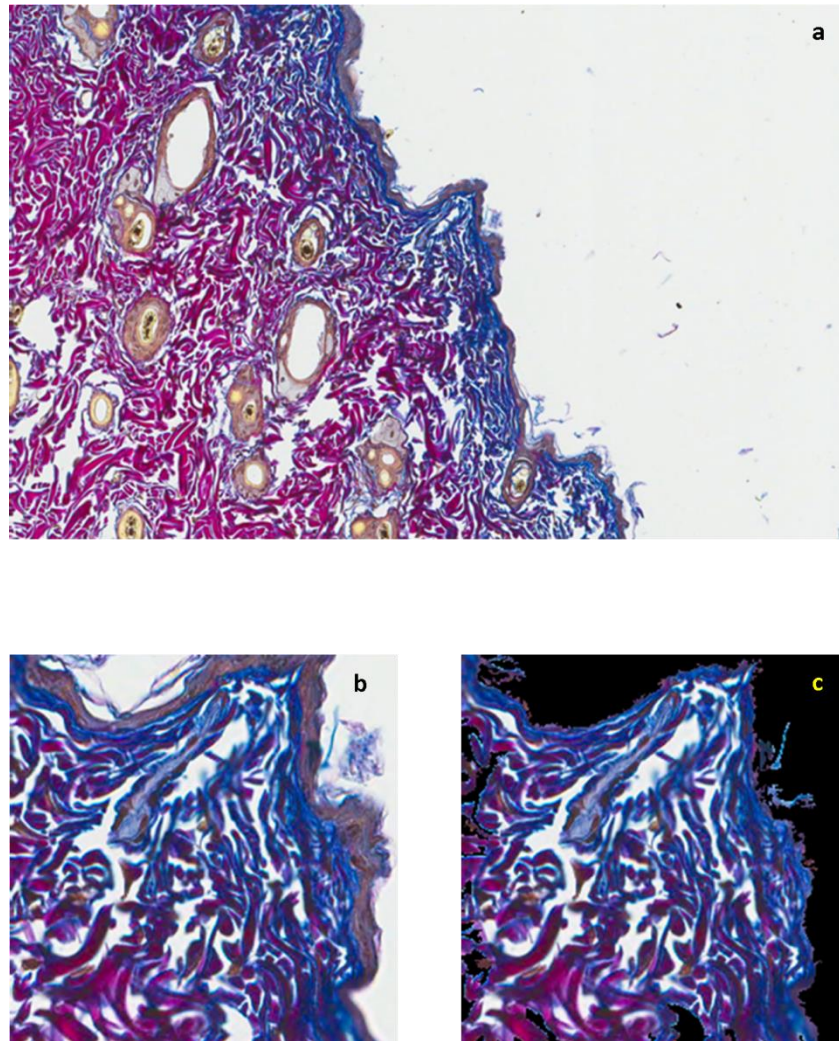


Figure 2. 28: ROI selection in a typical Herovici stained image of *wt* mouse. a) the original 20X magnification image, b) ROI without any skin appendages, c) automatically cropped region.

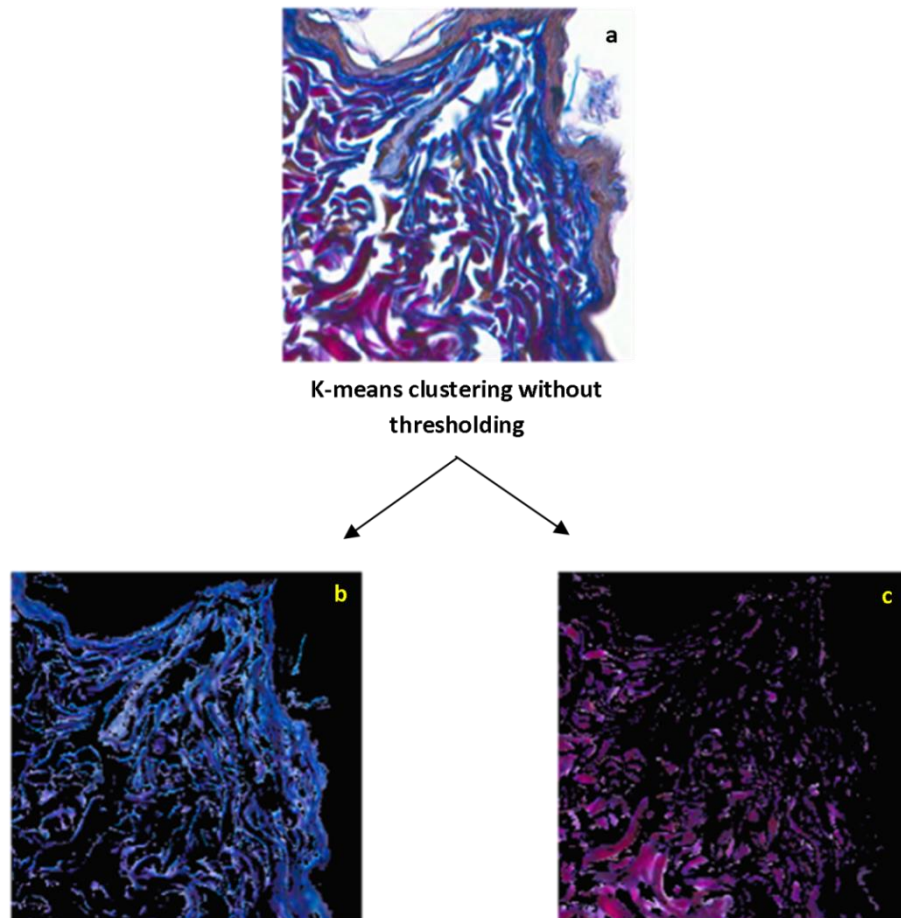


Figure 2. 29: Segmentation using *k*-means clustering without thresholding. a) original cropped Herovici stained skin image, b) blue pixels (young collagen), c) red pixels (mature collagen).

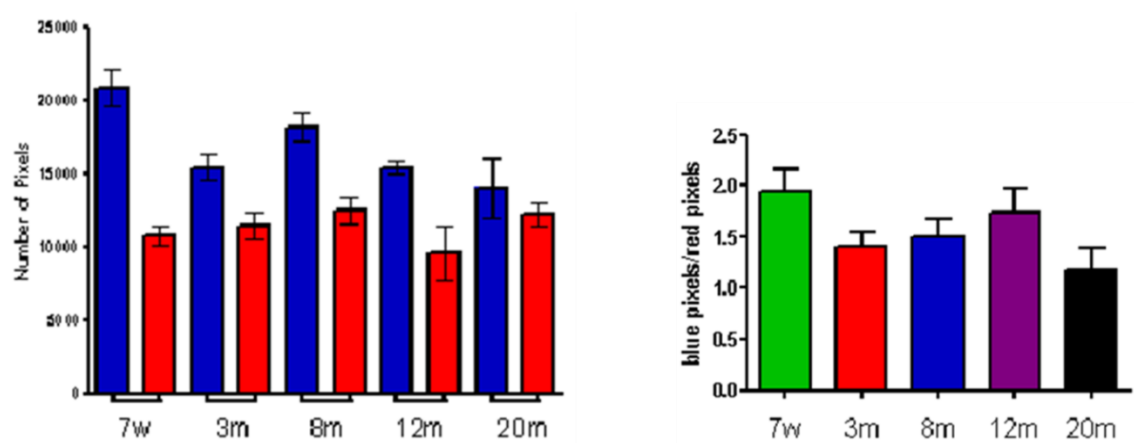


Figure 2. 30: Quantification of the ratio of blue pixels to red pixels in different age groups without post-process thresholding in *wt* animals. At least 3 animals per each age group, 3-4 images per each animal.

2.3.3.3 Use of Thresholding to Improve Colour Segmentation

The procedure starts with cropping the dermis layer (ROI) to facilitate collagen segmentation as described in section 2.3.3.2c. Figure 2.31 shows a flow chart of this process with the result of the original and cropped images. Image contrast enhancement was performed as before, based on a contrast stretching technique during pre-processing to increase the dynamic range of an input image. Contrast enhancement was implemented by the MATLAB function “*imadjust (I,stretchlim(I))*” that maps the intensity values in grayscale image I to new values in result image, such that 1% of all pixel values are saturated at low and high intensities of I .

The RGB colour space was then converted to L^*a^*b . k -means clustering was then used to cluster the pixels in the image into three clusters as described in section 2.3.3.2b. This was followed by image histogram-based threshold to remove bright pixels from segmented images. Figure 2.32 illustrates the resulting cluster images.

2.3.3.4 Collagen Dynamics in an Ageing Series

Herovici stained skin images were segmented (Figure 2.32) and analysed to investigate collagen dynamics. Pixel values and the ratio of blue to red collagen using the k -means clustering are shown in Figure 2.33. My quantification method did reveal an inverse correlation between the ratio of newly-synthesized collagen relative to mature collagen and age ($R^2=0.9438$, p value <0.05 ; Figure 2.33).

2.3.3.5 Collagen Dynamics in a Model of Diabetes

A change in dermal layer thickness in diabetes is associated with collagen orientation changes, as described previously (Al-Habian, 2011). To assess any changes in collagen dynamics, Herovici images from at least 3 *db/db* animals per group at 6 weeks, and 3, 5 and 6 months were analysed using my colour segmentation method. I observed a variation in the ratio of blue to red collagen in the dermal layer, which is comparable to the previous result from *wt* skin samples as shown in Figure 2.34. The ratio of blue to red collagen varied in the diabetic model between different age groups, and was distinct from the *wt* result.

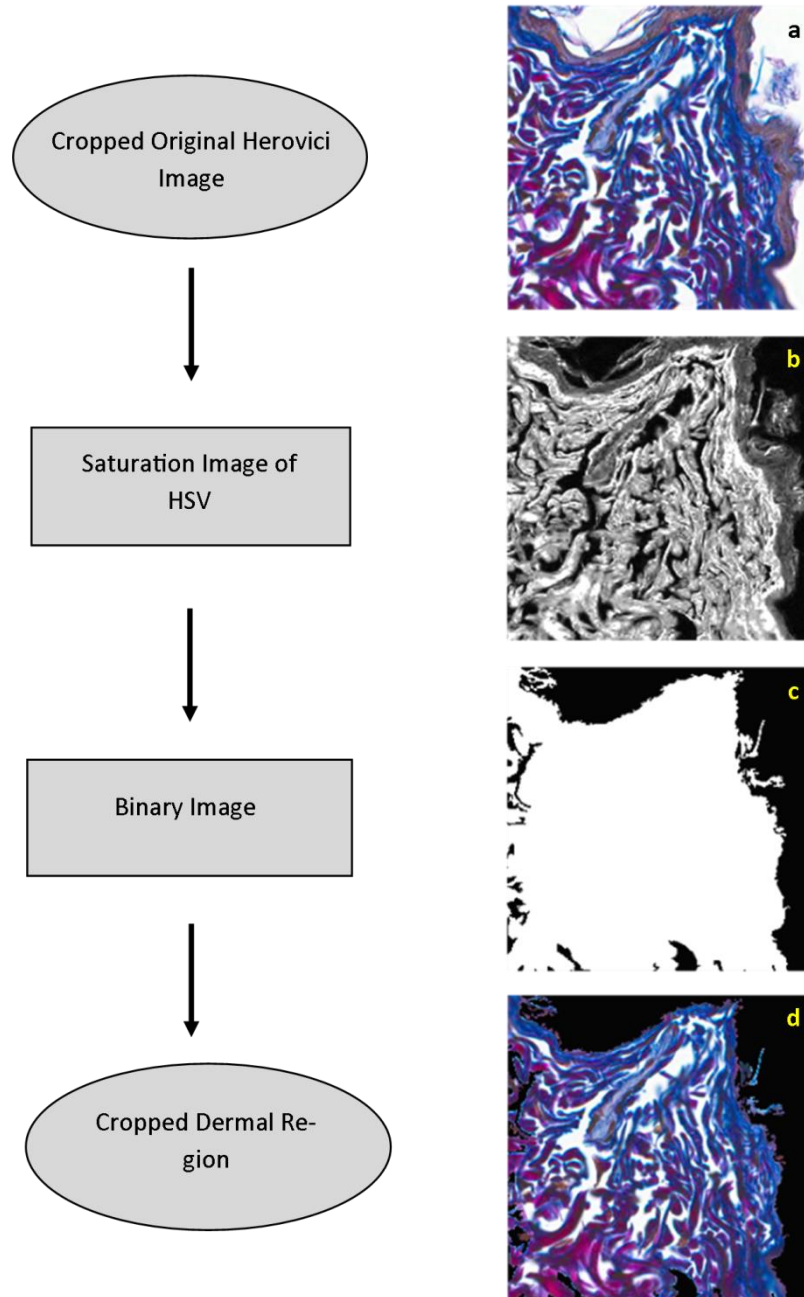


Figure 2. 31: Automated ROI cropping and removing image background. a) original Herovici image, b) saturated image, c) binary of the saturated image, d) cropped ROI (dermal layer only).

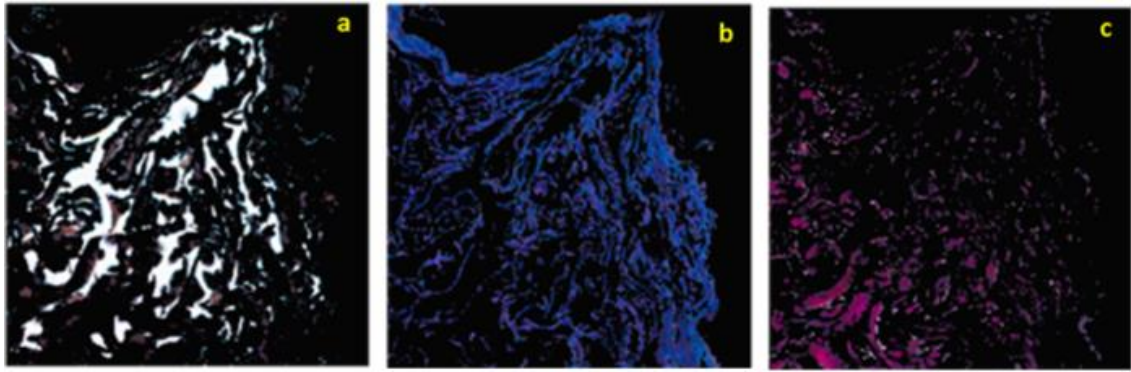


Figure 2. 32: *k*-means clustering method with thresholding. a) cluster 1: non-objects, b) cluster 2: blue pixels, c) cluster 3: red pixels.

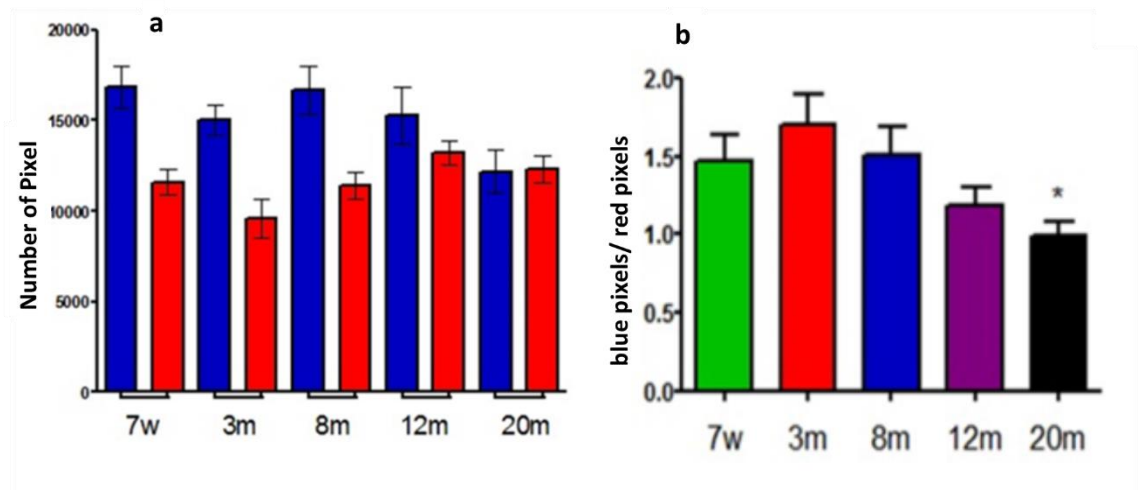


Figure 2. 33: Collagen dynamics in an ageing series in wt mice. a) red and blue pixel values achieved using *k*-means clustering for segmentation and thresholding, b) ratio of blue to red pixels (i.e. young to old collagen), p value<0.05 represented with *. At least 3 animals per each age group, 3-4 images per each animal.

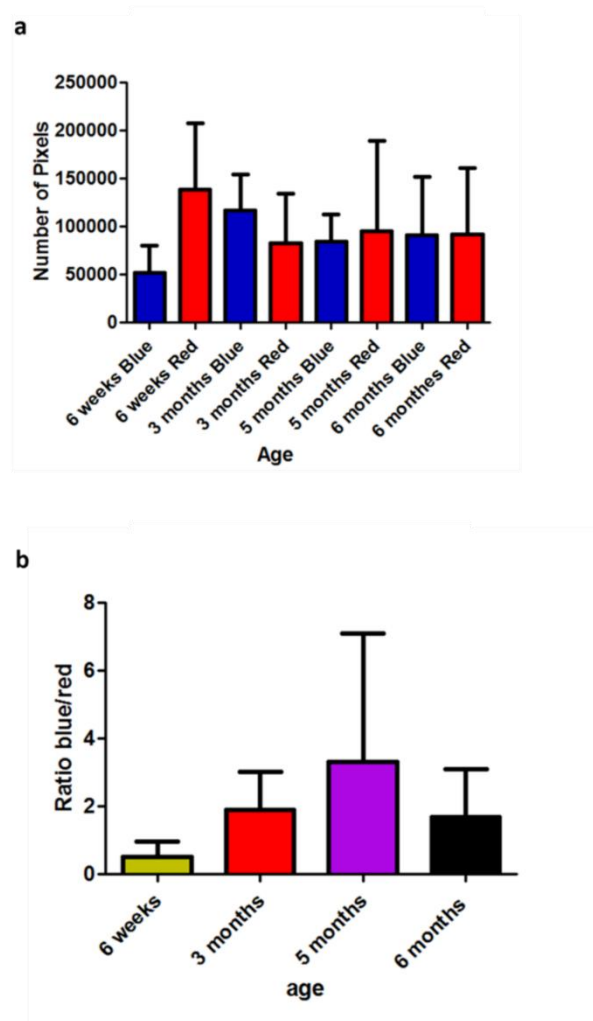


Figure 2. 34: Collagen dynamics in an ageing diabetic series. a) red and blue pixels, b) the ratio of blue to red pixels (i.e. young to old collagen).

2.4 Discussion

Image analysis techniques that exploit the frequency domain are attractive as they generate spectra informed by texture. The combination of a Gabor filter and FFT can reveal important information about texture and structural organisation in an image, and the Gabor filter has been used to improve orientational edge detection prior to application of an FFT. This was demonstrated in the assessment of collagen orientation in cross-polar picosirius stained images, and the combination of these two image processing procedures have shown to have utility beyond the quantification of skin texture and biological imaging. The FFT technique was used by other researchers in the investigation of dermal structure to study fibrosis in human skin (van Zuijlen, Angeles et al. 2002; van Zuijlen, de Vries et al. 2002; Khorasani, Zheng et al. 2011; Verhaegen,

Marle et al. 2012). However, these methods are neither being used in mouse skin tissue, which has considerably finer collagen structure, nor to discriminate more subtle age related changes in the structure, (e.g. in mouse skin between 8 and 12 months). MPM images of mouse dermis were quantified using FFT for assessing structural changes in collagen (Wu, Li et al. 2011), but this was not designed to specifically assess basket-weave, and also it is an expensive technique. The use of a Gabor filter prior to the FFT in cross-polar images of picrosirius stained histological skin sections yielded a more complex FFT power spectrum. By quantifying pixel distributions in four planes, I was able to create a sensitive collagen orientation index. In this way, I was able to detect subtle changes in collagen that were not revealed using the technique of FFT alone. My improved method also enabled me to assess subtle age-related differences in the sub-compartments of the dermis and, more importantly, to quantify collagen damage in models of diabetes (Osman, et al. 2013).

I also assessed collagen basket-weave in skin samples prepared from mice of increasing age, and was able to demonstrate a significant inverse correlation between time and collagen bundle thickness using the above combination of frequency domain techniques. I have exploited different properties of the elliptical shapes, formed by binarizing the maximum frequency of the FFT power spectrum, and measuring the distance between the ellipse foci and the vertex. The sequential application of edge enhancement using the unsharp mask filter, followed by the computation of the maximum frequency of FFT and quantifying the distance measurements in the resulting ellipse added to the efficiency and the performance of my algorithm in assessing subtle changes in the bundle thickness with age (Osman et. al., 2014).

The use of the k -mean clustering in colour segmentation overcomes problems associated with the widely used pixel intensity threshold (Rich and Whittaker 2005; Cisneros, Cordero et al. 2011). This is necessary due to the variation in colour and intensity in histological images resulting from variation arising from small inconsistencies in tissue fixation, staining and capturing images. I used the spatial domain and colour segmentation in my Herovici analysis method to measure collagen dynamics. Motivated by the use of the k -means clustering in other applications (Wu, Lin et al. 2007; Chitade and Katiyar 2010), I developed the idea of using clustering for segmentation and the result of the analysis confirmed the efficiency of the methods' performance (Osman et. Al., 2014).

Conclusions

Skin damage can arise from chronological aging, disease or from the effects the environmental challenges such as sun exposure. The ability to measure these changes accurately is, therefore, of clinical relevance.

The computational techniques proposed in this Chapter were able to determine dermal structure and collagen orientation using texture information, providing crucial information in the evaluation of the level of damage in the dermal skin layer. The combination of a Gabor filter and FFT demonstrated the capability to detect more subtle changes in collagen orientation in ageing and diabetic skin than existing techniques.

Collagen dynamic assessment in Herovici's polychrome stained skin sections was achieved using an efficient colour segmentation method that exploits *k*-means clustering rather than simple thresholding alone. Having experimentally-tested clustering based segmentation in different images, I found that the ratio of new collagen to mature collagen decreased gradually with age. Collagen bundle thickness quantification was based on my proposed method of selecting the maximum amplitude of FFT spectrum, and this revealed a noticeable decrease in the bundle thickness with age.

Having developed techniques to assess collagen structure and dynamics accurately within the skin, and having assessed the effectiveness of these methods in chronologically aged samples, I am now in a position to use these techniques to assess the effect of other environmental stressors, such as UV radiation. More importantly, these techniques can be used to assess the efficacy of potential therapeutics on collagen structure and dynamics, with cosmetic and therapeutic implications. Specifically, I am now in the process of analysing collagen integrity in diabetic skin exposed to insulin sensitising agents. Topical application of these agents may not only restore skin integrity, but could potentially improve wound healing, a major problem for those with type 2 diabetes mellitus. These techniques could also be used to evaluate collagen architecture in high throughput analysis and provide important information relevant pathology in a timely manner.

CHAPTER 3

High Throughput Cutaneous Phenotype Detection and Quantification

3.1 Background

Cutaneous phenotype detection in huge numbers of gene knockout mice can take ages using conventional methods to extract features related to a particular phenotype. Automated image analysis to extract features in skin tissue sections can facilitate the process of phenotype detection in high-throughput analysis to find interesting morphological and metabolic phenotypes.

3.1.1 H&E Staining of Skin

Crucial features in different pathological cases can be highlighted using H&E stained tissue sections. The main advantage of using this staining method is its ability to reveal considerable information about tissue organisation and structure (Bancroft and Gamble 2008). H&E stained histological sections have been used in many projects, such as the morphometry of skin layer features such as area, depth, length and shape (Bapure 2011). This staining can also be used in evaluating the extracellularmatrix (ECM) and overall structure of the dermis in terms of the collagen organisation and structure (de Vries, Enomoto et al. 2000). It can help visualize the hair follicle in the skin, and thereby reveal useful information such as their size, number and orientation (Bancroft and Gamble 2008). Traditionally, histological changes are qualitatively assessed by manual methods, but this is time consuming and the results subject to observer bias. This Chapter is devoted to the development of automated techniques to detect changes in morphology of the skin layers to detect interesting early phenotypes in a high-throughput genetic screen.

3.1.2 Wellcome Trust Mouse Genome Project

The Wellcome Trust Sanger Institute (WTSI) generates mouse genetic and phenotypic data, and distributes this data and resources to the scientific community. Our collaboration with WTSI focuses upon the phenotyping of a subset of genetically

Chapter 3

knockout mice. The program at WTSI to functionally annotate the mouse genome is illustrated in Figure 3.1.

The primary phenotyping data generated by WTSI aims to discover genes involved in diseases, and the influence of diet. There are many other research projects that focus on the biological functions of genes in the mouse genetics area by WTSI, such as mouse behaviors, cancer and developmental genetics (Liakath-Ali, Vancollie et al. 2014). Data can be accessed via the mouse resources portal (<http://www.sanger.ac.uk/mouseportal/>).

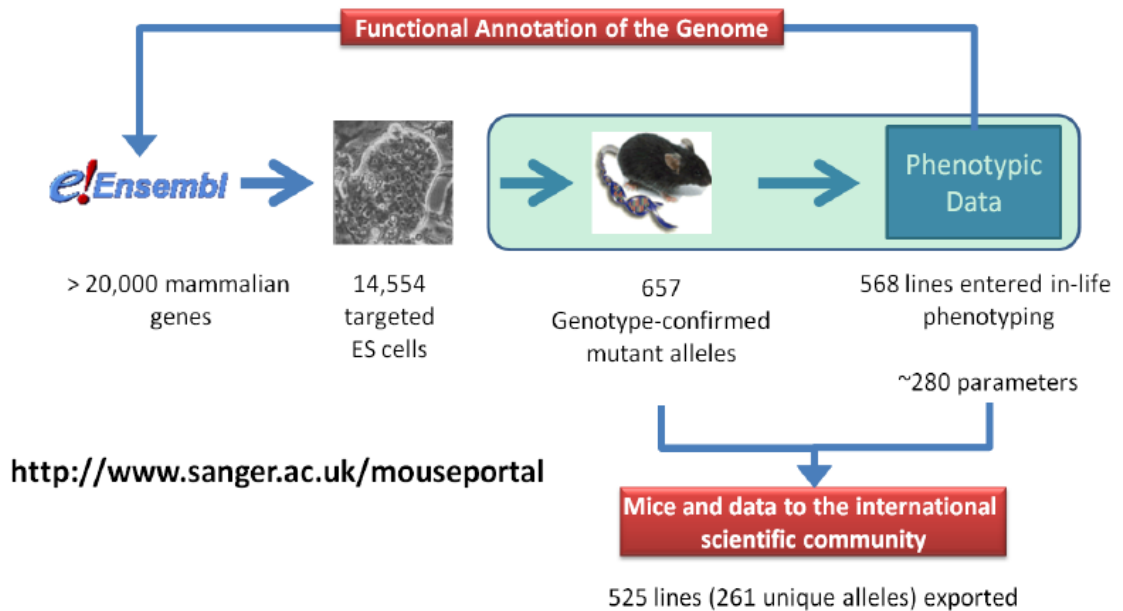


Figure 3. 1: Overview of the functional annotation process by the Mouse Genome Project (MGP) at the start of this project. Many more lines are now available to study. Image courtesy of the WTSI.

3.1.3 Secondary Phenotyping from WTSI Resources

Secondary phenotyping is about the detection of interesting features in gene-knockout tissue sections to detect early phenotypes. One example of secondary phenotyping is in the assessment of genetic determinants of bone mass and strength, which can be involved in the pathogenesis of osteoporosis (Bassett, Gogakos et al. 2012). Using high throughput investigation of mouse skeletons, biomechanical testing and statistical analysis of 100 mice generated by the MGP pipeline, nine new genetic determinants of bone mass and strength were found (Bassett, Gogakos et al. 2012).

3.1.4 Skin Histopathological Image Analysis

The WTSI Biobank maximizes the value of data on knockout mice but also helps to investigate new ideas to develop high-throughput analysis. The tissue biobank is a resource of many tissues from mice in the pipeline that can be used to follow up any novel findings from primary and secondary phenotyping. In this Chapter, I report the use of this resource to investigate skin phenotypes using histology image segmentation, and on linking phenotypes to biological information. Some work on annotation of skin features in knock-out mice was already done by the WTSI in collaboration with Ian Smyth and colleagues, although the focus of this work was on hair follicles rather than skin strata (Liakath-Ali, Vancollie et al. 2014). Moreover, this work relied on visual assessment of phenotypes.

Image segmentation generally aims to partition an image into different regions that are different in intensity and texture. There are many segmentation processes used to isolate the desired object in a tissue section and prepare these areas for analysis. Segmentation techniques include thresholding and edge detection, which can segment regions of pixels with similar intensity, or by the gradient by the boundary of the object respectively. In biological image processing, and specifically histology analysis, common techniques used for segmentation are pixel intensity-based technique (such as thresholding) that depend on the intensity value and colour of the pixels in that image to isolate the foreground and background (Otsu 1975). The output image of thresholding is a binary image. Typically the white pixels represent the foreground and the black pixels are the background, or vice versa. There are different techniques of thresholding. Global thresholding sets the pixels above the threshold to foreground value, and all remaining

pixels to a background value in the overall image. Adaptive thresholding changes the threshold dynamically across the image. Edge-based segmentation has also been used widely in biological image analysis, and this technique is based on the uncertainty between the background and the boundary of the object. A sudden change in the intensity value of pixels in an image indicates the boundary of an object in the image.

In order to select the appropriate automatic image segmentation method, I shall next describe the relevant skin features to be detected and quantified in histopathological images, and review existing techniques to deal with these tasks.

3.1.5 Existing Skin Feature Quantification Techniques

Changes in the size and number of adipocytes in skin tissue are one of the important skin features that reflect changes in metabolism i.e. an increase in adipocyte size and number correlates with metabolic diseases such as diabetes and obesity. Fat cell size is an important parameter that influences the cellular rate of metabolism. Adipocyte size can be quantified using efficient and accurate automated methods instead of manual calculation, which is very complicated and time consuming (Björnheden, Jakubowicz et al. 2004). Adipocyte size in the reproductive fat pad was determined efficiently using computer image analysis by measuring cross-sections of cell (Chen and Farese 2002). The images were analysed by converting into grayscale and then to binary format, before a watershed algorithm was used to detect the edges of the adipocytes. The binary image was then refined using erosion and a paint brush using existing tools. The results showed an increase in mean adipocyte size, and a great number of large adipocyte in mice fed a high-fat diet. However this method was supervised, and results might vary from one observer to the next. Moreover, the watershed algorithm sometimes segments individual cells into smaller cells. The cell diameter was determined using both manual methods (as a reference method), before the automated methods, based on the computerized image analysis, in the study of the adipose tissue metabolism (Björnheden, Jakubowicz et al. 2004). Human subcutaneous adipose tissue was obtained from 26 subjects, and cells were isolated using collagenase in order to allow efficient separation. Cell diameters were measured by photomicroscopy in one visual field at a time until all cell diameters were determined. The distribution of cell diameters was found using computer assisted image analysis, whereby image contrast was enhanced and images transformed to bitmaps in which fat cells were identified according to the

Chapter 3

roundness and smoothness of the contours using a KS 400 computerized image analysis system (Carl Zeiss, Oberkochen, Germany). The advantages of the computerized method is that it can calculate a huge number of cell sizes in adipose tissue in a short time (10 fold more cells than with manual analysis) without any observer bias. Moreover, the images can be stored and used again as a future reference. However, the quantification of the cell size is compromised as the circles created to represent idealised cells do not exactly match “real” fat cell outlines in this study.

Epidermal thickness has been evaluated manually, and the relationship between the thickness of the stratum corneum and the cellular epidermis was investigated to find any correlation between age, gender, body site, pigmentation, blood content, smoking history and skin type (Sandby-Møller et. Al., 2003). Biopsies were taken from different areas such as dorsal forearm, shoulder and upper quadrant of the buttock. The results showed a significant influence of these factors on epidermal thickness.

Thickness of the malphigian epidermis, stratum corneum, suprapapillary epidermis (a small area of dermis between rete pegs) and papillary dermis, as well as rete length were measured in psoriasis patients through the development of an H&E stained skin image analysis technique. The analysis of relationships between the above parameters and the age of the patient, type of psoriasis, total body surface area involvement, scalp and nail involvement, duration of psoriasis, and family history of the disease was performed (Alper, Kavak et al. 2004). Malphigian layer and stratum corneum thickness, as well as rete length in psoriasis was generally greater than in the control group, whereas the suprapapillary epidermis in both groups was similar. Although this study provided objective measurements, the number of subjects was not sufficient, and a limited number of parameters was measured. This study did, therefore, reinforce a need for the use of automated, unsupervised techniques to assess skin in high throughput histopathological analyses.

3.2 Automated Cutaneous Phenotyping based on Morphological Features

The main objective of this analysis was to detect early skin phenotypes (mice were sacrificed at 16 weeks) in knockout mice generated by the WTSI MGP using automated high throughput analysis. I sought to develop methods to quantify the depth of the epidermis and dermis, and also assess changes in the size and number of adipocytes in the subcutaneous layer to identify genetic determinants of skin organisation.

The plan of work divided into two parts. Firstly I shall describe algorithms to partition regions of interest in histopathological skin images into three layers (i.e. epidermis, dermis and subcutis). Secondly, I shall focus on developing and testing the performance of algorithms for the automatic quantification of biologically relevant parameters associated with each of these layers in images generated by the MGP.

In this section, I propose a system to detect morphological features of the epidermis, dermis and subcutaneous layers of the skin. I introduce image processing techniques to segment the cutaneous layers and highlight objects for subsequent quantification.

3.2.1 Skin Layer Segmentation using Active Contour Models

Herein, I describe the use of active-contour segmentation for automatic partitioning of H&E stained mouse skin images into different skin layers to enable measurement. Firstly, I describe attempts to use existing methods to segment skin layers and discuss their effectiveness.

3.2.1.1 Existing Image Segmentation Methods

There are existing segmentation techniques, such as a threshold or the edge detection, however, these techniques might be not effective enough to isolate the layers in H&E stained skin sections because of homogeneity of colour intensities in the overall image that might affect the thresholding process.

The simplest method to segment an image into different regions is the use of a global threshold, especially if the regions are different enough in terms of the intensity to allow the separation of the object and the background (Otsu 1975). Colour segmentation is widely used to separate image content into different regions. Some colour segmentation techniques were described in Chapter 2, but these could only be used only if the image

Chapter 3

has sufficient variation of colour (Muthukannan and Moses 2010). Entropy calculation is another way of segmenting regions that possess the maximum value of entropy (Leung and Lam 1994). Figure 3.2 illustrates segmentation output results from existing methods, such as Otsu-based thresholding (Figure 3.2b), entropy-based thresholding (Figure 3.2c) and k -means clustering of $L^*a^*b^*$ colour space of the image (Figure 3.2d) (Muthukannan and Moses 2010). However, the results of these techniques do not always individually yield effective segmentation of the different skin layers, but each of these techniques may help with highlighting certain image features in other images stained with other staining methods.

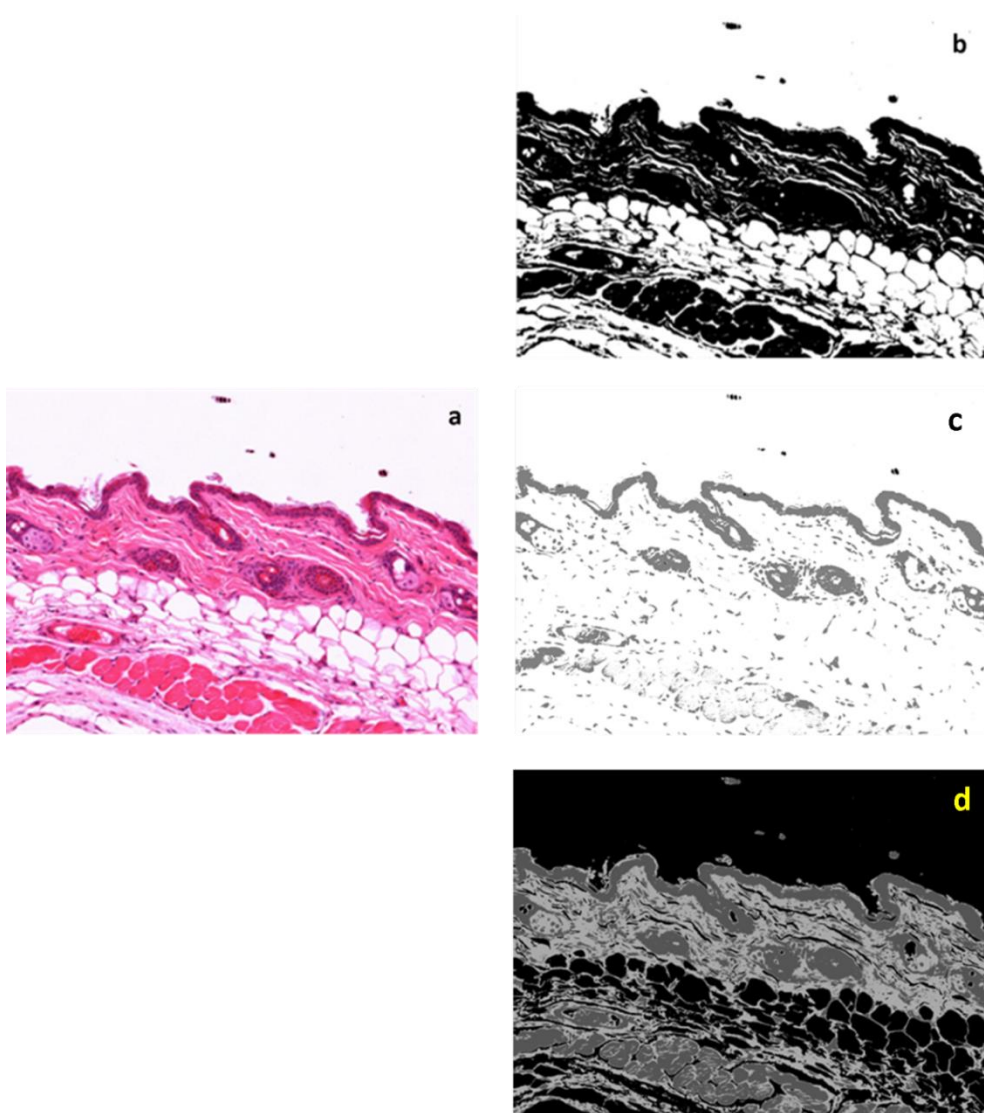


Figure 3. 2: Image segmentation with existing methods. a) original *H&E* stained image, pixel dimensions = 2000×1470 pixels, 645×474.07 μm , b) thresholding binary image, c) the result of computing maximum entropy in the image, d) k -means clustering output image ($k=3$).

3.2.1.2 Active contour model-based segmentation

One of the most successful segmentation method, which is relevant to my investigation of the separation of different skin layers, is the active contour model (Yun, Ming-quan et al. 2009). This is based on global information about intensity and texture in the image. Active contour segmentation has many advantages over classical segmentation methods. It is robust to noise and has better accuracy in segmenting objects and preserving boundaries by tracing a curve that moves forward until there is a significant change in spatial image information. Active contour is easy to implement and at the end, results to a closed contour as a segmented image (Yun, Ming-quan et al. 2009).

The active contour model starts by creating an initialized curve that moves to reach the boundary of the object that is to be segmented using energy minimization (Chan, Sandberg et al. 2000; Chan and Vese 2001). This model is either implemented using a snake model that depends on the image gradient for energy minimization (Kass, Witkin et al. 1988), or by using the region-based active contour without an edge, whereby the energy minimization depends on the global image information. The classical snake active contour model segmentation is based on the following energy formula:

$$E_{active\ contour} = E_{internal} + E_{external}$$

Where $E_{internal}$ represents the internal energy of the contour and controls the smoothness of the contour, while $E_{external}$ attracts the contour to the boundary of the object in the image where:

$$E_{internal} = \alpha \int_0^1 |c'|^2 ds + \beta \int_0^1 |c''|^2 ds$$

and

$$E_{external} = -\delta \int_0^1 |\nabla I|^2 ds$$

The snake active contour is given by the following equation (Kass, Witkin et al. 1988):

$$E_{active\ contour} = \alpha \int_0^1 |c'|^2 ds + \beta \int_0^1 |c''|^2 ds - \delta \int_0^1 |\nabla I|^2 ds \quad (eq3.1)$$

Where α , β and δ are positive parameters, c is the contour, c' and c'' represent the regions inside and outside the contour C , and ∇I is the gradient of the image (known as an edge detector).

The region-based active contour method proposed by Yun et al. (Yun, Ming-quan et al. 2009), is based on global information in the image instead of the gradient or local information in the image. It speeds up the curve evolution and reduces the effect of noise in the image. This segmentation process is based on the minimization of energy due to the fact that the boundary of an object is the curve energy minimizer that fits the curve to the target object. This report demonstrated the ability to detect objects in noisy images without the implementation of a second initial curve, and they detected objects of different intensities. It can also detect lines and curves that do not necessarily become closed. The resulting segmented images were compared to the result of the classical snake active contour model, to confirm better performance, especially in images that had a very smooth boundary. This method was compared to edge-based active contour and the region-scalable fitting energy (RSF) methods (Li, Kao et al. 2008) in terms of the accuracy of segmentation. The differences between this method and the classical active contour Chan-Vese model (Chan and Vese 2001) is that the initial curve was required to be directly on the boundary of the object because the edge-based active contour (snake method) utilizes the image gradient to stop the further movement of the curve on the boundary of the object.

There are numerous other examples in biomedical research. An edge-based active contour model was used to automatically segment and classify different types of spiral bacterial cells in digital micrographs (Hiremath and Bannigidad 2012). An active contour model without edges was used for follicle recognition in ovarian ultrasound images in order to extract important information relevant to ovarian ages (Hiremath and Tegnoor 2010).

Embedding the technique of edge detection into the active contour model was also shown to improve the process of segmentation to measure cellular bio-mechanical responses during cancer radiotherapy in human prostate cells (Aymeric Histace 2014). This group used this method to develop a computational image analysis tool to segment cell membranes and track cell divisions. Cancer cell membranes were segmented in fluorescence confocal microscopy images using approximate entropy (ApEn) as an edge detector that was embedded into the geodesic active contour (GAC). However, an adaptive strategy was required to segment all cells in an image in terms of initialization,

and also validation with clinical analysis was required to see if the method could find correlations with clinical parameters in larger number of images.

3.2.2 A Method for Automatic Skin Layer Segmentation

I shall now describe my adaptation of an active contour based segmentation method to develop an automatic tool for cutaneous analysis. The complete automated layer segmentation process for high throughput analysis is summarised below in Figures 3.9. The model starts with pre-processing followed by layer segmentation using automated active contour-based segmentation. The process was developed through the following three stages:

Stage 1: Pre-processing for Image Enhancement

Pre-processing to enhance images was required prior to the next step of segmentation. For quantitative analysis, I needed to segment each of the three major skin layers (epidermis, dermis and fat layer). At the beginning, the grey level image was used as an input image in the segmentation process, but the resulting segmented image was not optimal to identify epidermis and dermis layers. Figure 3.3 shows the result of segmentation when using grey scale images. This illustrates a significant shortcoming of such an approach as part of the dermis is missing. Later in this section, I shall show how to remedy this kind of problem using a refined segmentation method when applied to the saturation image channel obtained by converting RGB colour space into HSV colour space.

Multiple pre-processing and refinement steps are needed in the development of an effective segmentation method, each of which helps improve and extend its predecessor. Pre-processing stages are:

- a) Contrast enhancement using image histogram stretching.
- b) Noise reduction using a median filter to remove noise and slide preparation artefacts.
- c) Adding the image to the image itself by adding each pixel intensity in the image with the corresponding pixel intensity in same image to produce an output image more suitable to detect epidermis in the image by turning epidermis region to darker area than other regions in the output image. In the rest of the section.

Chapter 3

I will introduce refinement steps and provide a rationale before arriving at what I believe to be sufficient for my intended segmentation application. Figure 3.4 illustrates the use of the absolute difference of the grey level image and the complement image of an image (Figure 3.4a), followed by the application of the active contour model (Figure 3.4b). As one can see, segmentation showed an overestimation of the region of interest.

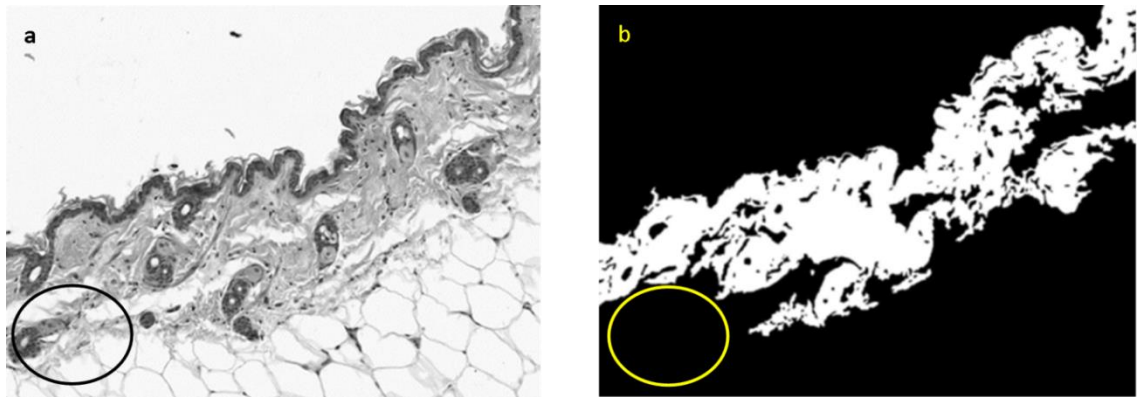


Figure 3. 3: Result of active contour- based segmentation in grayscale image. a) grayscale image, b) segmented epidermis and dermis showing a missing region.

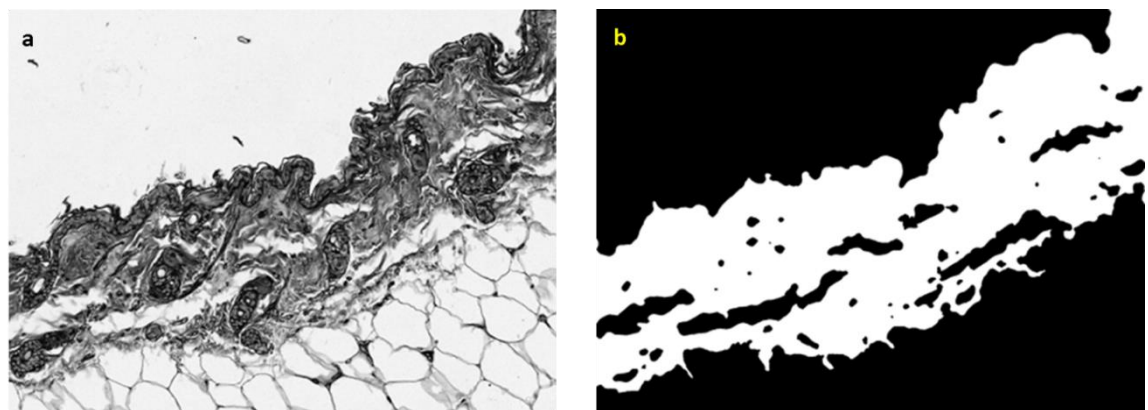


Figure 3. 4: Result of active contour-based segmentation using absolute difference of greyscale. a) output image of absolute difference of the grayscale and the complement image, b) overestimated segmented image.

Stage 2: Transformation of Colour Space

Individual red, green and blue channels of the RGB colour image (Figure 3.5) were used for segmentation using global thresholding. However, the segmentation result was not promising. For this reasons I converted RGB colour image to HSV colour space and the saturation channel was selected for the segmentation process because the region of interest (epidermis and dermis) contained saturated colours in the HSV colour space as shown in the figure 3.6. The saturation channel in the HSV colour space shows all the intensities of the colours in the image. In the data set provided by the WTSI, the saturation channel for all the images produced a bright area containing the epidermis and dermis layers.

Stage 3: Segmentation by Active Contour without Edge Detection

After pre-processing the original image and converting the RGB colour space to HSV colour space, and the selection of the saturation image, the active contour without edge was then applied to segment the image into sub-regions of contiguous layers. The active contour edge based functional energy is given by the following equation (Chan and Vese 2001):

$$\begin{aligned} F(c_1, c_2, C) = & \mu L(C) + \nu A(\text{inside}(C)) \\ & + \lambda_1 \int_{\text{inside}(C)} |u_0(x, y) - c_1|^2 dx dy \\ & + \lambda_2 \int_{\text{outside}(C)} |u_0(x, y) - c_2|^2 dx dy \end{aligned} \quad (\text{eq3.2})$$

Where the L is the length of the curve and A is the area of the region inside the curve, μ , ν , λ_1 and λ_2 are fixed parameters, where $\mu \geq 0$, $\nu \geq 0$, λ_1 and $\lambda_2 \geq 0$, c_1 and c_2 are the means of the region inside and outside C .

The energy minimization process using equation eq3.2 is an iterative procedure to minimize the energy of the curve that is based on global information of the image to stop the curve on the desired boundary of the object, independent of the gradient of the image. Using my method to segment skin layers, the initial curve to start the active contour was created from the object itself (epidermis and dermis region) automatically, which speeds object boundary detection by reducing iterations of the energy minimization process (i.e. evolving the initial curve to detect boundary of the object).

Figure 3.7 illustrates the segmentation process using the active contour model without edge. The limitation of this stage was the huge number of iterations of curve evolution required to segment the skin layers, and the variation in the location and orientation of the region of interest in data set images.

Generating an Initialisation Curve

To reduce the number of iterations and develop a fast segmentation independent of the object location, I developed the following stepwise automated initialization curve generated from the ROI itself, using MATLAB functions below:

- Convert RGB colour space to HSV space.

```
ConvertedImage = rgb2hsv(image);
```

- Select the saturation channel from HSV colour space.

```
SelectetImage = ConvertedImage (:, :, 2);
```

- Threshold the saturation image into a binary image using Otsu method to partition the image into two components with white pixels being the region of the epidermis and dermis, and the black pixels being the background.
- Select the largest object in the binary image that represents the initial curve.

```
[L, N] = bwlabel(segmented region);  
D = regionprops(L, 'area');  
w = [D.Area];  
LargestObject = find(w == max(max(w)));  
Segmented_LargestObject = ismember(L, LargestObject);
```

- Apply the “open” morphology operator using the disk structuring element of size 4, to make the initialize curve cover the whole area of the dermis and epidermis in the original image.

```
StructuredElement = strel('disk',4);  
InitilizedCurve = imopen(Segmented_LargestObject,se);
```

This process of generating the initialize curve is illustrated in the Figure 3.8.

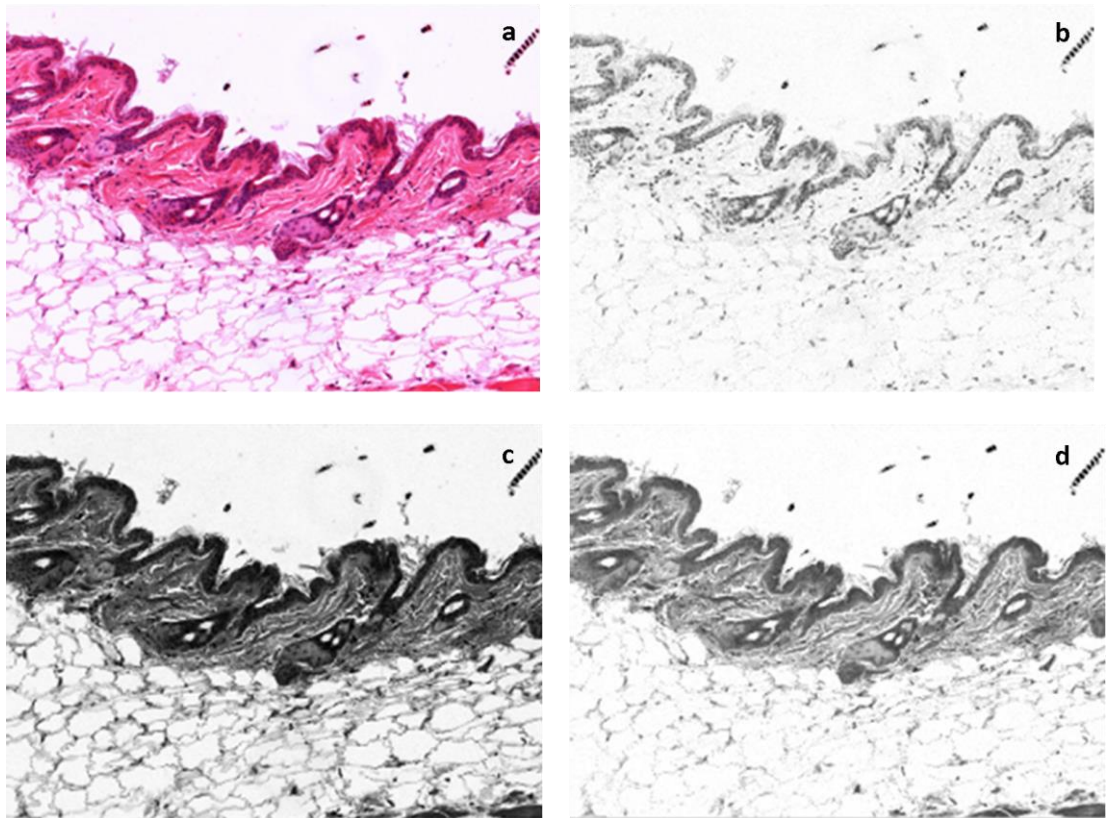


Figure 3. 5: Use of RGB colour space. a) RGB model, b) red, c) green, and d) blue colour band.

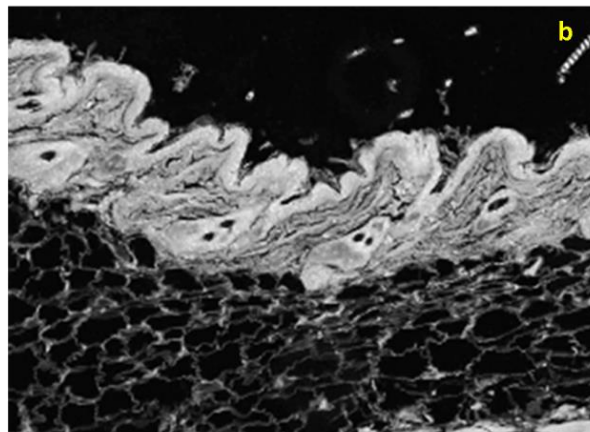
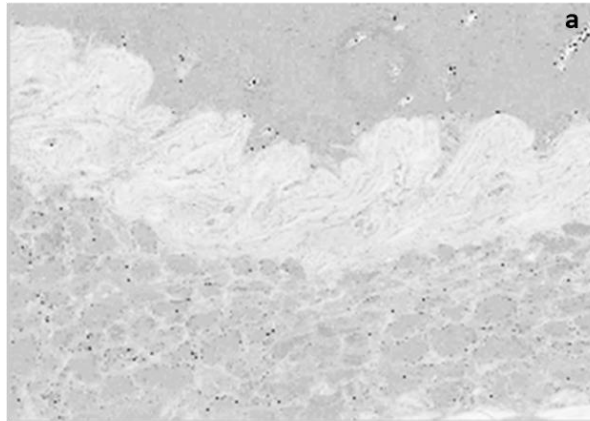


Figure 3. 6: HSV colour space. a) hue channel, b) saturation channel, c) value (brightness).

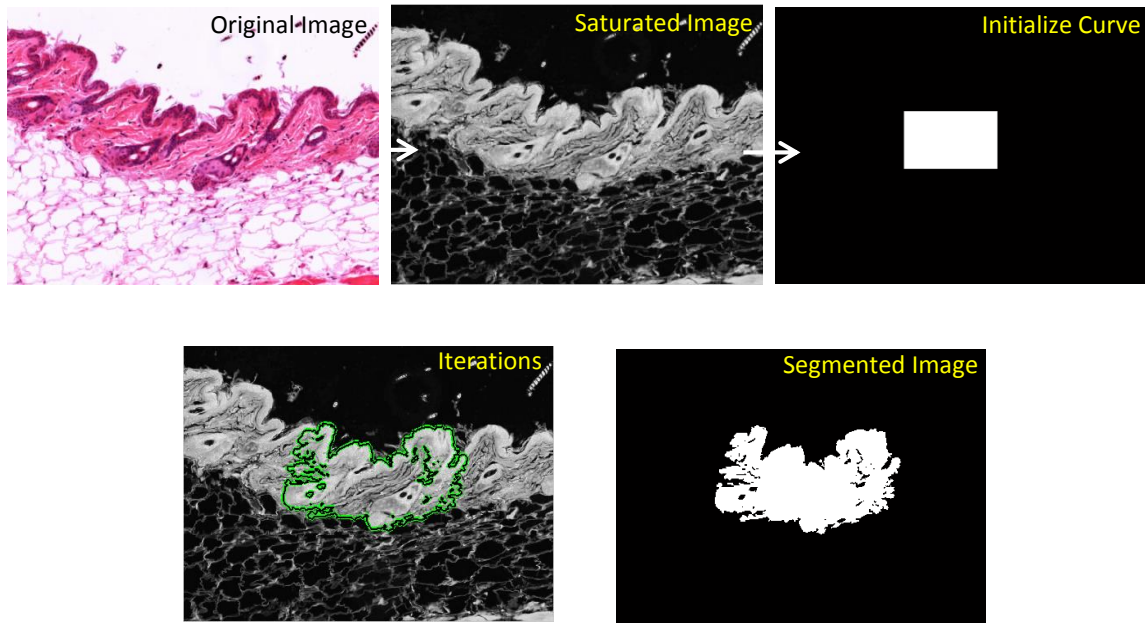


Figure 3. 7: Segmentation process using the active contour model applied to H&E stained image and segmented image after 1000 iterations.

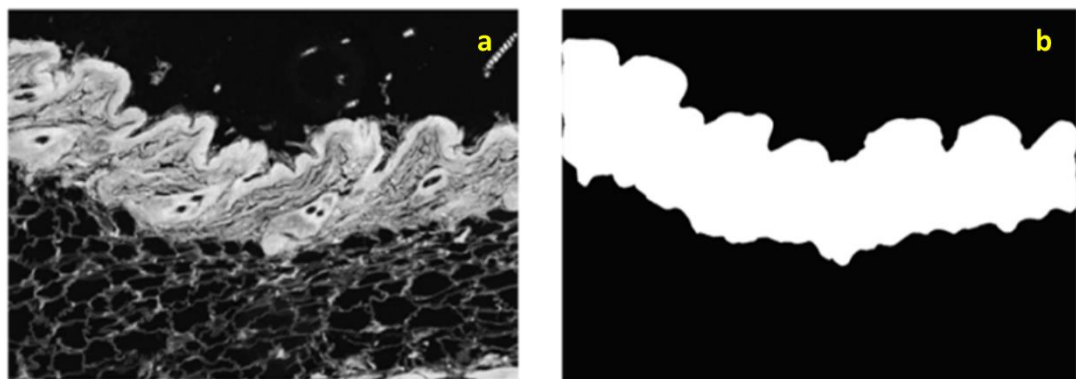


Figure 3. 8: Generating an initialization curve. (a) saturated channel image (b) initialize curve.

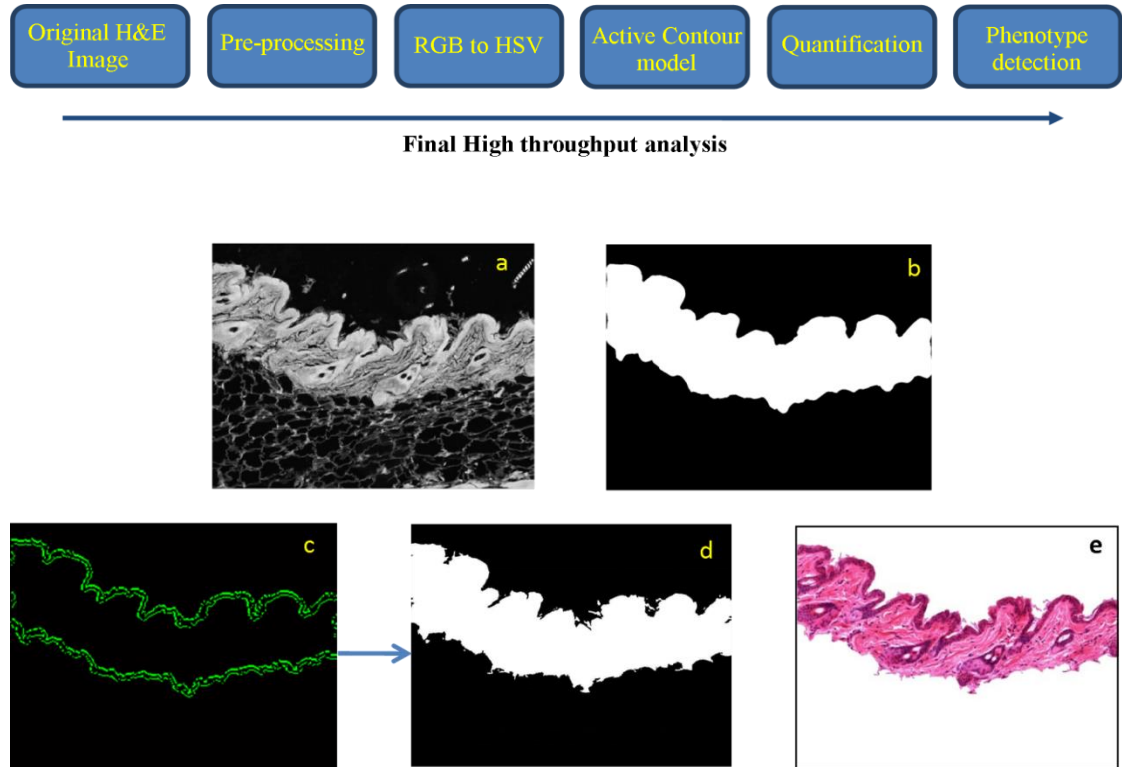


Figure 3. 9: Active contour iterations and segmented epidermis and dermis region. Top panel, overview of process. Lower panels: a) saturated channel of the *HSV* colour space, b) initialization start curve, c) curve evolution moves to the object boundary (iterations), d) segmented binary epidermis and dermis, e) superimposed epidermis and dermis.

In summary, automatic cutaneous layer segmentation by adapting pre-existing techniques allowed epidermis and dermis to be isolated. The epidermal layer was segmented by first segmenting the upper two layers of epidermis and dermis, with additional pre-processing (adding the segmented epidermis and dermis image to itself to improve epidermis segmentation as explained in stage 1) to enhance contrast of the epidermal region (Figure 3.10b). The dermis layer was then segmented by subtracting the segmented epidermis from the segmented epidermis with dermis image (Figure 3.11c), as illustrated in Figure 3.11e. The segmented epidermis and dermis depths were quantified using skeletonization-based quantification of segmented images, which was performed by measuring branch length in the skeletonized image (Figure 3.15).

The adipocytes are immediately adjacent to the epidermis and dermis, thus they were isolated using subtraction of the segmented epidermis and dermis from the saturation image as showed in Figure 3.12b. The process of adipocyte segmentation is described in detail in section 3.2.4. The process starts with background subtraction in the saturated

Chapter 3

image within the HSV colour space (Figure 3.12b), followed by the use of the piecewise grey level linear transformation to select the intensity range (0.079-0.125) that is equivalent to the intensity of the adipose cells in the image. Pixels in the selected range of intensity were converted to white, and the rest pixels were converted to black. The adipocyte segmentation was followed by fully automated post-processing steps to enhance cell boundaries, and fill holes and close gaps using mathematical morphology as shown in Figure 3.12c, d.

The outcome from segmentation of each of the layers in the H&E skin images those provided by WTSI are shown in Figure 3.13, and this feeds into the next step of the quantification of parameters associated with each layer.

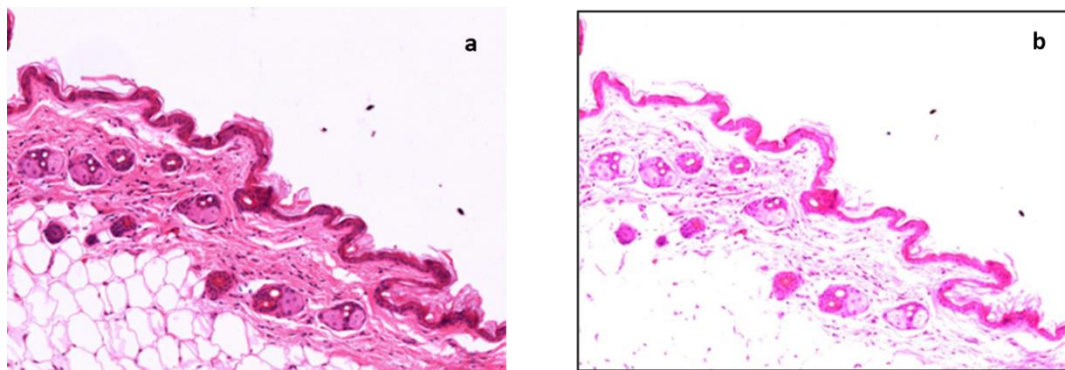


Figure 3. 10 Image pre-processing for epidermal segmentation. a) H&E stained image, b) the result of function `imadd()`, that adds the image to itself.

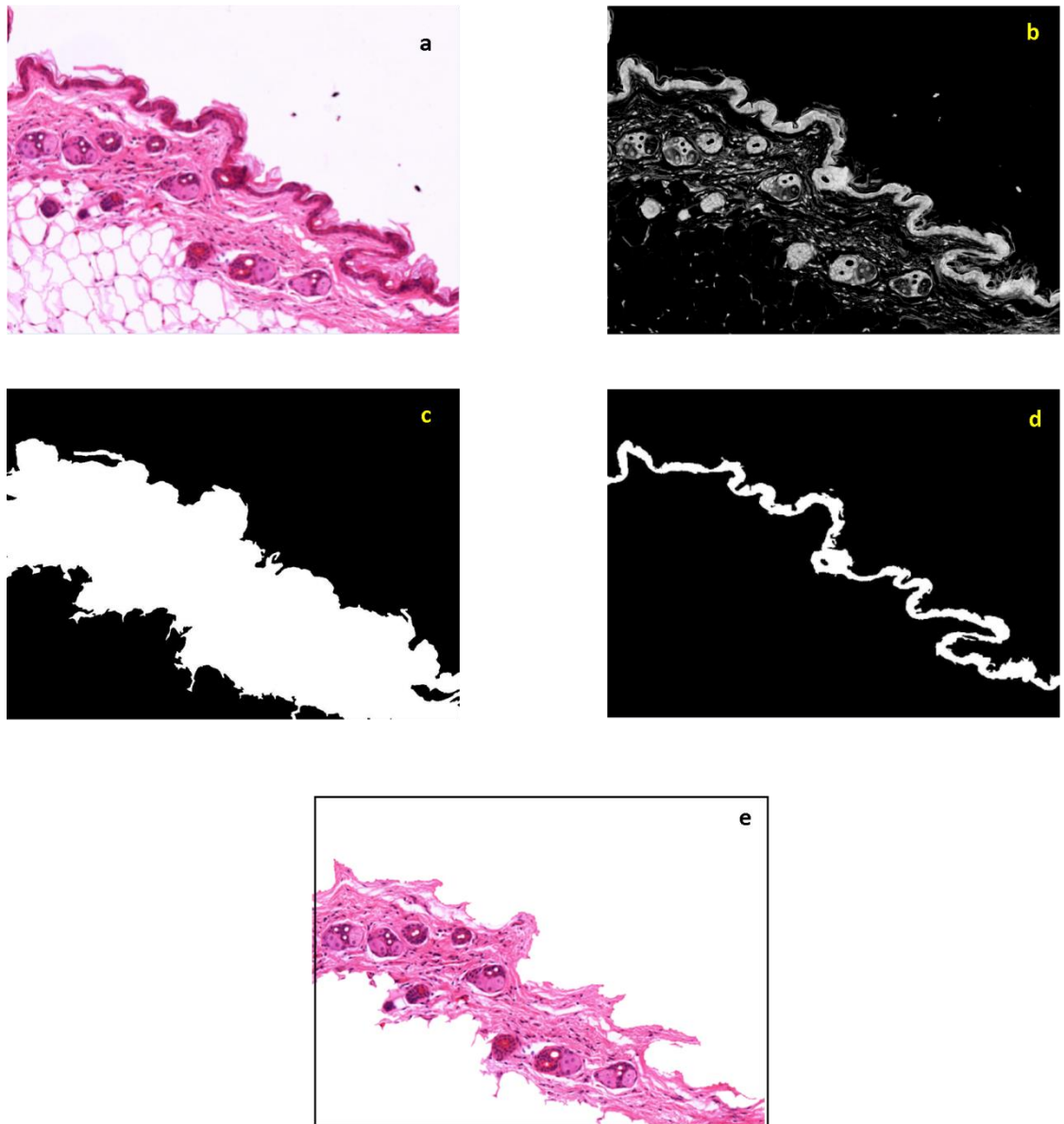


Figure 3. 11: Epidermis and dermis segmentation. a) original H&E image, b) saturated image following image-add, c) binary image of segmented epidermis and dermis (result of process in Figure 3.9), d) binary image of segmented epidermis from the result of the active contour on the image in step (b), e) superimposed segmented dermis image (result of subtracting image in step (d) from image in step (c)).

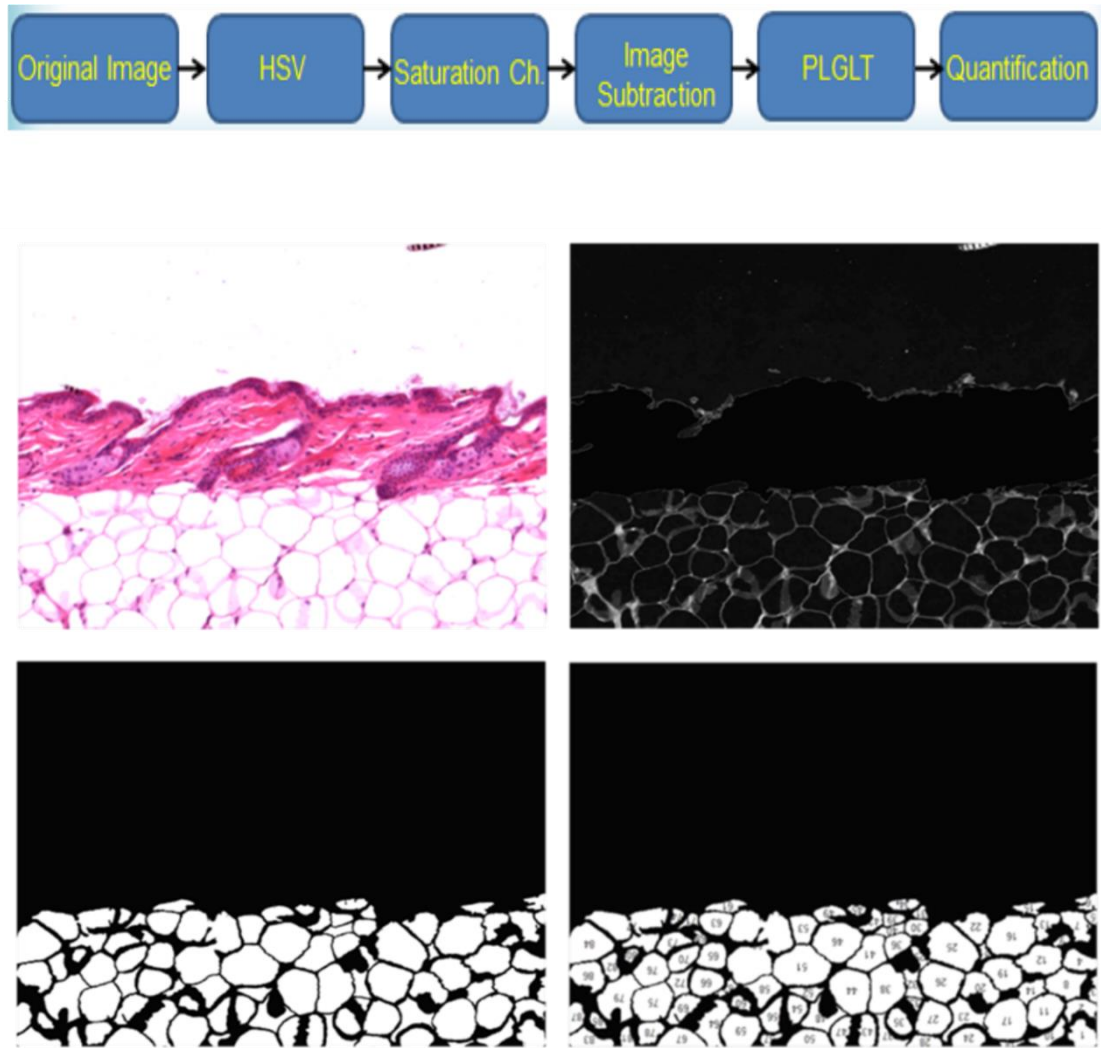


Figure 3. 12: Adipocyte segmentation and quantification. Upper left is the original image, and upper right is the saturated image, the lower left shows binary segmented adipocytes and lower right is the binary image of labelled cells.

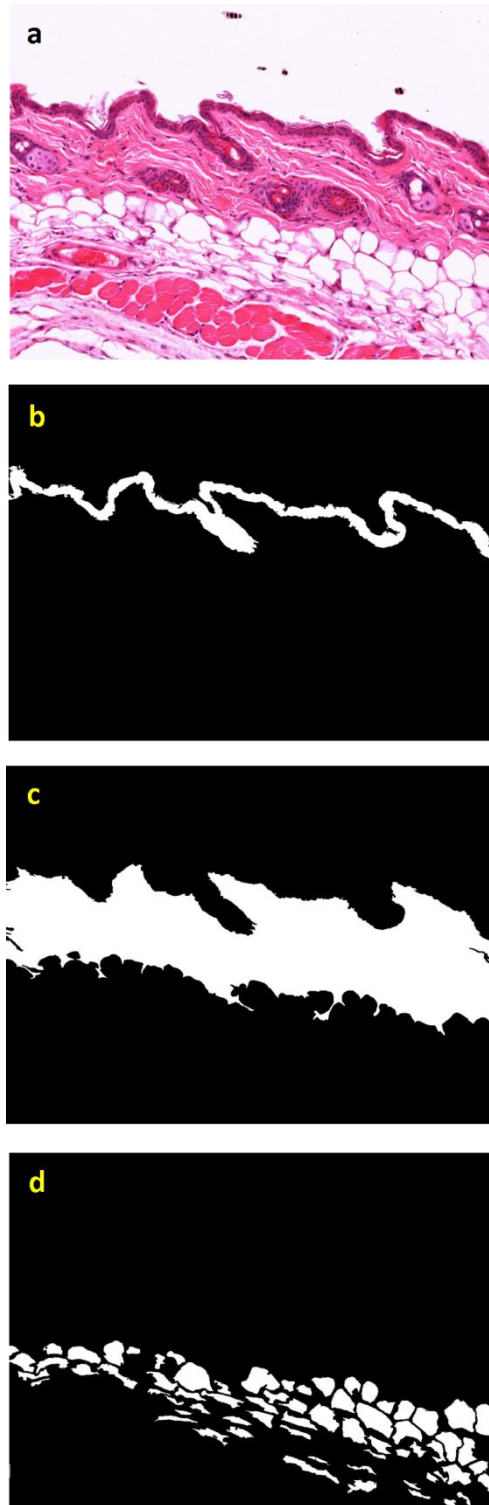


Figure 3. 13: Result of active contour-based segmentation. a) H&E image, b) segmented binary epidermis, c) segmented binary dermis, d) segmented binary adipocytes.

3.2.3 Quantification of Cutaneous Features

The quantification of biologically relevant parameters follows the segmentation of each skin layer using the active contour method. Each skin layer contains features that help to evaluate morphological changes in order to find out if there is a phenotype associated with a particular knockout mouse model.

3.2.3.1 *Skin Layer Depth Quantification*

The thickness of the epidermis and dermis was calculated in different ways in the development stage. Initially, the boundary lines of the epidermis were selected (the upper line and the bottom line; Figure 3.14b) and then the length of the two lines was normalized to calculate the distance of the opposite points of the two lines (Figure 3.14c). The limitation by using this calculation was that the two lines may not have the same length, which causes splay between the two opposite points, so increasing the measured distance. One of the causes of variation between the two lines is the inclusion of hair follicles that cause an expansion of the bottom line and skew the whole measurement. This epidermis depth measurement method was then modified by calculating the distance from one point on the upper line of the layer to the closest point on the bottom line. Unfortunately, the result of calculating distance between two described points was not more successful than before due to the fact that the upper and lower boundary lines are highly irregular making it difficult to measure the real depth of the layer (Figure 3.14d). Another modification was tried, again with limited success, to quantify the thickness by calculating the length of the perpendicular line from points on the upper line (upper boundary of epidermis) that intersects with the second line that represent lower boundary of epidermis (Figure 3.14e).

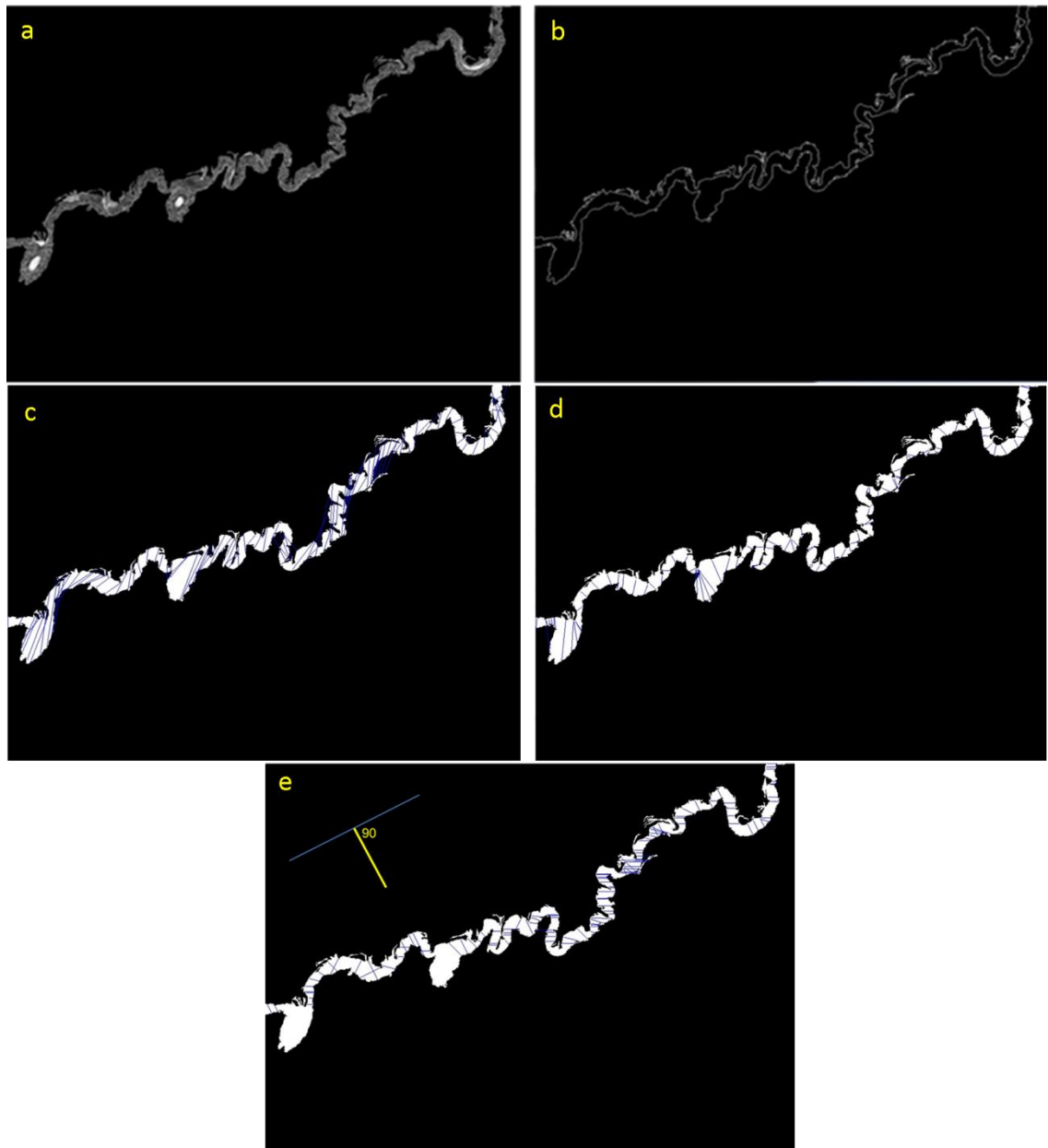


Figure 3. 14: The development of thickness measurements. a) typical segmented epidermal layer, b) upper and lower lines delineating the boundary of the layer, c) depth distribution based on normalized length of the two lines I_1 , I_2 and distance between two opposite points, d) depth distribution based on the distance between one point the first line and the closest point on the second line, e) depth distribution based on the length of the perpendicular line that intersects with the corresponding point on the second line.

Chapter 3

A final and more successful, approach to measure the depth distribution of the epidermis and dermis was by measuring the length of skeleton branches resulting from a skeletonization process, as described in the following section.

3.2.3.2 An Accurate Depth Quantification Method

The depth of each of the segmented epidermal and dermal layers was calculated automatically by generating a skeleton of the binary image of each layer using skeletonization (Gonzalez, Woods et al. 2004), after which the skeleton branches were used to quantify the depth by measuring the length of the branches to yield half the depth of the object. The number of branches of each image is different, and depends on morphology of the layer as described in Chapter 1, section 1.3.2.3. Figure 3.15 illustrates depth measurements made using skeletonization and the quantification method flowchart up to this stage.

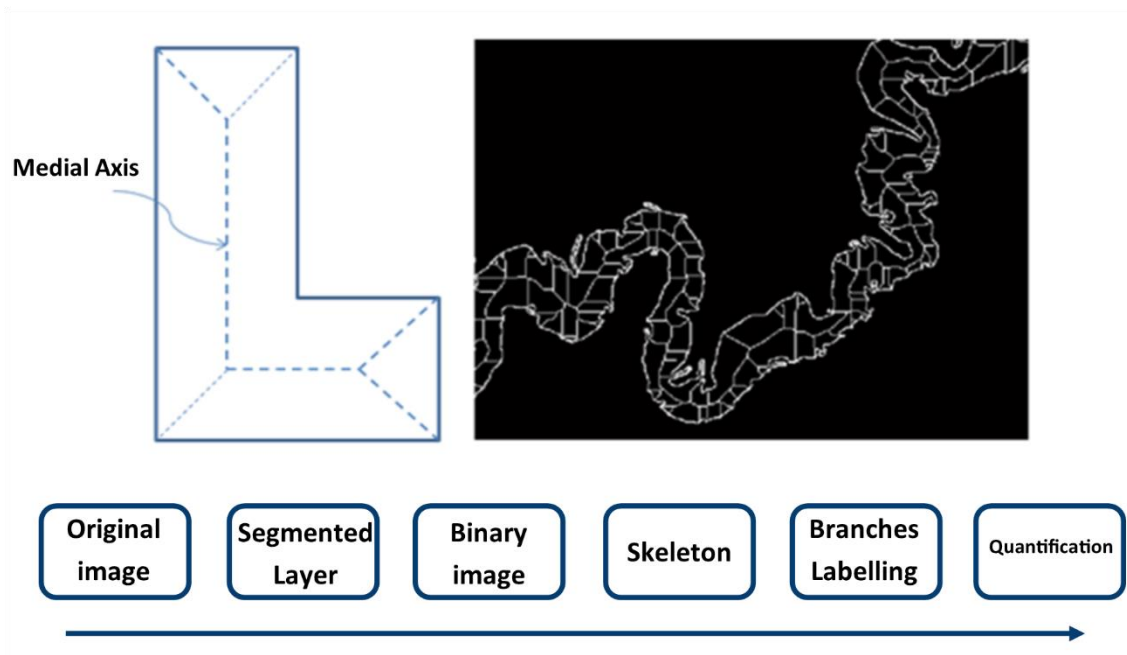


Figure 3. 15: Skeletonization process and flowchart of skin layer depth quantification.

3.2.3.3 Adipocyte Size and Number Quantification

Following fat cell segmentation (as described in section 3.2.2) adipocyte size and number were calculated. Existing manual methods for measuring adipocyte size measure major and minor axis of adipocytes in grids overlayed on micrographs, which is extremely time consuming. Moreover, this approach produces only an approximate area rather than the exact cell area as cell shape is approximated by an ellipse that can be calculated by estimating major and minor axes according to eq3.3.

$$Area = \pi * \frac{1}{2} major * \frac{1}{2} minor \quad (eq3.3)$$

Where major is the long axis of the ellipse that fits the fat cell and the minor is the short axis of that ellipse. Figure 3.16 illustrates the calculation of an ellipse manually, providing a comparison with the actual shape of the cell (which can only be identified using automated methods as described below). Manual methods for quantifying adipocytes in images of gonadal fat in a model of obesity were previously performed in the BITM by Dr Malgosia Kepczynska over a period of many months. A method to automatically determine the cross-sectional area of cells from actual pixel values (that can be converted to μm^2 by exploiting image resolution and original magnification), is therefore, essential for high-throughput studies.

$$Area = \pi * A * B$$

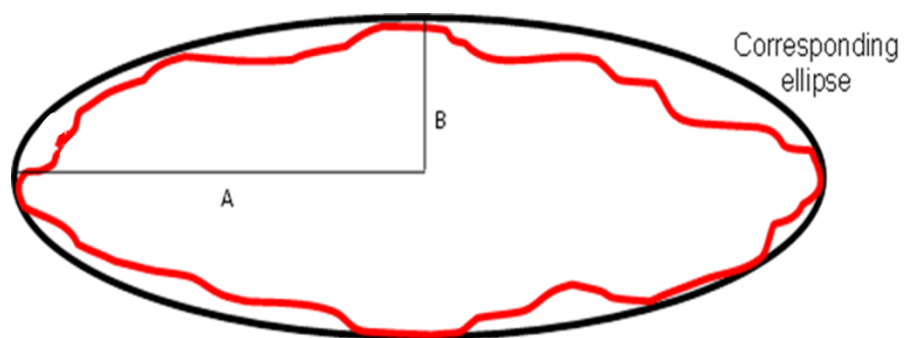


Figure 3. 16: An explanation of manual method for calculating size on an individual adipocyte (actual cell represented in red). A is the major axis and B is the minor axis of the corresponding ellipse.

3.2.3.4 Segmentation and Quantification Summary

The summary of the whole technique for segmenting and quantifying the epidermis, dermis and subcutaneous in images supplied by the WTSI is described below.

1. Image pre-processing to improve object detection. I needed to prepare the image for the next step of segmentation by applying contrast enhancement, noise reduction using a median filter, and converting the colour space from RGB (red, green and blue) to HSV (hue, saturation and value) colour space, from which I selected the saturation channel.
2. Region-based active contour model without an edge. This segments objects with different properties from surrounding objects, e.g. in isolating the epidermis-dermis and the subcuticular fat layer. For epidermis segmentation, I applied the MATLAB function `addimage` (which adds the image to itself), because this helps significantly in highlighting the epidermis in the image.
3. Measuring the branches of the skeletonised binary image to measure depth in segmented epidermis and the dermis.

```
branchesLabeled = bwlabel( branches, 4 ); // Label connected components  
ba = regionprops( branchesLabeled, 'Area' ); // Extract branch number of pixels
```

4. Accurate adipocyte size and number quantification from segmented adipocytes using a piece-wise linear transformation.

$$\text{TransImage}(I, j) = \begin{cases} \text{Image}(i, j) & 0.079 < \text{Image}(i, j) < 0.125 \\ 0 & \text{else} \end{cases}$$

3.2.4 Automated Adipocyte Size and Number Quantification

3.2.4.1 Adipocyte Image Data Set

The method described herein is an automated process to determine the size of adipocytes in H&E stained paraffin sections, initially of murine gonadal adipose sections. I sought to detect all adipocytes in an image using segmentation, and then measure the size of the cells in each tissue sample. Adiposity increases with mammalian body weight, so I compared adipose organisation in biological replicates of lean mice (n=4 C56bl6 animals per group fed standard diets) with a model of obesity (n=5 high-

fat fed C56bl6 animals per group), with two tissue sections per animal collected at 6 weeks of age. These images came from a pre-existing study of manual adipocyte size quantification in the University's Institute for Translational Medicine, and no animals were sacrificed specifically for this work. All work was performed under the terms of our Home Office licence, with local Ethical Review Board permission. Images were captured from two histological slides from each animal using an Aperio ScanScope CS whole slide scanner at optical magnification 40X, and at least 10 snapshots were used per slide (approximately 180 images in total).

3.2.4.2 Adipocyte Segmentation

The procedure starts by transforming the original RGB image to HSV colour space, from which the saturation image was selected (Figure 3.17). Background subtraction was implemented as a pre-processing task on the saturation channel only with a median filter of 71×71 pixels to remove any dark areas in the image that could affect edge detection. Figure 3.18b illustrates the resulting segmented image with background subtraction, and Figure 3.18c without background subtraction. As can be seen, the version without background subtraction misses some small fat cells whose boundaries overlap with those of neighbouring cells. Next, the intensity transformation piecewise linear grey level transform was applied to the saturation image. This was done in order to change the range of intensities in the grey level that represents the adipose cell pixels into ON pixels (white) and all other intensity values converted to OFF (black) pixels to improve accurate cell segmentation.

After segmentation, the resulting image was in a binary form almost ready for quantification after further post-processing to remove some artefacts. For example, some segmented cells were connected to each other by thin objects and mathematical morphology operations were used solve such problems and isolate cells (Figure 3.19). Specifically, an opening operator was used to solve the problem of connected cells, which was followed by applying a dilation operator using a disk structuring element with two elements. Dilation reconnected some pixels that were removed by the opening operator (Figure 3.19) near the end of thin connections. The partial cells at the boundary of the image were removed via a MATLAB function (`imclearborder (image)`) to clear image borders by suppress the objects that are connected to the image border, as shown in Figure 3.18b.

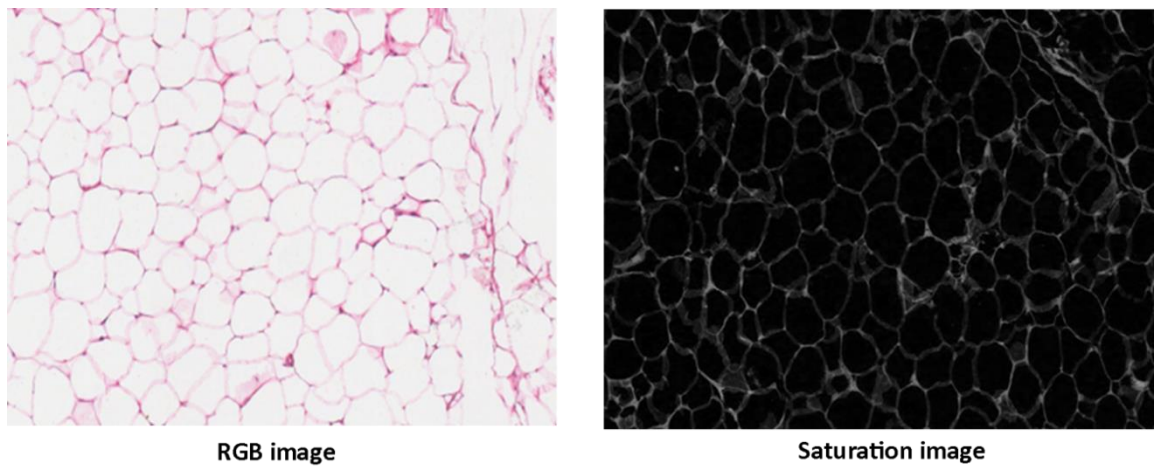


Figure 3. 17: Transformation to HSV colour space. Original RGB image (left), pixel dimensions = 1712×1074 pixels, and the saturation channel of HSV colour space (right).

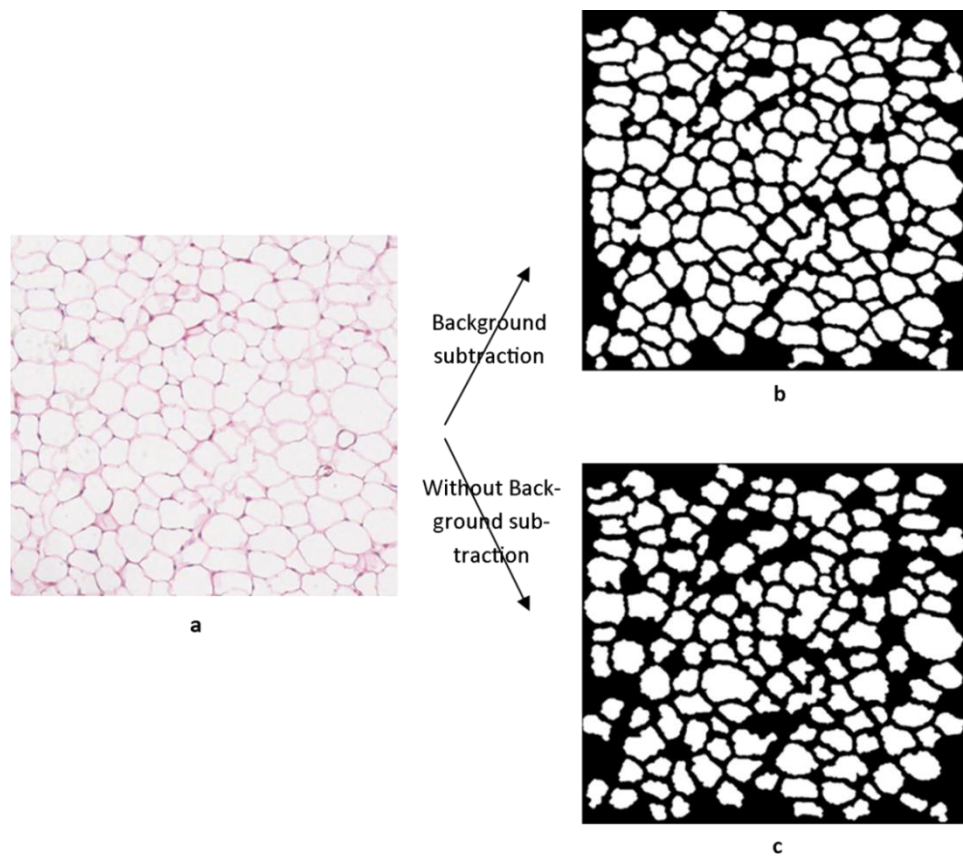


Figure 3. 18: Use of background subtraction to improve adipocyte segmentation. a) cropped original RGB image of gonadal fat pad, b) segmented fat cells after image background subtraction, c) segmented cells without image background subtraction.

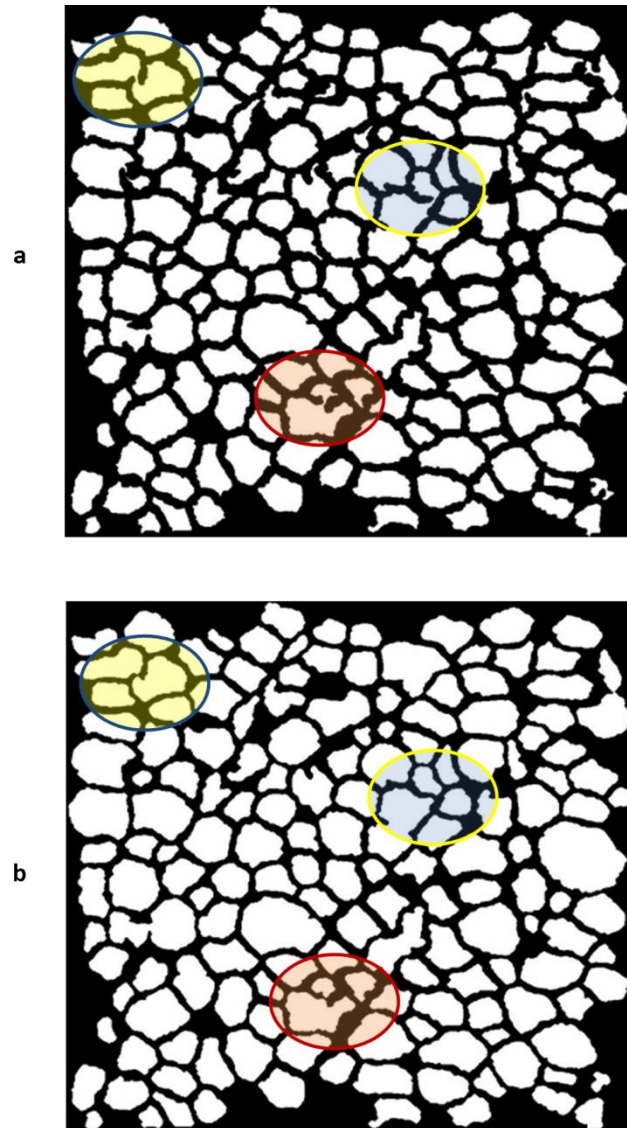


Figure 3. 19: Use of morphological operators to improve fat segmentation. a) segmented fat cells are connected in many regions before applying the morphological process, b) the connected cells are disconnected using automated morphological opening operations. Areas of particular interest are circled.

3.2.4.3 Adipocyte Quantification

After labelling adipocytes in the binary image utilizing the MATLAB function below, the actual area of the cells was calculated by counting constituent pixels (Table 3.1).

```
[L, num] = bwlabel (BW, n);
```

This function returns the number (num) and labels (L) of the connected objects in binary image BW.

The cells were then grouped into different size groups or bins. The smallest group consists of all cells with an area <2000 pixels, with each group incrementing by 2000 pixels. The largest of the ten groups contained cells with an area >18000 pixels. The size groups were then converted to μm^2 according to the spatial resolution of the images. Typically, with the image resolution used in this analysis, each pixel equates to an area of $0.25 \mu\text{m}^2$. Thus the bins range from <500 μm^2 (consistent with a small, immature adipocyte) increasing by 500 μm^2 up to the last group of very large adipocytes (>4500 μm^2). In this way, a biologically meaningful range was created. Finally, a size threshold was applied to exclude cells of area < 240 μm^2 , because below this size object were likely to be artefact.

3.2.3.5 Results of Adipocyte Quantification

Adipocyte size and number were measured in different mouse models. Figure 3.21 contrasts automated and manual methods for measuring adipocytes in the mouse model of obesity. The only size category where I saw a significant difference between automated and manual quantification was <500 μm^2 . These differences were due to the differences in calculating adipocyte area by each method (Figure 3.16). The automated method allowed more accurate size quantification, particularly at smaller sizes, as adipocytes have an irregular shape as shown in Figure 3.20 with examples of differences between the two methods. Two different measurements lead to a shift in the normal distribution of adipocytes size to the left using the automated method as shown in Figure 3.23. It is also possible that the automated method will include small cells more consistently than manual methods. Figures 3.24b and 3.24a show results with and without small cell thresholding respectively.

Chapter 3

When ellipse measurements are made entirely manually, long and short axes may vary according to observer may vary, while this can be partially automated if computational methods are used to calculate the axes of the fitted ellipse, and so reduce observer bias. I recalculated these values automatically from the manual measurements (Figure 3.23). However, the final automated method that calculates the area of each cell in μm^2 provides the most reliable measure of adipocyte size, because it is less influenced by possible errors in fitting an ellipse into a cell.

Although I saw differences in average adipocyte size in automated and manual methods, both methods identified significant differences between normal and high fat diets.

I compared the method developed herein to an existing watershed-based method that splits large cells using the freely available ImageJ adipocyte tool macro. The ImageJ macro also led to an over-estimation of cells in the smallest size category Figure 3.22. I observed that the ImageJ watershed algorithm split larger adipocytes into many separate cells (Figure 3.22c), which obviously skews the results. Moreover, unlike my method, the ImageJ macro tool only handled individual images and was, therefore, not suitable for batch analysis. Therefore, my tool is a novel and accurate method for automated image analysis that can used in high-throughput analysis, as illustrated in Figures 3.22b and 3.22d.

Fat Cell	MajorAxisLength (A)	MinorAxisLength (B)	Area (Pixel)	Aria I μm^2	Pi* $0.5A*0.5B$
1	199.99	96.84	11418	2854.50	3802.9
2	131.86	71.39	7082	1770.50	1848.5
3	118.69	63.13	5527	1381.75	1471.5
4	138.53	55.93	5448	1362.00	1521.5
5	78.44	20.34	980	245.00	313.4
6	60.53	15.38	608	152.00	182.8
7	161.94	121.45	15130	3782.50	3861.8
8	50.193	13.76	456	114.00	135.6
9	132.87	73.88	6287	1571.75	1927.6
10	77.58	39.40	2148	537.00	600.3

Table 3. 1: Comparison of typical measurements from a subset of adipocytes obtained by manual and automated methods. The area in μm^2 was calculated by the automated method, whereas the final column is derived from the manual measurement method.

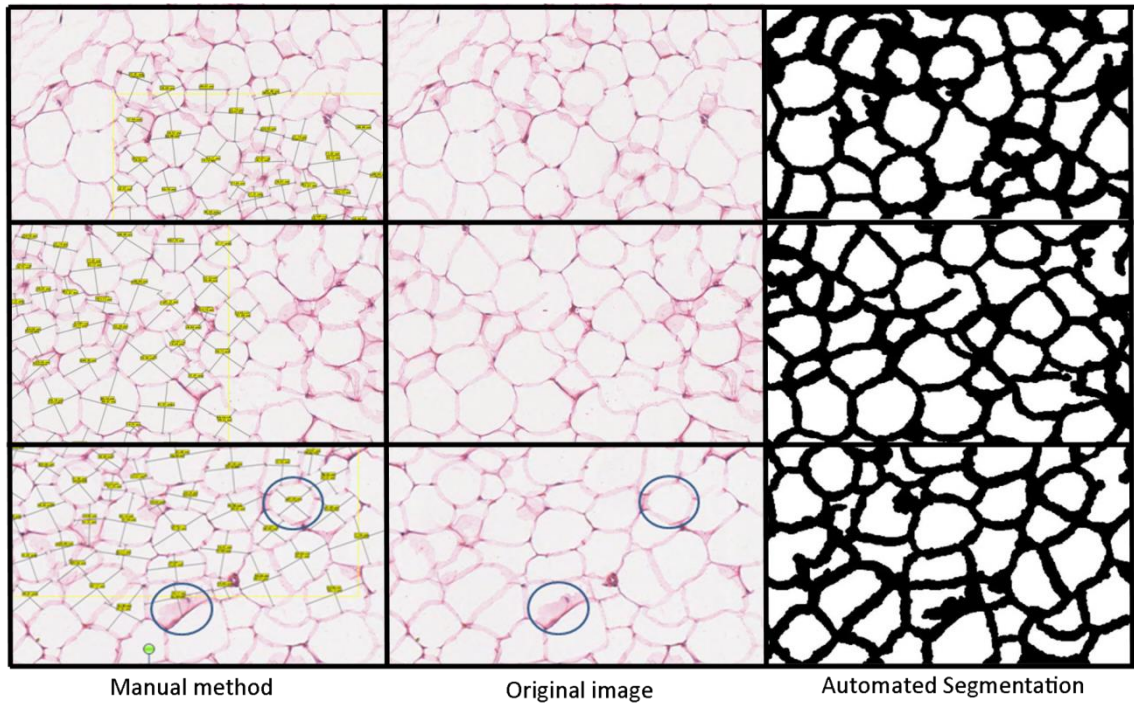


Figure 3. 20: Three typical examples of comparison between manual and automated methods. Segmented adipocytes using automated method include cells overall the image including small cells. Note that all cells in the image were counted with the automated method.

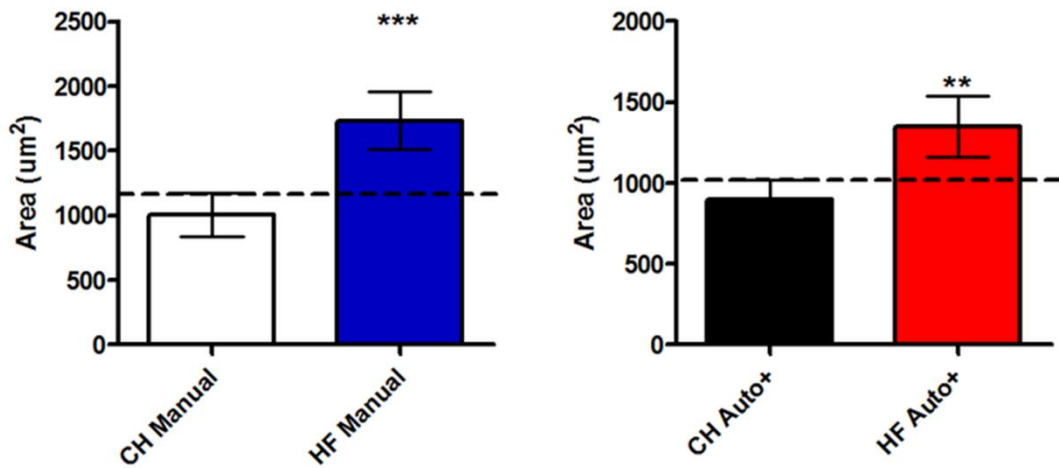


Figure 3. 21: Comparison of automated and manual methods to determine adipocyte size in a model of obesity. The left panel shows a significant increase in mean adipocyte size in high fat diet animals (HFD) compared to chow diet animals (CF), p value= 0.0004 represented with ***. The results were consistent with automated measurements, which are shown in the right panel (p value= 0.0043, **).

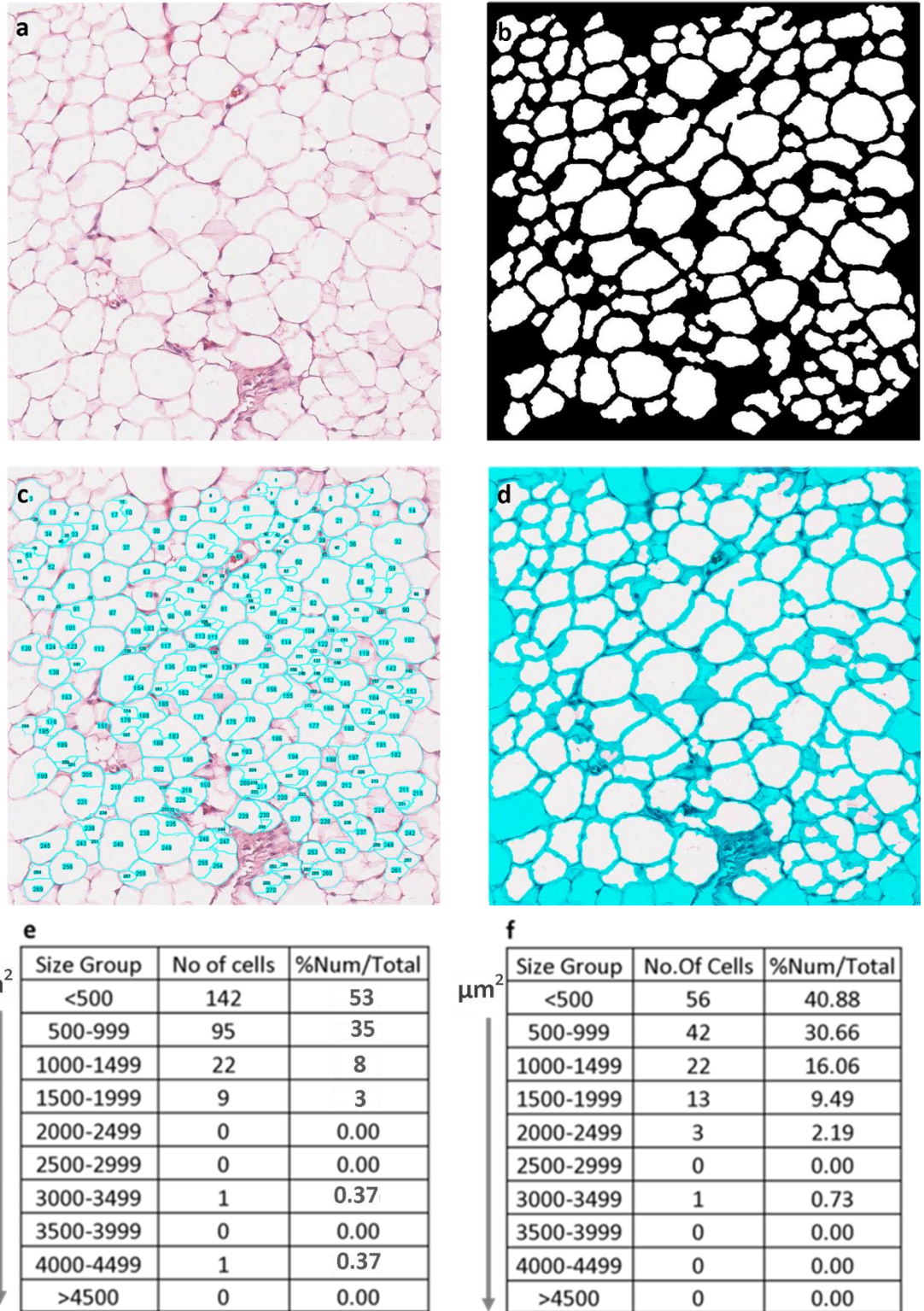


Figure 3. 22 Comparing the automated technique with the imageJ macro tool in terms of segmentation and quantification. a) original adipose tissue image, b) segmented cells using my method, c) watershed-based segmentation with ImageJ, d) superimposition of b) on a), e) ImageJ quantification results, f) output with my method. Note overestimation of small cells with watershed method.

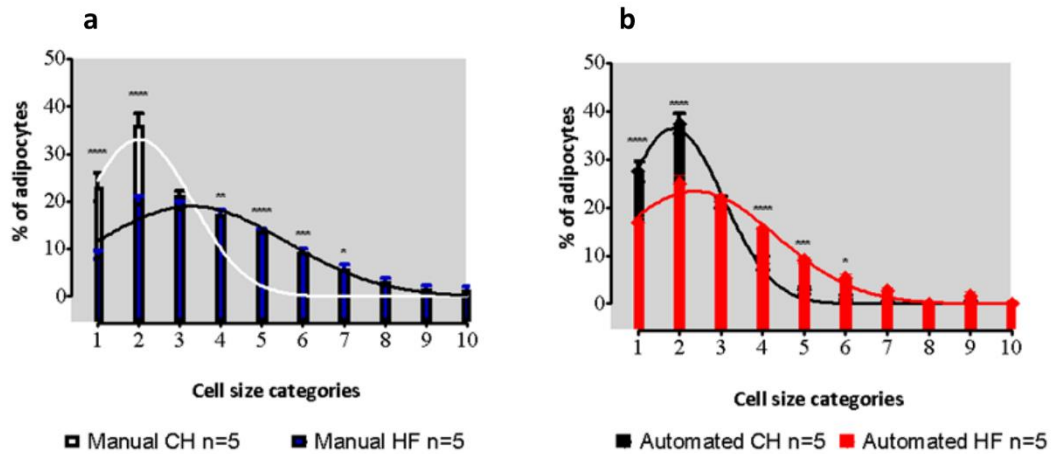


Figure 3. 23: Adipocytes size distribution in chow and high fat diet of gonadal adipose sections using manual and automatic quantification method. a) manual method b) automated method with small size thresholding. Both methods showing significant increase of small size categories adipocytes.

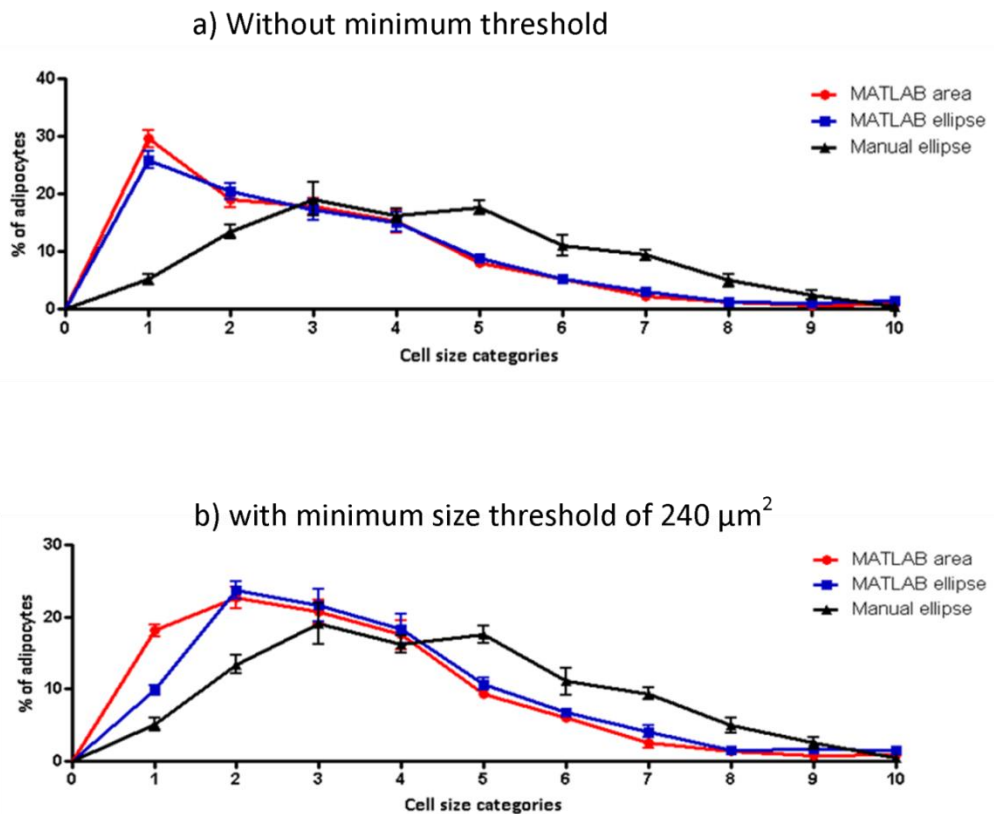


Figure 3. 24: Adipocyte quantification of gonadal adipose tissue using different methods. Using automated method by measuring cross section cells area (MATLAB area), and the manual method with both manual (Manual ellipse) and automated determination of ellipses by measuring major and minor axis of adipocyte fitted ellipse (MATLAB ellipse). This was performed with and without the use of a minimum adipocyte size threshold of 240 μm².

3.3 Results and Discussion

3.3.1 Data Sets and Experimental Protocol

My final method for high-throughput analysis was applied to three partitions of the MGP dataset. These were:

1. **Wild-type images**

H&E stained skin from 16 week-old female *wt* animals were from two genetic backgrounds (B6Brd;B6Dnk;B6N-Tyrc-Brd,B6N), and I wanted to test if this would impact my results. I also wanted to evaluate the effect of diet on my results.

2. **Development data set**

Development Data set was contain 202 H&E stained image with 20X of magnification and pixel dimensions 2000×1459. The images contained 15 *wild-type* (*wt*) animals and 187 knockout animal selected randomly by WTSI. The data set was used to test my automatic method with respect to segmentation and quantification of all of the three skin layers.

3. **Full data set**

Full data set was contain H&E stained images (pixel dimensions = 1440×908; 464.4×292.83) of skin section of 34 *wt* high fat diet animals, 8 chow diet animals and 475 knockout mouse of high fat and chow diet animals. The design of the MGP pipeline (use of diets and genetic backgrounds etc. is beyond the scope of this thesis). There were 2-3 slides available from each animal, and 6-10 images per slide (captured at the magnification and resolution above) were created.

3.3.2 Measurement of Skin Phenotypes in a High-throughput Screen

An automated segmentation protocol using an adaptive active contour model was developed for object detection and feature extraction in H&E images of mouse skin as described above. This method was shown to successfully segment and quantify the epidermis, dermis and subcutis. This method was then applied to H&E images from the WTSI MGP to enable investigation of the effect of different genes or environmental factors such as diet, on the morphology of the epidermis, dermis and subcutis in high-

throughput screen. The process is summarised in the flow chart in Figure 3.9, and the results of segmenting each slide is shown in Figure 3.13.

3.3.3 Quantification of *Wild-type* Data

Quantification was applied to all *wt* images in the first instance, consisting of 34 high fat diet fed mice, and 8 chow fed (lean) mice in two genetic backgrounds (B6Brd;B6Dnk;B6N-Tyr<c-Brd>,B6N). The total number of images was in the order of 1000 in this experiment.

3.3.3.1 Epidermal Depth Quantification

The depth of epidermal layer was quantified by calculating the skeleton branch length and determining the statistical moments of the distribution of widths of sections along the length to provide a representation of epidermal depth. Mean values from all images sampled is shown in Figure 3.25. This Figure illustrates that the distributions of depth along the length of the epidermis are not significantly different between the two different diet groups in a combined genetic background.

3.3.3.2 Dermis Depth Quantification

The dermis depth was calculated as above (Figure 3.26). Unlike the epidermis, a significant change in dermis depth characterised different diet groups.

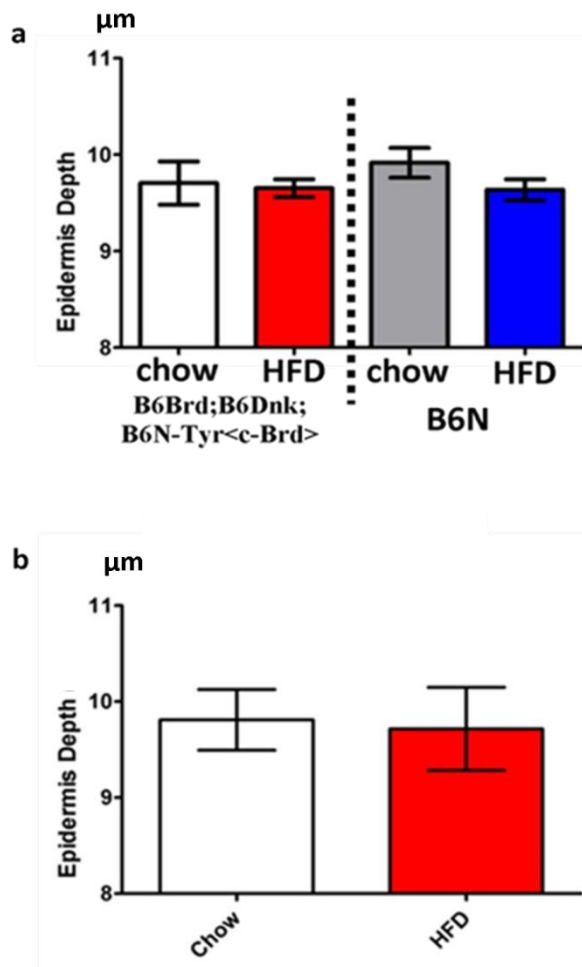


Figure 3. 25: Effect of diet on epidermal depth in *wild-type* animals. a) the influence of diet (chow or high fat diet (HFD) in two genetic backgrounds (B6Brd;B6Dnk;B6N-Tyr<c-Brd>,B6N). b) Effect of diet with combined genetic background does not show significant alteration in epidermis thickness. 34 HFD animals and 8 chow animals, 2-3 slide per animal and 4-10 images per slide.

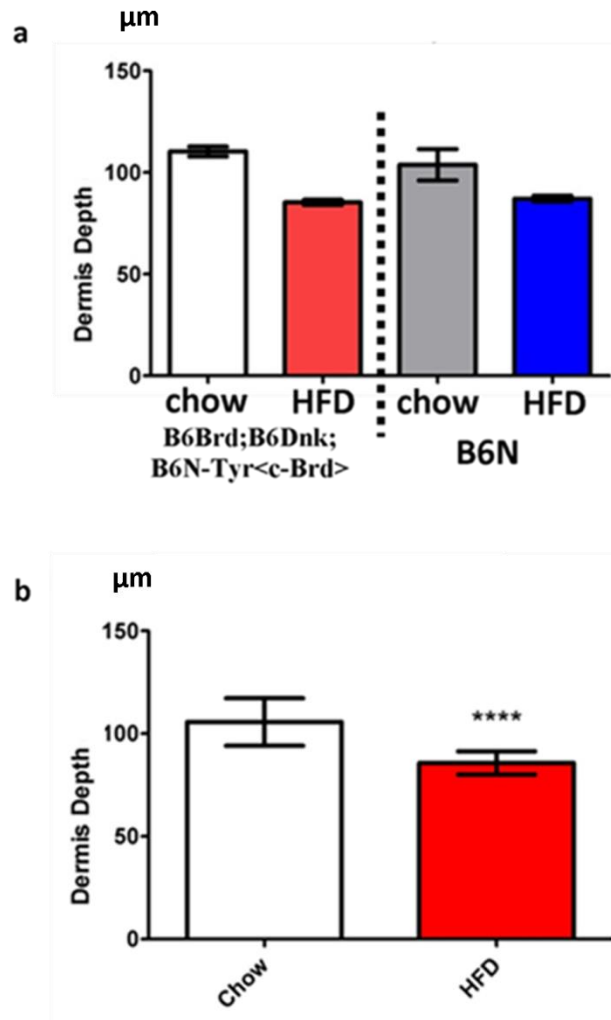


Figure 3. 26: Effect of diet on dermal measurement in *wild-type* animals. a) the influence of diet (chow or high fat diet [HFD]) in two genetic backgrounds (B6Brd;B6Dnk;B6N-Tyr<c-Brd>,B6N). b) Effect of diet with combined genetic background. Dermis depth decreased significantly in HFD animals (P value < 0.0001, ****). 34 HFD animals and 8 chow animals, 2-3 slide per animal and 4-10 images per slide.

3.3.3.3 Adipocyte Number and Size

Adipocyte analysis was applied to the *wild-type* images described above (Figure 3.27). The mean result in separate genetic backgrounds is shown in Figure 3.27a, and combined genetic background in Figure 3.27b.

From the adipocyte quantification, I found that chow fed animals contained a higher number of small adipocytes compared to high fat fed animals (Figure 3.30a).

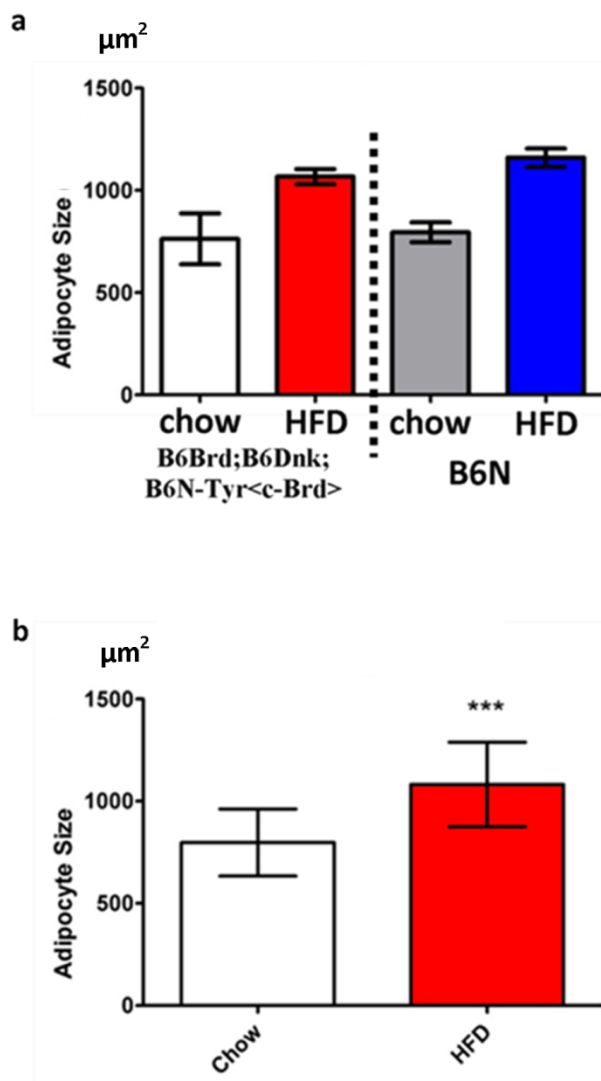


Figure 3. 27: Effect of diet on adipocyte size in *wild-type* animals. a) the influence of diet (chow or high fat diet [HFD]) in two genetic backgrounds (B6Brd;B6Dnk;B6N-Tyr<c-Brd>,B6N). b) Effect of diet with combined genetic background. Significant increase in adipocyte size in HFD animals (P value= 0.0007, ***). 34 HFD animals and 8 chow animals, 2-3 slide per animal and 4-10 images per slide.

3.3.4 Analysis of the Development Set

I then went on to study the development images that included 202 snapshots of H&E mouse skin images. This training data set included *wt* skin images along with a selection of images from knockout animals to provide a proof of principle that my method could isolate interesting phenotypes in each skin layer. Figure 3.28 shows genes associated with variation in adipocyte size, and Figure 3.29 shows an example of these interesting genotypes, specifically *Myo5a* that increase adipocyte size and *D11Wsu99e* that is associated with a decrease in adipocyte size. Some genotypes are associated with changes in adipocyte size distribution, such as *Vangl1/Vangl1* and *Ush1c/+* (Figure 3.30).

The results of applying the developed method to the training test of images are shown in Figures 3.31, 3.32 and 3.33 showing the interested genotypes in each of the dermis, epidermis and adipocyte altered phenotype respectively.

The MGP describe a stringent process to identify genotypes for further analysis, and I used the same criteria (Bassett, Gogakos et al. 2012). A comparison was performed between genetically-matched *wt* animals and individual genotypes by calculating a relative range (RR) for each genetic background, with mean, median and 95% confidence intervals (CI) determined. Individual genotypes were deemed to impact upon cutaneous morphology when at least 70% of the data points extracted for a feature were outside the RR 95% CI. Values of depth distribution in epidermis and dermis, and adipocyte size distributions were used to compute the 95% CI. The lower and upper 95% CI were computed by the following equations:

$$\text{Lower 95\% CI} = \bar{x} - z * \left(\frac{S}{\sqrt{n}} \right) \quad (\text{eq3.4})$$

$$\text{Upper 95\% CI} = \bar{x} + z * \left(\frac{S}{\sqrt{n}} \right) \quad (\text{eq3.5})$$

Where the \bar{x} is the mean of the data, z is a constant that equal to 1.96 for 95%CI, S is the standard deviation and the n is the number of entries.

The number of the entries that have smaller or bigger value as the lower and upper 95% CI in each *wt* *+/+* section has been counted. Then for each tissue section, the number of

Chapter 3

entries those were smaller than the lower 95% CI, and larger than the upper 95% CI of the *wt* data were counted. If the number of entries below the lower 95% CI was >70%, it was considered to be a hit, otherwise it was considered to be in the normal range. Likewise, if the number of entries above the upper 95% CI was >70%, it was considered to be a hit, otherwise it was considered to be in the normal range.

From this initial analysis 24 genotypes exhibited changes in the epidermis thickness (Figure 3.32), and 41 genotypes demonstrated alteration in the dermis depth, many of which have no previous known association with cutaneous function (Figure 3.31). We have identified 31/187 (16.5%) genotypes that are associated with altered adipocyte size compared to the 15 *wt* (+/+ locked) images, including 3 genotypes with altered metabolic phenotyping data in the MGP as illustrated in the figure 3.33.

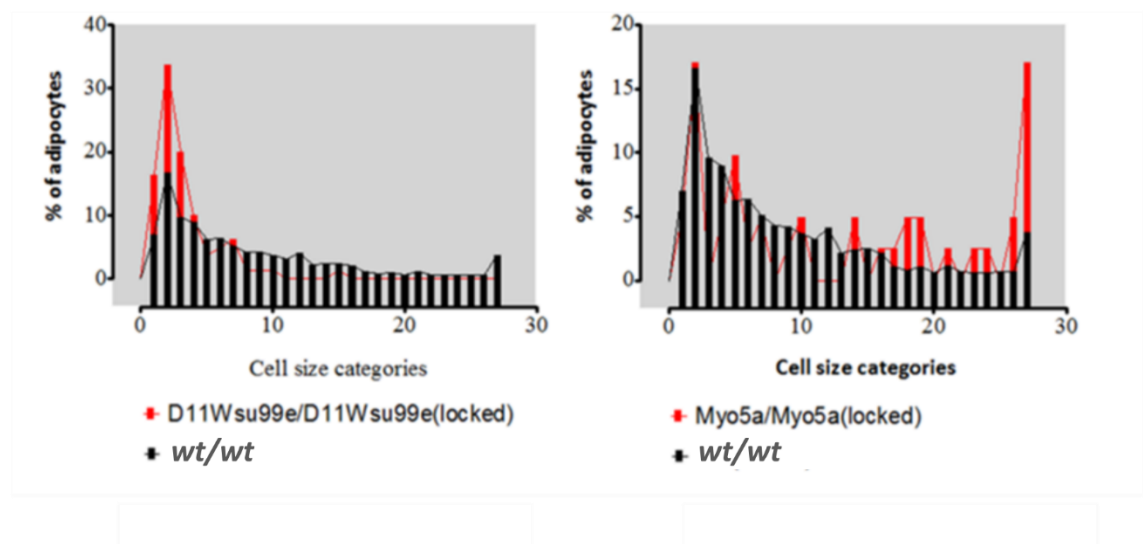
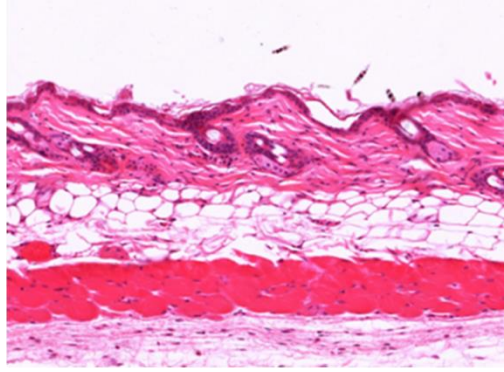
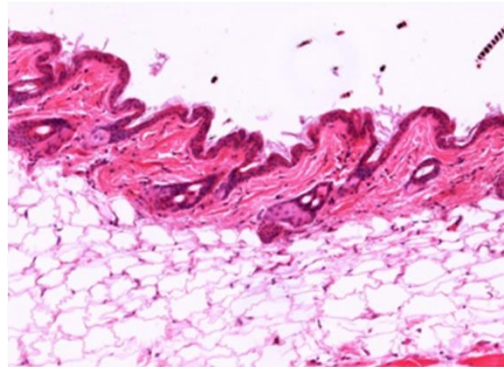


Figure 3. 28: Comparison of adipocyte size distributions between specific knockouts and *wt* animals. Left panel, an example of a knock-out that decreases adipocyte size. Right panel, an example of a knock-out that increases adipocyte size.

D11Wsu99e



+/+ (locked)



Myo5a

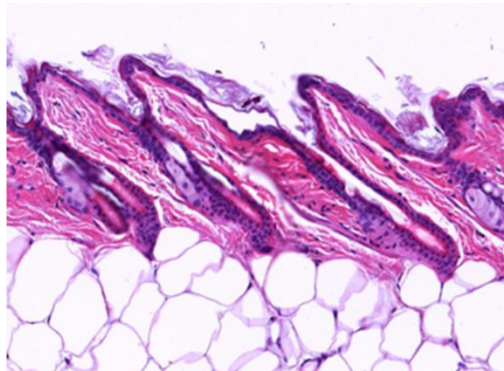


Figure 3. 29: Images of genotypes with that influence adiposity compared to *wt* from development data set (202 images at 20X magnification).

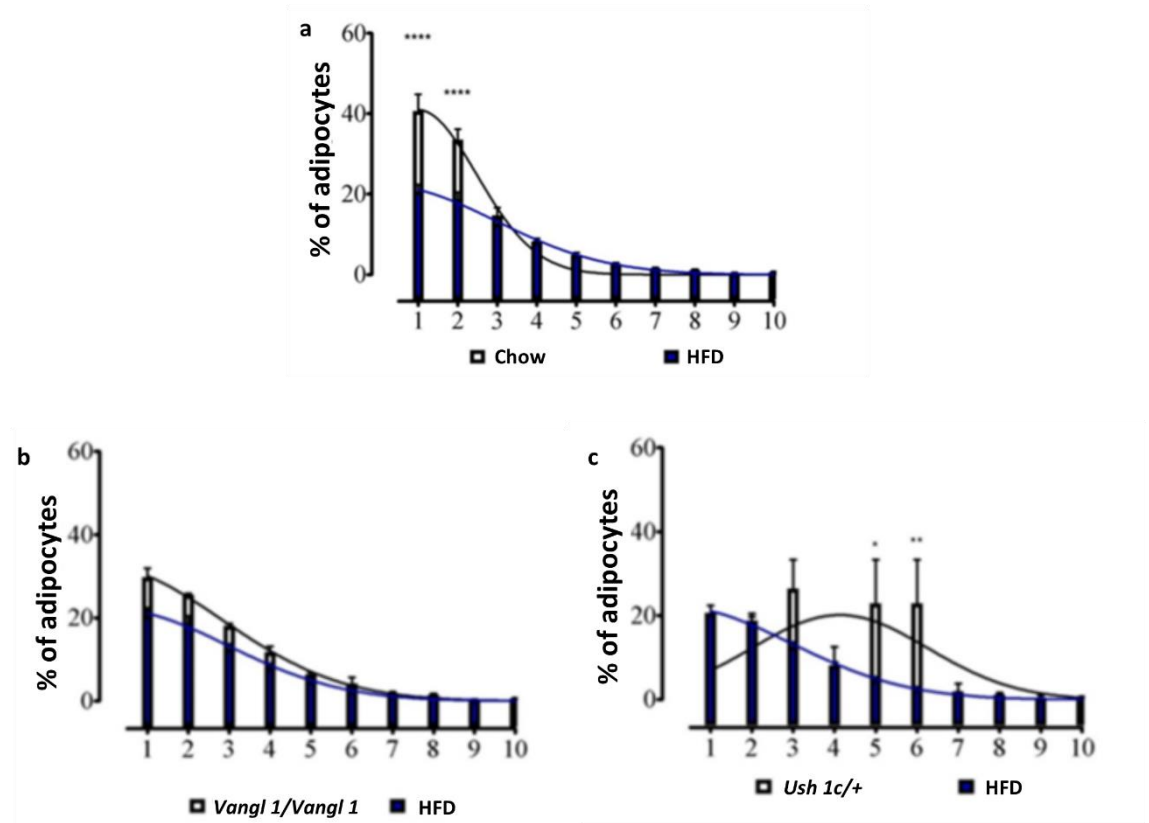


Figure 3. 30: Adipocytes distribution in *wild-type* animals in development data set. a) adipocyte size distribution in *wt* chow and HFD, b) distribution in *Vangl 1/Vangl 1* and HFD, c) distribution in *Ush 1c/+* and HFD animals.

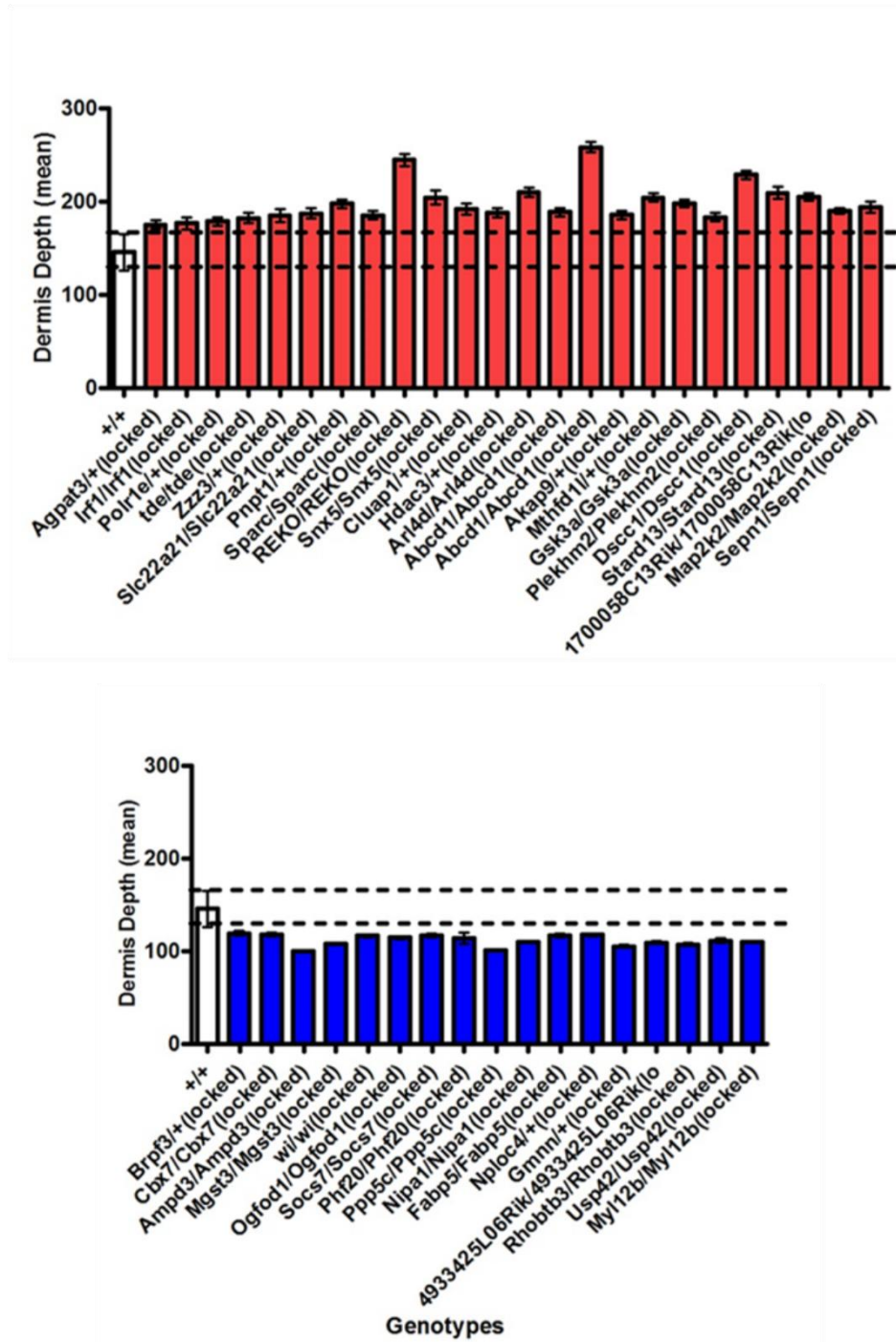


Figure 3. 31: Dermis measurements in development data. From analysing 202 development images for 187 KO mouse, 24 genotypes showed dermal depth increased (top), 17 genotypes showed a decreased in dermal depth (bottom). 202 images in total (187 knockout animals and 15 wt).

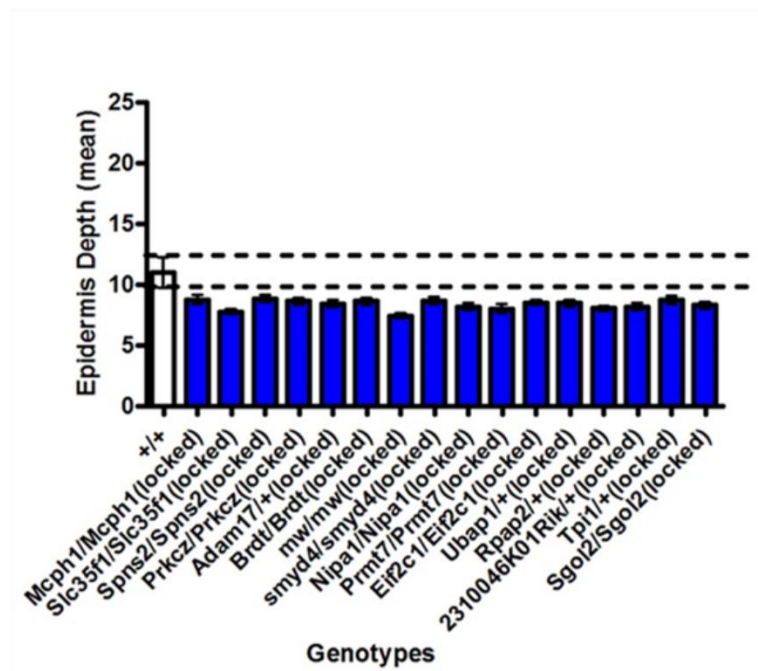
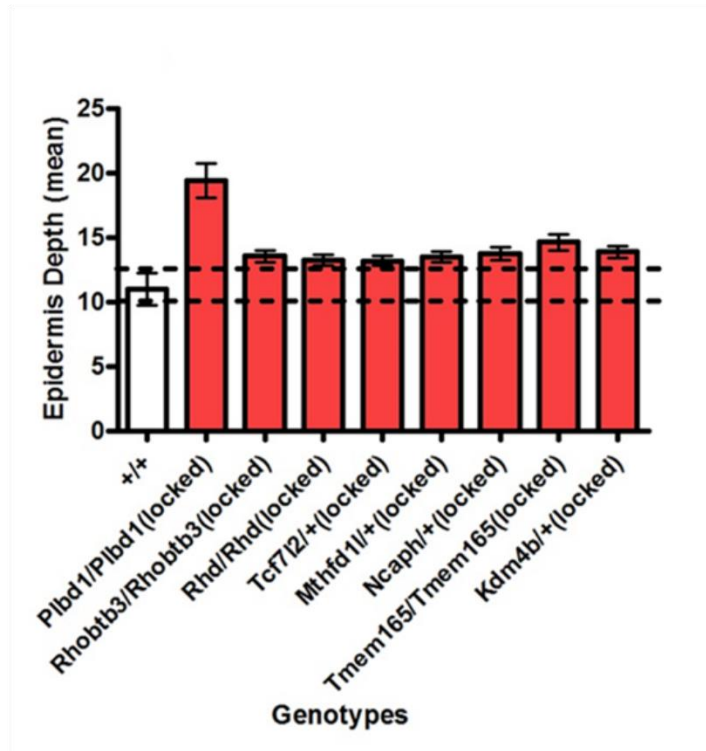


Figure 3. 32: Epidermis depth measurements in development data. From analysing 202 training images for 187 KO mouse, 8 genotypes showed epidermal depth increased (top), 16 genotypes showed a decreased in epidermal depth (bottom). 202 images in total (187 knockout animals and 15 wt).

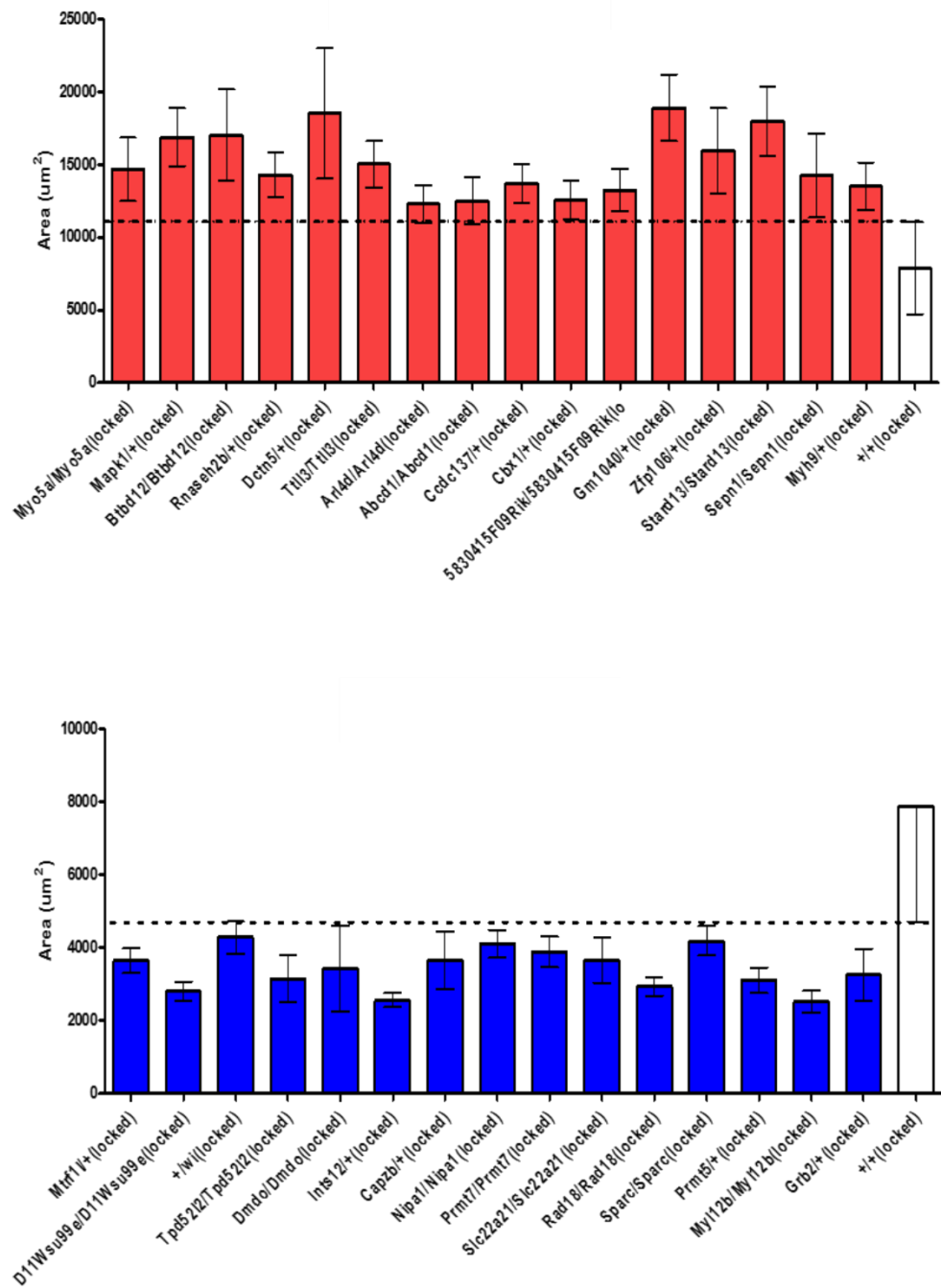


Figure 3. 33: Adipocyte quantification result of development data. From analysing 202 training images for 187 KO mouse, 16 genotypes 7.9% showed adipocyte size increased (top). 15 genotypes 7.4% showed decreased in adipocyte size (bottom). 202 images in total (187 knockout animals and 15 wt).

3.3.5 Analysis of the Full Dataset

Having successfully analysed the developmental data set and obtained encouraging results, I applied my active contour-based analysis technique to images from 475 knockout mice and 35 *wt* animals. The same RR and 95% CI criteria were used to select hits, and genotypes impacting each compartment (in either dimension) are represented in a Venn diagram in (Figure 3.34) with an effect in both high fat diet and chow fed animals. It is interesting that no one knockout was associated with an effect in all compartments, and only one gene, *Map3kl*, showed an effect in more than one compartment (adipocyte and dermis). All 74 knockouts that were associated with cutaneous phenotypes are listed in Table 3.3.

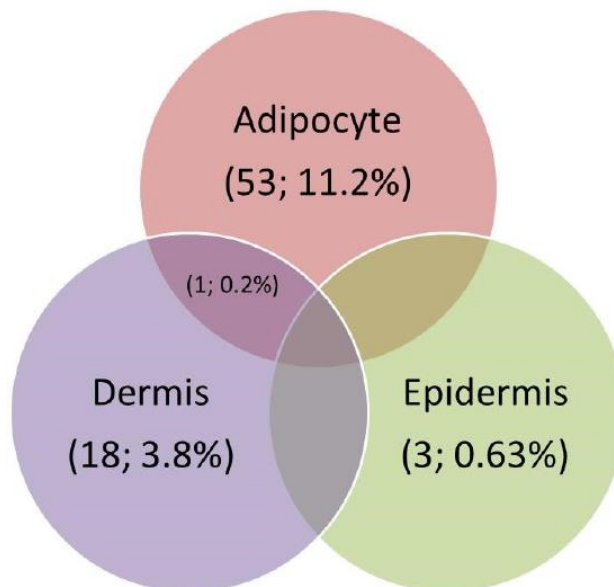


Figure 3. 34: Number of hits in each skin layer and overlap. Interesting phenotype in each of skin layer of 475 knockout animals. One gene overlapped between fat layer and dermis (*Map3kl*).

Chapter 3

Adipocyte Hits		Dermis Hits		Epidermis Hits	
<i>Chow</i>	<i>HFD</i>	<i>Chow</i>	<i>HFD</i>	<i>Chow</i>	<i>HFD</i>
Spns2(b)	Agpat3	Trpc2	Ldha	Dph2	Gatc
Scn3b	Sympk	Fggy	Gsk3a		Pnpt1
Tmc6	Sparc	Mrap2	-		
Cbx5	Mir96	Wnt3	-		
Wdr37	Prmt5	Secisbp2(c)			
Mapk10	Eif2c1	Abca4			
Acsl4	Anks4b	Actr6			
Mlec	Fkbp7	Map3k1			
Arhgef7	Appl2	Inpp1(b)			
Map3k1	-	Xbp1			
Ralb	Irf1	Coq4			
Creb3l1(e)	Sgol2	Trim29			
1700042B1 4Rik	Tpi1	Ido2			
Cand2	Zfp106	Arvcf			
Nacad	Stard13				
4932438H2 3Rik	Myh9				
Myo7a	Uba2				
Ush1c	3010026O0 9Rik				
Eil2	Zmynd8				
Leprot	Fto				
Ccdc160	Ccdc137				
Fam175b	Amfr				
Ift80	Rhot1				
Rab5c	Prmt3				
Arpc3	Dscc1				
-					
-					
-					

Table 3. 2: Knockout mice whose phenotype impacted on the dermis, epidermis and adipose.

3.3.6 Comparison with Other WTSI Phenotyping Data

The MGP makes available an extensive range of phenotyping data from these animals via clickable hit maps, however, a detailed analysis is beyond the scope of this study, but I did look at the intersection between genes associated with a cutaneous phenotype, and those considered to express a metabolic phenotype, as shown in Figure 3.35.

Epidermal depth-associated genes are shown in Table 3.3, and illustrated in Figure 3.36. One gene with an epidermal phenotype shared a metabolic phenotype, protein kinase C zeta, *Prkcz*. MGP phenotyping results indicated a change in plasma chemistry, and it will be interesting to investigate this relationship in more depth in future studies. It is also of note that a hair follicle phenotype was identified in an unrelated study. A more systematic analysis of these data are now underway.

Dermal depth impacting genes are shown in Table 3.4, and illustrated in Figure 3.37. Seven genes were also known to express a metabolic phenotype: *Dusp3*, *Map2k2*, *Mapk1*, *Ppp5c*, *Rhobtb3*, *Myl12b* and *Phf20*.

From the analysis of adipocyte size and number, eight fat phenotypes were detected, as shown in Table 3.5, and Figure 3.38 illustrates the genes associated with adipocyte size and number alteration. Two of the genes also have a metabolic phenotype, *Bbx* and *Phf20*, and again these are of interest for future study.

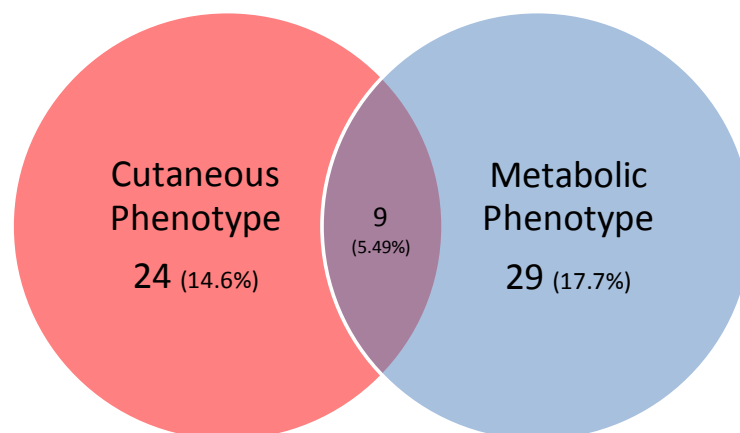


Figure 3. 35: Venn diagram of the cutaneous and metabolic phenotypes.

Colony Prefix	Allele Name	Strain	
MBGM	Dctn5<tm2a(KOMP)/wtsi>	C57BL/6J.Tyr.C57BL/6N	
MBSD	Gap43<tm1a(EUCOMM)/wtsi>	C57BL/6J.Tyr.C57BL/6N	
MBGK	Pkcz<tm1a(EUCOMM)/wtsi>	C57BL/6J.Tyr.C57BL/6N	
MBBM	Sympk<tm1a(EUCOMM)/wtsi>	C57BL/6J.Tyr.C57BL/6N	
			Viability at weaning
			Recessive Lethal Study
			Fertility
			Embryo LacZ Expression
			Adult LacZ Expression
			General Observations
			Weight Curves
			Open Field
			Modified SHIRPA
			Grip Strength
			Hot Plate
			Dysmorphology
			Rotarod
			Non-Invasive Blood Pressure
			Prepulse Inhibition
			Indirect Calorimetry
			Glucose Tolerance (ip)
			Auditory Brainstem Response
			Body Composition (DEXA)
			X-ray Imaging
			Stress Induced Hyperthermia
			Eye Morphology
			Plasma Chemistry
			Plasma Immunoglobulins
			Haematology (CBC)
			Peripheral Blood Lymphocytes
			Micronuclei
			Tissue Biobank
			Heart Weight
			Heart Histology
			Tail Epidermis Wholemount
			Skin Histopathology
			Brain Histopathology
			Eye Histopathology
			MicroCT & Quantitative Faxitron
			Salmonella Challenge
			Citrobacter Challenge
			Epidermis
			Dermis
			Subcutis Adipocyte

Table 3. 3: A typical hit map of phenotyping information curated by the MGP for four genotypes with epidermal impact.

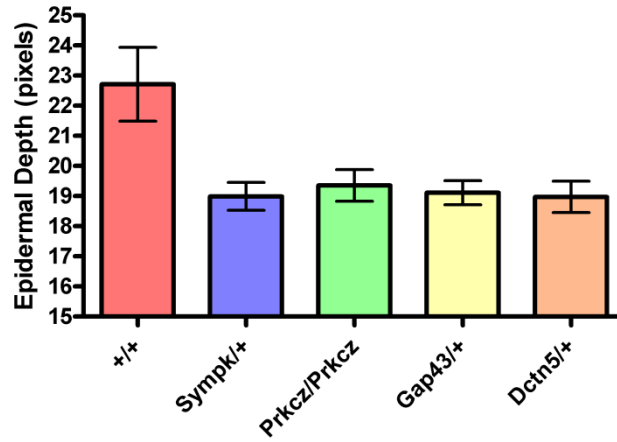


Figure 3. 36: Epidermal depth in four genotypes in relation to *wt*.

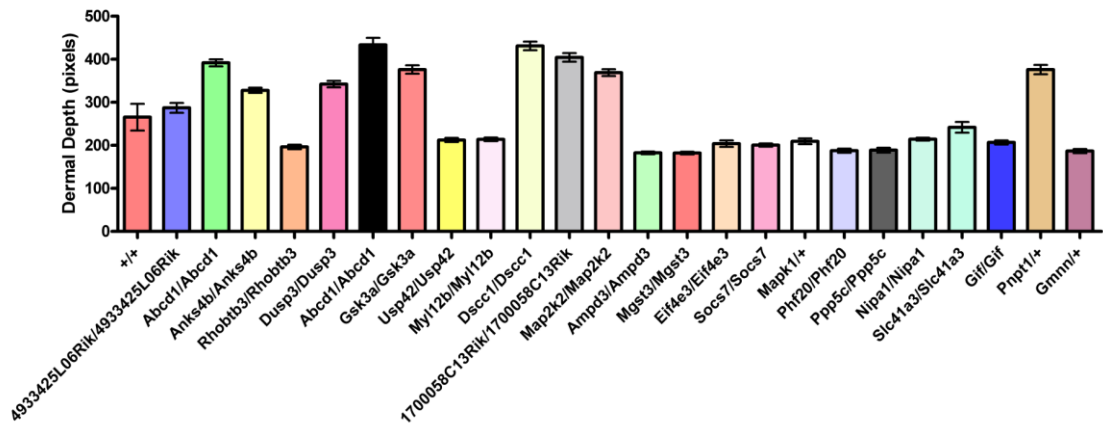


Figure 3. 37: The dermal depth in 24 different genotypes in relation to *wt*.

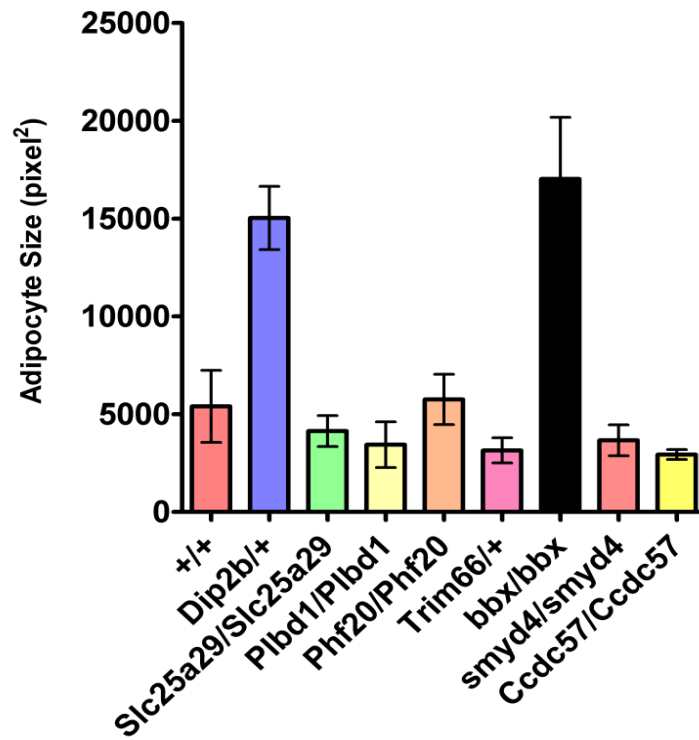


Figure 3. 38: Adipocyte size and numbers in eight different genotypes in comparison to *wt* skin.

3.4 Conclusion and Future Work

Automated cutaneous phenotyping was presented in this Chapter, in which I extracted morphological features from skin layers in high a throughput screen. I sought to deal with many problems that face high-throughput analysis, notably as time, reproducibility and cost.

The use of the active contour algorithm to adaptively segment skin layers in a huge number of H&E stained images solved the problem of the variation in intensity and colour arising from the use of multiple laboratories and investigators, and between experiments performed in the same laboratory at different times. The novel depth quantification obtained by computing the length of skeleton branches was used successfully to quantify the depth of both the epidermis and dermis to identify interesting skin phenotypes.

Quantifying adipocytes in gonadal fat H&E-stained images provided important information in determining the effect of a high fat diet on adipocyte size and number (Jo, Gavrilova et al. 2009). Adipose tissue expands by two mechanisms: hyperplasia (cell number increase) and hypertrophy (cell size increase). My adipocyte quantification method allows an assessment of the both of these factors within a tissue specimen (Osman, et. al. 2013). The automatic method also provides accurate measurements of the cross-sectional area of adipocytes in histological sections. The performance of the automated algorithm was consistent compared to the utilized manual methods and, moreover, the accuracy of the unsupervised area measurements is increased. This determined that the manual method of calculating the cross-sectional area of adipocytes uses assumptions that lead to an over-estimation of cell size.

Changes in the epidermis may reflect hyperplasia or inflammation, both key biological processes, whereas changes to the dermis may reflect an impact on connective tissue (with implication for processes such as scarring or wound healing). Perhaps more importantly, changes in adiposity may reflect local or systemic metabolic changes (or both). The genes that were identified as exhibiting interesting phenotype are shown in Table 3.2. Some of these phenotypes are novel, while others were not previously reported. Selection of candidate genes for further investigation may be informed by the use of MGP primary phenotyping data, and this is a rich area for future study.

Chapter 3

Moreover, more knockouts are emerging from the pipeline, and I will screen these as they become available.

In conclusion, I have developed an automated high throughput screening method for the segmentation and quantification of cutaneous sections. This has enabled the identification of specific gene knockouts that results in a cutaneous phenotype, which would not have been possible (or at least realistic) using existing manual methods. My approach utilises novel techniques, specifically an active contour region-based model to isolate and quantify features of the epidermal, dermal and fat layers of the skin that can be output to an Excel spreadsheet to facilitate further analysis. It is likely that this rationale could be adapted for other tissue types.

Future Work

I would like to utilise other image data from the WTSI. This includes additional H&E stained skin and other tissues, as well as skin samples stained by immunohistochemistry to identify the epidermal proteins K10 (mature keratinocytes) and K14 (immature keratinocytes). As additional H&E images become available, I will expand the analysis across the whole pipeline of animals that are being phenotyped in the MGP, as shown in Figure 3.1. I am also in the processes of gaining access to the H&E original slides, as I would like to exploit eosin autofluorescence to provide both 3D visualisation, and higher resolution collagen imaging. If unstained slides became available, then picrosirius and Herovici staining could be used to image collagen basket-weave and inflammatory cells (and elastic fibres) respectively.

With immune-stained skin, I would like to go on to investigate hair follicle organisation using K14 images and use the region-based active contour to segment the epidermis (Figure 3.39b) to investigate the orientation, size and number of follicles (Figure 3.39d). The genetic basis of disorders of hair follicles (such as alopecia) is of great scientific interest, and may yield novel treatments.

Another technical aspect that I need to consider in future developments is to make the system adaptive in order to be applied to other data sets. For example, my techniques should be able to be applied to images from any laboratory, but this is complicated variation in contrast due to subtle differences in fixation, sectioning and staining. While

great care has been taken to minimise technical variation, inconsistency in colour and intensity, seen when the same staining method is performed at different times and in different places will significantly affect morphometry. By creating an adaptive technique to solve the problem of colour and intensity variation, I have thought about adding colour normalization as a pre-processing step. This normalise colour distribution across a range of source images (Magee, Treanor et al. 2009). An example of such colour normalization is shown in Figure 3.40, achieved by mapping the colour distribution of source images (over or under stained) to that of an ideal target image (well stained image).

Finally, in order to assess the effectiveness of my segmentation and quantification technique in the identification of genes that exhibit significant cutaneous phenotypes, I would like to use depth and size measurements to compute the Mahalanobis distances to find outliers in the whole data set. This was done previously to provide a quality control check on secondary phenotyping from WTSI MGP data (Bassett, Gogakos et al. 2012). Briefly, this will calculate the distance between each animal depth result and the centre of the cluster, and these clusters will hopefully represent ‘normal’ and ‘interesting’ phenotypes. In this way, I hope to maximise the impact that the MGP will have on our understanding of the genetic basis of disease.

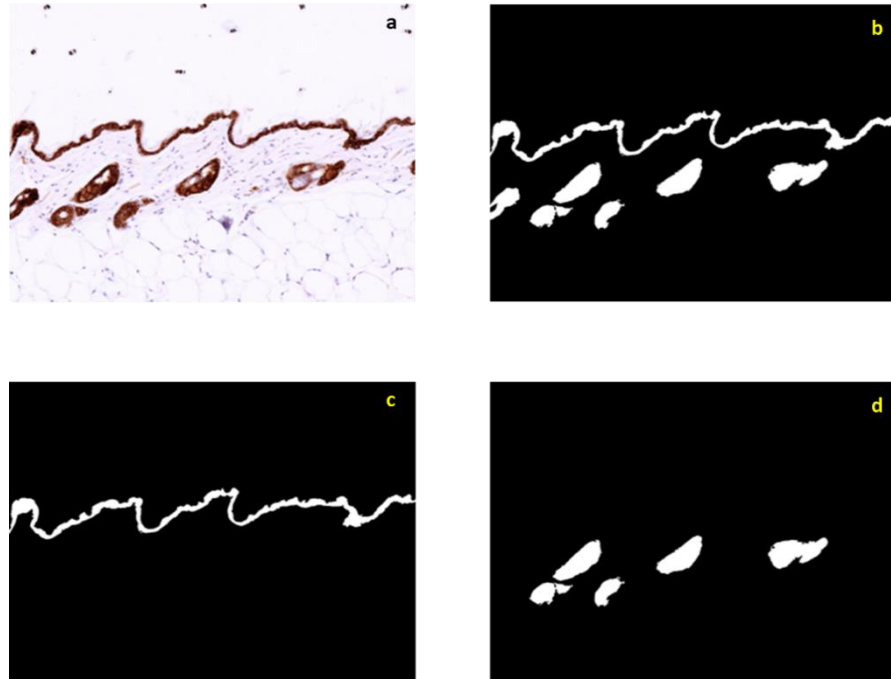


Figure 3. 39: Segmentation of immature keratinocytes and hair follicles. a) K14 stained image from the training data set, b) segmented binary image of the epidermis and hair follicle/ sebaceous gland, c) epidermis, d) segmented hair follicles.

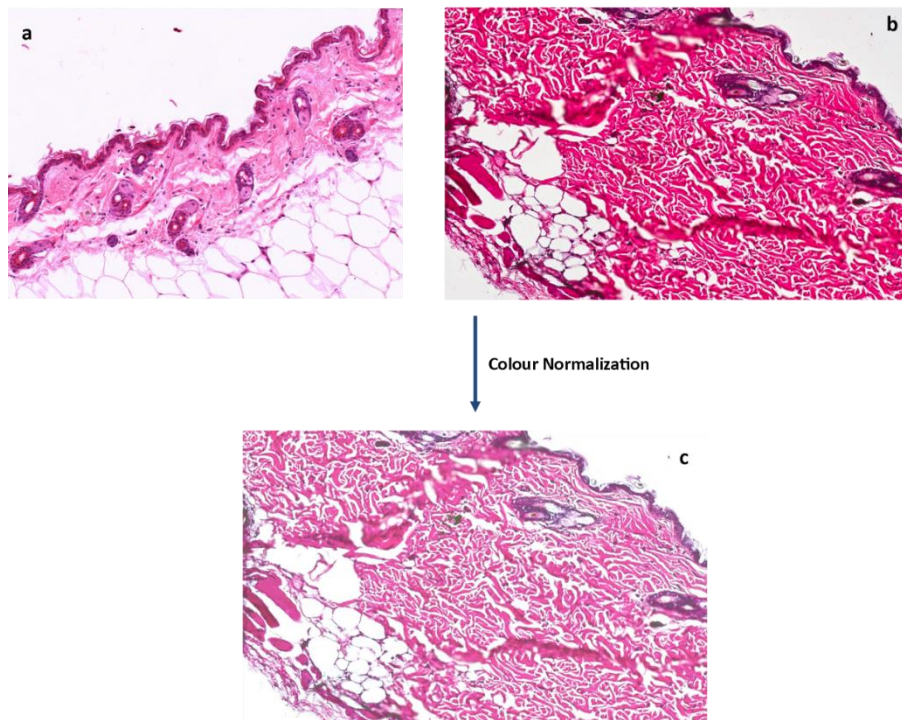


Figure 3. 40: Colour normalization. a) target H&E stained image, b) source image, c) source image adjusted to exhibit the same colour distribution as the target.

CHAPTER 4

Non-invasive Assessment of Skin Surface Structure

4.1 Introduction

The structure of the lines, ridges and wrinkles on the surface of skin may reflect important information about pathological and environmental effects. In this Chapter, the degree of change in skin surface structure using automated texture information extraction is described, with related experimental results. I shall investigate and develop a computational procedure for the analysis of the skin surface texture from a non-invasive imaging method that can be used to automatically extract and evaluate alterations of skin surface topography. I first introduce the use of silicone skin moulds to capture skin integrity. The following sub-sections describe the features that reflect environmental impact on skin, and the widely used manual Beagley-Gibson (BG) scoring system previously used to quantify skin surface data. In section 4.2, the aims and objectives of the work are described. In section 4.3, I introduce the image database, the related individual clinical parameters and describe manual analysis. In the following sections, I describe computational skin surface texture analysis. I conclude this Chapter with results discussion.

A skin mould is the impression of the micro-topography of the skin surface generated from a flexible material. In this instance, the mould is made from silicone, and a skin impression is made by the placement of the silicone on the surface of the skin. This provides a negative of the topography of the skin.

The strategy of generating an impression of the skin has many advantages over the techniques discussed in previous Chapters. It is non-invasive and does not alter topography, unlike the process of biopsy and subsequent histology as discussed in Chapters 2 and 3. Furthermore, several studies have suggested that skin ridges and wrinkles correlate with dermal as well as epidermal changes (Gherardi 2008; Mizukoshi and Takahashi 2014; Trojahn, Dobos et al. 2014). From a cosmetic or pharmaceutical perspective, the use of skin moulds or impressions can allow the degree of the damage

to be assessed in a controlled and quantitative manner that is not feasible with invasive techniques, enabling larger multi-centred studies.

4.1.1 Skin Surface Topography

Healthy skin displays a regular pattern of furrows or lines (visible to the naked eye), but depth and definition can change with age, and deeper wrinkles appear progressively. The texture of the skin surface is not the same in different regions of the body. For example the pattern of lines and pores on the face, arm and the soles of the feet vary considerably (Gherardi 2008; Sparavigna and Marazzato 2010). However, the skin over all these surfaces has common features, consisting of different shapes and patterns determined by different length and depth of lines. There are primary lines, which are wide, long and deep, and these primary lines are connected by shorter secondary lines which are finer (Tchvialevaa, Zenga et al. 2010). The intersections of primary and secondary lines form polygonal shapes of varying sizes. The size of the polygonal shapes and distances between the lines can be used as a pattern to distinguish between skin of different individuals (Seddon, Egan et al. 1992). Various studies have demonstrated that the texture of the skin can vary with different life histories, and with different factors including environmental exposure, pathology, scars and chronological ageing (Gao, Hu et al. 2011). In order to investigate the different classes of skin texture patterns, and to quantify the impact of each of the age-related and environmental factors on these patterns, one needs a measure of similarity/dissimilarity that can reflect changes to the patterns. I shall introduce one such measure and discuss its computation.

4.1.2 Skin Surface Structure Analysis

The impression of the skin surface contains lines and shapes formed by the intersection of the parallel organised lines (primary lines) and intermediate lines between the primary lines (secondary lines). The organisation of the lines and the shapes formed from their intersection are the most important features of the skin surface, and alteration in their patterns may reflect interesting phenotypes caused by environmental impact or disease.

4.1.2.1 Beagley-Gibson Scoring

The clinical “gold-standard” for investigating skin surface structure is the Beagley-Gibson (BG) scoring system, which was developed to classify skin structures into six

groups that differ in the regularity of the lines and shapes on the skin surface as shown in Figure 4.1 (Seddon, Egan et al. 1992). The first score has a perfect structure, with regular intersecting primary and secondary lines forming star shapes. Skin deteriorates progressively to score 6, which has no discernable regular structure, with large flat spaces between deep and irregular primary lines. The BG score reflects, therefore, a global analysis that refers to a multiplex of parameters used to measure different skin topography features, e.g. number of primary and secondary lines, the number of grids, number of closed polygons that are formed by the lines, and the mean area of blocks. Briefly, skin is categorised as follows: score 1, primary and secondary lines are visible and of similar depth, forming star shapes; score 2, some of the secondary lines are flattened; score 3 the primary lines become uneven, the secondary lines flattened with little star formation score 4 is identified by deeper primary lines with loss of secondary lines; score 5 has flat areas between primary lines with few secondary lines; and score 6, there are no secondary lines with large flat spaces between deep primary lines.

BG scoring has been used many times in evaluating skin integrity, for example skin micro-topography has been evaluated from skin moulds and compared to skin biopsies to assess elastosis (Seddon, Egan et al. 1992). The aim of this literature was to determine if any clinical parameters were correlated with skin structure on the dorsum of the hand. There were a number of significant correlations with micro-topography, including changes in texture in ageing, cigar smoking, lighter iris and skin color, male gender, and sun exposure. One interesting observation was that there was no significant correlation between biopsy scoring of elastosis and the BG score, suggesting that changes in elastic fibres may not be reflected in skin surface structure.

There have also been many instances where individual features of the BG scoring method have been utilised to assess skin topography. The number of primary and secondary lines provides a grading parameter, alongside the BG score, to assess the level of sun exposure (Weiler, Knight et al. 2007). The number of primary and secondary lines in one square centimetre of the skin impression was calculated, with fewer lines indicating the highest level of sun exposure, and higher line counts associated with low levels of sun exposure. Skin line counting and BG scoring along with a self-reported indicator of lifetime sun exposure was used to examine the relationship between sun exposure, vitamin D intake and breast cancer risk (Weiler,

Knight et al. 2007). That study found associations between skin texture and many factors including age, skin colour, ethnicity and many other lifestyle variables. Both skin line count and BG scores showed significant association between alterations in the skin surface structure with age, sun, UV light and other variables, however, the BG system showed a greater age difference between higher and lower sun exposure than did the skin line counts.

The closed polygonal shapes that are formed by the intersection of the primary and secondary lines are known as the grid structure. The number of grids in skin topography was used as another BG-related parameter to evaluate the effect of age and the level of sun exposure on skin surface structure (Gao, Hu et al. 2011). A higher number of grids was associated with a more intact skin structure. This study used an automated assessment of five parameters derived from the intersection of lines and textures on the skin surface. Three of these parameters, the difference between the angles, maximum angles and the distance between the primary lines, associated positively with the BG score. The other two parameters, the number of angles and grids, associated negatively with the BG score. In addition, these five parameters were compared to clinical information. There was a correlation between age, distance and grid structure, whilst maximum angle and angle difference correlated with sun exposure. The results of automated texture evaluation correlated with BG scores, however, the correlation was found only when considering only one texture parameter, while the BG system depends on many parameters to grade skin integrity (Gao, Hu et al. 2011).

Changes in skin surface texture are associated with skin aging, which can be caused by physiological aging or from environmental effects, or both (Gao, Yu et al. 2013). Results from a non-invasive method for analysing skin surface texture were compared to demographic factors and lifestyle of individuals. Different texture parameters were evaluated, including the angles formed by the intersection of the lines, the distance between the primary lines and the number of grids as well as BG scores. This analysis showed an association between the grading scores, age and sun exposure, and individuals with high grades were more likely to smoke and drink.

The correlation between the number of closed polygons (NCP) observed on the skin surface, and roughness parameters (smoothness, roughness, scaliness and wrinkles) with ageing has also been described (Trojahn, Dobos et al. 2014). In this article, three age

groups (children, teenagers and adults) were used to calculate the NCP and roughness parameters in volar forearm skin by three independent observers. Grayscale images were used in this study, taken by the use of a Visio Scan VC 98 device and the software SELS 2000 (Courage + Khazaka electronic GmbH, Cologne, Germany) to calculate the NCP and the roughness parameters. A negative correlation was found between NCP/mm² and age, while roughness parameters positively correlated with age. This article suggested that for a larger number of subjects an automated system for calculating the NCP was required, and also that replicates from other skin regions can improve analysis.

Another parameter S_{Pm}, defined as mean area of blocks of different shapes formed by the intersection of primary and secondary surface lines was described to assess skin topography (Zou, Song et al. 2009). The goal of this work was to evaluate skin ageing in healthy volunteers (without a history of smoking) using image processing techniques. Many different techniques were used, for instance a region growing algorithm was used to remove hair on the skin surface, followed by histogram equalization to reduce the effect of light variation in the image. Noise reduction and line detection were done using the watershed segmentation algorithm. The S_{Pm} was computed for all images of the dorsal and ventral hand and compared to age. A relationship was found between S_{Pm} values and age, with the value of S_{Pm} increasing in both dorsal and ventral skin in both male and females with time.

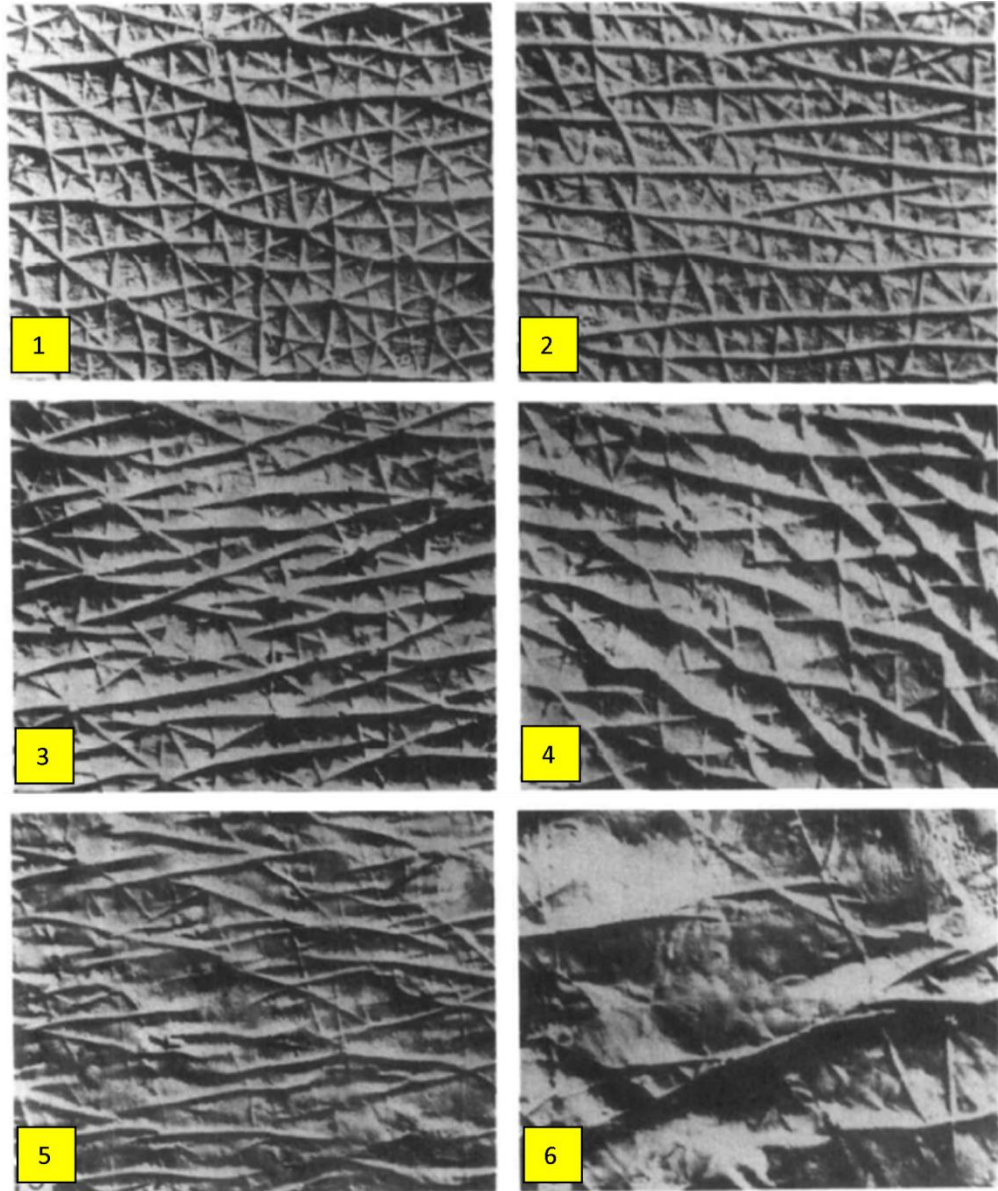


Figure 4. 1: Example images representing BG categories. (Seddon, Egan et al. 1992).

4.1.2.2 Computational Methods Exploiting Novel Features

A reliable skin topographic measurement that used a capacitive device to provide an absolute measure of skin surface structure was reported by Bevilacqua et al (Bevilacqua, Gherardi et al. 2006). The device captured details by direct contact with the skin using an active capacitive pixel

sensing technology, and this was compared to profilometric analysis of the surface topography from silicone moulds of the same region of the skin. The inter-wrinkle distance (IWD) represented the distance between two adjacent wrinkles in the images produced from capacitive device, and for the profilometer analysis, the darker pixels corresponded to wrinkles (Peaks) and brighter pixels to line depth (Valley shapes) in the skin tissue. The result of both methods showed high correlation, with $R^2=0.998$. However, the maximum depth that was detected with the capacitive device was limited, and both methods required expensive instruments.

4.2 Aims and Objectives

The aim of this Chapter was to extract skin surface texture information associated with chronological and photo-aging from a range of skin mould images.

To achieve this overall aim, I sought to address the following objectives:

- Explore appropriate automated image processing and analysis techniques
- Compare these techniques to the “gold-standard” BG scoring method
- Apply the optimal method to a range of skin mould samples
- Assess the correlation of clinical parameters, such as body mass index (BMI) and ageing, with texture measurements.

4.3 Towards Automatic Skin Texture Analysis

In this section, I describe the skin image impression database, and related clinical parameters of each individual to find the possible relationship between skin surface structure and clinical parameters such as BMI, age, waist-hip ratio, blood glucose and total freckles (kindly provided with permission by Dr Veronique Bataille of the TwinsUK Registry, King's College London). I shall describe the development of automated image analysis to evaluate any degradation in skin surface structure, and compare results with manual assessment using the BG scoring system.

4.3.1 Clinical Parameters and Skin Impression Moulds (TwinsUK Database)

The skin moulds and the clinical parameters that I have used were provided by TwinsUK, which is the biggest adult twins registry in the UK. It collects data to help researchers in the study of genetic and environmental effects, in ageing and disease. The database includes DNA profiles (which were not available for the individuals in this study), clinical data and questionnaires, used to estimate the genetic and environmental contribution to common conditions such as diabetes, osteoporosis and asthma by comparing the similarities and differences between the identical and non-identical twin pairs.

The TwinsUK skin topography dataset, contains over 300 silicon moulds from 157 individuals. Each individual has two moulds, one from the forehead, a sun exposed site, and one from the inner arm, a sun protected site. Associated clinical data is shown in Table 4.1. Note that the time of mould capture and clinical information varied between patients. Each mould was imaged with between 4 and 10 images captured per silicon mould using a standard Olympus dissecting binocular microscope under low magnification, equipped with a Nikon CCD camera and illuminated from above with a separate bright-field incident light source.

	<i>BMI</i>	<i>Age</i>	<i>Waist-Hip Ratio</i>	<i>Blood Glucose</i>	<i>Total Freckles</i>
Mean	25.1	52.9	0.7	4.8	37.2
Standard Error	0.4	0.5	0	0.07	4.8
Median	24	52.4	0.7	4.8	2
Mode	21.5	50.8	0.7	4.7	0
Standard Deviation	5.3	6.1	0.07	0.74	40.5
Sample Variance	28	37.3	0	0.55	164
Range	33.5	28	0.7	3.8	160
Minimum	18.1	40.6	0.6	2.6	0
Maximum	51.7	68.7	1.3	6.4	160

Table 4. 1: Clinical information from the TwinsUK phenotyping clinic.

4.3.2 Manual Analysis Using Beagley-Gibson Scoring

Before I discuss the automatic BG score-compatible texture analysis techniques developed herein, I discuss the performance of the manual BG scoring system. Skin mould images were graded using the BG system by two independent expert observers in the Institute for Translational Medicine at the University of Buckingham. The images were scored from 1 to 6, as standard. The result of BG scoring can be used as a baseline for automated skin mould analysis. The final score for each image was averaged for each observer, and then the 4-10 images scores were averaged for each silicon mould.

The effectiveness of the BG scoring system was analysed using Cohen’s kappa calculation to look at inter-observer reliability, which shows the degree of agreement ranging from 0 to 1, with 0 indicating perfect disagreement and 1 is perfect agreement. The Cohen’s Kappa was 0.229 as shown in Table 4.2, which suggests a poor agreement between observers, and the correlation for observer scoring of all images is shown in Figure 4.2. However, when I separated the silicon moulds into different sites, sun protected and sun exposed, there were a higher level of agreement in face skin moulds (0.48; Table 4.3) than arm skin moulds (0.229; Table 4.4), and the correlation is shown in Figure 4.3 and 4.5. This indicates that the scoring process is easier and more reliable for sun exposed skin using the BG scoring system than in sun protected skin.

Chapter 5

Linear regression was performed for each image of the skin moulds, and a slope of best-fit value of 0.886 ± 0.011 was determined, with an R^2 of 0.776, $p < 0.0001$ (Figure 4.2a). However, when the values for each patient were averaged from each observer and then linear regression, performed a slope of best-fit value of 0.918 ± 0.025 was determined, with an R^2 of 0.818, $p < 0.0001$ (Figure 4.2b).

For sun exposed skin sites, the values for each patient were averaged from each observer and then linear regression performed, a slope of best-fit value of 0.265 ± 0.066 was determined with an R^2 of 0.097, $p < 0.0001$ as shown in Figure 4.3b. For each individual image of sun protected side, I performed linear regression and determined a slope of best-fit value of 1.34 ± 0.042 , with an R^2 of 0.527, $p < 0.0001$. Figure 4.4a illustrates this correlation, when the values for each patient were averaged from each observer and then linear regression performed, a slope of best-fit value of 1.587 ± 0.099 was determined with an R^2 of 0.637, $p < 0.0001$ as shown in Figure 4.4b.

		Observer 1						Total
		1	2	3	4	5	6	
Observer 2	1	126	24	26	3	0	0	179
	2	97	78	203	122	12	0	512
	3	0	0	15	92	102	4	213
	4	0	0	2	8	52	19	81
	5	0	0	0	19	98	395	512
	6	0	0	0	3	16	341	360
Total		223	102	246	247	280	759	1857

Cohen's Kappa	0.229
Std Error	0.013

Table 4. 2: Matrix of scores and calculation of Cohen's kappa for all images.

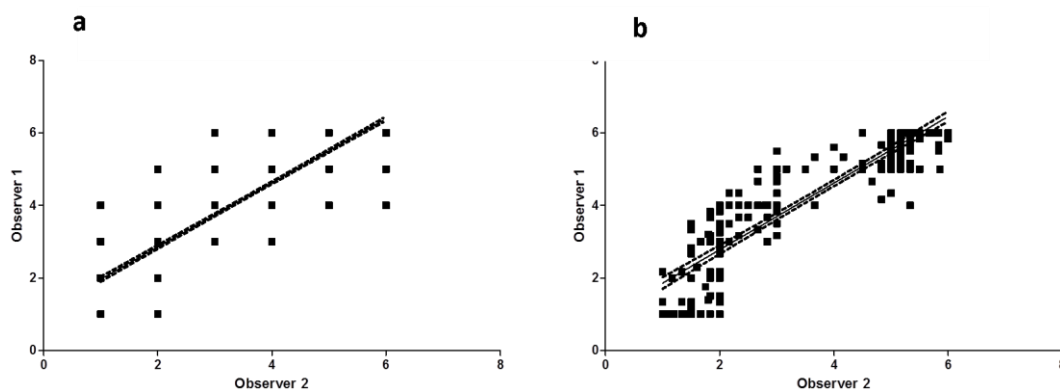


Figure 4. 2: Correlation of observer scoring for all images using BG score. a) correlation between two observers for each individual image score, b) correlation of the average of scores for each individual by both observers.

		Observer 1						Total
		1	2	3	4	5	6	
Observer 2	1	0	0	0	0	0	0	0
	2	0	1	0	0	2	0	3
	3	0	0	0	0	9	1	10
	4	0	0	0	2	24	17	43
	5	0	0	0	19	98	395	512
	6	0	0	0	3	16	341	360
Total		0	1	0	24	149	754	928

Cohen's Kappa	0.48
Std Error	0.016

Table 4. 3: Matrix of scores and calculation of Cohen’s kappa for sun exposed silicone mould images.

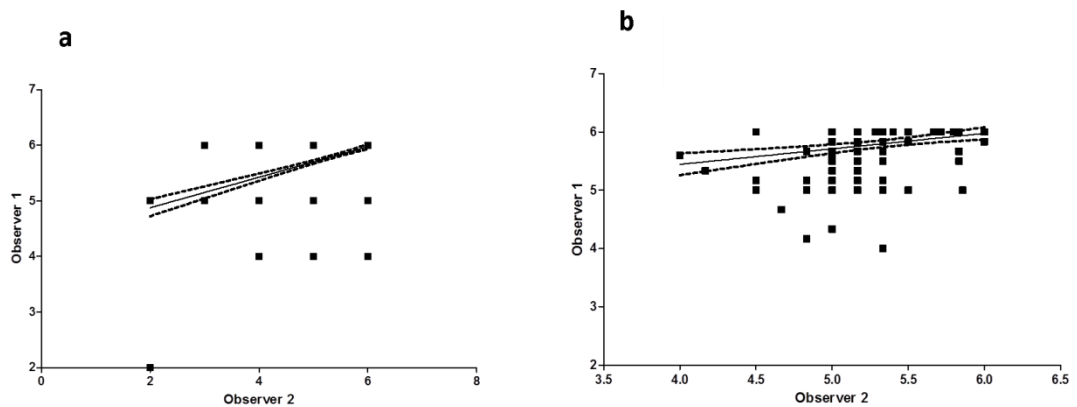


Figure 4. 3: Correlation of observer scoring in images of silicone moulds from sun exposed skin. Individual images (a) and the average score of each patient (b).

		Observer 1						Total
		1	2	3	4	5	6	
Observer 2	1	126	24	26	3	0	0	126
	2	97	77	203	122	10	0	509
	3	0	0	15	92	93	3	203
	4	0	0	2	6	28	2	38
	5	0	0	0	0	0	0	0
	6	0	0	0	0	0	0	0
Total		223	101	246	223	131	5	929

Cohen's Kappa	0.215
Std Error	0.015

Table 4. 4: Matrix of scores and calculation of Cohen’s kappa for sun protected silicone mould images.

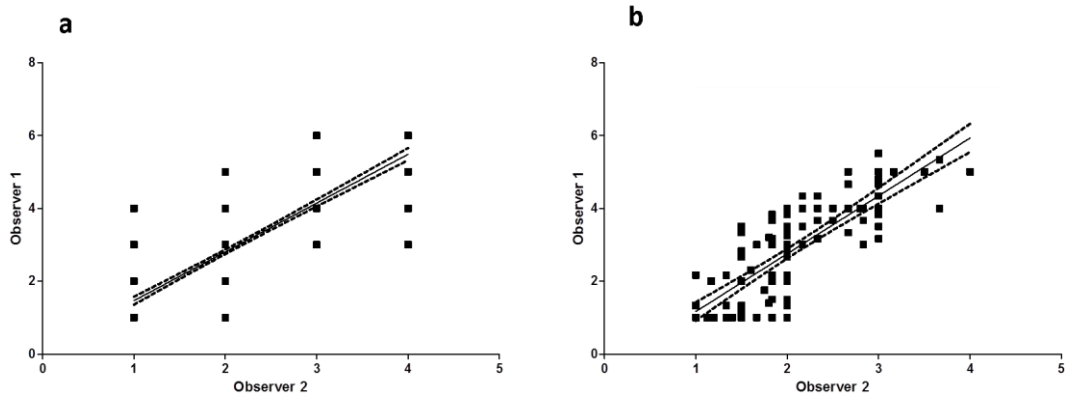


Figure 4. 4: Correlation of observer scoring in images of silicon moulds from sun protected skin. Individual images (a), and the mean score of each patient mould skin images (b).

4.3.3 Methods

Image texture provides important information about the spatial arrangement of variations in intensity and colour across images. These variations in colour and intensity represent the smoothness and coarseness of any surface. The texture from one skin surface is different to another in term of roughness, smoothness, lines and the difference from high to low points, and the space between these points (Gherardi 2008). Skin texture could be affected by many factors such diet, age, environmental effects and treatments (Sparavigna and Marazzato 2010). For example, with age skin becomes thinner with the appearance of wrinkles due to the deterioration of ECM caused by reduced production of collagen and elastic fibres by fibroblasts (Lagarde, Rouvrais et al. 2005). There are many different methods to extract textural information in an image. Which method to use, depends on the variation of the texture dimension. There are statistical-based approaches to extract the statistical texture characteristics. Transform-based methods provide another approach, such as Gabor transformation as described in Chapter 2. Structure-based texture analysis is uses the lines and shapes in the image, which provides an important description of image texture (Materka and Strzelecki 1998).

In this thesis, I describe automatic image-based skin surface structure analysis schemes that are compatible with BG scoring. My schemes are based on texture pattern recognition and use two steps: feature extraction and classification.

a) Feature Extraction

There are two categories of image texture related features that will be used in my work, together with various combinations of these categories. The first category is based on the use of Local Binary Patterns (LBP), which captures local texture in terms of variations in pixel values, and it may be extracted in different ways depending on neighbourhood window size, and on regional partitioning of images. The second category is the Gray Level Co-occurrence Matrix (GLCM), which is a common technique in pattern recognition to overcome the effect of variation in the distribution of illumination in texture parameters. GLCM is related to the distribution of repeated patterns of neighbouring gray values. The various features (i.e. parameters) for each of these two categories are describe in sections 4.4 and 4.5, respectively. The feature

extraction experiments in this thesis are described in the corresponding method development section.

b) Classification

Feature extraction steps result in feature vector representations of input images, for which the pattern recognition literature includes a variety of classifiers. Herein, I shall mainly use the Support Vector Machine (SVM) classifier for skin mould image classification, following different feature extraction techniques. I shall also use a kNN classifier for comparison with SVM in terms of performance.

SVM classification works by selecting 500 random samples of arm skin and 500 samples from face. The classification process starts by selecting one sample from each site as data testing, and compares this with the rest of the images, which act as training data, for all 500 samples. From each SVM classification, a score of the classification was found by finding the distance of the feature vector of the sample from the hyper-plane of the SVM by *eq. 4.1* (Cristianini and Shawe-Taylor 2000). Figure 4.5 shows the SVM hyper-plane, and the support vector example.

$$score = \sum_{i=0}^n \alpha_i k(V_i, x_1) + b \quad (eq4.1)$$

Where V is the support vectors set, n is the size of V , α is the alpha weights of V , K is a kernel function (a dot product $\langle V_i, x_1 \rangle$ in this case) and b is the bias.

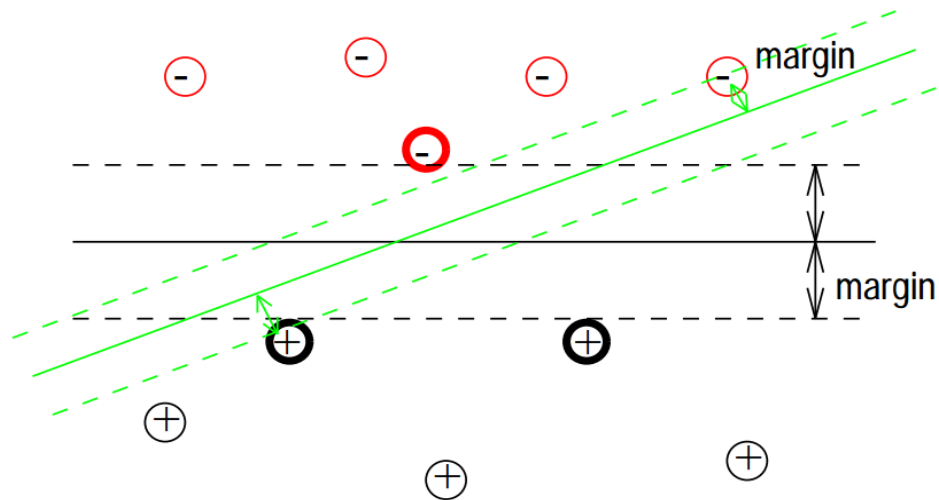


Figure 4. 5: Example of an SVM classifier with an optimal hyper-plane between the two classes of support vectors. The red vectors represent arm skin mould images, and black vectors represent face skin mould images. The hyper-plane separates the two classes after finding the optimal line between them.

The another Classifier is the k-nearest neighbour (k-NN), which works on the same number of random samples (as used in SVM classifier) to compute dissimilarity between the test and training samples for all data sets by measuring the Euclidean distance using equation eq4.2.

$$d(x, y) = \sqrt{\sum_{i=1}^n (x_i - y_i)^2} \quad \text{eq 4.2}$$

The idea in k-NN classification is to identify k samples in the training set whose independent variables (x) are similar to (y).

With this classifier, I have classified the images into two classes when $k = 3$. The result of classification compared to SVM classifier result, kNN classifier was not effective as much as the SVM in term of classification accuracy result to classify two classes of skin mould images.

4.4 Local Binary Pattern of Image-based Texture Analysis

The first proposed category of texture-based analysis uses the Local Binary Pattern (LBP) of the original image applied in different ways. LBP provides discriminating texture information with invariant against monotonic grey level changes and its implementation is computationally simple (Ojala, Pietikainen et al. 2002). Figure 4.6 shows the process of calculating LBP for one pixel and Figure 4.7 shows the result of calculating the LBP for the whole image for two different LBP window sizes, different window sizes are shown in figure 4.8a and 4.9b.

The value of the LBP of the centre pixel (x_c, y_c) is calculated by:

$$LBP_{P,R} = \sum_{p=0}^{P-1} s(g_p - g_c)2^p \tag{eq 4.3}$$

Where the g_p and g_c are the grey values of the neighbouring pixels and the centre pixel respectively, and $s(x)$ is described as:

$$s(x) = \begin{cases} 1, & \text{if } x \geq 0; \\ 0, & \text{otherwise.} \end{cases}$$

The process of LBP-based score analysis starts with creating an LBP image from the original skin mould image. The resulting intensity histogram of the LBP image was used in SVM classification.

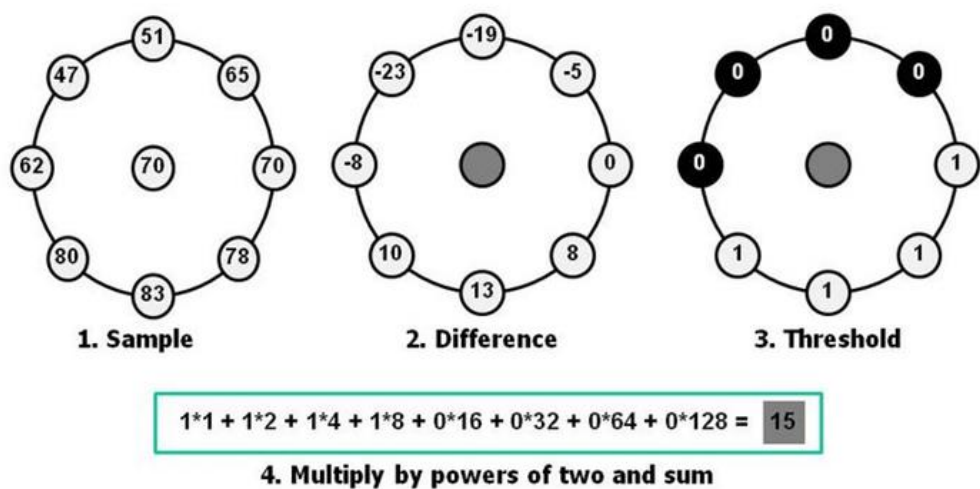


Figure 4. 6: Calculation of the LBP value for each pixel. 1) sample block containing the centre pixel and 8 surrounding pixels, 2) result of $g_p - g_c$ for each of the 8 neighbour pixels, 3) if the value of the result ≥ 0 , then the result of function $s(x)$ is 1, otherwise it is 0, 4) the output binary patterns added together (Pietikäinen, Hadid et al. 2011).

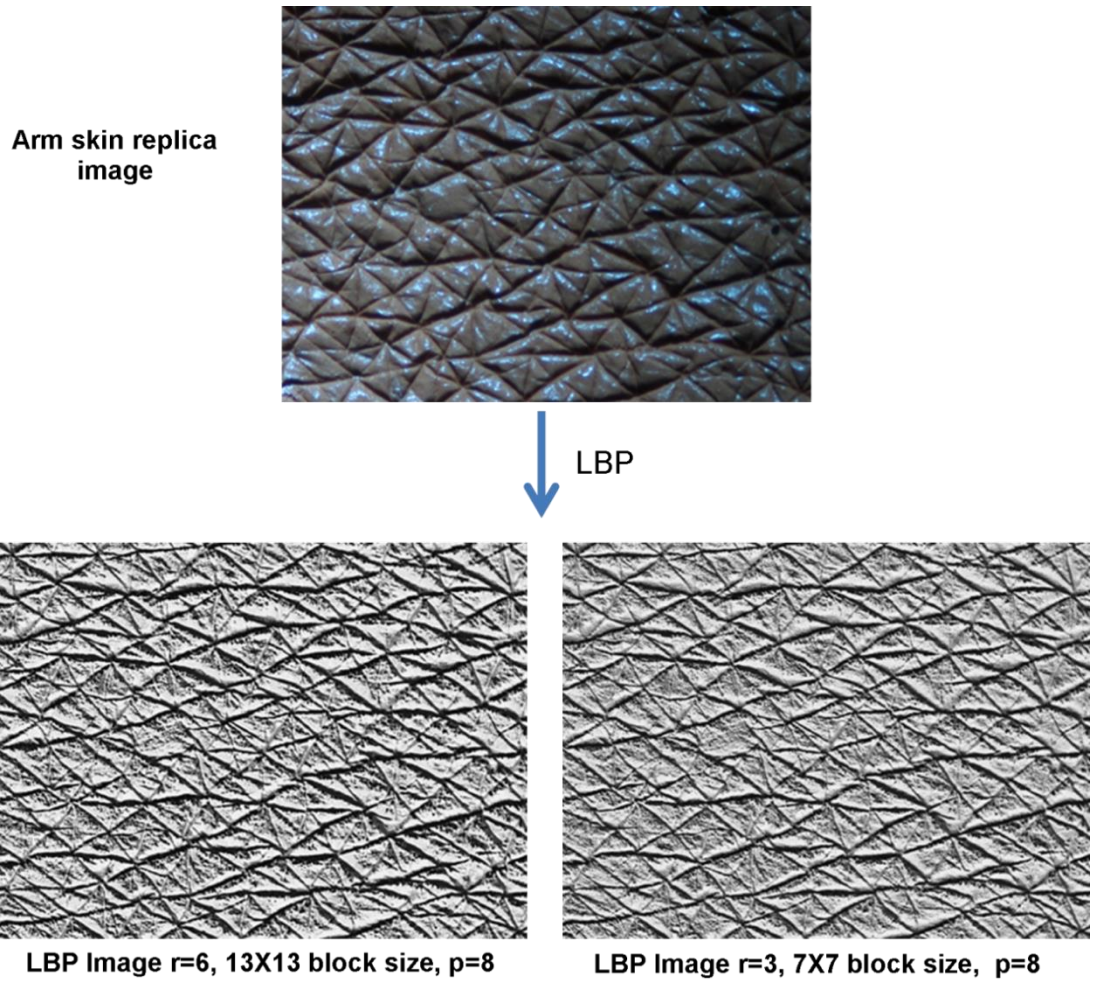


Figure 4. 7: LBP transformation outputs. Original skin mould image (top) and LBP image (bottom-left) from calculating a LBP value with 8 neighbor pixels ($r=6$, block size is 13×13), and bottom-right LBP when $r=3$ and the block size is 7×7 .

4.4.1 Evaluation and Results of LBP 3rd Neighbour Pixel Calculation

The first method for texture-based analysis using LBP was done by using 8 neighbour pixels with $r=3$ from the centre pixel of each block of the skin mould images (Figure 4.8a). The feature was extracted from each image in the data set by calculating the histogram of the LBP image and the number of pixels in each intensity value in the histogram, which was saved in a vector to represent the image in the classification step.

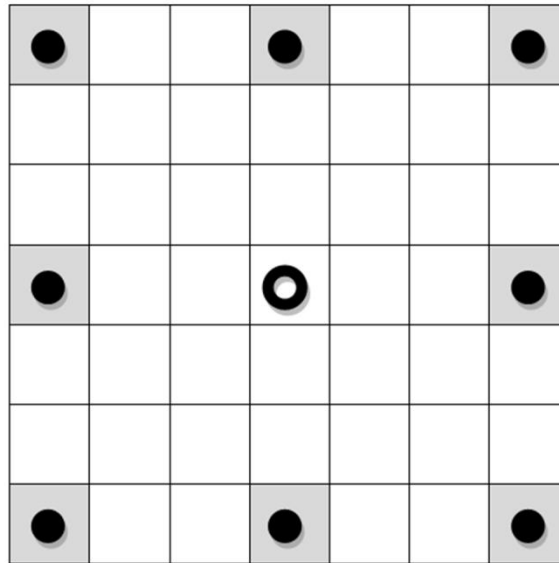
All vectors (representing all images) were classified using SVM (as described in section 4.3.2b) and the accuracy of the classification (97.52) with respect to negative class identification (sensitivity, 97.81) and positive class identification (specificity, 97.22) was found as shown in Table 4.6 in section 4.7. By applying the SVM to my two classes of images, the mean SVM scores was calculated for each individual from the median of scores of multiple images, and then correlated with BG scores. The correlation was with linear regression of 0.823, as illustrated in the Figure 4.8b.

4.4.2 Evaluation and Results of LBP 6th Neighbour Pixel Calculation

In the second method, the LBP was calculated in all skin mould images in the data set, but this time the selected block size for the calculation was 13×13 . In this experiment, the 8 neighbour pixels with $r=6$ distance from the centre pixel were selected to generate the LBP image, and the one block example is shown in the Figure 4.9a. Selecting the 6th pixels from the centre of the block was due to edge preservation of the lines of interest in the image, as shown in Figure 4.7.

The result of SVM scores was averaged for each individual, and correlated with BG scores, and the linear regression was found to be 0.8247 (Figure 4.9b). This shows that selecting a block size of 13×13 for the LBP calculation achieves higher accuracy in classifying my two classes of arm (sun protected) and face (sun exposed) images, and higher correlation with the BG score. The accuracy of the classification was (98.84), sensitivity (99.12) and specificity (98.57), as shown in Table 4.6 in section 4.7.

a



b

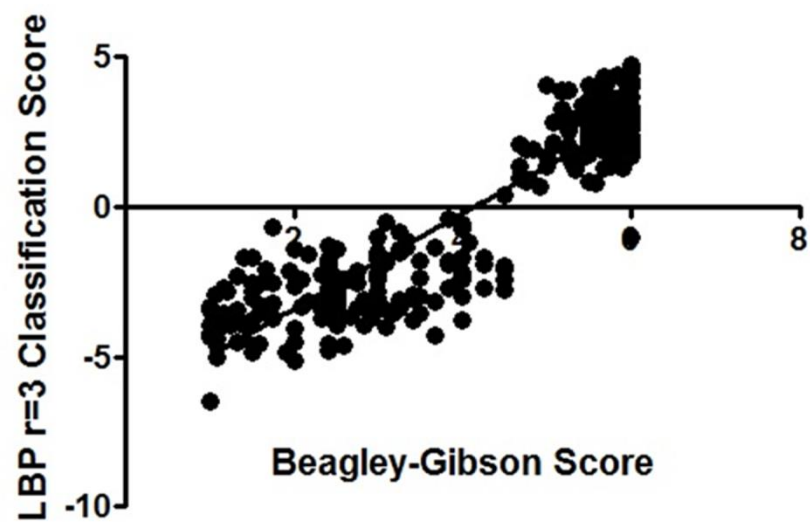
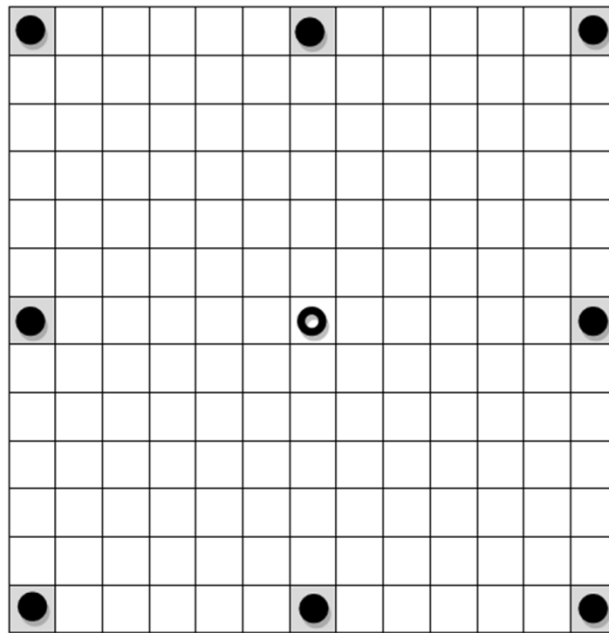


Figure 4. 8: Texture based analysis using 3rd LBP neighbourhood. a) example of the 3rd LBP neighbourhood of 8 neighbouring pixels in 7×7 window size, b) comparison with BG scores.

a



b

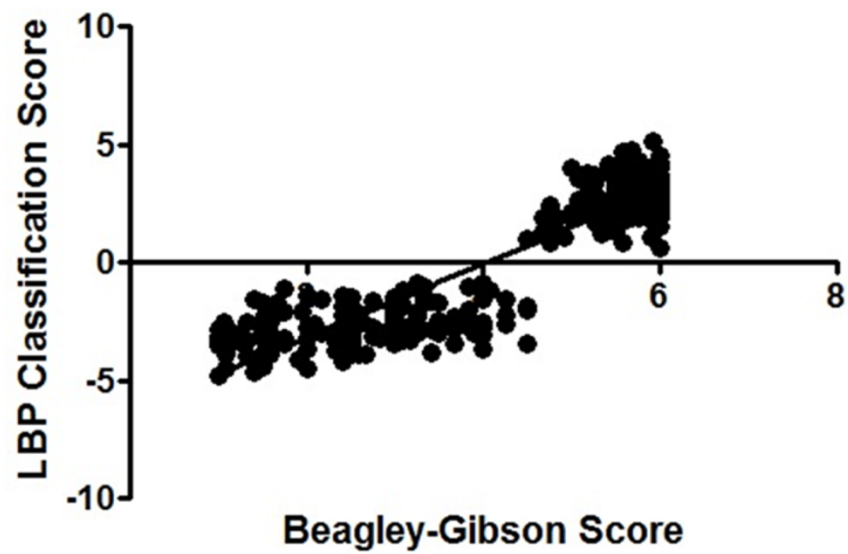


Figure 4. 9: Texture based analysis using 6th LBP neighbourhood. a) example of the 6th LBP neighborhood of 8 neighbouring pixels in 13×13 window size, b) comparison with BG scores.

4.4.3 A Block-based LBP Approach

The third method utilising LBP begins by dividing the LBP image into 4 blocks, and histogram features were extracted from each block. These features were concatenated into a vector prior to classification (Figure 4.10). This was attempted due to variations in illumination by capturing the skin mould impression images, and blurring in different regions of the image, which potentially affect feature extraction.

Results of the SVM classifier were found and correlation with BG scores was computed. Figure 4.11 shows this correlation with a linear regression=0.763. The accuracy of the classification was (98.46), sensitivity (98.40) and specificity (98.53). The accuracy was lower than the use of previous method in section 4.4.2 as shown in Table 4.6 in section 4.5.6, this was due to the variation in illumination in different regions of the image, however, LBP image were consistent in term of distribution of the overall texture in the image, the problem of variation illumination and blurring were solved by calculating LBP of original image.

Thus, dividing the LBP image into 4 blocks didn't improve classification accuracy, moreover, the correlation with BG scoring decreased. As this approach did not improve classification, this indicates that LBP calculation of the whole image as one block was able to handle variations in image brightness.

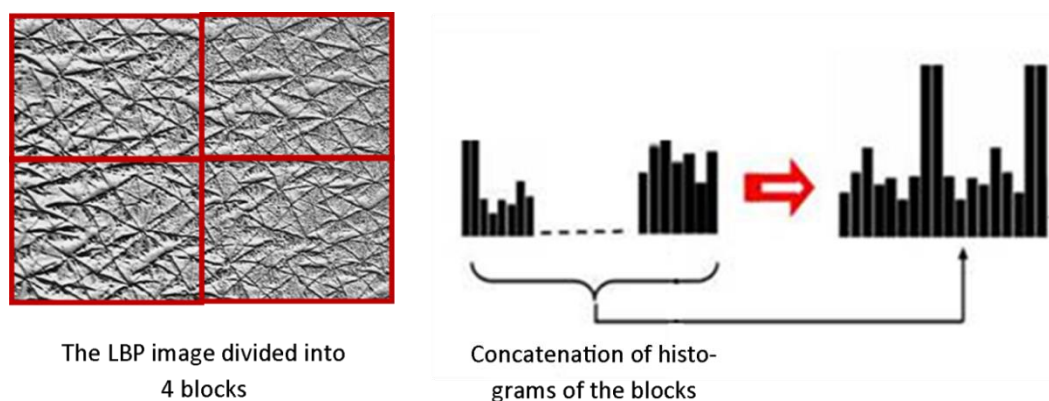


Figure 4. 10: Block-based LBP feature extraction. Typical image divided into 4 blocks (left panel), associated histograms (centre panel) and results of concatenation (right panel).

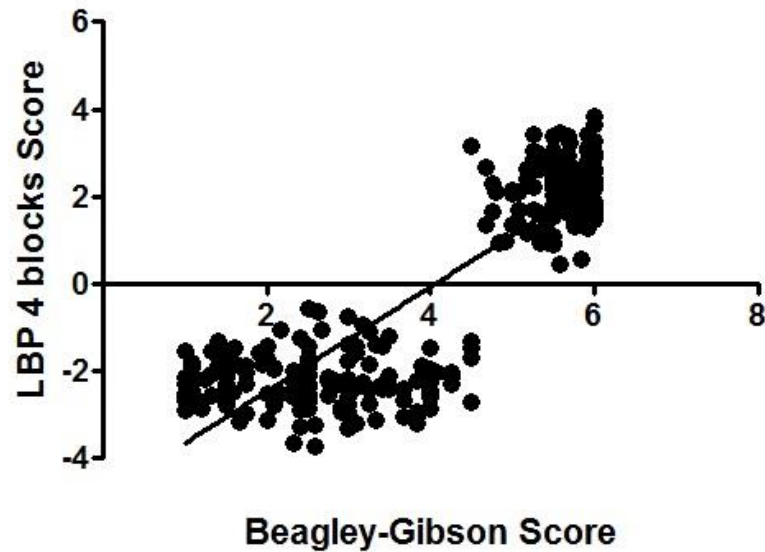


Figure 4. 11: Comparison of LBP using 4 blocks with radius=6 with BG Scores.

4.4.4 The Uniform LBP Approach

The fourth method used was the analysis of uniform LBP images ($r = 3$) that reduce the features and detect uniform local binary pattern to investigate if there is improvement in texture detection. Binary patterns in the LBP calculation were produced by applying LBP operators containing different bit strings in 0 and 1 form. To produce the uniform LBP, the binary pattern should not contain more than two bitwise transitions from 0 to 1 or vice versa, e.g. the value 10111011 has four transition (Wang, Mu et al. 2008). By computing the histogram in uniform LBP, all binary patterns that have more than two transitions (i.e. a non-uniform pattern) will localize in the 59th bin of the histogram, and the other uniform patterns in the histogram will localize in bins 1-58. SVM classification scores in this experiment were computed by classifying the uniform LBP images by taking each histogram as a vector, and each vector was classified as one of my two classes (arm or face). SVM classification was compared to BG scoring (Figure 4.12), and the accuracy of the classification (96.40), sensitivity (96.81) and specificity (96.00) were determined, and the comparison with other method is shown in Table 4.6 in section 4.7.

Chapter 5

I found lower accuracy compared to using LBP images with all binary patterns. This was likely to be due to the loss of texture information by using only uniform binary patterns. However, the correlation achieved with this method was high ($R^2=0.834$), but this didn't necessarily indicate better classification, as the accuracy, sensitivity and specificity were lower than with the use of LBP with $r=6$. Low classification accuracy indicates the loss of the information, particularly information that represents the space between the lines on the skin surface, which might have been localized in the 59th bin of the histogram.

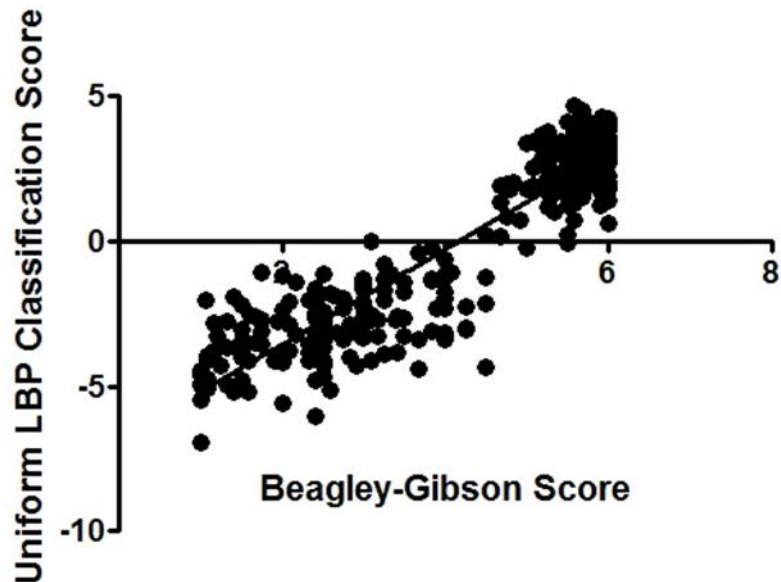


Figure 4. 12: Comparison of uniform LBP with radius = 6 performance with BG scores.

4.5 Grey Level Co-occurrence Matrix (GLCM) Feature-based Analysis

The second general skin mould texture-based analysis method utilised a Gray Level Co-occurrence Matrix (GLCM), which is widely used in image texture measurements. GLCM estimates image properties related to second-order statistics, and shows the relationship between two neighbouring pixels, and how different groups of pixel values occur in that image, these relationships illustrated in Figure 4.13 (Haralick, Shanmugam et al. 1973; Kumar 2013). The proposed method for classifying skin mould was done by creating a GLCM for each image, and the relationship between pixels was found in four directions (horizontal $p(i; j; d; 0^\circ)$, vertical $p(i; j; d; 90^\circ)$, left $p(i; j; d; 135^\circ)$ and right diagonal $p(i; j; d; 45^\circ)$), as illustrated in Figure 4.14. Texture features were calculated by averaging over the four direction co-occurrence matrices, and were compared with texture features found in other images to classify skin moulds into two different classes using the SVM classifier.

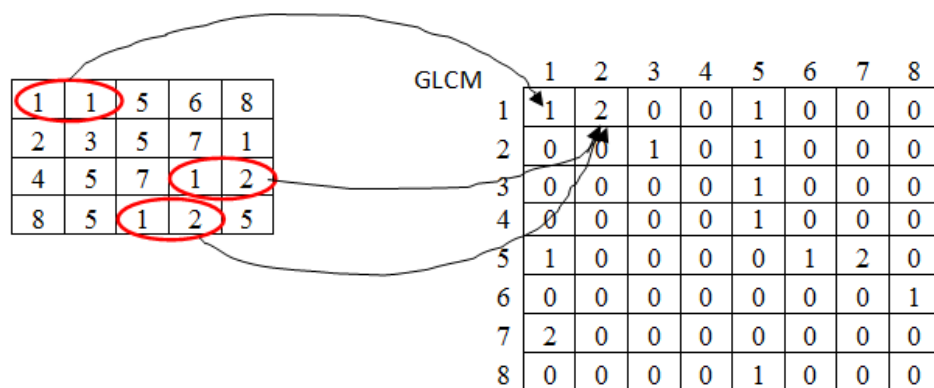


Figure 4. 13: GLCM analysis. a) 4X5 matrix of intensities ranging from 1-8, b) an example of the GLCM, and the relationship between two pixels in one direction.

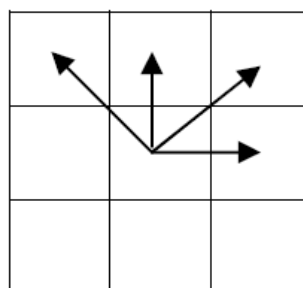


Figure 4. 14: Four directions for finding the relationship between pixels to calculate texture features.

4.5.1 Calculating the GLCM of the Original Training Skin Mould Images

The fifth specific method for analysing skin topography was achieved by creating the GLCM for each skin impression image of arm and the face skin, and extracting 14 features from the five statistical measurements (contrast, correlation, homogeneity, entropy and energy) of the GLCM in four directions (Elshinawy and Adviser-Chouikha 2010; Zulpe and Pawar 2012), and then the result of all directions was averaged for each of the 14 features.

The five statistical measurements used for feature extraction in the GLCM are listed below with their equations:

- **Contrast:** calculates the local variations in the *GLCM* by:

$$cont = \sum_{i,j} |i - j|^2 p(i,j) \quad (eq4.4)$$

- **Correlation:** calculates the joint probability occurrence of the specified pixel pairs by:

$$corr = \sum_{i,j} \frac{(i - \mu_i)(j - \mu_j)p(i,j)}{\sigma_i \sigma_j} \quad (eq4.5)$$

- **Homogeneity:** calculates the close values on the main diagonal of the matrix by:

$$Hom = \sum_{i,j} \frac{p(i,j)}{1 + |i,j|} \quad (eq4.6)$$

- **Entropy:** calculates the certainty in the co-occurrence matrix by:

$$Entropy = \sum -p(x_i) \log p(x_i) \quad (eq4.7)$$

- **Energy:** measures the uniformity that is equal to the sum of squared elements in the co-occurrence matrix, calculated by:

$$Energy = \sum_{i,j} p(i,j)^2 \quad (eq4.8)$$

Chapter 5

The previous five statistical measurements along with the following features were calculated for each image, and used in the classification step:

- *Sum of average*
- *Sum variance*
- *Information measure of correlation1*
- *Information measure of correlation2*
- *Maximum probability*
- *Sum of entropy*
- *Sum of squares*
- *Inverse difference moment*
- *Difference entropy*

The flow chart in Figure 4.15 illustrates the methodology of this texture-based analysis using the GLCM that starts with calculation of the GLCM of the whole image as one block, followed by feature extraction.



Figure 4. 15: Illustration of the methodology of GLCM texture based analysis.

For each image, 14 features were generated to create a vector that represents the image, and then the vector was compared to other images in the SVM classifier. An example of the vectors with corresponding images is illustrated in Figure 4.16 for arm and face skin mould impression images.



	F1	F2	F3	F4	F5	F6	F7	F8	F9	F10	F11	F12	F13	F14
Arm 1	12.3	0.99	0.47	96.4	11294	6.98	-0.48	0.99	0.01	5.29	0.012	3074	0.403	17.6
Arm 2	13.7	0.99	0.45	100	11922	7.07	-0.47	0.99	0.009	5.32	0.011	3242	0.390	19.2
Face 1	6.7	0.98	0.48	98.4	9946	6.53	-0.46	0.99	0.015	4.94	0.016	2725	0.415	11.4
Face 2	8.7	0.98	0.46	102	10900	6.64	-0.44	0.98	0.014	4.96	0.016	2975	0.391	13.9

Figure 4. 16: Fourteen feature measurements from twins from the training data set for arm and face skin images.

Where F1-F14 are defined as below:

- F1= Contrast*
- F2= Correlation*
- F3= Homogeneity*
- F4= Sum average*
- F5= Sum variance*
- F6= Entropy*
- F7= Information measure of correlation1*
- F8= Information measure of correlation2*
- F9= Maximum probability*
- F10= Sum of entropy*
- F11= Angular second moment*
- F12= Sum of squares*
- F13= Inverse difference moment*
- F14= Difference entropy*

4.5.2 Evaluation of GLCM of Whole Images

SVM classification was used to grade images. The median result from different images of the same skin mould was calculated, and then the mean was used to find the correlation between the result from the automated method and the BG score ($R^2=0.6024$; Figure 4.17). The accuracy of classification (69.51), sensitivity (96.54) and specificity (42.48), this compared to other methods as shown in Table 4.6 in section 4.7. The linear regression of this method with BG values was lower than with LBP-based analysis, and the accuracy of the SVM classifier also was lower than using LBP images to classify arm and face skin images.

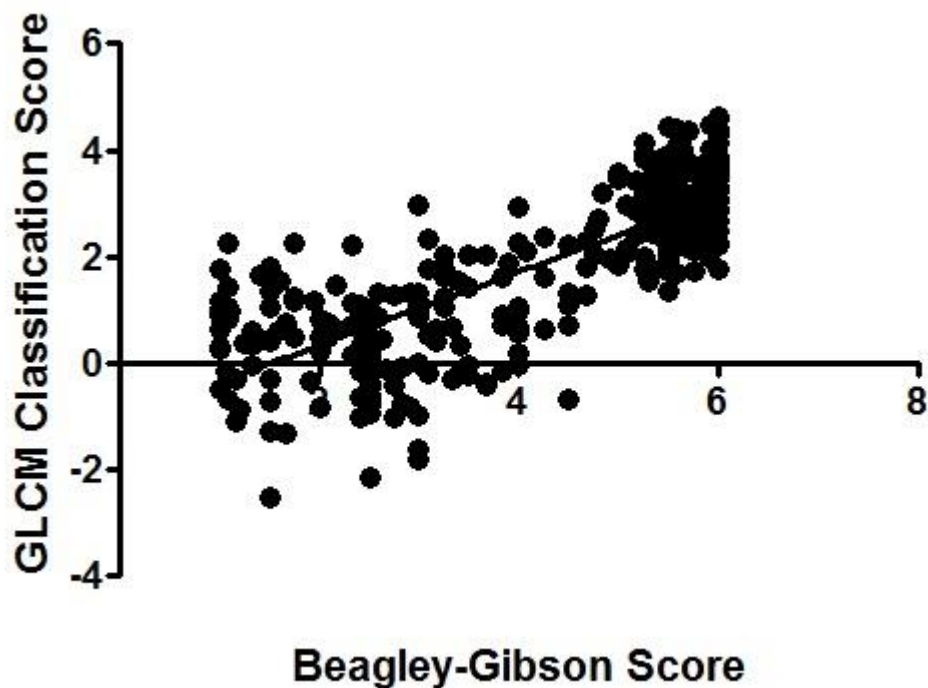


Figure 4. 17: Comparison of GLCM grading scores with BG scores.

4.5.3 Evaluation of GLCM of LBP Images

GLCM was applied to LBP images of the whole data set. After calculating the LBP for skin impression images, as described above, a GLCM was created from LBP images. The 14 features were extracted and then classified using SVM. The scores from this process were correlated with BG scoring (Figure 4.18), however, linear regression ($R^2 = 0.7316$) showed lower correlation than with previous methods, and the GLCM of the LBP image has more information to assess the structure of the skin mould images. Accuracy of the classification was (94.14), sensitivity (94.73) and specificity (93.54), which compared to result of other experiments as shown in the Table 4.6 in section 4.7, revealing the inefficiency of the GLCM-based method in classifying arm and face skin images in my dataset.

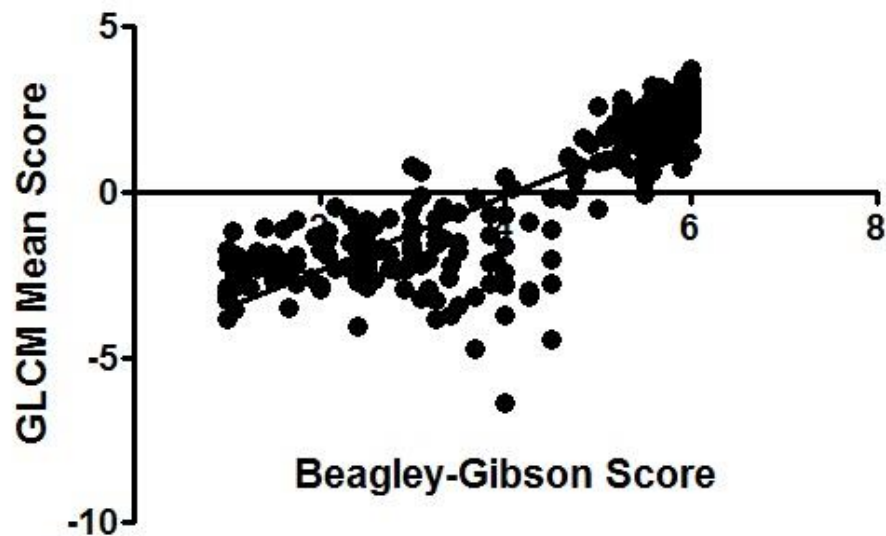


Figure 4. 18: Comparison of GLCM of LBP image grading scores with BG scores.

4.6 Development of Structure-based Analysis

The texture of skin mould images is composed of well-defined elements, e.g. the arrangement of lines, and the polygonal shapes and angles created by line intersections (Seddon, Egan et al. 1992; Gao, Hu et al. 2011). In structure-based analysis, I tried to extract most of the structural information that reflect the level of damage that is known to be caused by environmental effects and diseases.

4.6.1 Feature Extraction from Skeletonized LBP Images

From the promising results of feature extraction with LBP, I thought about combining the LBP technique with a mathematical morphology process, such as skeletonization, to extract the lines and polygon shapes in the skin mould images. I used a structure-based skeletonized LBP image analysis to assess alteration in texture.

LBP images were created from original skin mould images as described in section 4.4, and then the LBP image was transformed into its binary form. In this step, the advantages of using LBP images are the reduction of the effect of illumination and blurring in different regions of original images, as described in the Figure 4.19. The reason for transforming the LBP image into its binary form is to facilitate the extraction of structure information (Figure 4.20a). The next step was the use of a skeletonization technique, applied to the binary image, and this was followed by a pruning process to remove unnecessary short branches, before taking the inverse of the resulting skeleton image as illustrated in Figure 4.20c. In Figure 4.21, I have shown inverse skeletonized images of typical arm (Figure 4.21a and b), and face skin mould images (Figure 4.21c and d). The whole process of structure-based analysis is illustrated in the flow chart in Figure 4.20.

The size and number of polygons was quantified to represent the extent of the flattened area of the skin surface. According to the BG scoring system (Seddon, Egan et al. 1992), larger flattened areas represent a higher level of damage, and the skeletonised image was transformed to its negative to facilitate quantification (Figure 4.20c).

Chapter 5

For each inverse skeletonized image, eight measurements were calculated to describe the structure (features) in each image, as described below:

1. The ratio of the polygonal area to the total image area (**RatioTotalArea**).
2. The total number of the shapes in the image (**ShapeNum**).
3. Difference of the maximum area and minimum area of the shapes (**AreaDiff**).

$$Da = \text{Maximum area} - \text{minimum area}.$$

4. Number of polygons those have area less than 4* standard deviations (STD) from mean area of all the polygons in the image (**CloseArea**).
5. The means area of polygons those have area <4* STD (**CloseAreaMean**).
6. Difference of the maximum line distance and minimum line distance in the whole image (**DisDiff**).
7. Number of lines those have length less than 4 standard deviations (<4* STD) of length of all lines overall the image (**CloseDis**).
8. The mean distance of the lines that are smaller than 4* STD (**ClosDisMean**).

For each image, a vector of the eight parameters was used in the classification stage, and an example is shown in Table 4.5. SVM scores represent the distance of the vector from the SVM hyper-line between the two classes of the sun exposed and sun protected skin as described in section 4.3.3b. Skin impressions were graded according to SVM score, the smallest value representing least damage and the largest values the most damage.

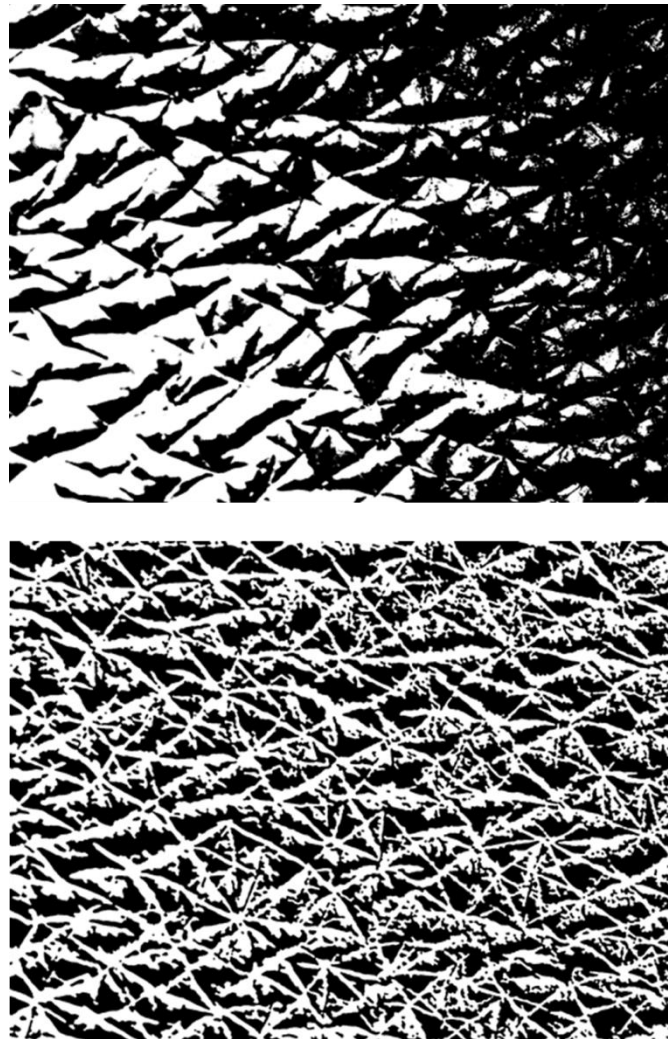


Figure 4. 19: Difference between the binary of the original image without LBP transformation. (top panel) and the binary image from the LBP image (lower panel).

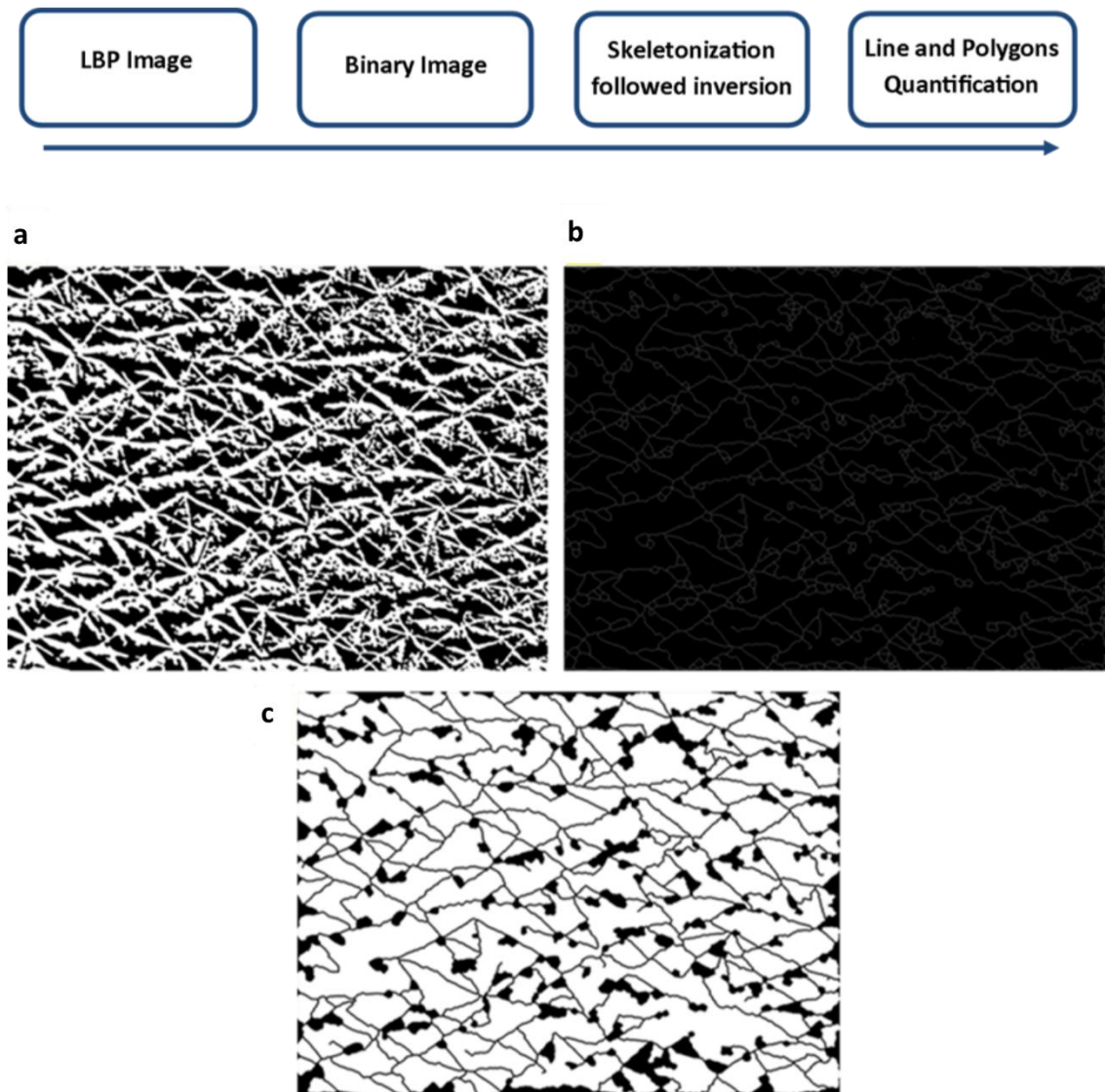


Figure 4. 20: Overview of the structure- based analysis process. A flow diagram is shown in the top panel. a) binary LBP image, (b) skeleton of the binary image, (c) the inverse image of the skeleton with artefact removal .

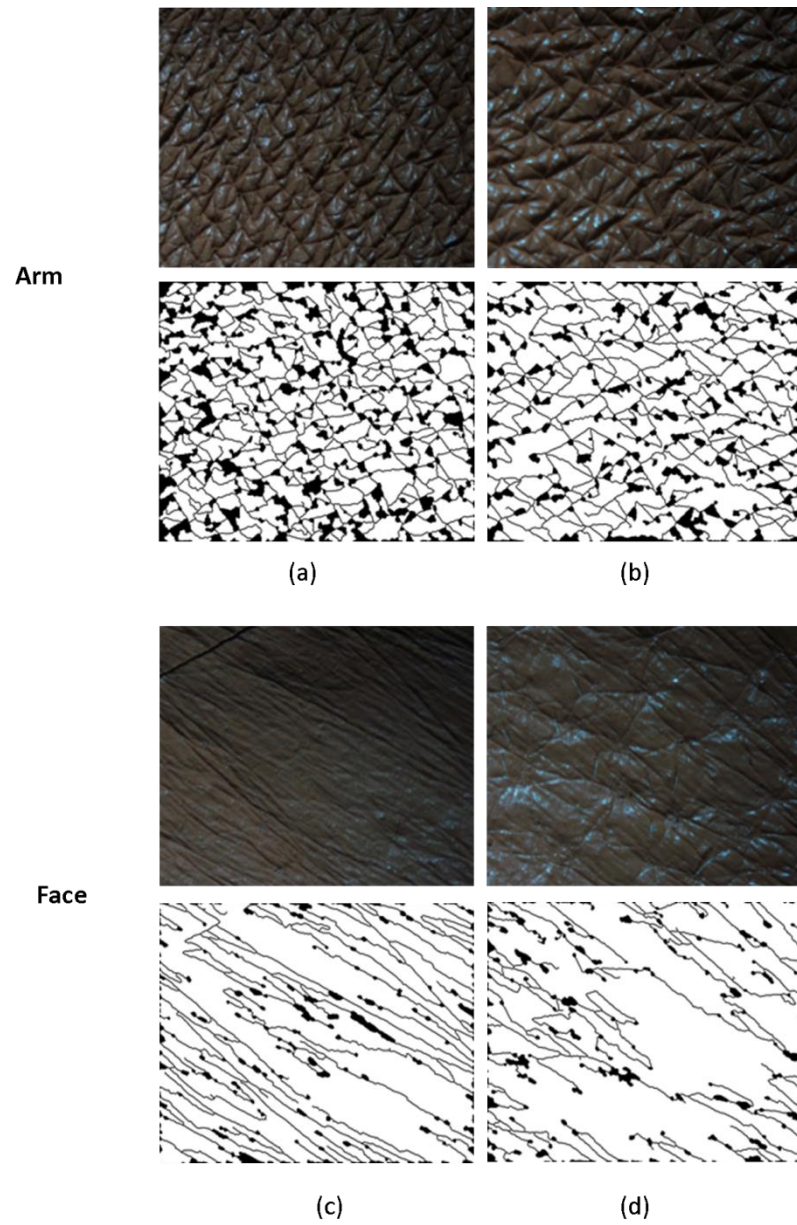


Figure 4. 21: Inverse skeletonised images of arm and face. (a,b) arm skin mould images and associated inverse skeleton images, (c, d) face skin mould images and associated inverse skeleton images.

Image	RatioTotalArea	ShapeNum	AreaDiff	CloseArea	CloseAreaMean	DisDiff	CloseDis	ClosDisMean
1	0.81	134	239298	50	46372	350.72	75	122
2	0.84	146	303700	74	37795	419.32	101	119
3	0.85	119	174044	57	44017	332.02	89	117
4	0.85	146	169252	69	41468	242.12	98	104
5	0.86	99	367930	51	61713	358.45	63	127
6	0.85	123	706681	63	46392	1364.8	83	118
7	0.86	103	323992	50	59651	360.24	61	124

Table 4. 5: Typical structural information from 8 measurements extracted from images of the arm and face.

4.6.2 Structure-based Analysis using LBP (3rd Neighbour Pixel)

The LBP was computed for the all images using $r=3$, binarised and then skeletonised as illustrated in figure 4.18. The result of classification of the extracted features of all LBP images acquired using 7×7 blocks to compute LBP (Accuracy of the classification was (91.72), sensitivity (93.06) and specificity (90.38)), this was compared to result of BG scores. Correlation with $R^2= 0.826$ was found as shown in figure 4.22. This method, therefore, showed a high correlation with BG scores.

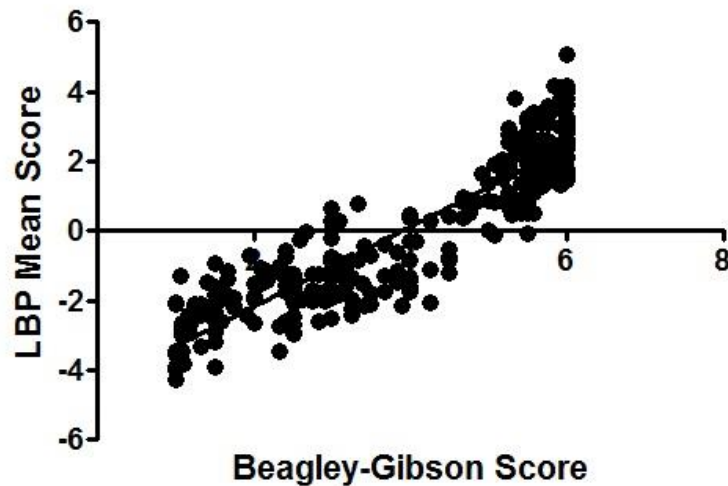


Figure 4. 22: Comparison of structure-based LBP ($r=3$) performance with BG Scores.

4.6.3 Structure-based Analysis of LBP (6th Neighbour Pixel)

For calculation of the LBP of the skin replica image, 8 neighbour pixels compared with the centred pixel with radius equal to 6, which means the window of LBP calculation is 13×13 for each pixel. The result of SVM scoring using my structure-based technique was compared to the BG scores, $R^2 = 0.826$ was found as shown in Figure 4.23. The accuracy (91.6), sensitivity (92.57) and specificity (90.62) were found using the structure-based method for LBP block size 13×13 . This values were lower than with the use of the LBP images alone for classification as shown in Table 4.6, in section 4.7.

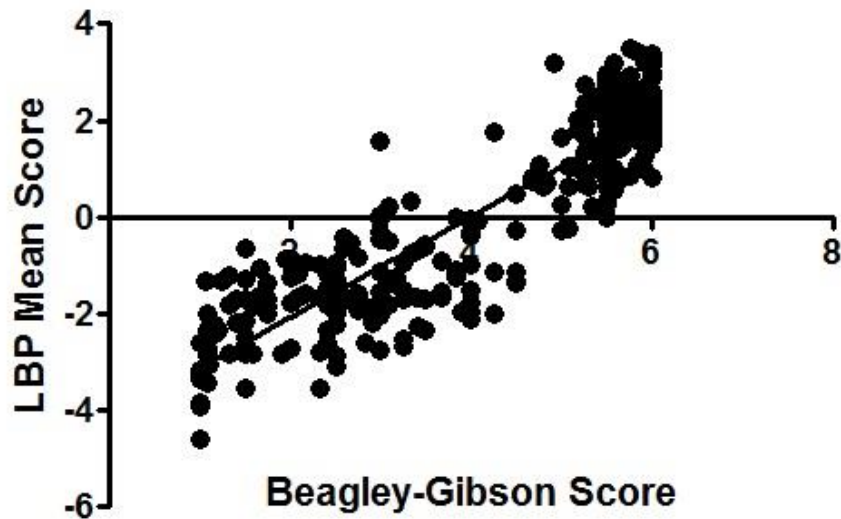


Figure 4. 23: Comparison of structure-based LBP (r=6) performance with BG Scores.

4.7 Novel Methods Performance Compared to BG Scoring

Herein, I describe the use eight different methods to analyse skin mould images, and results are summarised in Table 4.6, with linear regression values and p values for each method compared to BG scores. The accuracy of the classification was lower than the use of texture-based analysis using LBP in both structure-based methods with $r=3$ and $r=6$. I have developed structure-based LBP methods to compare each of the line and shape measurement with clinical parameters and BG scores to see if there was any link between individual measurement, and any clinical parameter as shown in Figure 4.26. Figure 4.26 shows the comparison of the result from the structure-based analysis $r=3$ with clinical parameters, and structure-based LBP with $r=3$ showed higher accuracy and linear regression than with $r=6$ (Table 4.6).

There are two main objectives for choosing this method as a final structure-based method for skin mould analysis:

1. Extraction of all texture information by analysing lines and shapes in images automatically.
2. Separation of structural information and finding associations between each of these structures with the clinical parameters such as age and BMI.

Methods	Accuracy	Sensitivity	Specificity	Linear regression	P value
<i>LBP r=3</i>	97.52	97.81	97.22	0.82	< 0.0001
<i>LBP r=6</i>	98.84	99.12	98.57	0.82	< 0.0001
<i>LBP 4 blocks</i>	98.46	98.4	98.53	0.76	< 0.0001
<i>Uniform LBP</i>	96.40	96.81	96	0.83	< 0.0001
<i>GLCM original image</i>	69.51	96.54	42.48	0.6	< 0.0001
<i>GLCM of LBP</i>	94.14	94.73	93.54	0.73	< 0.0001
<i>Structure LBP r=3</i>	91.72	93.06	90.38	0.83	< 0.0001
<i>Structure LBP r=6</i>	91.6	92.57	90.62	0.81	< 0.0001

Table 4. 6: Summary of automated measurements and BG scoring.

4.8 Comparison with Clinical Parameters

I shall compare the results of automated methods and manual BG scoring in this section with clinical parameters such as BMI and age. I shall also describe the correlation between these parameters with each individual feature extracted from structure-based analysis.

4.8.1 Correlation between BG Scores and Clinical Data

The average BG score for each individual was compared to clinical data. Linear regression was performed comparing arm or face scores to each different clinical parameter to establish if BG scoring could indicate if there was any relationship between the skin integrity and clinical measurements.

4.8.1.1 *Skin Integrity and BMI*

Using all subjects that had sufficient clinical information available to calculate their BMI, the average BMI of the group was 25.1 ± 5.3 (STD), with minimum and maximum values of 18.16 and 51.68 respectively. When compared to the BG score, I could observe no correlation between BMI and skin integrity at either sun-exposed ($R^2 = 0.017$) or sun-protected sites ($R^2 = 0.022$; Figure 4.24).

4.8.1.2 *Skin Integrity and Age*

I had information on the age of 142 individuals. The average age of the group was 52.9 ± 6.1 years (STD, range 41 to 69 years). When compared to the BG score, I found no correlation between age and skin integrity at sun-exposed sites ($R^2 = 0.008$). There did appear to be a significant, albeit low, correlation between skin integrity and age at sun-protected sites ($R^2 = 0.142$; Figure 4.25).

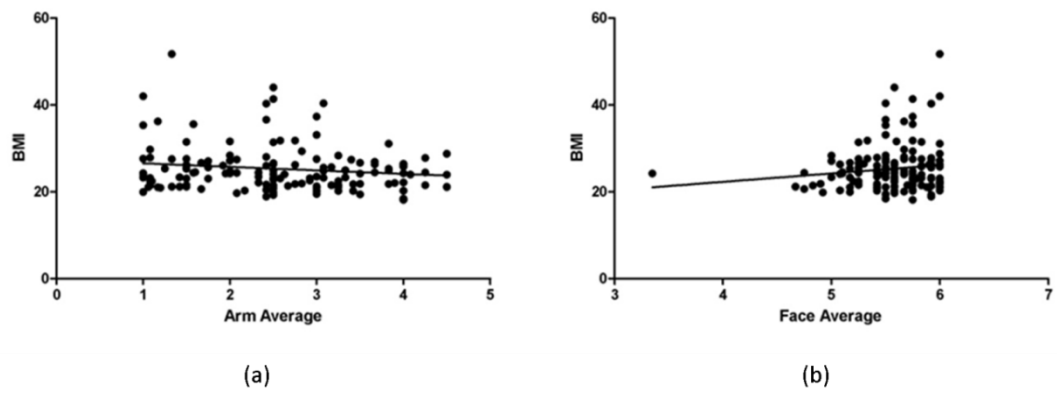


Figure 4. 24: Comparison of BG scores with BMI. Sun exposed skin (a), sun protected skin (b).

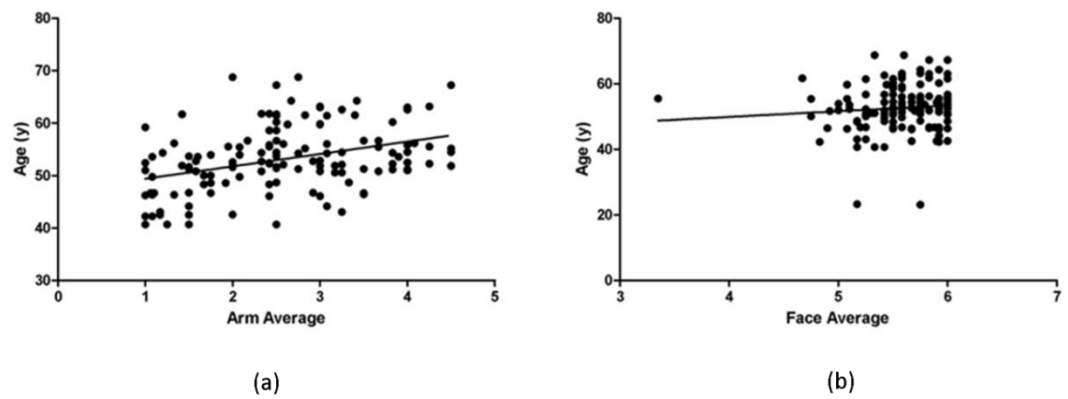


Figure 4. 25: Comparison of BG scores and age. Sun exposed skin (a), sun protected skin (b).

4.8.2. Comparison of Structure-based Method with Clinical Parameters

The results of analysis using LBP structure-based technique was compared to the clinical parameters BMI and age. The comparison is shown in Figure 4.26 and 4.27 respectively. When the LBP with $r=3$ structure-based scores were compared to the BMI, I observed no correlation at either the sun-exposed ($R^2= 0.0230$) or sun-protected sites ($R^2= 0.0001$; Figure 4.26). Also, when age was compared to structure-based scores, there was no correlation between age and skin integrity of the sun-exposed ($R^2= 0.0043$) or sun-protected sites ($R^2= 0.0423$; Figure 4.27).

Each feature extracted using structure-based methods was compared with age and BMI. I found four features associated with BMI, which are as follows:

1. The ratio of grid (polygon) areas to total image area.
2. Number of grids.
3. Number of grids close to the mean of the area of the grids.
4. Number of secondary lines.

Figure 4.28 illustrates the correlation of these four features with BMI from all individuals. Correlation was not very high, perhaps because of the limited number of subjects. The experiments didn't show any association between the age and extracted features. This may be due to relatively limited age range (40-70 years) of the subjects.

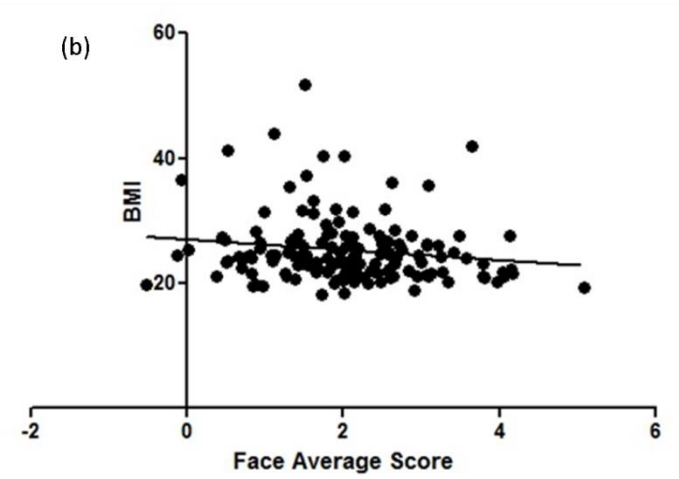
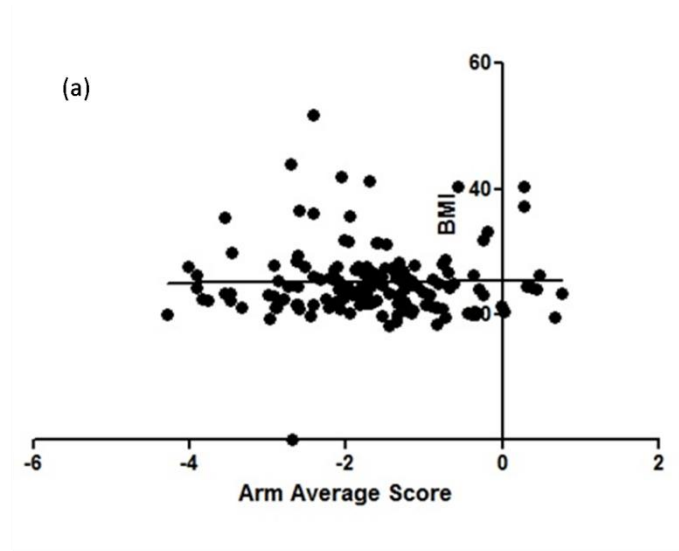


Figure 4. 26: Comparison of LBP structure-based scores and BMIs. a) arm, b) face.

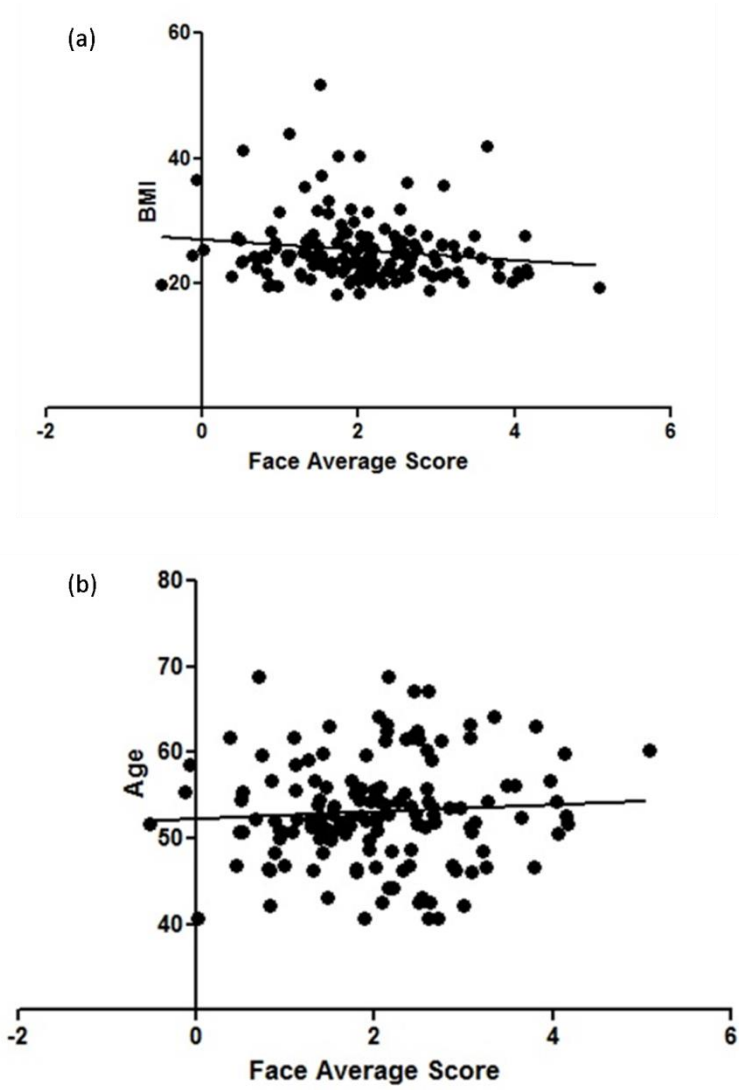


Figure 4. 27: Comparison of LBP structure-based scores and age. a) arm, b) face.

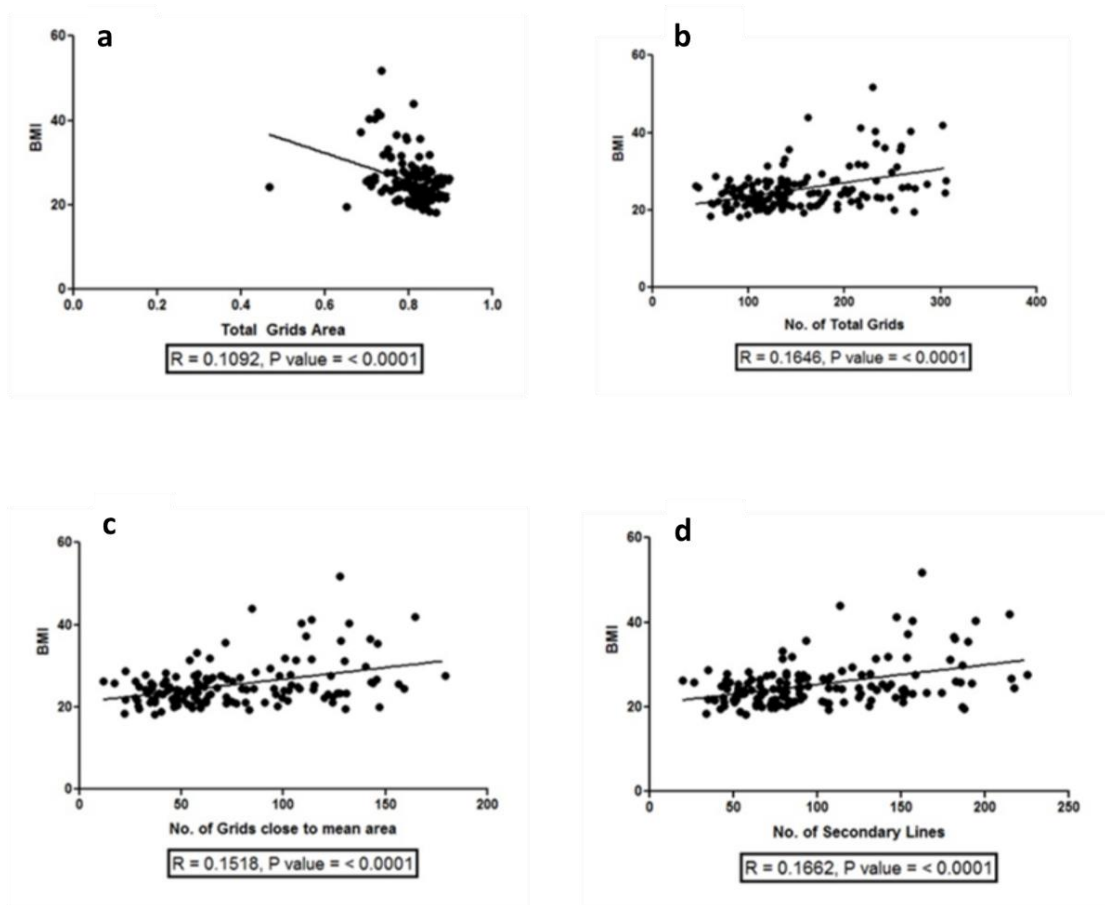


Figure 4. 28: Correlation between features from structure-based analysis with BMI. a) shape area with BMI, b) number of grids with BMI, c) number of grids of area less than 4*STD with BMI, d) number of secondary lines with BMI.

4.8.3. Correlating Structural Features with BG Scores

Structure-based analysis involved the extraction of eight features, as described in section 4.6.1. Each individual feature was compared to BG scores. The correlation was low, but there were five features that correlated with BG scores in sun protected samples (Figure 4.29). The correlation between the feature that described the difference of the maximum secondary line length and minimum line with BG scores was higher than other features in sun exposed skin (Figure 4.30). From the linear regression, I observed five features in particular that correlated with BG scores (Figure 4.29), which I would recommend for future analysis.

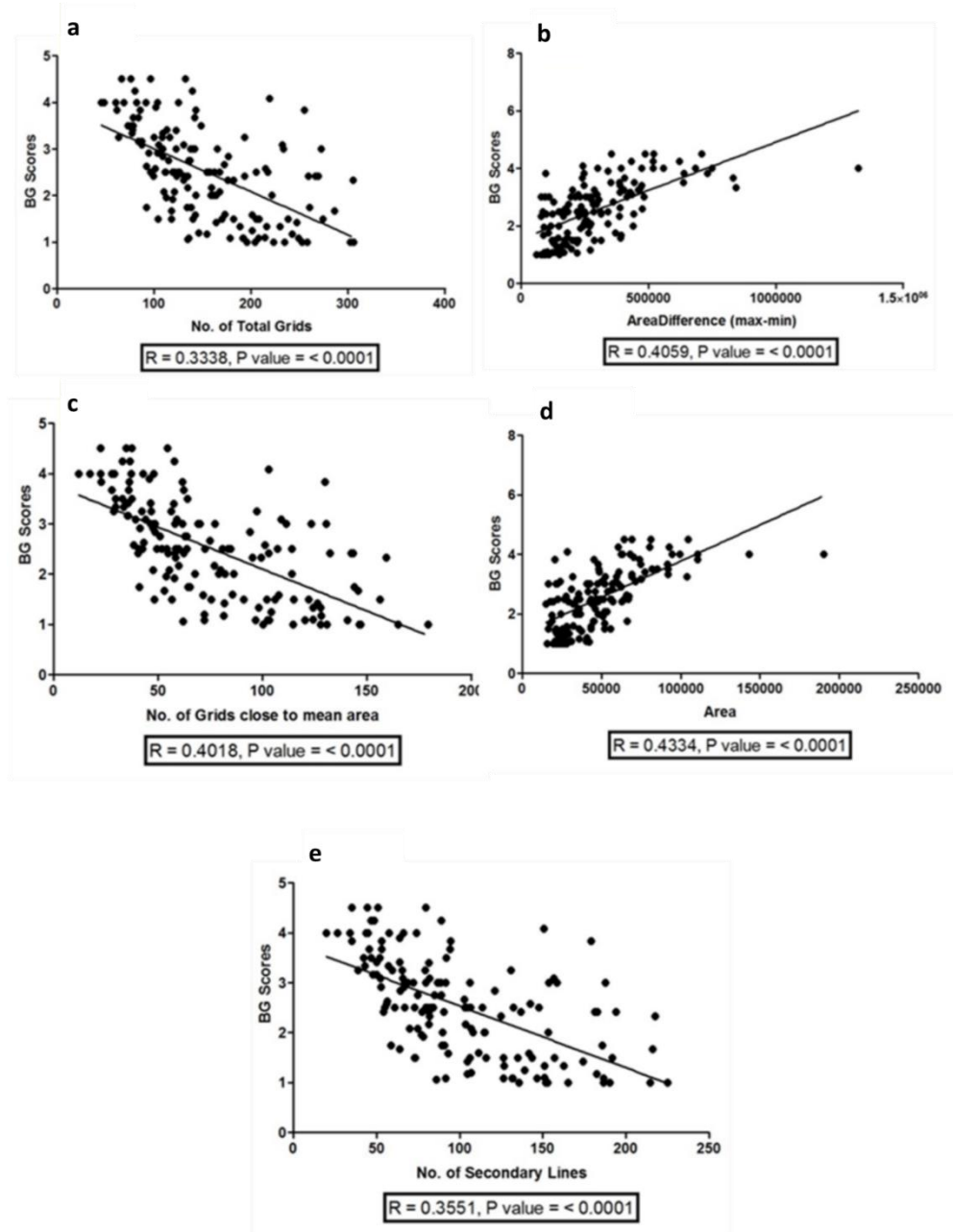


Figure 4. 29: Correlation between various structural features and BG scores in sun protected skin. a) correlation with the number of polygon shapes, $R=0.33$, b) correlation between the difference between the maximum area and the minimum area of the grids, $R= 0.4$, c) correlation with the number of polygons of area $<4*STD$ (close to the mean), $R= 0.4$, d) correlation between the area of the shapes in (c), $R= 0.43$, e) correlation with the number of secondary lines $R= 0.35$.

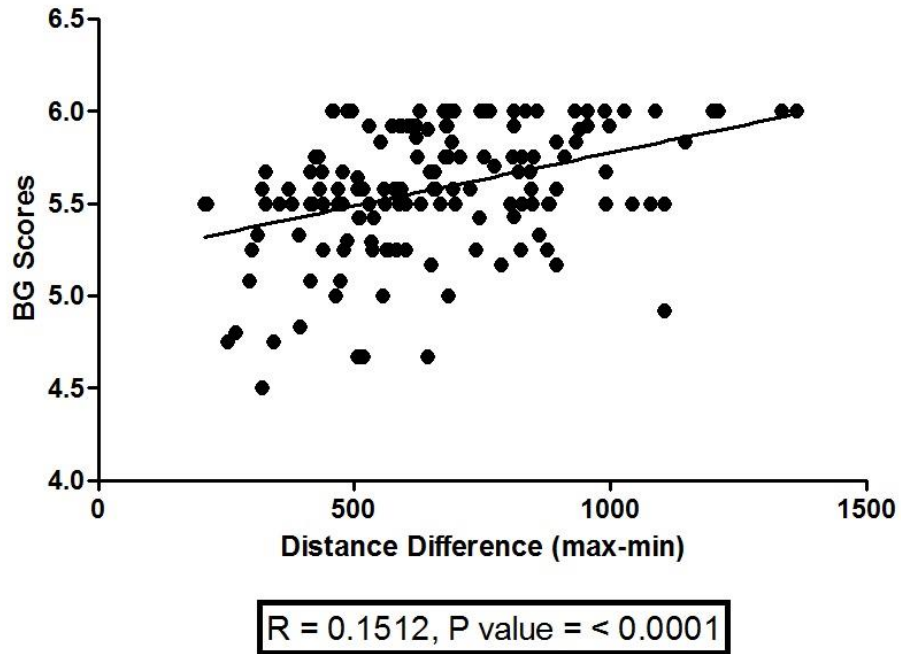


Figure 4. 30: Correlation between structural features in sun exposed skin and BG scores.
Comparison of the difference between maximum and minimum secondary lines and BG scores, $R=0.15$.

4.9 Discussion

Healthy skin has a regular pattern of furrows or lines, the loss of which is associated with chronological and biological age. Disrupted skin topography may also reflect underlying pathology. A method to quantify such features, particularly in the context of the TwinsUK study for which a great deal of genetic and clinical information is available is, therefore, of huge potential benefit. Moreover, an effective non-invasive technique, such as that provided by skin moulds, is very attractive for larger, population based studies. However, existing methods (most notable BG scoring) are time consuming, require expert analysis, and are inconsistent

The LBP $r=6$ method used the local pattern of image pixels, rather than information about general structure, to extract texture information. This method able to extract texture information by compute LBP histogram, that can define the edges (lines) and shapes formed by line intersections were detected efficiently. The result of SVM classification in terms of accuracy, sensitivity and specificity utilizing this method, were higher when compared to other methods, as shown the Table 4.6. In order to further understand the relevance of the extracted features in classification by SVM, I also tested another (k-NN) classifier (Du 2010), where $k=3$, to classify the data set into two classes,

the result of classification showed lower accuracy 94.48% than the use of SVM (98.84%).

The final method (LBP with $r=6$), was able to classify two different classes in the dataset (sun-protected and non-protected skin), even when samples had apparently similar texture to images in the other class, which was not achievable by existing means.

Although the BG score is the “gold-standard” for structure-based analysis, I observed that the BG score was not perfect. By investigating skin mould images, there were many images were scored using the BG system by two observers as highly structured (grades 1 or 2), where in fact they had less organised structures indicative of a 5 or 6 grades (this was checked by comparing the manual and automated result, also checked manually by experts). Furthermore, when I considered the Cohens kappa value between two observers using BG scoring, I found a low agreement (0.229), which indicates a limitation of manual scoring. BG scoring does not, therefore, provide a “ground truth” for comparison with novel methods. In contrast, SVM classification accuracy was high, especially using LBP texture analysis. Due to difficulties in comparison with inconsistent BG values, I suggest that my novel methods are actually more accurate than the results of linear regression and accuracy results suggest.

A better approach would be use a calibration set of histological images, from which much more quantitative data can be extracted (as described in previous Chapters). By analysis of a matched set of images derived from non-invasive means (i.e. moulds), I could more effectively validate my methods. This does, of course, present a number of challenges in execution, but could be possible in individuals undergoing skin biopsies in the course of treatment for other purposes. They would have to consent to having a skin mould made at the same time.

The automated grading method described herein allows the discrimination of subtle variations with a continuous scale, as opposed to that provided a six scale method. This may also improve classification using SVM on the LBP features. Confidence levels were determined using the STD of the testing data to find the high, low and medium levels of confidence (Shan et. al., 2014), and in my experiment using optimal LBP $r=6$ method, these were found to be 99.75%, 93.54% and 99.78% respectively. The

detection of subtle variations makes my method more suitable for cosmetic and pharmaceutical research, where changes in the skin surface may be small but of great clinical or cosmetic relevance.

The correlation between scores and clinical parameters was low, and this may be due to limited variation in the clinical data. For example, age of the subjects was between 41 and 69 years. Therefore, to find any significant correlation between scores and clinical data, more mould data from more subjects is required.

Although overall structural analysis was not the highest ranked of the techniques used, some of the features considered were components of the BG scoring system. Individually, any of the eight features isolated might significantly correlate with clinical data or BG scoring. However, I observed no correlation between sun protected skin and the extracted features. I did find a small significant correlation between some of the features and sun exposed skin, however the correlation was low, perhaps because of the limited number of samples. A comparison of each feature with clinical data might help to find the features that are changed in UV affected skin but not changed in chronological aged skin or vice versa. This classification of features into those affected by intrinsic and extrinsic ageing could then be used in drug discovery techniques to find an efficient treatment.

Future Work

The main objective in the future is to try to apply these techniques to a larger and more varied dataset. However, comparison of scores with other clinical parameters might also be interesting, notably waist-to-hip ratios and blood glucose concentrations. As these may be indicators of type 2 diabetes mellitus (i.e. acquired insulin resistance), such analysis could be of utility in the early diagnosis of diabetes.

To provide more precise analysis and validate the results of these techniques, I would like to analyse skin moulds alongside matched biopsy samples for each individual. Availability of histological data would a much more robust “ground truth” for the evaluation of non-invasive methods.

3D image analysis may lead to important developments in skin structure analysis. By imaging skin moulds with surface scanning confocal microscopy, assessment of texture

in three dimensions would allow one to exploit all skin surface detail. The exact measurement of the contours, rather than primary and secondary lines, would provide more meaningful analysis. Moreover, 3D histology images created by confocal microscopy would also give more information about structure and volume in optical sections, which would again provide more information to inform a non-invasive skin grading system.

Fusion of GLCM and LBP features might result in more accurate scores, because each technique gives different texture information. GLCM gives information about the relationships between neighbouring pixels in a whole image, whereas LBP can provide local texture patterns. The result of texture information extraction from the use of two techniques might provide higher classification accuracies compared to one technique.

Clustering techniques, such as *k*-means clustering, might help in finding correlations with clinical parameters. For example, one could apply clustering to different age ranges to see how the skin degrades with age at sun exposed or protected sites.

Conclusions

The skin surface contains a large amount of texture information, changes in which reflect processes such as sun exposure and ageing. I was able to quantify loss of regular structure with sun exposure using an automated method (LBP with $r=6$) that could not be determined by existing, manual, methods. The development of effective, non-invasive and wholly unsupervised techniques would facilitate high-throughput analysis in cutaneous research, with potential applications to screening and drug discovery.

CHAPTER 5

5.1 Overall Conclusion and General Discussion

This thesis has demonstrated the utility of combining computational spatial and frequency domain image processing techniques and the automated high-throughput image analysis tools that are designed primarily to detect, segment and quantify various components of skin tissue images. Moreover, the methods that have been developed are adapted to deal with different microscopic images and the snapshots of the tissue section images from whole slide scanner. The developed methods are able to enhance the images automatically to make sure that the methods can adaptively analyse the images with variation in colour distribution and intensity, that followed by extracting the interesting changes in texture and morphological feature in the skin tissue section.

In Chapter 2 I have focussed on extracting and quantifying orientation and other information on collagen bundles in the dermis layer. Firstly I have used the combined techniques of Gabor filter and FFT to assess the collagen organisation in the papillary and reticular dermis which in turn facilitates the evaluation of age in terms of collagen orientation and organisation. This has been done by highlighting the collagen directions in the skin and quantifying the amount of collagen directed in each of selected directions. In the same Chapter, I have quantified collagen thickness by analysing the FFT spectrum of picrosirius images. The maximum frequency of the FFT spectrum provided sufficient information about the bundle thickness. Finally, in Chapter 2, I have used *k*-means clustering to cluster the colour components in an image combined with the mathematical morphology operation to segment and analyse the young and mature collagen in the dermis, in an attempt to assess collagen dynamics.

In Chapter 3, I have developed a high-throughput automated image analysis system to detect interesting cutaneous phenotypes in gene-knockout mice provided by WTSI. This was developed using an active contour-based segmentation procedure to work adaptively by generating the initialized curve from the object itself in the H&E stained images. Each layer of the mouse skin tissue has been segmented and analysed using the ability of the adaptive active contour followed by mathematical morphology operations and intensity transformation to gain an accurate segmentation result.

The non-invasive analysis of skin surface structure using the impression of the skin surface in moulds, provided by the TwinsUK twin registry in Chapter 4 provided another opportunity to combine computational techniques to answer biologically meaningful questions. Different techniques as LBP, GLCM and skeletonized structure based method have been used to extract the features in the mould skin images and the most efficient and accurate technique has been chosen to score the skin into six different grades from protected skin gradually to the sun exposed skin. The novelty of this system can be attributed to the use of SVM classification scores to grade the images automatically. The selection of the LBP window size has also provided accurate information about the secondary and primary line and all the shapes that formed from the intersection of these lines.

5.1.1 Application of Techniques to Different Image Datasets

General Considerations for Histology

Variation in tissue processing during specific staining schemes produces variation in the intensity and colour of the target objects. For this reason automated methods have been created to work adaptively with these variations in different datasets. Techniques used in this research and work adaptively with different datasets include the active contour-based analysis that starts by initializing a curve automatically from information known about the object itself. This internal control makes the system adapt to the intensity and colour variation in the images. Moreover the use of k -means clustering for colour segmentation in this work is also robust to the variation in images. In the future shall investigate the use of colour normalization to be applied to the whole dataset to reduce the variation in the set of images as described in Chapter 3, (see conclusion section 3.4).

Application in Human Histology

Although not reported in this thesis, I have applied some of the techniques described in this body of work on human skin histology. Generally I found that the pre-processing techniques need to be adapted across the two models of mouse and human, but sometimes novel techniques have been required. One example of this, is computing the local entropy in the image to successfully segment the epidermis sub-layers by segmenting the compact layer between the stratum corneum and malpighian, that because the gradient in intensity between this layer in between and the other two sub-layers. The need for different techniques for analysis is probably due to the difference between the

skin of those two models e.g. the thickness of the layer and the thin epidermis layer in mouse models, make the feature extraction more difficult in this layer. The texture-based template matching to isolate the stratum corneum and malpighian layer in human samples is a new development in human skin histology as we have investigated, but this might be applicable to mouse skin as well with some pre-processing considerations.

5.1.2 Application of Computational Techniques in Industry

Automated skin image analysis has a crucial role in the context of drug discovery, by improving high-throughput analysis to detect changes in skin morphometry and structure in response to different drugs. One of the most important areas of skin research is in structural changes, both in ageing (intrinsic aging) but also in disease and as a result of environmental exposure (extrinsic aging). Skin ageing alters the skin structure and the skin tissue fibres, both from physiological and morphological viewpoints (Farage, Miller et al. 2010). This thesis is centred around developing novel systems that enhance skin histopathology research to assess the skin structure changes that caused by aging, diseases and the effect of different genetics.

Human skin equivalents are used widely by pharmaceutical and cosmetics industry to develop treatments as an alternative to *in vivo* studies (Mertsching, Weimer et al. 2008). The skin equivalent has been generated from human keratinocyte on a collagen gel substrate. There are many *in vitro* assays that have been used in the test of drugs, but none of them can accurately predict patient response to treatment (Benbrook 2006). However, obtaining human skin slices is difficult in the drug discovery and development process. In the skin equivalent that could be prepared in the laboratory, it is possible to culture or select a cell of particular genotype and phenotype to manipulate the cellular structure of the skin (Bell, Sher et al. 1983). Therefore, the relatively easy manipulation, monitoring and low cost of the organotypic model make the use of this model more suitable for high throughput screening.

The model of the skin equivalent or artificial skin offers all the flexibility that is required in any commercial system to make the high throughput screening possible. However, controlling, detecting and analysing the changes in a cutaneous high-throughput screen require a strategy with powerful automated computational techniques. At present appropriate tools that are suitable for use by industry do not appear to be

evident in the field. I have investigated and experimented with specific techniques in a high-throughput environment and have had preliminary success to extract the morphological information automatically using automatic image processing and analysis techniques.

The artificial skin image analysis enables the drug efficiency and reaction to be verified as a non-invasive method to detect any change in the skin in the context of drug discovery. Bringing these aspects together can produce a powerful tool in the research and drug discovery settings, allow new ideas and therapeutics to be tested efficiently and cost-effectively for the development of new compounds for cutaneous disease which in turn can be brought to the clinic quicker. Image processing techniques to reduce the cost and time of drug discovery and development, have already been demonstrated in measuring drug efficacy of chemical compounds in cultured cells, by tracking the cells in the fluorescence images (Yoshida, Yoshiura et al. 2008). However the ultimate and realistic contributions of automated image analysis techniques in the drug discovery are yet to be realised, Here, we proposed automatic image analysis methods that facilitate the drug discovery and development for skin diseases and rejuvenation while reducing financial risk of such research. By developing techniques applicable for histology images from biopsies or in artificial skin these techniques can automatically assess drug efficiency, disease severity or disease resolution. Furthermore, the application of these automated and rapid techniques to non-invasive structural analysis methods such as artificial skin mould analysis provides a novel pipeline for drug discovery and drug evaluation not currently available to the research community.

Novel Developments of this Work

A number of image processing and analysis techniques have been developed in this research project. We have described these novel biological image analysis methods and their use to evaluate the degradation of the skin collagen fibres and assessment of collagen dynamics. Assessment of the structural features of collagen fibres were based on using a novel combination of Gabor filter and FFT power spectrum analysis techniques. The excellent performance of this new technique was demonstrated on large set of skin images. Assessment of changes in the skin layer morphology, were based on using adaptive active contour without edges technique. The suitability and performance

of this novel technique have been demonstrated in the high accuracy detection of interesting textural features in the skin section in different environmental and disease condition as well as assessment of specific cellular content in cutaneous specimens.

The quantification and analysis of different layers of skin tissues using developed image-based techniques have been instrumental for gaining insight into cutaneous biology. Specifically, these techniques helped analysing the dermis and collagen structure and identifying a calibrated decrease in collagen structure in ageing and in diabetic models. Moreover, the decrease in the ratio of young to mature collagen and the decrease in the bundle thickness with age have been identified.

The Gabor filter and Fast Fourier Transform (FFT) elliptical analysis has been developed and used to quantify the collagen architecture in the extracellular matrix (Osman, Selway et al. 2013). The collagen directions specified by detecting the edges in different direction using Gabor filter, this gives novelty to the system in such application of analysis in picrosirius stained images. Also the way of quantifying the amount of collagen in each direction from the FFT power spectrum of each direction is a novel way to describe the subtle change in the collagen organisation. I have illustrated that this is a significant improvement upon existing methods (de Vries, Enomoto et al. 2000). Using my developed method, the overlap of the collagen bundles did not affect the quantification, because the quantification is done in the FFT power spectrum which each pixel in the power spectrum gives information about all the pixels in the spatial Gabor filtered image. This method is unlike the quantification in the spatial image, e.g. converting the image to its binary form, to quantify the collagen orientation (Noorlander, Melis et al. 2002). Analysis in spatial skin section affect by overlapping the collagen bundles in the particular skin tissue section.

Collagen bundle thickness measurements have been developed using FFT highest frequencies in the transformed image. The high frequency in the image indicates the sudden change of intensity in the image that represents the collagen bundle edges in picrosirius stained skin images. The automated thickness quantification from the elliptical shape of the FFT spectrum has been used as a novel method to assess the change in collagen bundle thickness in different group ages. The quantification has been done by considering the ellipse parameters reflect the collagen thickness in the spatial

image. Such analysis has been done previously, using existing software, and supervised by the expert users using different parameters (Verhaegen, Marle et al. 2012).

The assessment of collagen dynamics in the Herovici stained skin has been developed by combining different techniques: *k*-means clustering and colour filters. The colour dimensionality has been reduced in this method by converting the colour space from RGB to $L^*a^*b^*$ to facilitate the clustering step. Using *k*-means clustering method to partition the image content into different clusters allowed more accurate segmentation result in the dataset that exhibits noticeable variation in the colour and intensity.

The developed techniques from Chapter 3, including the novel active contour procedure, have allowed the quantitative measurement of all the three structural layers epidermis, dermis and subcutaneous fat in H&E mouse and human skin. One novelty in this system is the ability of the technique to create the initialize curve automatically from the object itself and start the active contour model to segment the object. This helps to reduce the iteration of using the active contour model and make the model faster than the snake model (Kass, Witkin et al. 1988).

A technique for automatically and accurately assess adipocyte size has also been developed and successfully deployed (Osman, Selway et al. 2013). I have proposed a novel adipocyte size quantification from computing the total pixels of each cell instead of the calculating the area manually as described by (Björnheden, Jakubowicz et al. 2004). Using this developed method to assess the morphology of skin layers and adipose tissue size and number using active contour model and intensity transformation to segment the adipocytes, have identified interesting phenotypes. The study of the epidermis, dermis and adipocyte phenotypes using the methods described in Chapter 3, has shown the ability to detect known and novel phenotypes in each of the skin layers in H&E stained mouse skin images.

Texture-based analysis methodology has been developed to extract features from mould skin images to assess the skin surface topography. This technique differs from the conventional BG score system (Seddon, Egan et al. 1992). The novel analysis of the texture in the skin surface images, using fully automated texture feature extraction through the use of LBP, provides accurate information about the skin surface structure. Using non-invasive techniques to assess skin structure, it has been possible to describe

the effect of environmental factors on the structure of human skin surface. The skin impressions have been classified into protected and sun exposed skin and the high classification accuracy results proved the efficiency of the developed method.

Overall I believe that these techniques are novel, automated unsupervised methods, which have been validated by comparing them to other techniques and manual methods. Moreover all of these methods build on standard and commercially available tools, including existing computational spatial and frequency domain image processing tools (i.e. FFT reference) or gold-standard manual or qualitative techniques (i.e. BG scoring reference).

The Significance of this Work

Biological image processing and analysis provides techniques that help scientists to evaluate the effects of environmental exposure and physiological changes in a research context. These techniques may also be used to evaluate the effect of the treatments and drug efficiency in the context of the drug discovery. All of these analysis techniques could also be applicable clinically. In all applications, novel combinations of image processing/analysis techniques and pipelines will save time and are expected to produce more accurate results that will ultimately help or improve the speed and quality of dermatology and cosmetic treatments.

The high-throughput analysis application of our developed techniques is particularly evident in Chapter 3. However all the techniques can be utilised in this manner because of their automated and adaptive nature. The collagen organisation assessment in Chapter 2 and the skin surface structure analysis in Chapter 4 are all capable of high-throughput analysis but some further work may be required for fully adaptive automation.

The results from using the image analysis and quantification techniques have proved that these methods are reliable and accurate without any user interaction. Moreover, the techniques are easy to use with little/no special knowledge of image processing. This illustrates the utility of this type of translational research. The reality of some of these packages is that they utilise some standard and well-known concepts in the field of image processing and analysis. For example the use of threshold and other intensity transformations, such as piecewise linear transformation, is common in computational image processing (Gonzalez, Woods et al. 2004). These techniques are sometimes used

and have been integrated into commercial software but not necessarily applied to specific biological problems through the lack of expertise in the histology field, which can cause problems in diverse image datasets. In this PhD research I have attempted to address this issue.

5.2 Future work

One future objective would be to make all the developed methods adaptive to different datasets. For example we shall attempt to develop appropriate image transformations that could be applied all the image dataset the same colour distribution using colour normalization (Reinhard, Ashikhmin et al. 2001). This technique has been used in the histopathological study to map the colour distribution of bad stained images, e.g. over stained or under stained onto an image that exhibit characteristics of a well stained image (Magee, Treanor et al. 2009). To some extent this has been achieved and investigated already as described in the conclusion section 3.4 of Chapter 3, when we used a technique based on the texture and other structural information rather than the colour distribution and intensity in the image, as well as the use of Gabor filter to detect the collagen in the dermis. However, images with high variation in intensity and colour present a real challenge. The underlying variation is often caused by variable laboratory procedures in the production of these image datasets, specifically during tissue processing, sectioning and staining.

Though, these methods have proved the efficiency and capability of skin analysis using combination of different image processing techniques. The automated skin image analysis can be further improved. In particular, one could utilize the method of collagen architecture analysis using Gabor filter and FFT in a high-throughput analysis to assess the skin integrity in the human skin samples. This method helps the detection of the important pathological information and precise change in the collagen structure in the dermis. The assessment of the skin structure could also facilitate the evaluation of the effect of the use of different cosmetically treatments, and also more analysis in other mouse model and different disease state and diabetic pathologies.

One could also extract more information from the picrosirius images and determine the type of collagen in the picrosirius stained skin section using image processing technique to differentiate between the thin and thick collagen, which is probably defined as the

collagen type I and type III respectively. The colour and intensity are two critical features to be utilized in identifying the type of collagen, because the thin and thick materials appear in different colour and intensity in the histological section. Similar analysis has been done to segment the young and mature collagen in the Herovici stained image in as described in Chapter 2 section 2.3.3.

In the high-throughput active contour method phenotype detection, there are possible ways to improve the algorithm by conducting statistical analysis and classification to detect outlier data and remove their effects in order to classify interesting phenotypes related to different skin layers in gene-knockout mouse. For example, one may use the mahalanobis distance to identify the outliers as described in a recent paper (Bassett, Gogakos et al. 2012).

I would also like to apply the texture and structural-based skin topographic techniques to a larger range of patients with a broader spectrum of clinical information such as age and BMI. This may improve the performance of the system to find the skin topographic structure that correlates to any clinical parameter e.g. correlation between the primary and secondary lines with BMI.

One future development could involve the use of texture-based template matching techniques to analyse the human epidermis layers. I have completed some preliminary work using different techniques such as LBP in combination with extracted features from GLCM. The fusion of the extracted texture information from these algorithms in the pilot study has resulted in positive improvement of segmentation.

Two graphical user interfaces (GUIs) have been created, one for the collagen architecture assessment, and the second tool is for accurate adipocyte quantification. As a future work for this research I would like to facilitate the use of various combination analysis tools to be used as a biological tool to assess the skin integrity. The GUI is important for the biologist to have a simple effort by following the GUI instruction, to get the analysis result quickly and gain an accurate result of analysis without bias that could affect the diagnosis. This can be used in the future as a part of WTSI pipeline to take a part in the phenotyping process, and also can be used as plug in for free analysis sources as imageJ to be available and accessed in biological image analysis. It would also be useful for training purposes.

Chapter 5

Finally, a combination of image processing and analysis techniques can be used automatically in the high-throughput analysis to evaluate skin conditions in different diseases such as skin cancer, inflammatory disorders and cosmetic dermatology. My techniques can overcome the problem of the variation in histology and work with different staining to visualize and analyse the features that reflect some biological phenomenon. The analyses in this field can be continued by developing an image analysis source to help solve concerning issues of time consumption and inaccurate assessments. And also there are opportunities for using such system in other application of medical image analysis e.g. ultrasound, magnetic resonance image MRI, x-ray images by modifying these techniques to help the researchers in this field.

REFERENCES

- Alper, M., A. Kavak, et al. (2004). "Measurement of epidermal thickness in a patient with psoriasis by computer-supported image analysis." *Braz J Med Biol Res* **37**(1): 111-117.
- Aymeric Histace, E. B., Luis Garrido, Bogdan J. Matuszewski and Mark Murphy (2014). Active Contour Segmentation based on Approximate Entropy. International Conference on Biosignals. Anger, France.
- Baecker, V. (2010). Image processing and analysis with ImageJ and MRI Cell Image Analyser.
- Bailey, A. J., R. G. Paul, et al. (1998). "Mechanisms of maturation and ageing of collagen." *Mech Ageing Dev* **106**(1-2): 1-56.
- Bancroft, J. D. and M. Gamble (2008). *Theory and practice of histological techniques*, Elsevier Health Sciences.
- Bapure, K. (2011). *Automated Image Analysis for Nuclear Morphometry Using H&E and Feulgen Stains in Prostate Biopsies*, University of Illinois at Chicago.
- Bassett, J. H., A. Gogakos, et al. (2012). "Rapid-throughput skeletal phenotyping of 100 knockout mice identifies 9 new genes that determine bone strength." *PLoS Genet* **8**(8): e1002858.
- Bell, E., S. Sher, et al. (1983). "The reconstitution of living skin." *J Invest Dermatol* **81**(1 Suppl): 2s-10s.
- Benbrook, D. M. (2006). "Organotypic cultures represent tumor microenvironment for drug testing." *Drug Discovery Today: Disease Models* **3**(2): 143-148.
- Bevilacqua, A., A. Gherardi, et al. (2006). Measuring Skin Topographic Structures through Capacitance Image Analysis. Proceedings of the IEEE International Conference on Video and Signal Based Surveillance, IEEE Computer Society.
- Björnheden, T., B. Jakubowicz, et al. (2004). "Computerized determination of adipocyte size." *Obesity research* **12**(1): 95-105.
- Bologna, J. L., J. L. Jorizzo, et al. (2008). "Bologna dermatology." *Wound closure materials and instruments*: 2188.
- Britannica, E. (2014). "Adipose cell." from <http://www.britannica.com/EBchecked/topic/5944/adipose-cell>.
- Brox, T., Y.-J. Kim, et al. (2006). Fully-automated analysis of muscle fibre images with combined region and edge-based active contours. *Bildverarbeitung für die Medizin 2006*, Springer: 86-90.
- Burns, T., S. Breathnach, et al. (2010). *Rook's Textbook of Dermatology*, 4 Volume Set, John Wiley & Sons.
- Chan, R. H., C.-W. Ho, et al. (2005). "Salt-and-pepper noise removal by median-type noise detectors and detail-preserving regularization." *Image Processing, IEEE Transactions on* **14**(10): 1479-1485.
- Chan, T. F., B. Y. Sandberg, et al. (2000). "Active contours without edges for vector-valued images." *Journal of Visual Communication and Image Representation* **11**(2): 130-141.
- Chan, T. F. and L. A. Vese (2001). "Active contours without edges." *IEEE Trans Image Process* **10**(2): 266-277.
- Chen, H. C. and R. V. Farese, Jr. (2002). "Determination of adipocyte size by computer image analysis." *J Lipid Res* **43**(6): 986-989.
- Chitade, A. Z. and S. Katiyar (2010). "Colour based image segmentation using *k*-means clustering." *International Journal of Engineering Science and Technology* **2**(10): 5319-5325.
- Cisneros, F. J., P. Cordero, et al. (2011). "Histology image segmentation." *International Journal of Information Technology and Management* **5**(1): 67-76.
- Collins, T. J. (2007). "ImageJ for microscopy." *Biotechniques* **43**(1 Suppl): 25-30.
- Cristianini, N. and J. Shawe-Taylor (2000). *An introduction to support vector machines and other kernel-based learning methods*, Cambridge university press.

References

- Dadwal, M. and V. Banga (2012). Color Image Segmentation for Fruit Ripeness Detection: A Review. International Conference on Electrical, Electronics and Civil Engineering, ICEECE.
- de Assis Zampirolli, F., B. Stransky, et al. (2010). Segmentation and classification of histological images-application of graph analysis and machine learning methods. Graphics, Patterns and Images (SIBGRAPI), 2010 23rd SIBGRAPI Conference on, IEEE.
- de Vries, H. J., D. N. Enomoto, et al. (2000). "Dermal organisation in scleroderma: the fast Fourier transform and the laser scatter method objectify fibrosis in nonlesional as well as lesional skin." *Laboratory investigation* **80**(8): 1281-1289.
- Deng, Y., B. S. Manjunath, et al. (1999). Color image segmentation. Computer Vision and Pattern Recognition, 1999. IEEE Computer Society Conference on., IEEE.
- Du, H. (2010). Data mining techniques and applications: an introduction, Course Technology Cengage Learning.
- Elshinawy, M. Y. and M. F. Adviser-Chouikha (2010). Pre-CAD normal mammogram detection algorithm based on tissue type, Howard University.
- Farage, M., K. Miller, et al. (2010). Textbook of Aging Skin., Springer-Verlag: Berlin Heidelberg.
- Fisher, R., S. Perkins, et al. (2005). HIPR2: Image processing learning resources.
- Fligel, S. E., J. Varani, et al. (2003). "Collagen degradation in aged/photodamaged skin in vivo and after exposure to matrix metalloproteinase-1 in vitro." *J Invest Dermatol* **120**(5): 842-848.
- Ford, A. and A. Roberts (1998). "Colour space conversions." Westminster University, London **1998**: 1-31.
- Gao, Q., L. W. Hu, et al. (2011). "Skin texture parameters of the dorsal hand in evaluating skin aging in China." *Skin Res Technol* **17**(4): 420-426.
- Gao, Q., J. Yu, et al. (2013). "Automatic measurement of skin textures of the dorsal hand in evaluating skin aging." *Skin Res Technol* **19**(2): 145-151.
- Gawkrodger, D. (1997). "Dermatology: An Illustrated Colour Text Churchill Livingstone." New York.
- Gherardi, A. (2008). "A skin surface characterisation system based on capacitive image analysis."
- Gogly, B., G. Godeau, et al. (1997). "Morphometric analysis of collagen and elastic fibres in normal skin and gingiva in relation to age." *Clin Oral Investig* **1**(3): 147-152.
- Gonzales, R. and R. Woods Digital Image Processing. 2002. ISBN: 0-201-18075-8, Prentice Hall, New Jersey, USA.
- Gonzalez, R. C., R. E. Woods, et al. (2004). Digital image processing using MATLAB, Pearson Education India.
- Grunkin, M. (2008). "Working With Visiomorph." Hoersholm, Denmark: Visiopharm A/S.
- Haggerty, J. M., X. N. Wang, et al. (2014). "Segmentation of epidermal tissue with histopathological damage in images of haematoxylin and eosin stained human skin." *BMC Med Imaging* **14**: 7.
- Haralick, R. M., K. Shanmugam, et al. (1973). "Textural features for image classification." *Systems, Man and Cybernetics, IEEE Transactions on*(6): 610-621.
- He, L., L. R. Long, et al. (2010). Local and global Gaussian mixture models for hematoxylin and eosin stained histology image segmentation. Hybrid Intelligent Systems (HIS), 2010 10th International Conference on, IEEE.
- Hiremath, P. and P. Bannigidad (2012). "Spiral Bacterial Cell Image Analysis using Active Contour Method." *International Journal of Computer Applications* **37**.
- Hiremath, P. and J. R. Tegnoor (2010). Follicle detection in ultrasound images of ovaries using active contours method. Signal and Image Processing (ICSIP), 2010 International Conference on, IEEE.
- Hosea, S. P., S. Ranichandra, et al. (2011). "Color Image Segmentation–An Approach." *Color Image Segmentation–An Approach* **2**(3).

References

- Hosea, S. P., S. Ranichandra, et al. (2011). "Color Image Segmentation—An Approach." *Color Image Segmentation—An Approach* **2**(3): 0.00.
- Jafari-Khouzani, K. and H. Soltanian-Zadeh, Sr. (2005). "Radon transform orientation estimation for rotation invariant texture analysis." *IEEE Trans Pattern Anal Mach Intell* **27**(6): 1004-1008.
- Jo, J., O. Gavrilova, et al. (2009). "Hypertrophy and/or Hyperplasia: Dynamics of Adipose Tissue Growth." *PLoS Comput Biol* **5**(3): e1000324.
- Junqueira, L. C., G. Bignolas, et al. (1979). "Picrosirius staining plus polarization microscopy, a specific method for collagen detection in tissue sections." *Histochem J* **11**(4): 447-455.
- Kass, M., A. Witkin, et al. (1988). "Snakes: Active contour models." *International journal of computer vision* **1**(4): 321-331.
- Key, M. (2006). "Immunohistochemistry Staining Methods." *Education Guide Immunohistochemical Staining Methods Fourth Edition*: 47.
- Khorasani, H., Z. Zheng, et al. (2011). "A quantitative approach to scar analysis." *Am J Pathol* **178**(2): 621-628.
- Korde, V. R., H. Bartels, et al. (2009). "Automatic segmentation of cell nuclei in bladder and skin tissue for karyometric analysis." *Anal Quant Cytol Histol* **31**(2): 83-89.
- Kueh, H. Y., E. Marco, et al. "Image analysis for biology."
- Kumar, M. M. (2013). "A STUDY ON TEXTURE FEATURE ANALYSIS AND EFFECT OF WINDOW SIZE ON TEXTURE." *Journal of Research in Electrical and Electronics Engineering (ISTP-JREEE)* **2**(1).
- Lagarde, J. M., C. Rouvrais, et al. (2005). "Topography and anisotropy of the skin surface with ageing." *Skin Res Technol* **11**(2): 110-119.
- Leung, C.-K. and F.-K. Lam (1994). Image segmentation using maximum entropy method. *Speech, Image Processing and Neural Networks, 1994. Proceedings, ISSIPNN'94., 1994 International Symposium on, IEEE*.
- Li, C., C.-Y. Kao, et al. (2008). "Minimization of region-scalable fitting energy for image segmentation." *Image Processing, IEEE Transactions on* **17**(10): 1940-1949.
- Liakath-Ali, K., V. E. Vancollie, et al. (2014). "Novel skin phenotypes revealed by a genome-wide mouse reverse genetic screen." *Nature communications* **5**.
- Magee, D., D. Treanor, et al. (2009). Colour normalisation in digital histopathology images. *Proceedings of Optical Tissue Image Analysis in Microscopy, Histopathology and Endoscopy (MICCAI Workshop)*.
- Mahmood, N. H., M. R. M. Razif, et al. (2011). "Comparison between Median, Unsharp and Wiener filter and its effect on ultrasound stomach tissue image segmentation for Pyloric Stenosis." *International Journal of Applied* **1**(5).
- Marr, D. and E. Hildreth (1980). "Theory of edge detection." *Proc R Soc Lond B Biol Sci* **207**(1167): 187-217.
- Materka, A. and M. Strzelecki (1998). "Texture analysis methods—a review." *Technical university of lodz, institute of electronics, COST B11 report, Brussels*: 9-11.
- Mays, P. K., R. J. McAnulty, et al. (1995). "Age-related alterations in collagen and total protein metabolism determined in cultured rat dermal fibroblasts: age-related trends parallel those observed in rat skin in vivo." *Int J Biochem Cell Biol* **27**(9): 937-945.
- Meas-Yedid, V., E. Glory, et al. (2004). Automatic Color Space Selection for Biological Image Segmentation. *ICPR* (3).
- Medical, N. (2013). "Obesity and Skin Problems." from <http://www.news-medical.net/health/Obesity-and-skin-problems.aspx>.
- Meijering, E. and G. van Cappellen (2006). "Biological Image Analysis Primer."
- Menesatti, P., C. Angelini, et al. (2012). "RGB color calibration for quantitative image analysis: the "3D thin-plate spline" warping approach." *Sensors (Basel)* **12**(6): 7063-7079.
- Mertsching, H., M. Weimer, et al. (2008). "Human skin equivalent as an alternative to animal testing." *GMS Krankenhhyg Interdisziplin* **3**(1): Doc11.
- Minimas, D. A. (2007). "Ageing and its influence on wound healing." *WOUNDS UK* **3**(1): 42.
- Mizukoshi, K. and K. Takahashi (2014). "Analysis of the skin surface and inner structure around pores on the face." *Skin Res Technol* **20**(1): 23-29.

References

- Montagna, W., A. M. Kligman, et al. (1992). Atlas of normal human skin, Springer Verlag.
- Montes, G. S. and L. C. Junqueira (1991). "The use of the Picrosirius-polarization method for the study of the biopathology of collagen." *Mem Inst Oswaldo Cruz* **86 Suppl 3**: 1-11.
- Muthukannan, K. and M. Moses (2010). Color image segmentation using *k*-means clustering and optimal fuzzy C-means clustering. *Communication and Computational Intelligence (INCOCCI), 2010 International Conference on, IEEE*.
- Noorlander, M. L., P. Melis, et al. (2002). "A quantitative method to determine the orientation of collagen fibres in the dermis." *J Histochem Cytochem* **50(11)**: 1469-1474.
- Ojala, T., M. Pietikainen, et al. (2002). "Multiresolution gray-scale and rotation invariant texture classification with local binary patterns." *Pattern Analysis and Machine Intelligence, IEEE Transactions on* **24(7)**: 971-987.
- Osman O., S., Harikumar P., Jassim S. and Langlands K. (2014). Automated Analysis of Collagen Histology in Ageing Skin. International Conference on Bioimaging, France.
- Osman, O. S., J. L. Selway, et al. (2013). "A novel method to assess collagen architecture in skin." *BMC Bioinformatics* **14**: 260.
- Osman, O. S., J. L. Selway, et al. (2013). "A novel automated image analysis method for accurate adipocyte quantification." *Adipocyte* **2(3)**: 160-164.
- Otsu, N. (1975). "A threshold selection method from gray-level histograms." *Automatica* **11(285-296)**: 23-27.
- Petrofsky, J. S., M. Prowse, et al. (2008). "The influence of ageing and diabetes on skin and subcutaneous fat thickness in different regions of the body." *JOURNAL OF APPLIED RELIABILITY* **8(1)**: 55.
- Philips, J. B.-T. W., D. P. P. Scheunders, et al. (2005). "Advanced Concepts for Intelligent Vision Systems."
- Pietikäinen, M., A. Hadid, et al. (2011). Computer vision using local binary patterns, Springer.
- Polesel, A., G. Ramponi, et al. (2000). "Image enhancement via adaptive unsharp masking." *Image Processing, IEEE Transactions on* **9(3)**: 505-510.
- Puizina-Ivi, N. (2008). "Skin aging." *Acta Dermatoven APA* **17(2)**: 47.
- Reinhard, E., M. Ashikhmin, et al. (2001). "Color transfer between images." *IEEE Computer graphics and applications* **21(5)**: 34-41.
- Rich, L. and P. Whittaker (2005). "Collagen and picrosirius red staining: a polarized light assessment of fibrillar hue and spatial distribution." *Braz J Morphol Sci* **22(2)**: 97-104.
- Rittscher, J., R. Machiraju, et al. (2008). Microscopic image analysis for life science applications, Artech House.
- S.p.A., D. (2013). Diapath Special Stains Handbook.
- Sabol, F., N. Bobrov, et al. (2014). "Skin wound healing in obese and lean male adolescent rats submitted to pre-weaning litter size manipulation." *Folia Biol (Praha)* **60(1)**: 21-27.
- Sadeghian, F., Z. Seman, et al. (2009). "A framework for white blood cell segmentation in microscopic blood images using digital image processing." *Biol Proced Online* **11**: 196-206.
- Sandby-Møller, J. (2003). Epidermal Thickness at Different Body Sites: Relationship to Age, Gender, Pigmentation, Blood Content, Skin Type and Smoking Habits. *Acta Derm Venereol* 410-413
- Sauermann, K., S. Clemann, et al. (2002). "Age related changes of human skin investigated with histometric measurements by confocal laser scanning microscopy in vivo." *Skin Res Technol* **8(1)**: 52-56.
- Scherzer, O. (2011). Handbook of Mathematical Methods in Imaging: Vol. 1, Springer.
- Seddon, J. M., K. M. Egan, et al. (1992). "Evaluation of skin microtopography as a measure of ultraviolet exposure." *Invest Ophthalmol Vis Sci* **33(6)**: 1903-1908.
- Selesnick, I. W., R. G. Baraniuk, et al. (2005). "The dual-tree complex wavelet transform." *Signal Processing Magazine, IEEE* **22(6)**: 123-151.
- Sertel, O., J. Kong, et al. (2009). "Histopathological image analysis using model-based intermediate representations and color texture: Follicular lymphoma grading." *Journal of Signal Processing Systems* **55(1-3)**: 169-183.

References

- Shan, K. (2014). "Automated Classification of Static Ultrasound Images of Ovarian Tumours Based on Decision Level Fusion."
- Shimizu, H. (2007). Shimizu's Textbook of Dermatology, Hokkaido University.
- Sparavigna, A. and R. Marazzato (2010). "An image-processing analysis of skin textures." *Skin Res Technol* **16**(2): 161-167.
- Tchivalevaa, L., H. Zenga, et al. (2010). "Skin roughness assessment."
- Toennies, K. D. (2012). "Guide to Medical Image Analysis."
- Trojahn, C., G. Dobos, et al. (2014). "Relation between skin micro-topography, roughness, and skin age." *Skin Res Technol*.
- Turner, N. J., M. A. Pezzone, et al. (2013). "Quantitative multispectral imaging of Herovici's polychrome for the assessment of collagen content and tissue remodelling." *J Tissue Eng Regen Med* **7**(2): 139-148.
- van Zuijlen, P. P., A. P. Angeles, et al. (2002). "Scar assessment tools: implications for current research." *Plast Reconstr Surg* **109**(3): 1108-1122.
- van Zuijlen, P. P., H. J. de Vries, et al. (2002). "Morphometry of dermal collagen orientation by Fourier analysis is superior to multi-observer assessment." *J Pathol* **198**(3): 284-291.
- Varani, J., M. K. Dame, et al. (2006). "Decreased collagen production in chronologically aged skin: roles of age-dependent alteration in fibroblast function and defective mechanical stimulation." *Am J Pathol* **168**(6): 1861-1868.
- Varani, J., R. L. Warner, et al. (2000). "Vitamin A antagonizes decreased cell growth and elevated collagen-degrading matrix metalloproteinases and stimulates collagen accumulation in naturally aged human skin." *J Invest Dermatol* **114**(3): 480-486.
- Verhaegen, P. D., J. V. Marle, et al. (2012). "Collagen bundle morphometry in skin and scar tissue: a novel distance mapping method provides superior measurements compared to Fourier analysis." *J Microsc* **245**(1): 82-89.
- Wang, Y., Z.-c. Mu, et al. (2008). Block-based and multi-resolution methods for ear recognition using wavelet transform and uniform local binary patterns. *Pattern Recognition, 2008. ICPR 2008. 19th International Conference on, IEEE*.
- Watt, F. M. and H. Fujiwara (2011). "Cell-extracellular matrix interactions in normal and diseased skin." *Cold Spring Harb Perspect Biol* **3**(4).
- Watt, F. M. and H. Fujiwara (2011). "Cell-extracellular matrix interactions in normal and diseased skin." *Cold Spring Harb Perspect Biol* **3**(4): a005124.
- Weiler, L., J. A. Knight, et al. (2007). "Comparison of self-reported lifetime sun exposure with two methods of cutaneous microtopography." *Am J Epidemiol* **165**(2): 222-230.
- Wu, M.-N., C.-C. Lin, et al. (2007). Brain tumor detection using color-based *k*-means clustering segmentation. *Intelligent Information Hiding and Multimedia Signal Processing, 2007. IHMSIP 2007. Third International Conference on, IEEE*.
- Wu, S., H. Li, et al. (2011). "Quantitative analysis on collagen morphology in aging skin based on multiphoton microscopy." *J Biomed Opt* **16**(4): 040502.
- Yoshida, T., T. Yoshiura, et al. (2008). "Image Processing for Drug Discovery Test With Cultured Cells." *YOKOGAWA TECHNICAL REPORT-ENGLISH EDITION- 45*: 31.
- Yun, T., Z. Ming-quan, et al. (2009). A region-based active contour model for image segmentation. *Computational Intelligence and Security, 2009. CIS'09. International Conference on, IEEE*.
- Zaidi, Z. and S. W. Lanigan (2010). *Skin: structure and function. Dermatology in Clinical Practice, Springer*: 1-15.
- Zhuo, S., J. Chen, et al. (2009). "Extracting diagnostic stromal organisation features based on intrinsic two-photon excited fluorescence and second-harmonic generation signals." *J Biomed Opt* **14**(2): 020503.
- Zou, Y., E. Song, et al. (2009). "Age-dependent changes in skin surface assessed by a novel two-dimensional image analysis." *Skin Res Technol* **15**(4): 399-406.
- Zulpe, N. and V. Pawar (2012). "GLCM Textural Features for Brain Tumor Classification." *International Journal of Computer Science Issues (IJCSI)* **9**(3).